

University of Southampton

# **Sub-Newton Monopropellant Thrusters for Small Spacecraft Propulsion**

by

**Ewan Fonda-Marsland**

ORCID ID: [0000-0002-1584-0067](https://orcid.org/0000-0002-1584-0067)

A thesis for the degree of  
Doctor of Philosophy

in the  
Faculty of Engineering and Physical Sciences  
Department of Aeronautical and Astronautical Engineering

November 2021



## **Abstract**

Faculty of Engineering and Physical Sciences

Department of Aeronautical and Astronautical Engineering

Doctor of Philosophy

by Ewan Fonda-Marsland

This thesis documents the design and testing of a sub-newton High Test Peroxide (HTP) monopropellant thruster architecture, suitable for micro and nanosatellite applications. The main goals were to demonstrate that a thruster targeting a 0.1 N thrust level could achieve a high-performance, and to investigate the fundamental processes governing its operation.

The thruster design exhibited high thermal performance using 87.5 %wt. HTP, with chamber temperatures in excess of 600 °C, corresponding to characteristic velocity efficiencies approaching  $0.963 \pm 0.004$  ( $1\sigma$ ). These values are similar to equivalent larger-thrust systems. The thruster was also tested with 98.0 %wt. HTP, with temperatures approaching 800 °C. These results represent some of the highest performance of an HTP monopropellant system, and is a first at sub-newton thrust levels. The experimental results were collected by direct measurement of the internal fluid conditions, something not previously achieved on a thruster of this scale. This was made possible by the novel application of conventional metal additive manufacturing techniques, permitting the inclusion of integrated instrumentation standpipes and other complex ancillary geometry.

The manufacturing process also enabled the production of a large number of different catalyst bed designs for use in one of the most extensive experimental studies on the impact of the catalyst bed geometry. The geometry was parametrically defined by the catalyst bed loading and aspect ratio, with respective values ranging from  $1.48 \text{ kg.m}^{-2}.\text{s}^{-1}$  to  $64.8 \text{ kg.m}^{-2}.\text{s}^{-1}$  and 0.33 to 6. The baseline thruster design, with a nominal bed loading of  $10 \text{ kg.m}^{-2}.\text{s}^{-1}$  and an aspect ratio of 2, had the highest demonstrated performance. However, data analysis suggested that lower catalyst bed loadings and aspect ratios, i.e. shorter and wider beds, should be more optimal over a blowdown range.

The study provided data towards validating a simplified pseudo-physical front model of the catalyst bed. This model describes the phase transition between the cool liquid/multiphase and the hot gas regimes. The phase change front was found to be axially close to the complete decomposition front, representing the maximum temperature in the bed. The catalyst bed flooding condition was used to relate the fundamental reactivity of the catalyst bed to the pseudo-physical front model. It was proposed that the reactivity can be used to size a bed with minimal experimental testing, through the Damköhler number: the estimated liquid-phase decomposition rate was greater than the rate of forced propellant diffusion for nominal catalyst bed operation. The pressure roughness phenomenon was also investigated using spectral analysis. These results were used to justify the proposed local oscillatory diffusion process in the catalyst bed. This is responsible for the pressure roughness, as well as the localised choking in the upstream liquid/multiphase regime that causes high pressure drop over this region.

An extensive study on microinjectors was also conducted. This is a field of limited published research. The study characterised the performance of Poiseuille-type microbore tube and Venturi-type orifice plate injectors. Poiseuille injectors demonstrated stable performance while orifice injectors were challenging to manufacture and prone to blocking. 'Chugging' flow instabilities were also captured, and it is proposed that the onset of this condition is tied to the inertia of the propellant flow through the injector. This, along with the minimum critical flow rate for the Venturi cavitation phenomenon, suggests that the Poiseuille microinjectors are a more robust architecture and better suited to sub-newton monopropellant thrusters.

# Table of Contents

Abstract .....	i
Table of Contents .....	ii
Table of Tables .....	v
Table of Figures.....	vii
Declaration of Authorship .....	xiii
Acknowledgements .....	xiv
Nomenclature.....	xv
Acronyms.....	xv
Symbols.....	xvi
Subscripts .....	xvii
1. Introduction.....	1
1.1. Background .....	1
1.1.1. Small Satellites and NewSpace .....	1
1.1.2. Propulsion Systems .....	2
1.1.3. Propellants and High Test Peroxide.....	6
1.2. Research Scope and Aims .....	8
1.2.1. Research Goals .....	8
1.2.2. Thesis Structure .....	8
2. Monopropellant Theory and Review of Literature.....	11
2.1. The Monopropellant Thruster System.....	11
2.1.1. The Rocket Nozzle.....	13
2.1.2. Monopropellant Catalyst Beds.....	19
2.1.3. Propellant Microinjectors.....	27
2.1.4. A Survey of Existing Micro-Monopropellant Propulsion Systems.....	30
2.2. Characterising Propulsion Performance.....	38
2.2.1. Steady State Performance .....	38
2.2.2. Quasi-Static Performance .....	40
2.2.3. Transient Effects .....	41
2.3. Review Summary.....	42
3. Experimental Methodology.....	45
3.1. Chemical Micropropulsion Lab Development.....	45
3.2. Instrumentation and Measurement Uncertainties .....	52
3.3. Summary .....	55
4. Baseline Thruster Development.....	57
4.1. Aims and Scope .....	57
4.2. Thruster Design.....	58
4.2.1. Blowdown System Model .....	58
4.2.2. Baseline Thruster Design .....	61
4.3. Thruster Manufacture .....	64
4.3.1. Baseline Thruster Manufacturing and Components.....	64
4.3.2. Thruster Inspection .....	66
4.3.3. Nozzle Characterisation .....	70

4.3.4.    Injector Selection .....	72
4.3.5.    Catalyst Bed Material and Retention.....	74
4.4.    Thruster Design Summary .....	79
5.    Baseline Thruster Testing and Performance .....	81
5.1.    Aims and Scope.....	81
5.1.1.    Test Campaign Methodology .....	81
5.1.2.    Example Test Run .....	82
5.2.    Steady State Performance.....	84
5.2.1.    Temperature and Thermal Performance.....	84
5.2.2.    Characteristic Velocity.....	87
5.2.3.    Pressure .....	90
5.3.    Quasi-Steady Performance.....	94
5.3.1.    Steady State Pressure Roughness .....	94
5.3.2.    Pressure Roughness First Significant Peak .....	95
5.3.3.    Pressure Coupling .....	98
5.4.    Summary of the Baseline Thruster Performance .....	100
6.    Catalyst Bed Study .....	101
6.1.    Aims and Scope of the Study .....	101
6.2.    Catalyst Bed Geometry Study.....	103
6.2.1.    Catalyst Bed Design .....	103
6.2.2.    Catalyst Bed Manufacture .....	105
6.2.3.    Catalyst Bed Test Campaign.....	106
6.2.4.    Catalyst Bed Performance.....	107
6.2.5.    Decomposition Plane Analysis .....	118
6.2.6.    Catalyst Bed Roughness and Quasi-Steady Performance .....	123
6.3.    Catalyst Material Study .....	126
6.3.1.    Catalyst Material Comparison .....	126
6.3.2.    Test Campaign .....	129
6.3.3.    Results .....	131
6.4.    Propellant Enthalpy Study .....	136
6.4.1.    Propellant Comparison .....	136
6.4.2.    Test Campaign .....	137
6.4.3.    Results .....	138
6.5.    Summary of the Catalyst Bed Study .....	141
7.    Micro-Injector Study .....	143
7.1.    Introduction and Scope .....	143
7.1.1.    Aims and Scope .....	143
7.1.2.    Study Methodology .....	144
7.2.    Injector Design and Manufacture.....	145
7.2.1.    Poiseuille Injectors .....	145
7.2.2.    Venturi Injectors.....	149
7.2.3.    Thruster Integration .....	154
7.3.    Cold Flow Characterisation .....	156
7.3.1.    Scope and Test Campaign .....	156
7.3.2.    Poiseuille Injector Cold Flow Characterisation .....	157

7.3.3. Orifice Injector Cold Flow Characterisation.....	160
7.4. Hot Firing Testing .....	164
7.4.1. Scope and Test Campaign.....	164
7.4.2. The Flow Coupling Condition.....	165
7.4.3. Quasi-Steady Performance.....	168
7.4.4. Spectral Analysis .....	171
7.4.5. Thruster Start-Up Performance.....	174
7.5. Summary of the Microinjector Study .....	177
8. Research Conclusions and Suggestions for Future Work.....	179
8.1. Conclusions .....	179
8.1.1. Demonstrating the Sub-Newton Microthruster Architecture.....	179
8.1.2. Optimising Microthruster Catalyst Beds.....	180
8.1.3. Micro Monopropellant Catalyst Bed Processes .....	181
8.1.4. Microinjector Architectures, and Flow Coupling Instabilities.....	182
8.2. Suggestions for Future Work .....	184
9. References.....	187
Appendix A: Experimental Data Analysis Techniques.....	195
A.1. Preliminary Data Processing .....	197
A.1.1. Data Preparation.....	197
A.1.2. Experimental Phenomena .....	198
A.2. Steady State Determination.....	202
A.3. Regression Fitting and Convergent Analytical Model .....	204
A.4. Spectral Analysis .....	205
A.5. Signal Correlation.....	211
Appendix B: Injector Computational Modelling .....	213
B.1. Injector Computational Modelling.....	213
B.2. Simulation Specification .....	214
B.3. Measurements .....	217
B.4. Finite Difference Mesh Study .....	219
B.5. Simulated Injector Designs.....	221

## Table of Tables

Table 1.1	- A selection of commercially available small and microscale chemical monopropellant microthrusters, with data taken from publicly available online sources and marketing collateral.....	5
Table 1.2	- Performance summary for different monopropellants. Note that values have been aggregated from the different propellant formulations. ....	6
Table 2.1	- A list of platinum-catalysed HTP reaction rates, extrapolated for HTP concentrations of 87.5 %/wt. at 25 °C. The specific Arrhenius factors for these conditions are included here, but they may be expressed differently in the literature source given the specific study focus.....	23
Table 2.2	- A list of the design architecture and nominal performance parameters of small and micro monopropellant thrusters, targeting thrusts $\leq 1$ N, using catalytic decomposition as their primary source of enthalpy.....	31
Table 2.3	- A list of the nozzle design parameters of small and micro monopropellant thrusters, targeting thrusts $\leq 1$ N, using catalytic decomposition as their primary source of enthalpy.....	33
Table 2.4	- A list of the catalyst bed design parameters of small and micro monopropellant thrusters, targeting thrusts $\leq 1$ N, using catalytic decomposition as their primary source of enthalpy.....	35
Table 2.5	- A list of the injector design parameters of small and micro monopropellant thrusters, targeting thrusts $\leq 1$ N, using catalytic decomposition as their primary source of enthalpy.....	37
Table 3.1	- The key fluid and instrumentation components in the micropropulsion lab PDS. ....	48
Table 3.2	- A list of the chemical micropropulsion lab PDS wetted materials and uses. ....	50
Table 3.3	- A list of the chemical micropropulsion PDS and thrust stand instrumentation. ....	52
Table 3.4	- Example expected measurement and propagated uncertainties from the instrumentation specification, expressed as a percentage of the signal value. ....	54
Table 4.1	- A list of the model parameters for the example simulation results in Figure 4.1. ....	61
Table 4.2	- Baseline thruster parameters including values from the model and literature, as well as the selected design. ....	62
Table 4.3	- A full list of the baseline thruster components, including any ancillary items for instrumentation and sealing. ....	65
Table 4.4	- Baseline thruster nozzle characterisation table, including the additional model parameters. ....	72
Table 6.1	- Absolute and parametric geometry for the selected catalyst bed designs. ....	104
Table 6.2	- Catalyst bed experimental nozzle flow characterisation results and updated catalyst bed loadings.....	106
Table 6.3	- Catalyst bed test campaign steady state results over the full tested range. ..	108

Table 6.4 – Catalyst bed packing parameters and estimated specific reactivities.....	121
Table 6.5 – A comparison of the catalyst bed packing parameters and estimated specific reactivities for the baseline and variant catalyst material .....	130
Table 6.6 – Steady state performance comparisons of the baseline and variant catalyst materials.....	134
Table 6.7 – A comparison of the 87.5 %/wt. and 98.0 %/wt. HTP propellant, showing key ideal performance metrics for the baseline catalyst bed and material.....	137
Table 7.1 – Ideal Poiseuille absolute and fractional pressure drops for 87.5 %/wt. HTP, considering the standard diameters of available microbore tubing, with a length of 100 mm. ....	146
Table 7.2 – Selected Poiseuille injector designs, including the number procured, including their expected fractional pressure drop and highest (BoL) expected Reynolds numbers. ....	147
Table 7.3 – Selected orifice plate injector design, including selected manufacturing process. ....	151
Table 7.4 – Ideal orifice plate absolute and fractional pressure drops for 87.5 %/wt. HTP, considering the selected injector designs .....	152
Table 7.5 – A list of the manufactured orifice plate injectors, by design, including the orifice geometry measured using optical inspection.....	154
Table 7.6 – A comparison of the different characterisation method results for the 7-50 and 10-100 Poiseuille injectors, including the resulting coefficients of discharge and model goodness of fit.....	158
Table 7.7 – A list of the successfully cold flow-tested orifice plate injectors.....	163
Table 7.8 – A list of the hot fire-tested injectors and their expected performance from the cold flow characterisation results over the nominal $0.05 \text{ g.s}^{-1} \leq m \leq 0.3 \text{ g.s}^{-1}$ range. ....	164
Table A.1 – A list of the main operational regimes of a standard thruster test.....	196
Table A.2 – A list of non-typical non-steady state operational modes affecting some thruster runs, including the significance of the apparent cause to the operation of the catalyst bed (i.e. a flight-optimised thruster design rather than the experimental lab thruster). ....	200
Table B.3 – Working fluid parameters for injector computational modelling.....	216
Table B.4 – A list of the base meshing parameters used for the mesh sensitivity study....	219
Table B.5 – A list of the simulated Poiseuille and orifice injectors designs. ....	221

## Table of Figures

Figure 1.1 – Typical performance approximations for different types of propulsion system [11]. Regions are coloured by their mode of thrust generation.....	3
Figure 1.2 – A schematic of a simple monopropellant propulsion system design.....	4
Figure 2.1 – Monopropellant propulsion system schematic and corresponding discretised flow elements.....	12
Figure 2.2 – A schematic of the principal isentropic nozzle flow, including nomenclature..	14
Figure 2.3 – Example sketches of axisymmetric (left) and planar (right) nozzle geometries.	17
Figure 2.4 – The simple one-dimensional model of the catalyst bed, including the expected static pressure and temperatures, along with the key pseudo-physical fronts.	21
Figure 2.5 – Cutaway sketches of the axisymmetric packed bed (left), axisymmetric monolithic (right) catalyst bed architectures.....	25
Figure 2.6 – Cutaway sketches of the two-dimensional packed bed (left) and integrated monolith (right) catalyst bed architectures.....	26
Figure 3.1 – A photograph of the chemical micropropulsion laboratory fluidic system, showing the thrust stand (downstream of MV5) on the left and the rest of the system on the right.....	46
Figure 3.2 – A schematic of the chemical micropropulsion lab PDS and thrust stand.....	47
Figure 3.3 – Example time domain data for the propellant tank mass and steady state mass flow rates, showing good agreement between the Coriolis mass flow meter and the propellant tanks load cell data. ....	53
Figure 4.1 – A schematic of the blowdown thruster model algorithm, including parameters and analytic equations. Iterative outputs generated at each time step are shown in red. ....	59
Figure 4.2 – Typical outputs of the blowdown model, generated using the example input parameters listed in Table 4.1. The nominal design point is indicated on each curve.....	60
Figure 4.3 – An engineering drawing of the highly-instrumented baseline thruster variant, including a detail view of the nozzle.....	63
Figure 4.4 – A photograph of the as-printed baseline thruster components. ....	64
Figure 4.5 – A photograph of the assembled standard variant baseline thruster. ....	66
Figure 4.6 – A micrograph section through the central axis of the highly-instrumented baseline thruster variant CT scan. The absolute pixel brightness has been adjusted to better visualize the catalyst pellets, also increasing the relative effect of the x-ray shadowing artifacts. ....	67
Figure 4.7 – 3D geometry of the CT scan surface data and the CAD design showing the distortion of the nozzle resulting from the inclusion of the plenum standpipe. ....	68
Figure 4.8 – Micrograph sections through the central axis and the plane of the nozzle throat of the highly-instrumented baseline thruster variant CT scan. ....	69

Figure 4.9	- Nozzle geometry parameters, extracted from the highly-instrumented baseline thruster variant CT scan. ....	69
Figure 4.10	- Example nozzle characterisation for the standard baseline thruster variant, showing data in the time domain (top) and characterisation domain (bottom). ....	71
Figure 4.11	- Baseline Poiseuille injector characterisation showing the time-series data (top) and the characterisation curve (bottom).....	74
Figure 4.12	- A example optical EFI micrograph of the catalyst material.....	75
Figure 4.13	- Statistical distribution of some of the geometric parameters of the catalyst material.....	75
Figure 4.14	- Baseline catalyst bed packing data taken from x-ray CT scan data, including the $1\sigma$ confidence interval. Packing is shown with respect to the axial (top) and radial (bottom) positions in the bed.....	77
Figure 5.1	- Example time domain test data of the standard baseline thruster variant, with a target inlet pressure of 10 bar. Firing valve actuation times are indicated....	83
Figure 5.2	- Steady state temperatures for the standard and highly-instrumented baseline thruster variants. Static ( $T_{in} = 25^{\circ}\text{C}$ ) and preheat-corrected adiabatic temperatures are included. ....	84
Figure 5.3	- Steady state temperature differences in the baseline thruster variant catalyst beds.....	85
Figure 5.4	- The catalytic thermal efficiency of the baseline thruster variants. A convergent model is fit to the data. The $1\sigma$ confidence interval of the model and the mid-bed thermal efficiency are included. ....	86
Figure 5.5	- Steady state characteristic velocities of the baseline thruster variants using the pressure and temperature methods. Adiabatic characteristic velocities are also included.....	88
Figure 5.6	- The ratio between the values of the two steady state characteristic velocity methods (left), and the pressure-derived characteristic velocity efficiency with tails showing the propagated instrumentation uncertainty (right).....	89
Figure 5.7	- Steady state thermal characteristic velocity efficiency of the baseline thruster variants. The $1\sigma$ confidence interval of the model is included.....	90
Figure 5.8	- Steady state pressures for the baseline thruster variants at different instrumentation positions.....	91
Figure 5.9	- Steady state pressure drops for the baseline thruster variant tests across the injector and the catalyst bed.....	92
Figure 5.10	- Highly-instrumented baseline variant catalyst bed pressure ratio, $dP_{upstream} / dP_{downstream}$ .....	93
Figure 5.11	- Absolute $1\sigma$ steady state pressure roughness for the baseline thruster variants at different instrumentation positions. ....	95
Figure 5.12	- Example time domain (top) and spectral response (bottom) data for the four pressure channels of the highly-instrumented baseline thruster. The thruster firing valve actuation times are indicated. ....	96

Figure 5.13	- First significant peak centre frequencies for the four pressure transducer channels.....	98
Figure 5.14	- Baseline quasi-steady pressure correlation of the DFTs across the injector (left) and the full bed (right). .....	99
Figure 6.1	- A photograph of all of the manufactured thruster variations, labelled with their corresponding notation. A 1 EUR coin is included for scale.....	105
Figure 6.2	- Modelled vs measured mass flow rate for each thruster. The expected equivalence line is plotted. .....	108
Figure 6.3	- Mean and absolute spread of the catalytic thermal efficiencies for the different catalyst bed geometries. .....	109
Figure 6.4	- Example time domain data for thruster tests with poor thermal performance. These tests are for the 3.5Ø14.0L – high aspect ratio bed, and the 3.5Ø3.5L – low aspect ratio bed.....	111
Figure 6.5	- Pressure and thermal characteristic velocity efficiencies plotted against propellant mass flow rate.....	113
Figure 6.6	- Thermal characteristic velocity efficiency regression-fitted models plotted against catalyst bed loading.....	115
Figure 6.7	- Variation of the fit coefficient $a$ (maximum characteristic velocity efficiency) for the analytical model with respect to the area (left) and aspect ratio (right) of the beds.....	116
Figure 6.8	- Variation of the fit coefficient $c$ (rate of convergence to maximum characteristic velocity efficiency) for the analytical model with respect to the area (left) and aspect ratio (right) of the bed.....	117
Figure 6.9	- Catalyst bed superficial residence time vs respect to catalyst bed loading. A subset (right) of the full dataset (left) is included to highlight $t_{bed} \leq 0.50$ s. Flooded tests are highlighted (circled) and the mean flooding onset time is shown with $1\sigma$ uncertainty bar.....	119
Figure 6.10	- Calculated Damköhler numbers from testing, highlighting flooded runs (circled). The mean flooding onset Damköhler number is shown with a propagated uncertainty bar, determined from the estimated parameter ranges. ....	122
Figure 6.11	- The $1\sigma$ pressure roughness for the full dataset of catalyst beds. Raw data and linear fit models (per catalyst bed) are both shown.....	124
Figure 6.12	- First significant peak centre frequencies for the chamber pressure channel for the full catalyst bed dataset.....	125
Figure 6.13	- A photograph for comparison of the variant (left) and baseline (right) catalysts.....	127
Figure 6.14	- The mean and $1\sigma$ confidence of the distribution of key variant catalyst geometric parameters.....	127
Figure 6.15	- A CT scan section through the central axis of the 1 N thruster to show the packing of the variant catalyst. The absolute pixel brightness has been adjusted to better visualize the catalyst pellets, also increasing the relative effect of the x-ray shadowing artifacts.....	128

Figure 6.16	- 1 N catalyst bed packing with the variant catalyst, with data taken from x-ray CT micrograph. Packing is shown with respect to the axial (top) and radial (bottom) positions in the bed.....	129
Figure 6.17	- Example time domain test data for 3.5Ø7.0L thruster with a target inlet pressure of 10 bar, for both baseline and H1820 variant catalysts. Firing valve actuation times are indicated.....	132
Figure 6.18	- Thermal characteristic velocity efficiencies of the variant thruster plotted against propellant mass flow rate. Flooded tests are highlighted (circled)..	133
Figure 6.19	- A direct comparison of the steady state chamber temperatures for the baseline thruster with the different concentration HTP propellants. ....	138
Figure 6.20	- Thermal characteristic velocity efficiencies of the baseline thruster with the two HTP propellant concentrations, plotted against propellant mass flow rate.	139
Figure 6.21	- Steady state chamber pressure roughness of the baseline thruster with the two HTP propellant concentrations, plotted against propellant mass flow rate.	140
Figure 7.1	- CT micrograph of the end section of a 254 $\mu\text{m}$ diameter Poiseuille injector. Sections showing the cross-sectional profile have been included.....	148
Figure 7.2	- Cross sectional area, circularity, and roughness (axial and circumferential) of the internal wetted surface, measured along the axial direction of the injector CT scan section from Figure 6.13. ....	148
Figure 7.3	- Drawings of the expected orifice injector radial wall profiles, manufactured using laser microdrilling (left) and double-sided chemical etching (right). ....	150
Figure 7.4	- A composite EFI reflection micrograph of a 1-120-50 etched orifice injector, showing the plate surface and the orifice. A higher resolution overlay is included. There is no appreciable difference on the reverse side, as expected due to the double-sided technique. ....	153
Figure 7.5	- A composite EFI reflection micrograph of the 6-36-50 etched orifice injector, showing the plate surface and the orifices. A higher resolution overlay shows the detail of a single orifice. This is imaged from the 'upper' surface with respect to the laser. ....	153
Figure 7.6	- A drawing illustrating the two methods for integrating both the Poiseuille (left) and Venturi (right) injector architectures into the system.....	155
Figure 7.7	- An example of the ideal computational model geometry of the 1-50-50 orifice injector, with the main regions and propellant flow indicated.....	156
Figure 7.8	- Example Poiseuille cold flow characterisations for 7-50 and 10-100 variants. The mass flow rate recast as the Reynolds number is shown, along with the turbulent transition region ( $1700 \geq Re \geq 1900$ ) highlighted.....	158
Figure 7.9	- Variation of the experimental (left) and computational (right) coefficients of discharge with respect to the Poiseuille injector geometric parameter, $\zeta_{pos}$ . ....	159
Figure 7.10	- Example Venturi-type 1-80-50 orifice injector characterisation showing the time-series data (top) and the characterisation curve (bottom). ....	160

Figure 7.11	- Optical micrographs (transmission and reflection) of an orifice injector pre and post cold flow characterisation showing the change in orifice throat geometry during testing.....	161
Figure 7.12	- Variation of the experimental and computational coefficients of discharge with respect to the Venturi-type orifice injector geometric parameter, $\zeta_{orf}$ .	162
Figure 7.13	- Static pressure field of different flows through the 1-100-50 orifice injector. The colour field is the static pressure, with colours normalised between $P_{amb}$ and $P_{in}$ , and clipped for $P \leq P_{vap, H2O} = 31.69 \times 10^{-3}$ bar. Streamlines are included to show the expected flow path, with the flow moving in the positive $I$ direction (from bottom to top).....	163
Figure 7.14	- Example time domain data of the thruster operating without any injector, with a set driving pressure of 2 bar and 10 bar.....	166
Figure 7.15	- Example time domain data of the thruster operating with pressure coupled across the injector. The two cases are for the 10-20 Poiseuille injector and the 1-120-50 orifice injector, both at a 5 bar target inlet pressure. ....	167
Figure 7.16	- Mass flow rate roughness' ( $1\sigma$ of the steady state) for the two injector architectures.....	168
Figure 7.17	- Fractional injector pressure drop ( $dP/P_c$ ) for the two injector architectures.	169
Figure 7.18	- Fractional pressure drop roughness, $\sigma P_c/dP_{inj}$ , for the two injector architectures.....	170
Figure 7.19	- First significant frequency peaks of the inlet and pre-bed pressure channels for both injector architectures.....	172
Figure 7.20	- Quasi-steady state correlation of the pressure channel DFTs across the Poiseuille and orifice injector architectures. ....	173
Figure 7.21	- Chamber pressure and temperature start-up transient times ( $\tau_{90}$ ) for both injector architectures.....	176
Figure 8.1	- A photo of a preliminary iteration of the vacuum thruster. ....	184
Figure 8.2	- An x-ray CT micrograph of a preliminary iteration of the vacuum thruster. ..	184
Figure A.1	- Example plots of the data from a typical thruster run.....	196
Figure A.2	- A typical plot of the inlet pressure signal and its time differential, demonstrating the actuation detection method. ....	197
Figure A.3	- An example of the quasi-steady trends affecting signals throughout a test. .	198
Figure A.4	- Examples of the non-typical transient modes showing the protracted start up (top), catalyst bed flooding (middle), and the pulsed steamy plume (bottom). ....	201
Figure A.5	- An example of the steady state analysis method results for a chamber temperature plot. This shows the time domain (top) and histogram data (bottom) along with the two resulting steady state regimes. ....	203
Figure A.6	- An of the effect of width of the window on the amplitude-normalised spectrograms of a chamber pressure dataset. The window sizes are 0.025 s,	

0.25 s and 1.0 s respectively, with the frequency domain clipped between 10 Hz and 300 Hz.....	207
Figure A.7 – An illustration on the effect of discontinuities in windowed sinusoidal signal (top), and the resulting DFT (bottom). The windowing function example uses a hanning function. ....	209
Figure A.8 – Examples of signal correlation outputs comparing the injector frequency coupling for strongly and weakly coupled systems.....	212
Figure B.1 – An example of the simplified injector geometry for computational modelling, showing the different partitioned regions (left), and mesh (right). .....	215
Figure B.2 – Example mass flow rate simulation data for a 4 bar pressure drop across a 1-100-50 injector.....	218
Figure B.3 – Computational results for the static pressure (left) and flow velocity magnitude (right) fields from a 4 bar pressure drop pressure drop across a 1-100-50 injector. ....	218
Figure B.4 – Mass flow rates results for the computational mesh refinement study.....	220

## Declaration of Authorship

I declare that this thesis and the work presented in it is my own and has been generated by me as the result of my own original research.

I confirm that:

1. This work was done wholly or mainly while in candidature for a research degree at this University;
2. Where any part of this thesis has previously been submitted for a degree or any other qualification at this University or any other institution, this has been clearly stated;
3. Where I have consulted the published work of others, this is always clearly attributed;
4. Where I have quoted from the work of others, the source is always given. With the exception of such quotations, this thesis is entirely my own work;
5. I have acknowledged all main sources of help;
6. Where the thesis is based on work done by myself jointly with others, I have made clear exactly what was done by others and what I have contributed myself;
7. Parts of this work have been published as:

Fonda-Marsland, E. A. P., Roberts, G. T., Ryan, C. N., Gibbon, D., "Methodology for Geometric Optimization and Sizing for Sub-newton Monopropellant Catalyst Beds", *J. Propuls. Power*, vol. 37, no. 2, pp. 713-724, Jun. 2021, doi: [10.2514/1.B38083](https://doi.org/10.2514/1.B38083);

"Development of a Low-Cost 0.1N High Test Peroxide Thruster Using Additive Manufacturing", in *AIAA Propuls. Energy 2019 Forum*, Indianapolis, IN (USA), Aug. 2019, doi: [10.2514/6.2019-4227](https://doi.org/10.2514/6.2019-4227);

Fonda-Marsland, E. A. P., Roberts, G. T., Gibbon, D., Ryan, C. N., "An Investigation into Injector Architectures for Sub-Newton Monopropellant Propulsion", in *8<sup>th</sup> EUCASS*, Madrid (Spain), Jul. 2019, doi: [10.13009/EUCASS2019-439](https://doi.org/10.13009/EUCASS2019-439);

Signature:

Date:

## Acknowledgements

I cannot possibly list everybody here who has helped me on this journey, but I would like to start by thanking everyone at Southampton who has supported me over the years. To all of the Astro group, current and past for keeping spirits high; lab technicians who showed me the ropes (and plasters), and everybody else who has kept me sane over the past years (Andrew, Pat I am looking at you): thank you all for seeing me through.

To the people from SSTL and LenaSpace, thank you for the amazing learning and fantastic experiences. I have definitely grown, and my work is richer because of it.

I would like to thank Dr Graham Roberts for all of his time, help, and insights into the world of monopropellants (and poor grammar). I hope I am not too bold to say that I am thankful for the bad weather cancelling your fishing trips: I know I would never have finished without you!

I am forever grateful for the support and patience of my supervisor Dr. Charlie Ryan. This undertaking has been a challenge and without doubt you are the only reason I stuck with it. Thank you for keeping me on track over the past 6 (?!?) years, it's certainly been a journey. I can honestly say that I've had a blast.

I would like to thank my family for their continuous love and support during the whole endeavour, especially to my mother who has suffered the brunt of my complaining and stunted grasp of the English language.

Finally, Lara. Thank you so much for putting up with my babbling and obstination, if you weren't as degil I don't think either of us would be sane! I know for certain that I wouldn't have made it to the end without you.

# Nomenclature

## Acronyms

ADN	Ammonium Dinitramide
AM	Additive Manufacture
AOCS	Attitude and Orbit Control System
BoL	Beginning-of-Life
BV	Bleed Valve
CAD	Computer Aided Design
CEA	Chemical Equilibrium Applications
COTS	Commercial off the Shelf
CT	Computed Tomography
DAQC	Data Acquisition and Control System
DFT	Discrete Fourier Transform
DI	Deionised (Water)
EFI	Extended Focused Image
EoL	End-of-Life
EP	Electric Propulsion
FFT	Fast Fourier Transform
GMM	Gaussian Mixture Model
HAN	Hydroxyl Ammonium Nitrate
HTCC	High-Temperature Co-fired Ceramic
HTP	High Test Peroxide
LEO	Low Earth Orbit
LEV	Local Exhaust Ventilation
LTCC	Low-Temperature Co-fired Ceramic
MEMS	Microelectromechanical Systems
MV	Manual Valve
NASA	National Aeronautics and Space Administration
NSTP	National Space Technology Programme
PDS	Propellant Delivery System
PFA	Perfluoroalkoxy Alkane
PPE	Personal Protective Equipment
PRV	Pressure Release Valve
PTFE	Polytetrafluoroethylene
SLM	Selective Laser Melting
SSA	Specific Surface Area
SSTL	Surrey Satellite Technology Ltd.
SV	Solenoid Valve
UKSA	UK Space Agency
UoS	University of Southampton

## Symbols

$a$	Acceleration [m.s <sup>-2</sup> ]; Coefficient - Maximum Equilibrium;
$A$	Area [m <sup>2</sup> ]
$AR$	Aspect Ratio
$c$	Effective Exhaust Velocity [m.s <sup>-1</sup> ]; Coefficient – Rate of Convergence to Maximum Equilibrium;
$c^*$	Characteristic Velocity [m.s <sup>-1</sup> ]
$C_F$	Coefficient of Thrust
$D$	Diameter [m]
$Da$	Damköhler Number
$\Delta v$	Change In Velocity [m.s <sup>-1</sup> ]
$dP$	Pressure Drop [bar]
$E_a$	Activation Energy [various]
$\eta_{c^*}$	Characteristic Velocity Efficiency
$\eta_{cat}$	Catalytical Thermal Efficiency
$F$	Thrust [N]
$Fq$	Frequency [Hz]
$G$	Catalyst Bed Loading [kg.m <sup>-2</sup> .s <sup>-1</sup> ]
$g_0$	Standard Acceleration due to Gravity, 9.807 [m.s <sup>-2</sup> ]
$\gamma$	Ratio of Specific Heats
$I_{sp}$	Specific Impulse [s]
$I_t$	Total Impulse [N.s]
$k$	Reaction Rate [various]
$L$	Length [m]
$\dot{m}$	Mass Flow Rate [g.s <sup>-1</sup> ]
$M$	Mass [kg]
$\mu$	Dynamic Viscosity [Pa.s]
$P$	Pressure [bar]
$R$	Radius [m]; Universal Gas Constant, 8.3145 [J.mol <sup>-1</sup> .K <sup>-1</sup> ];
$\rho$	Density [kg.m <sup>-3</sup> ]
$\sigma$	Standard Deviation [various]
$T$	Temperature [°C]
$v$	Velocity [m.s <sup>-1</sup> ]
$V$	Volume [m <sup>3</sup> ]
$w$	Propellant Mass Fraction
$z$	Non-Dimensional Wall Distance
$\delta z$	Wall Distance [m]
$\zeta$	Injector Geometric Parameter [m <sup>2</sup> ], [m <sup>3</sup> ]

## Subscripts

0	Initial Condition
1	Final Condition
<i>a</i>	Ambient
<i>ad</i>	Adiabatic
<i>c</i>	Chamber
<i>cat</i>	Catalyst
<i>e</i>	Exit
<i>flood</i>	Flooding
<i>inj</i>	Injector
<i>orf</i>	Orifice Injector
<i>P</i>	Pressure
<i>pos</i>	Poiseuille Injector
<i>rho</i>	Density
<i>spec</i>	Specific
<i>t</i>	Throat
<i>T</i>	Temperature
<i>vap</i>	Vapour



# Chapter 1

## Introduction

### 1.1. Background

#### 1.1.1. *Small Satellites and NewSpace*

The modern space industry is rapidly growing, fuelled by a significant interest from the commercial sector. Dubbed ‘NewSpace’, much of the growth is a result of the adoption of manufacturing at-scale and Commercial-off-the-Shelf (COTS) components. Mass manufacturing is essential to produce the large number of satellites required for mega constellations [1]–[3], while individual satellite customers have a growing interest in ‘Space-as-a-Service’: where a generic satellite bus may be used for a number of different missions [4]–[7]. Spacecraft designed for any of these applications require flexibility in the mission and orbit definition. This is enabled, in part, by the development of compact, low-thrust propulsion systems: Propulsion considerably expands the range of possible satellite missions, supplementing Attitude and Orbit Control System (AOCS) and allowing direct control of the orbit of small spacecraft. In addition, End-of-Life (EoL) debris mitigation is a growing concern, especially with the increased risk of space debris from large constellations. The most common mitigation strategy will use active propulsion to deorbit a satellite at EoL [8].

Another important trend in the space industry is miniaturisation. Many Space-as-a-Service providers are opting for small and microsatellite platforms with masses below 100 kg, and CubeSats formfactors are commonplace [9], [10]. Including a propulsion subsystem on this scale of satellite has traditionally been challenging given the constraints of volume and mass. However, with the advent of low-cost and reliable micropropulsion, defined here as systems where the thrust is below 1 N, the capabilities of these miniature spacecraft can approach parity with larger satellites.

### 1.1.2. Propulsion Systems

An understanding of the basic operation of propulsion systems is required to permit a comparison of different architectures and appropriate scales. From first principles, any propulsion system generates a thrust force by exchanging momentum with the environment [11]. In the case of propulsion systems using a propellant, mass is accelerated away from the engine to generate a force. Conservation of momentum describes the thrust generated as:

$$F = M_p a = \dot{m} c \quad (1.1)$$

Where  $M_p$  is the mass of the propellant and  $a$  is the acceleration of this mass. For a time-averaged stream of propellant, this is recast as the mass flow rate  $\dot{m}$  and the effective exhaust velocity  $c$ . The appropriate size of a propulsion system is chosen based on the application: the lower the mass of the satellite, the lower the required thrust for a given acceleration. Therefore, the thrust required by the modern miniature satellite buses must be considerably lower than for larger spacecraft.

The efficiency with which the exhaust mass generates thrust can be expressed using the specific impulse:

$$I_{sp} = \frac{I_t}{M_p g_0} = \frac{F}{\dot{m} g_0} = \frac{c}{g_0} \quad (1.2)$$

Where  $I_t$  is the total impulse imparted by the engine, and  $g_0$  is the standard acceleration due to gravity ( $9.8067 \text{ m.s}^{-2}$ ). Note that this derivation of the specific impulse is only true for steady state operation. The specific impulse is particularly important since  $I_{sp} \propto 1/M_p$ , so a higher value corresponds to a more efficient conversion of the propellant mass to thrust, reducing the amount of propellant on the satellite. This can therefore be used to compare the performance of different types of propulsion systems. The specific impulse is also directly proportional to the effective exhaust velocity, which is a measure of the enthalpy in the exhaust plume and therefore the thruster.

There are many different types of propulsion system in use on-orbit and in development today. The performance of each system is typically defined by the method of enthalpy generation. The relative performance values of the most common architectures are shown in Figure 1.1. These have been differentiated by their different methods for generating thrust. Electric Propulsion (EP) systems use electrical power to accelerate the exhaust, and have significantly higher specific impulses than those using physical nozzles. This is because they can achieve much higher effective exhaust velocities, but it comes at the cost of lower thrusts since the exhaust mass flow rates are lower. For small spacecraft low thrusts may not be an issue, however electric propulsion systems also require electric power. Raising this power may not necessarily be a challenge, but it will increase the complexity of the power subsystem. The higher thrust-to-power ratio will typically also decrease the thrust-to-weight ratio of an EP system [11].

In comparison, chemical propulsion systems use the release of enthalpy from chemical bonds in the propellant. The chemical enthalpy increases the temperature of the gases in the engine which are then accelerated using a nozzle to produce a high-speed exhaust. The exhaust is lower velocity than for an EP system, reflected in the reduced specific impulse, however they have much higher mass flow rates so produce more thrust. Chemical propulsion is less reliant on electrical power and

generally has a much higher thrust-to-weight ratio [11], making them attractive for small satellites where the mass is tightly constrained.

Given their higher thrust levels, chemical propulsion systems also enable a wide range of manoeuvres that require rapid velocity changes, including Beginning-of-Life (BoL) plane and altitude changes [12]. The change in velocity of a spacecraft can be calculated using the rocket equation [11]:

$$\Delta v = c \ln \frac{M_0}{M_1} = c \ln \frac{M_1 + M_p}{M_1} = c \ln \frac{1}{w} \quad (1.3)$$

Where  $M_0$  and  $M_1$  are the initial (wet) and final (dry) mass of the spacecraft, i.e.  $M_0 = M_1 + M_p$ . The mass fraction  $w = M_p/M_0$  is also commonly used as a design metric as it represents the fraction of the satellite that is propellant. Equation (1.3) shows that to achieve a particular  $\Delta v$ , the mass of propellant and exhaust velocity can be traded. While it is more efficient to maximise the velocity, e.g. using a high specific impulse EP system, the it is difficult to increase the propellant mass flow rate without very large electrical powers, increasing the manoeuvre time. Instead, low specific impulse chemical engines can exhaust a relatively much higher propellant mass so the manoeuvres are typically much shorter.

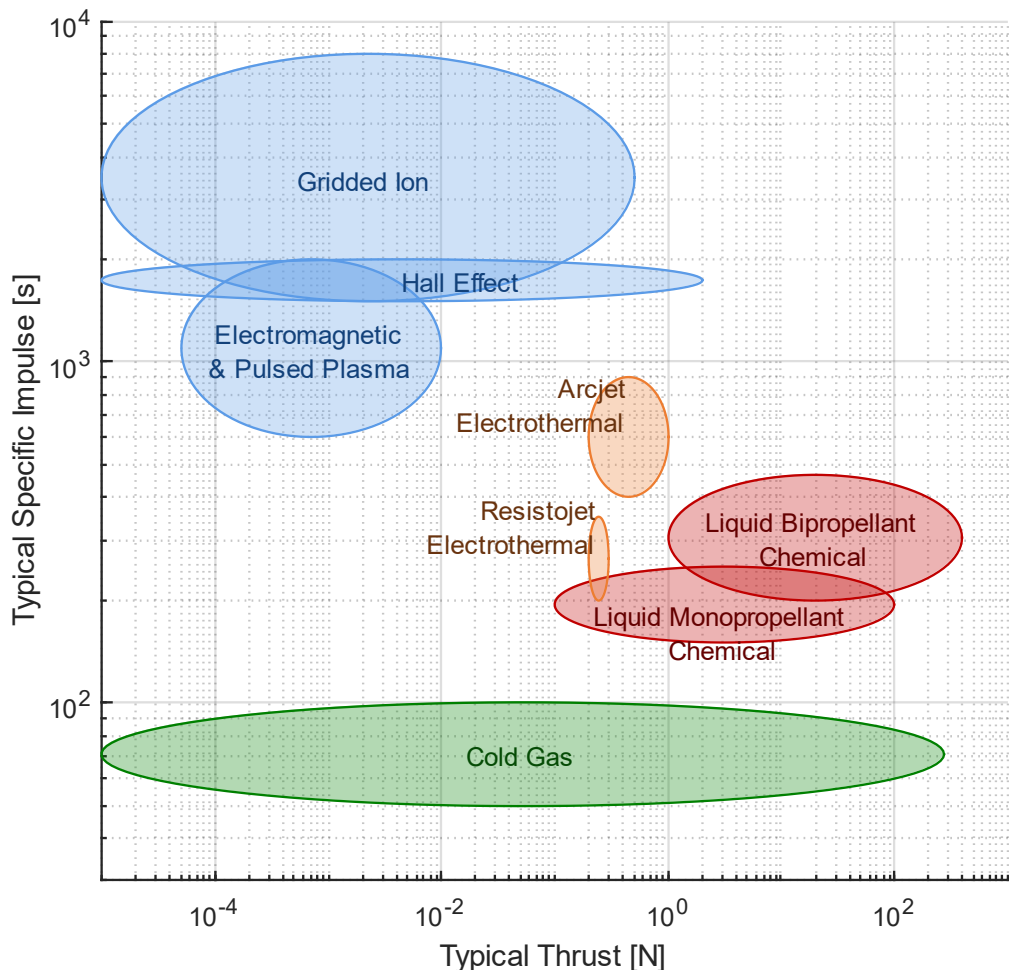


Figure 1.1 – Typical performance approximations for different types of propulsion system [11]. Regions are coloured by their mode of thrust generation.

A key challenge with chemical propulsion systems is the difficulty scaling them down to sub-newton thrusts, below 1 N. This is because they rely on tight tolerances on the geometry of their flow control components, including the physical nozzles used to accelerate the hot exhaust gases. The most suitable chemical propulsion system for these low thrusts are liquid monopropellant engines since they are the simplest type of liquid chemical engine and have the fewest components. They use only a single propellant to provide chemical enthalpy, which is typically a highly energetic and unstable chemical such as hydrazine [11]. The propellant will decompose in the thruster releasing enthalpy. This reaction is normally facilitated by a catalyst: a material which encourages the decomposition process, and therefore increases the decomposition rate.

In its most basic form, a monopropellant system consists of a thruster and a blowdown propellant storage/delivery system. A key benefit over bipropellant propulsion systems is that they only require a single propellant storage and delivery system, reducing the complexity and number of components. This comes with the trade-off of slightly lower thrusts and specific impulses, as illustrated in Figure 1.1. A monopropellant thruster is composed of three main elements: an injector to control the propellant flow, a catalyst bed to facilitate the decomposition reaction, and a nozzle to accelerate the hot reaction products to generate thrust. A schematic of this simple design is shown in Figure 1.2.

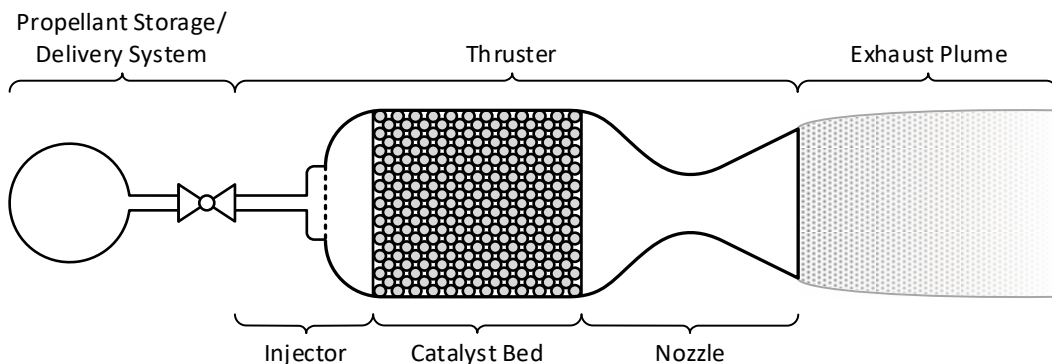


Figure 1.2 – A schematic of a simple monopropellant propulsion system design.

Given the simplicity of monopropellant thrusters, they are the best-suited liquid chemical propulsion system for a low thrust range. There are several documented modern commercial systems with nominal thrusts of 1 N and below, demonstrating moderate to high technological readiness levels. A selection of these is included in Table 1.1, listing the propellants and key performance ranges of each. The flight heritage of these systems is indicative of their relative novelty: There are unresolved issues with controlling the small-scale geometry of the components, and there are microflow effects that are not present at larger scales. These are discussed in more detail in a review of literature in Chapter 2, however these commercial systems and extensive research literature highlights the interest in chemical propulsion at low thrust ranges. Of particular note is that there are few commercial thrusters targeting thrusts below 1 N, and understanding the challenges of scaling monopropellant thrusters down to sub-newton thrust levels is an important topic in the field.

Table 1.1 – A selection of commercially available small and microscale chemical monopropellant microthrusters, with data taken from publicly available online sources and marketing collateral.

Organisation	System	Nominal (Range) Thrust [N]	Nominal (Range) Specific Impulse [s]	Propellant	Flight Heritage
Aerojet Rocketdyne	MR-401	0.09 (0.07 - 0.09)	– (180 - 184)	Hydrazine	Flown
Aerojet Rocketdyne	MR-103	1 (0.19 - 1.13)	– (202 - 224)	Hydrazine	Flown
Aerojet Rocketdyne	GR-1	1 (0.26 - 1.42)	235 (max.)	AF-M315E * <sup>1</sup>	Not Flown
ArianeGroup	1N Mono.	1 (0.32 - 1.10)	220 (200 - 223)	Hydrazine	Flown
Bradford ECAPS	100mN HPGP	0.1 (0.03 - 0.10)	– (196 - 209)	LMP-103S * <sup>2</sup>	Not Flown
Bradford ECAPS	0.5N HPGP	0.5 (0.12 - 0.50)	– (178 - 219)	LMP-103S * <sup>2</sup>	Not Flown
Bradford ECAPS	1N GP	1 (0.25 - 1.0)	– (194 - 227)	LMP-103S/LT * <sup>2</sup>	Not Flown
Bradford ECAPS	1N HPGP	1 (0.25 - 1.0)	– (204 - 231)	LMP-103S * <sup>2</sup>	Flown
Busek	BGT-X1	0.1 (0.20 - 0.18)	214 (max.)	AF-M315E * <sup>1</sup>	Not Flown
Busek	BGT-X5	0.5 (0.05 - 0.50)	– (220 - 225)	AF-M315E * <sup>1</sup>	Not Flown
IHI Aerospace	1N Mono.	1 (0.29 - 1.13)	– (208 - 215)	Hydrazine	Flown
MOOG	MONARC-1	1 –	228 –	Hydrazine	Flown
Northrop Grumman	MRE-0.1	1 –	216 –	Hydrazine	Flown
SSTL	1N Mono.	1 (0.27 - 1.05)	151 (149 - 160)	HTP 87.5%	Not Flown
Thales	1N Mono.	1 (0.36 - 1.45)	– (205 - 221)	Hydrazine	Flown

\*<sup>1</sup> Hydroxyl-ammonium-nitrate-based propellant.

\*<sup>2</sup> Ammonium-dinitramide-based propellant.

### 1.1.3. Propellants and High Test Peroxide

The selection of low thrust commercial systems in Table 1.1 are designed for a variety of different propellants. Many of these thrusters are using newer low toxicity green propellants based on ionic liquid blends. These were mainly developed as replacements to hydrazine due to its high toxicity and therefore increased handling costs [11]–[15]. The two main types of ionic liquid propellants are formulated from hydroxyl ammonium nitrate (HAN) or ammonium dinitramide (ADN). Some key physiochemical properties and performance values are shown for common propellant blends are included in Table 1.2. Given their highly energetic nature, these propellants boast better performance than conventional hydrazine monopropellant.

Another propellant with considerable heritage as a monopropellant and an oxidiser in bipropellant systems is High Test Peroxide (HTP) [11], [13], [15]. This is high concentration ( $\geq 60\%$  by weight) aqueous hydrogen peroxide and is particularly energetic. Typical concentrations for propulsion applications are between 87.5 %/wt. HTP and 98.0 %/wt. HTP. The performance range of these blends are also given in Table 1.2, showing generally lower performance than the other modern green propellants as well as hydrazine. HTP has a history of difficulties with safe and stable storage since hydrogen peroxide is relatively unstable and prone to react with a large number of chemicals [15], [16]. Along with the lower performance means that it is largely that it is not considered as a monopropellant for on-orbit propulsion.

Note that the data presented in Table 1.2, as well as throughout the remainder of this work, is calculated from the fundamental physiochemical parameters of the exhaust gases. These are derived using the thermodynamics and chemical equilibria model in the NASA Chemical Equilibrium Applications (CEA) software application [17], [18].

Table 1.2 – Performance summary for different monopropellants. Note that values have been aggregated from the different propellant formulations.

Criteria	Hydrazine	HTP	HAN [15]	ADN [15]
Formulation	–	87.5 %/wt. – 98.0 %/wt.	AF-M315E, SHP163, HNP221, HNP225, GEM	LMP-103S, FLP-103, FLP-106, FLP-107
Specific Impulse [s] <sup>*1</sup>	239	162 – 182	213 – 283	252 – 258
Density, $\times 10^{-3}$ [kg.m <sup>-3</sup> ]	1.01	1.37 – 1.45	1.16 – 1.51	1.24 – 1.36
Density Specific Impulse [s] <sup>*1</sup>	239	226 – 264	247 – 427	312 – 349
Adiabatic Decomposition Temperature [°C]	896	663 – 924	717 – 2130 <sup>*2</sup>	1630 – 1870

<sup>\*1</sup> Performance assumes ideal operation with 20 bar chamber pressure, 50:1 expansion ratio and ambient vacuum conditions.

<sup>\*2</sup> Excluding performance for GEM – a proprietary blend with limited public data.

Table 1.2 also lists the specific impulse recast as a ‘density’ specific impulse:

$$I_{sp,\rho} = I_{sp}\delta = I_{sp} \frac{\rho_p}{\rho_{H_2O}} \quad (1.4)$$

Where  $\delta$  is the propellant specific gravity, or the ratio of the propellant density  $\rho_p$  to the density of water  $\rho_{H_2O}$ . Note that the specific gravity is used rather than the propellant density since it provides a more direct comparison to the standard specific impulse. The density specific impulse is an important metric for spacecraft with limited volume budgets, such as microsatellites and CubeSats. For these applications, higher density propellants are favoured because they offer better performance per unit volume. This is especially interesting since HTP outperforms hydrazine considering this metric, i.e. it is well suited for low cost small satellite propulsion systems. Although despite this, the performance of modern ionic-liquid based propellants is still greater than HTP.

Given the higher performance and increased safety compared to hydrazine, there is considerable interest in ionic liquid-based propellants from industry. However, they are expensive and can be difficult to handle, requiring preheating to prevent precipitation of ionic salts and can be prone to detonation [13]–[15]. From the perspective of research, HTP is an excellent monopropellant. It is relatively low cost as lower concentrations of hydrogen peroxide are widely used in other industries [13], [15], [16]. It is also comparatively safe to handle, with a low toxicity and maximum decomposition temperature, simplifying operational procedures. Another benefit of the lower decomposition temperature is that it is compatible with common materials, including many stainless-steel alloys. This increases the range of materials suitable for the high temperature reaction chamber and nozzle. In comparison, higher enthalpy propellants require cooling to reduce the temperature of the thruster’s material, or they rely on using refractory materials with higher service temperatures [15]. One final advantage for HTP propellants is the relatively simple and well-understood chemistry [19]. The ionic liquid-based propellant blends include a variety of different organic chemicals and the reaction kinetics are not as well researched or documented. Further work is required to characterise how these propellants behave in catalysis, and there is less published literature covering reaction rates and kinetics than for aqueous hydrogen peroxide. As a result, HTP is ideal for developing an engineering breadboard thruster, suitable for investigating the impact of scaling a system down to sub-newton thrust levels.

## 1.2. Research Scope and Aims

### 1.2.1. Research Goals

The goal of the current research is two-fold. Firstly, as will be discussed later, there is a relative lack of clearly documented design methodology for high-performance chemical monopropellant microthrusters. The commercial thrusters in Table 1.1 do not provide details on their design and there is a lack of systematic scientific literature. In addition, the majority of published research studies on microthrusters suffer from poor performance or a lack of instrumentation. Therefore, this work will seek to demonstrate a high-performance monopropellant thruster targeting a nominal 0.1 N thrust. This will use 87.5 %/wt. HTP as a baseline propellant, and will be used to investigate suitable manufacturing techniques for at-scale or COTS production processes. A particular focus will be on presenting the methodology for design and manufacturing, as well as the performance data, with an aim to optimise the propulsion system.

Another goal of this research is to investigate the fundamental processes inside a microthruster. These include the catalytic decomposition and microfluidic effects, as well as the operation of microinjectors. These are likely to be impacted by the small scales in sub-newton catalyst beds, and since sub-newton thrusters are still fairly novel, at the time of writing there have only been initial studies into how the processes in macroscale thrusters scale down. Again, given issues with low performance or a lack of high-quality data, these studies typically rely on computational methods. This work will investigate a range of different thruster designs, varying the geometry of the catalyst bed and injector elements. This will make use of novel application of manufacturing techniques to allow direct instrumentation of the internal fluid conditions. These studies will provide insight into the fundamental processes and the impact of miniaturising a monopropellant thruster.

### 1.2.2. Thesis Structure

This thesis is divided into eight chapters, including this introduction. Chapter 2 presents a comprehensive literature review, introducing the key theory for the design and analysis of monopropellant microthrusters. This is supplemented by a presentation of the main efforts investigating similar scale systems from literature. A brief discussion also outlines the main analysis techniques used to characterise monopropellant thruster performance.

Since the majority of the research presented is experimental, details of the methodology are outlined in Chapter 3. There is a particular focus on data collection, as this underpins the entirety of the research and the contribution to the wider field: Ensuring the collection of high-quality data is important given the relative lack of information of the performance of sub-newton monopropellant thrusters.

Chapter 4 details the design, manufacture, and inspection of a baseline microthruster. The testing and analysis of the performance of this thruster is presented in Chapter 5. These two sections demonstrate the performance of the thruster architecture and detail the analysis techniques. These are essential as they form the basis of the research in the later studies.

A study into the design and optimisation of monopropellant microscale catalyst beds is presented in Chapter 6. The focus of this study is on the impacts of the catalyst bed design on the performance of a monopropellant microthruster. This also seeks to link the observed performance to the fundamental processes.

Chapter 7 covers the design and performance of microinjectors. This looks at different types of injectors, including how varying the geometry and manufacturing technique affect the propellant flow into the thruster, and therefore its performance and operation.

Finally, Chapter 8 brings together the key conclusions of this research from the perspective of the main goals: optimisation of the microthruster design, and key findings about the microscale processes. In addition, this chapter recommends some topics for future study to further advance the findings of this current work.

Two appendices are also included in this thesis. These document the experimental data analysis techniques and computational modelling methodology, both supporting the experimental results. Appendix A, the experimental data analysis techniques, is particularly important since many of the techniques used are novel to the monopropellant propulsion field, and there appears to be limited rigor in the data analysis in the monopropellant microthruster studies published to date. Appendix B describes the computational modelling methodology used to investigate the fluid flow in the injector, supporting the detailed experimental study in Chapter 7. The information in these Appendices is not included in the main body of the thesis since a detailed understanding of the techniques and methodology is not required for their application to the analysis in the main thesis.



# Chapter 2

## Monopropellant Theory and Review of Literature

To design and test a monopropellant thruster, it is essential to outline the underpinning theory and research efforts in the field. This chapter will introduce the theory required to design a HTP microthruster, and will also include a discussion of some key literature focusing on the specific challenges of micropropulsion. These are namely concerns arising from the microfluidic effects and aspects of small-scale design and manufacture. In addition, it is important to outline the specific methods of characterising the performance of a propulsion system.

### 2.1. The Monopropellant Thruster System

It is essential to define the governing processes and analytical theory of the system. A monopropellant thruster is a chemical thermal rocket that accelerates high pressure and temperature gases through a nozzle to generate thrust. The thrust is a result of momentum exchange between the high velocity exhaust with the environment, imparting a reaction force to the propulsion system and the attached spacecraft. This was introduced in Chapter 1, however a more complete model of the system is needed to be able to design and assess the performance of a thruster. Of note is that the flow through the system is coupled, i.e. the processes throughout the system affect the overall flow and performance of the entire thruster. The system is principally governed by mass flow continuity, where the mass flux throughout is constant. The mass flow rate can be calculated using:

$$\dot{m} = \rho v A = \text{const.} \quad (2.1)$$

Where  $\dot{m}$  is the mass flow rate,  $\rho$  is the local fluid density, and  $v$  is the fluid velocity passing through a cross-sectional area  $A$ . For conservation, this is valid at any cross-section in the system. It is worth noting that this only necessarily holds for mean (time averaged) flow. However, the local mass transport may vary transiently under some specific local conditions, such as in the highly turbulent reacting flow in the thruster. Despite this, these variations will average out to a constant mass flow rate and can be used to relate the flow in different regions of the thruster to each other.

Mass continuity allows the system to be discretised into a series of coupled flow elements, shown in the schematic of a monopropellant propulsion system in Figure 2.1. The corresponding elements from this figure are:

1. Pressurant tank and control system – The tank and flow control elements that maintains a driving pressure to move the propellant through the system.
2. Propellant tank – The main reservoir for storing the propellant.
3. Propellant delivery – The supporting flow control components required to deliver the flow to the thruster, including the main firing control valve.
4. Thruster injector – The components controlling the propellant flow rate and distribution into the thruster and catalyst bed.
5. Thruster catalyst bed – The region filled with catalytically active material used to decompose the propellant.
6. Thruster nozzle – The geometry that accelerates the flow of decomposed gases out of the propulsion system, resulting in thrust.

The pressurant, propellant storage, and propellant delivery elements are not strictly part of the thruster and can be grouped together into a Propellant Delivery System (PDS): the collection of components that control the propellant flow. In representative flight hardware, they will be integrated into a satellite propulsion subsystem, although these may be laboratory hardware for on-ground testing. From the perspective of the thruster, there should be little appreciable difference between the implementation of the PDS. The flow through the system is fundamentally dependant on the driving (tank) and ambient pressure, as well as the specific flow characteristics of each element, although the operation each elements can be described independently knowing the conditions at the up and downstream boundaries. The following sections details key supporting theory and literature, covering the nozzle, catalyst bed and injector components.

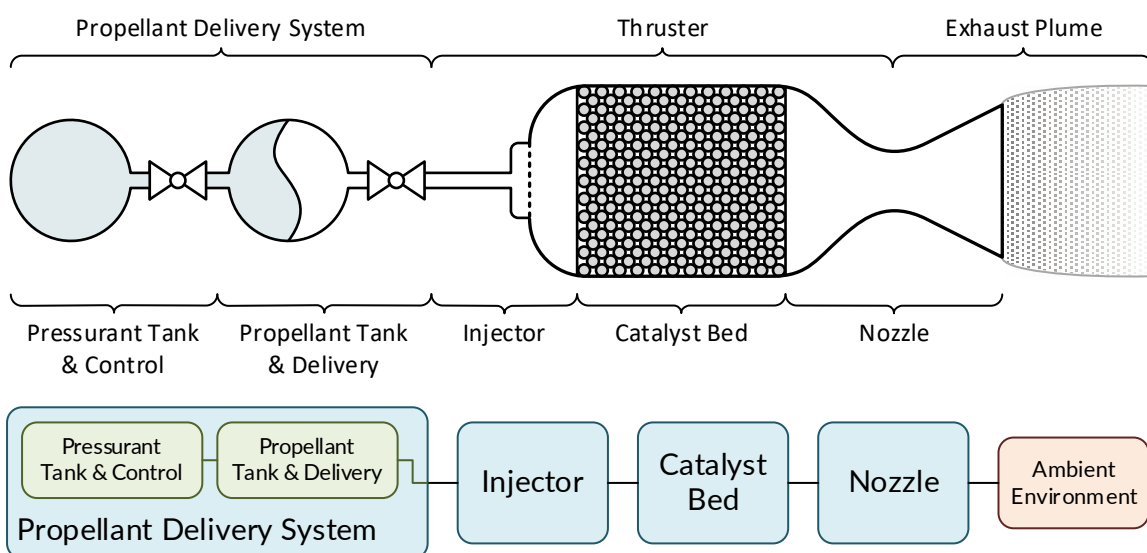


Figure 2.1 – Monopropellant propulsion system schematic and corresponding discretised flow elements.

### 2.1.1. The Rocket Nozzle

A rocket nozzle's primary purpose is generating thrust. Its design sets the mass flow rate of a thruster, and its operation introduces some constraints on the upstream elements of the system. The flow through a nozzle must therefore be described, and this section outlines some of the key equations. These are based on analytical isentropic compressible flow theory which is not included here. The full derivation steps can be found in a wide range of appropriate literature [11].

The thrust is a result of the momentum transfer from the nozzle to the environment by the exhaust gases. The momentum in the exhaust is due to the expansion of the high enthalpy flow, accelerating it to high velocities. This is typically achieved by using a specific nozzle geometry with a converging-diverging profile to accelerate the flow to supersonic conditions. The basic thrust equation generated by this momentum transfer was introduced in equation (1.1). This is overly simplified and is only valid under certain conditions, where the exhaust is ideally expanded, i.e. when the exhaust fluid pressure at the exit is equal to the ambient pressure. In any other case, there will be additional forces resulting from the pressure differential between the exhaust and the environment.

The thrust from a general nozzle is the sum of the 'Momentum thrust' and the 'Pressure thrust': the forces from the exhaust jet momentum transfer, and the pressure differential between the jet and the ambient environment at the nozzle exit plane respectively:

$$F = \dot{m}v_e + (P_e - P_a)A_e \quad (2.2)$$

Where  $v_e$  is the mean exit velocity,  $P_e$  and  $P_a$  are the nozzle exit and ambient pressures, and  $A_e$  is the nozzle exit area. In the ideally expanded case, there is no pressure thrust since  $P_e = P_a$ , so equations (1.1) and (2.2) are equivalent and the effective exhaust velocity  $c \equiv v_e$ . The thrust equation can be substituted into equation (1.2), to get the specific impulse including 'Pressure thrust':

$$I_{sp} = \frac{\left(v_e + \frac{(P_e - P_a)A_e}{\dot{m}}\right)}{g_0} \quad (2.3)$$

An issue with these two equations is that they require knowledge of the conditions at the nozzle exit plane. These are not readily measurable on a real thruster, or necessarily obvious from the upstream conditions, although they can be derived by taking the assumption of choked flow through the nozzle. This is a specific sonic condition where the fluid velocity at the smallest area of the constriction, the nozzle throat, is the same as the local speed of sound of the fluid. This, along with some additional parameters describing the upstream conditions allows the calculation of the exit conditions. A schematic of a converging-diverging nozzle and the key parameters needed to model of the flow are detailed in Figure 2.2.

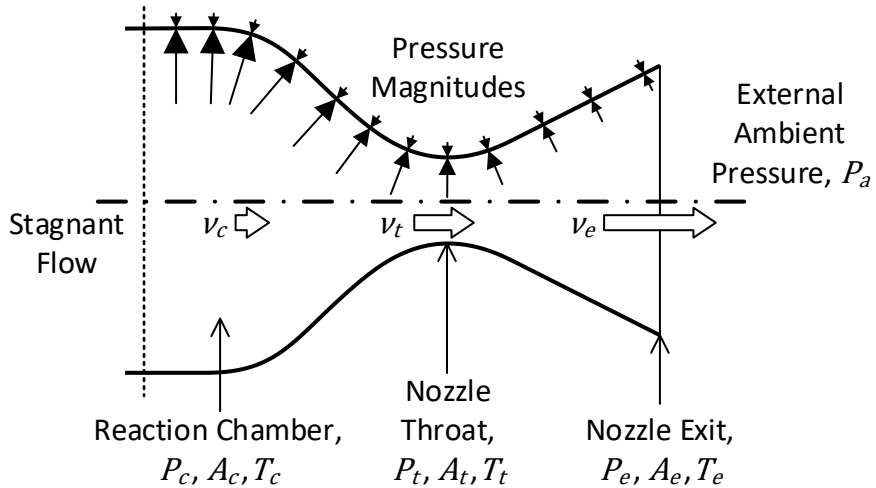


Figure 2.2 – A schematic of the principal isentropic nozzle flow, including nomenclature.

Isentropic compressible flow through a nozzle makes several implicit assumptions:

- Isentropic, adiabatic nozzle – the flow has no change in entropy through the nozzle and the enthalpy is conserved in the flow, i.e. no heat loss through the nozzle walls.
- Choked flow – the flow is supersonic with a Mach number,  $M = 1$  in the throat. This implies that the flow transitions from incompressible to compressible, and that any changes in the downstream environment will not affect conditions upstream of the throat.
- Steady flow – the fluid velocity is fully developed and constant with time.
- Attached flow – the flow separates at the nozzle exit plane.
- Frozen flow – the chemical species in the flow are fixed in composition and concentration, i.e. the propellant is fully decomposed before entering the nozzle. into the nozzle, i.e. the propellant is fully decomposed.
- Stagnated chamber – there is negligible flow velocity upstream of the nozzle.

Some of these assumptions are especially important when considering the design and operation of a sub-newton monopropellant thruster. The small size of the catalyst bed and the geometry of micronozzles will result in specific effects that impact the performance of a microthruster compared to a conventional macroscale thruster. These impacts will be discussed in more detail later.

By assuming upstream conditions and energy conservation, the exhaust velocity is described as a function of either the pressure or temperature ratios across the nozzle:

$$v_e = \begin{cases} \sqrt{R_{spec} \frac{2\gamma}{\gamma-1} T_c \left(1 - \frac{T_e}{T_c}\right)} & (2.4) \\ \sqrt{R_{spec} \frac{2\gamma}{\gamma-1} T_c \left(1 - \left(\frac{P_e}{P_c}\right)^{\frac{\gamma-1}{\gamma}}\right)} & (2.5) \end{cases}$$

Where  $P_c$  and  $T_c$  are the upstream chamber pressure and temperature,  $T_e$  is the nozzle exit temperature,  $R_{spec} = R/W$  is the specific gas constant defined as the ratio of the Universal Gas

Constant  $R$  (8.3145 J.K<sup>-1</sup>.mol<sup>-1</sup>) to the fluid mean molecular weight  $W$ , and  $\gamma = c_p/c_T$  is the ratio of specific heat capacity at constant pressure  $c_p$  and constant volume  $c_V$ .

The exhaust velocity and therefore the performance of the thruster are maximised as the chamber pressure and temperature are increased. The chamber temperature is especially important: from equation (2.5),  $P_e$  will be small for a well-designed vacuum nozzle. In this case varying the chamber pressure will have a minimal effect on the exhaust velocity. Therefore, the chamber temperature should be maximised to achieve the highest performance. The chamber temperature is limited by the chemical properties of the propellant and cannot exceed the adiabatic decomposition temperature  $T_{ad}$ . For any given propellant, the performance is limited by any thermal losses through the thruster walls.

The sonic condition in nozzle throat chokes the flow and sets the mass flow rate of the fluid through the nozzle. Sizing the throat will therefore determine the thrust. Assuming mass and energy conservation, the mass flow rate and the nozzle throat area  $A_t$ , are related through:

$$\dot{m} = \frac{A_t P_c \gamma}{\sqrt{\gamma T_c R_{spec}}} \sqrt{\left(\frac{2}{\gamma + 1}\right)^{\frac{\gamma+1}{\gamma-1}}} \quad (2.6)$$

This is a demonstration of the choking phenomenon: the mass flow rate depends only on the throat geometry, chamber conditions, and exhaust fluid physiochemical parameters, and there is no effect from the downstream environment. An important issue specific to microthruster nozzles is that, since  $\dot{m} \propto A_t$ , the lower mass flow rates will result in smaller nozzle throat cross-sectional areas. As the cross-sectional area of a flow decreases, viscous effects will have a greater impact, reducing the performance through friction. This is because the turbulent boundary layer will be make up a relatively larger proportion of the flow [20], [21].

The exit area of the nozzle is another essential geometric parameter for calculating the thrust. This affects the expansion ratio of the exhaust gases, and is commonly expressed as a function of the pressure ratio:

$$\frac{A_t}{A_e} = \left(\frac{\gamma + 1}{2}\right)^{\frac{1}{\gamma+1}} \left(\frac{P_e}{P_c}\right)^{\frac{1}{\gamma}} \sqrt{\frac{\gamma + 1}{\gamma - 1} \left(1 - \left(\frac{P_e}{P_c}\right)^{\frac{\gamma-1}{\gamma}}\right)} \quad (2.7)$$

The inverse of this,  $A_e/A_t$  is the area ratio of the divergent nozzle section. This depends on the chamber pressure but for  $P_c = 10$  bar, an ideal nozzle under atmospheric (sea-level) conditions, i.e. where  $P_e = P_a \approx 1$  bar, this is approximately 2.2. Most low-altitude nozzles use a design in the 3 – 30 range given the changing atmospheric density [11]. For vacuum conditions, an ideal nozzle area ratio will approach infinity so a design value between 200 and 300 is generally selected since a longer nozzle will increase the mass of the thruster and viscous losses [11]. This under-expanded nozzle will have non-ideal performance, but as  $P_e \sim 0$  the impact will be minor, since  $P_e \approx P_a$ . The exhaust velocity will also not significantly change: from equation (2.5), as  $P_e \rightarrow 0$ :

$$v_e = \sqrt{R_{spec} \frac{2\gamma}{\gamma - 1} T_c} \quad (2.8)$$

These analytical model equations represent the ideal flow through a nozzle and do not account for any inefficiencies and losses. In addition to any viscous boundary layer effects, losses also result from local flow structures such as separation and shockwave formation. These effects are more generally associated with the high-speed transonic and supersonic flow regimes in the throat and divergent regions. The tolerances and specific shape of the geometry in these regions is constrained by the manufacturing processes. Since the scale decreases as thrusts approach 1 N and below, it is common to simplify the complex nozzle profile. For example, conical divergent profiles and sharp-corner throat orifices may be used at these scales [12].

As mentioned, the problem is more pronounced in sub-newton thrusters, where the scales of the geometry further decrease:  $F_{ideal} \propto A_t \propto D_t^2$  where  $D_t$  is the throat diameter. The sonic velocity of the exhaust gases in the throat is independent of the geometry and thrust, so there is a greater effect from viscosity for lower thrust systems. The Reynolds number can give a measure of the significance of the viscous effects. It is defined as the ratio of the inertial forces to viscous forces in a flow:

$$Re = \frac{\rho v L}{\mu} = \frac{4\dot{m}}{\pi D \mu} \quad (2.9)$$

Where  $\mu$  is the dynamic viscosity of the fluid and  $L$  is the characteristic linear dimension of the flow, which in the case of a nozzle is the throat diameter. The Reynolds number has also been expressed in terms of the mass flow rate through a constant circular cross-section of diameter  $D$ . Higher values for  $Re$  indicate a greater relative dominance of inertial forces and a turbulent flow, while lower values are indicative of a viscous-dominated laminar regime. Experimental studies into nozzle performance for cold and warm gas nozzles with a nominal target thrust range of 0.1 mN – 1.1 mN show that for nozzles operating in low Reynolds number regimes, of the order of  $10 \leq Re \leq 1000$ , there are significant performance impacts due to the viscous losses [22]. It has been found through experimental and computational studies that larger diverging nozzle angles and shorter nozzle area ratios reduce the viscous losses. These studies looked at the performance of MEMS micronozzles, targeting thrusts around 1  $\mu$ N – 20  $\mu$ N [20], [21], [23]–[25]. The viscous boundary layers for  $8 \leq Re \leq 800$  are shown to create large subsonic flow regimes near the walls, so increasing the rate of expansion and shortening the nozzles helps to preserve the high exhaust velocities. This is true for both conical [20], [21] and bell-profiled micronozzles [23]. Increasing the divergence angle does result in losses due to higher non-axial flow components in the exhaust flow. Micronozzles benefit from comparatively higher divergence angles as the cross-sectional area increases faster, reducing the viscous boundary layer formation. Worth noting, the micronozzles in these studies target lower thrusts than the nominal 0.1 N goal in the current work, so viscous losses here should be less significant but still require consideration.

The ability to manufacture the nozzle geometry is another issue. Conventional machining of micronozzles is not appropriate and many of the experimental studies use more exotic manufacturing processes, such as etching. These are common MEMS manufacturing techniques, although they have drawbacks. The most significant is that they are principally a one-dimensional process, suited to creating channels with vertical walls. They also have issues with limited aspect ratios of these channels, i.e. the ratio of depth to width of geometry. As a result, micronozzles using etching processes are often planar two-dimensional designs rather than axisymmetric geometry. Sketches of these types of geometry are shown in Figure 2.3 to demonstrate the key differences.

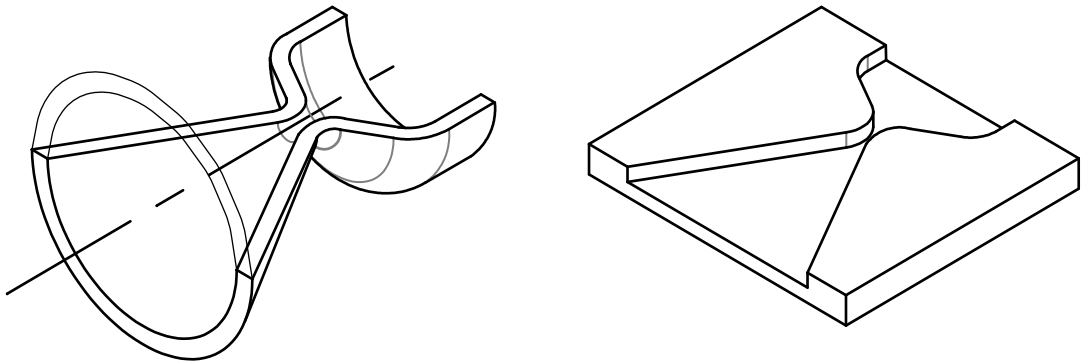


Figure 2.3 – Example sketches of axisymmetric (left) and planar (right) nozzle geometries.

Several different processes and materials have been demonstrated for manufacturing planar nozzles, including etching of silicon (MEMS) [26]–[31] and photosensitive glass [32]–[36]. Another technique uses low- and high-temperature co-fired ceramics (LTCC and HTCC), where a ceramic precursor material is shaped using moulding (for pastes), or cutting and forming (for ceramic tapes). The resulting nozzle geometry is then heated to sinter the ceramic precursor into the final material [37]–[42]. Each process and material has their own benefits and drawbacks, including thermal and chemical compatibility, cost and ease of manufacture, dimensional tolerances, and thermal conductivity. However, there are several critical issues that are common: The geometry is comprised of a stack of laminated wafers or layers, each with a two-dimensional nozzle profile. Aligning and successfully bonding the different layers is a challenge and results in a common delamination failure mode. Here individual layers separate, resulting in a leak or complete mechanical failure. This is exacerbated by the high temperatures and pressures in a thermal rocket nozzle and is in direct contention with maximising the temperature of the exhaust gases prior to expansion.

Another fundamental limitation of the planar nozzle architecture is that it increases the relative surface area to volume ratio of the nozzle, compared to optimum axisymmetric geometry. As the flow is in contact with a greater area, the thermal and viscous losses are higher. This can be somewhat mitigated by controlling the aspect ratio of the nozzle cross-section: In the extreme case, an infinitely deep nozzle profile will have negligible wall effects from the ‘top’ and ‘bottom’ faces. The limitation of this is that since the nozzle throat and exit areas are fixed for a specific thrust, increasing the depth of a planar nozzle will reduce the throat width. From simulations the depth of planar nozzles has a significant effect on the flow when of the same scale as the nozzle throat: For a nozzle with a  $90\text{ }\mu\text{m}$  throat width, the fraction of the flow in the subsonic boundary regime and therefore performance and thrust is sensitive when the depth is less than  $200\text{ }\mu\text{m}$ , and there are some residual minor effects even with deeper nozzle geometries [20]. This is expected given the area of the walls in the expanding section, but this also suggests that an axisymmetric nozzle will still have significant viscous losses, especially in the region around the throat which must have a smaller width. Another more practical challenge of increasing the nozzle depth is that either additional layers need to be manufactured and bonded, or a deeper etch is required will affect the controllability and quality of channel profile.

Given the drawbacks of the common planar nozzle architecture, it is worth highlighting the research into axisymmetric nozzle geometries using the micro manufacturing techniques. One approach uses stacks of axisymmetric nozzle sections which are laminated together as with the planar architectures, although in this case the profiles are circular. This technique has been demonstrated using silicon MEMS [43] and photosensitive glass [32] etching. These studies highlight that controlling the specific profile of deep etched materials and achieving a suitable nozzle profile is very difficult. These axisymmetric nozzles also have stepped profiles which are not ideal and result in flow separation and shocks. The axial alignment of each layer is especially important to control the profile, and preventing delamination is still a challenge. There is some preliminary research looking at using Additive Manufacture (AM) metal Selective Laser Melting (SLM) to manufacture small thrusters [44]. This study investigates the manufacture and testing of a 0.5 N monopropellant microthruster. The results demonstrate that this process is ideally suited to creating complex geometries at similar scales to the current work. However, this study was conducted at a similar time as the current research and was therefore not used for the initial literature survey to define the scope of this work.

The specific converging-diverging profile is also important: In large thrusters where the manufacturing techniques allow, the converging and diverging sections are often contoured (e.g. bell-shaped) and the throat has a radius between the sections for a gradually transition between the sub- and supersonic regions. The geometry is optimised to reduce shockwave formation to minimise the associated losses [11]. As discussed, small-scale nozzles around 1 N and lower commonly have conical profiles defined by a constant diverging angle. In many cases the nozzle throat is a sharp transition between the two regions [45], [46], or is drilled out [12], [22], [47]. While less optimal, these are easier to manufacture, and the benefits gained from a contoured profile are generally less than improving other parameters affecting performance. The diverging angles for macroscale thrusters are around 30 ° full angle [11], [12], but from simulations of micronozzles a shorter nozzle with higher angle may help to mitigate the microflow viscous effects in the throat region [25]. In these studies, 50 ° – 60 ° full angles are suggested to be optimal, balancing the reduced viscous effects with additional losses due to non-axial flow components. For non-conical nozzles, the initial small cross-sectional area of the nozzle near the throat may also benefit from having a higher rate of expansion, although this may be less performant than an optimised conical nozzle [23].

The analytical thruster model assumes isentropic flow. As the magnitude of the losses increase, the actual performance will deviate from this ideal. One method for accounting for these losses is to include an experimentally derived coefficient of discharge. This is defined as the ratio of the real and ideal mass flow rates,  $C_d = \dot{m}_{real}/\dot{m}_{ideal}$ . It is generally not used for larger scale thrusters as the flow rates are close to ideal [11], [16], [48]. In specific cases, for example low Reynolds number flows and small nozzle throat radius of curvature, the nozzle discharge coefficient for larger nozzles can drop significantly, in some cases below 0.9 [49], [50]. This dependence on the Reynolds number highlights the importance of the fluid viscosity. In computational and experimental research on smaller nozzles ( $D_t \leq 0.2$  mm) the discharge coefficients are low regardless of any geometric optimisations, e.g. the divergent section angle [51]–[53]. These studies find values for  $C_d$  are generally between 0.90 and 0.99, and they drop sharply for  $D_t \leq 0.1$  mm. The nozzle discharge coefficient therefore provides a method for assessing the significance of the expected losses in the flow through a micronozzle, and can be easily calculated based on the measured mass flow rate.

### 2.1.2. Monopropellant Catalyst Beds

The isentropic thermal rocket nozzle relies on the choked flow of a gaseous fluid. As discussed, the hotter the fluid upstream of the nozzle, the higher the performance of the system. In a typical monopropellant thruster, the high temperature results from the chemical enthalpy of the propellant which is liberated through a decomposition reaction. For liquid propellants, this will also vaporise the fluid so the exhaust will be gaseous. The decomposition is most often achieved by passing the propellant over a catalyst bed: the fluid element that contains catalyst material which facilitates the reaction. In general, a catalyst works by increases the rate of a particular reaction by providing a more favourable reaction pathway, and is not consumed (or is regenerated) in the process [16], [54]. The other main decomposition pathway is thermolytic, where the propellant temperature facilitates the decomposition.

#### **Fundamental Catalyst Bed Processes**

The most common type of catalyst in a monopropellant thruster is a heterogeneous catalyst bed: where the catalyst material is in a different phase to the propellant, most often a solid phase catalyst with a fluid propellant [16], [54]. In this type of catalyst bed, the catalytically active material is generally supported on an inert and stable material. This not only keeps the catalytically active material in place, but also maximises the surface area in contact the propellant flow. This is important because catalysis occurs where the propellant and active material physically interact. Optimising the design of a catalyst bed is essential for a high-performance monopropellant thruster, and should permit rapid and complete decomposition of the propellant. This will liberate the maximum enthalpy from the propellant, and will minimise the size of the catalyst bed to limit thermal and viscous losses.

The current work does not consider the design of a catalyst. However, understanding the fundamental chemical processes for the propellant-catalyst pair is important for both the design and analysis of a monopropellant microthruster catalyst bed. There are a number of experimentally validated models of HTP monopropellant catalyst beds in literature which provide a good insight into the fundamental processes.

Modelling the complex fluid flow and reaction processes in a catalyst bed is challenging given the wide range of length scales involved: from the intermolecular chemical reactions up to the relatively largescale flow. The computational models in literature tackle this by simplifying the processes. A typical approach reduces the numerical model equations to a single dimension, i.e. the fluid and reaction state along the length of the bed, and only considering bulk mass and energy transport [54]–[60]. These models have been validated by experimental testing of equivalent thrusters and the results show good agreement. It should be noted that experimental testing is limited by instrumentation: Measurements only capture a small subset of specific flow conditions, for example the pressure and temperature at chosen locations, and measurements such as the mass flow rate and thrust. Despite this limitation, experimental validation suggests that the simplified models capture the main bulk processes in the catalyst bed.

The models all show similar results: the liquid enters the catalyst bed and as the decomposition reaction, the enthalpy vaporises the propellant leading to an increased reaction rate. This boiling process can be modelled using a variety of methods. Simplified phase change models consider the

separate [59] or isothermal [55], [56], [58] boiling of the molecular species based on their individual liquid vaporisation temperatures. Interactions between different species are not typically considered, although more detailed mixture boiling models considering these have also been implemented [54], [57]. While the different models yield different results, for example in the temperature profile near the start of the bed, in general the variation is minor. The key observation here is that the models consistently show a region of relatively constant low temperature in the upstream region of the bed. The propellant boiling process is constrained by the latent heat of vaporisation of the cool liquid propellant. The temperature in this liquid is approximately steady and is around the boiling point of the propellant (~ 139 °C for 87.5 %/wt. HTP, but < 150.2 °C for hydrogen peroxide [61]–[63]). As the propellant continues to decompose, the additional enthalpy causes the liquid to boil. The models all predict a critical point where there is a bulk transition to the gas phase, and the temperature rapidly increases up to the maximum.

The models also provide the concentration profiles of the chemical species through the bed, i.e. a measure of the progress or completeness of the reaction. The initial liquid-heating region coincides with the rapid decrease in species fraction of hydrogen peroxide to roughly 0.5 - 0.6, followed by little change in the stable-temperature liquid-boiling regime [57]–[59]. The initial heating phase decomposes a lot of the propellant, and latent heat of vaporisation limits the remaining decomposition. There are some differences in the model results for the reaction after the phase transition, with one model suggesting that there is little increase in the decomposition rate in the gas phase [58], while others suggest rapid and complete decomposition of the remaining hydrogen peroxide after boiling [57], [59]. The decomposition rate is tied to the rate of temperature increase: For the model with the minimal rate change, the temperature rise is much slower. This is an obvious but important point since the enthalpy release is the cause of the temperature change. Another key observation is that for high fluid temperatures above 500 °C to 600 °C, the reactant species concentration drops to near-zero, indicating that the reaction is complete. Therefore, if temperatures measured in the catalyst bed and chamber are high, the reaction should be complete and the frozen flow condition in the nozzle is valid. It is important to note that these models all assume first order reaction kinetics, i.e. where the rate of reaction is dependent on the concentration of the hydrogen peroxide reactant species. This means that decomposition rates are limited by the diffusion of the species to the surface of the catalytically active material. These models show good agreement to the experimental data, although the validity of this catalysis mechanism is not possible to investigate with the simplified mass transport models.

The catalyst bed is also expected to cause a pressure drop in the fluid due to viscous losses. The models predict that the bulk of the pressure drop over the bed occurs in the downstream gaseous region. This is of note as the liquid propellant is expected to have a higher viscosity than the gas phase ( $1.23 \times 10^{-3}$  Pa.s for liquid 87.5 %/wt. HTP @ 25 °C vs  $4.32 \times 10^{-5}$  Pa.s for the fully decomposed exhaust @ 695 °C), and suggests that the flow in the gaseous regime has a high velocity. This high velocity is shown in the simulation results but would imply that the flow is not stagnant upstream of the nozzle as assumed. However, so long as the flow in this region is slow relative to the velocities in the nozzle the effect of non-frozen flow should be minor.

A simplified model of the processes in an HTP catalyst bed is presented in Figure 2.4, summarising the results of the modelling and experimental testing from this literature. This model has three distinct regions, defined by the governing processes:

- Liquid-dominated catalysis region – The cool propellant enters the bed as a liquid, and the region is dominated by liquid phase catalysis. After an initial temperature rise due to catalysis, the temperature is held around the propellant boiling point by the latent heat of vaporisation.
- Gas-dominated catalysis region – The bulk of the propellant is in the gaseous phase and decomposition is both catalytic and thermolytic. The enthalpy released from the reaction rapidly raises the temperature of the fluid.
- Post-decomposition region – The majority of the propellant has been decomposed and there is no significant enthalpy input into the fluid. The temperature flux is dominated by heat loss through the catalyst bed walls.

These regimes can be considered as distinct and separated by pseudo-physical fronts. This provides a simple way of relating the measurable conditions of the fluid to the decomposition reaction in the bed. The two boundaries are defined as the phase change front between the liquid-dominated and the gaseous decomposition regimes, and the full decomposition front between the regions with reactant species and the fully reacted flow. These do not represent strict geometric boundaries between regimes, but it is proposed that this may allow for analysis of the catalyst bed and nozzle performance by estimating the completeness of the chemical reaction processes. For example, these may provide insight into the thermal efficiency, validity of the frozen flow conditions and isentropic losses in the nozzle.

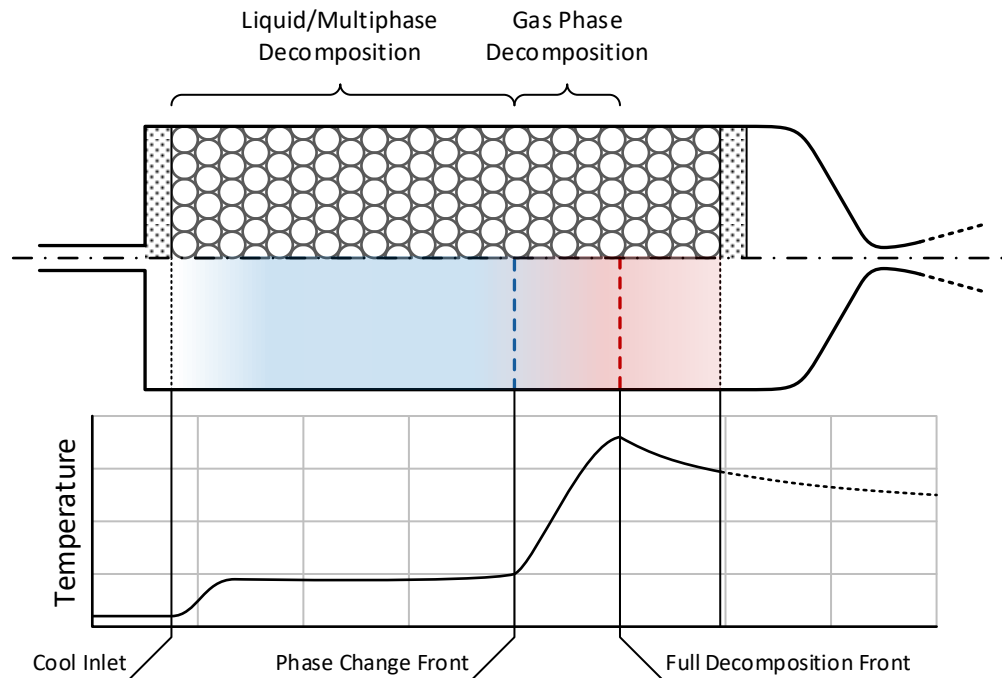


Figure 2.4 – The simple one-dimensional model of the catalyst bed, including the expected static pressure and temperatures, along with the key pseudo-physical fronts.

## Catalytic Reactivity

As demonstrated in the catalyst bed simulations, the performance of a given bed is highly sensitive to the reaction rate of the propellant-catalyst pair [54], [57]. These models assume that the catalytic decomposition of HTP is a first order reaction. This is generally accepted in HTP catalyst literature for many catalysts [16], [19], [64]–[68], and means that the rate-limiting step is the rate of hydrogen peroxide diffusion to the catalytically active material. For a high-performance thruster, the catalyst material must have a high catalytic activity, but should also have a high surface area to improve the amount of surface available for decomposition. The activity is determined by the choice of catalytically active material while the surface area results from the macro- and micro-structures of the catalyst support and surface preparation of the active material. As mentioned, catalyst design is an expansive topic that is not within the scope of this current research, but a brief discussion of the common HTP catalysts is provided.

A given propellant may be catalysed by many different materials: in the case of HTP it is known that the majority of chemicals or potential contaminants can catalyse the decomposition. The most common industrial catalysts for HTP include transition metals such as platinum, silver and iridium [19], [64], [69], [70], as well as metal oxides for example those of manganese, iron, tin [65], [70]–[72]. There are many studies looking at the relative reactivity of each of these candidates, however platinum is one of the most reactive [64], [67] and is therefore an ideal candidate. The specific reactivity of a given propellant and catalyst is generally measured using small samples of materials and at low concentrations under controlled temperatures and pressures [19], [73]. These results are then extrapolated to higher concentrations of hydrogen peroxide. This decouples the thermal and pressure effects and permits more accurate data collection [19], [64], [67]. The extrapolation assumes that the reaction kinetics do not change with temperature and pressure, and can be described using a regression-fitted modification to the basic Arrhenius model:

$$k = Ae^{-\frac{E_a}{RT}} \quad (2.10)$$

Where  $k$  is the reaction rate  $A$  is the pre-exponential term,  $E_a$  is the activation energy,  $R$  is the Universal Gas Constant, and  $T$  is the absolute temperature. Both the pre-exponential and exponential terms may change depending on the specific reaction for example the activation energy from the catalytic material, and conditions such as concentration and proton activity (i.e. the pH). These are therefore specific for a given catalyst material. Where appropriate these terms are broken out into additional factors: for example the concentration and proton activity may be separated from the pre-exponential factor [19]. This is important to improve the accuracy of extrapolation of the reactivity to higher concentrations. Note that for a strictly first-order reaction, the effect of concentration should be linear and described by:

$$k = k_1[H_2O_2]^1 \quad (2.11)$$

Where  $k_1$  is the first order reaction rate and  $[H_2O_2]$  is the molar concentration of hydrogen peroxide, in the equation raised to the exponent of the order of the reaction, i.e. in this case 1. In most experimental studies on the effect of concentration may not be exactly 1 so the exponent may vary slightly. This is tied to the specific catalyst and is assumed to be independent of the concentration [19], [73].

The phase of the propellant will affect the diffusion and therefore the catalysis rate. The catalyst bed modelling studies suggest that the rate-limiting step is the liquid-phase decomposition, since the gas phase reaction occurs rapidly after vaporisation. Therefore, the liquid-phase HTP catalytic decomposition rates should describe the performance-limiting step in a catalyst bed. Table 2.1 lists a number of these liquid phase rates for different platinum catalysts from literature. The rates are extrapolated for 87.5 %/wt. HTP under ambient conditions. The variations between different catalysts are caused by the structure and surface area. The specific catalytic surface area and microstructures may be characterised using surface sorption techniques (e.g. Brunauer–Emmett–Teller analysis) or electron microscopy [16]. They are often related to the catalyst loading parameter, defined as the fractional ratio of the mass of the catalytic active material to the total catalyst mass. Generally, higher catalyst loadings have higher reactivities and perform better [16].

Table 2.1 – A list of platinum-catalysed HTP reaction rates, extrapolated for HTP concentrations of 87.5 %/wt. at 25 °C. The specific Arrhenius factors for these conditions are included here, but they may be expressed differently in the literature source given the specific study focus.

Source	Catalyst	Study Type	Pre-Exponential Factor [s <sup>-1</sup> ]	Activation Energy [J.mol <sup>-1</sup> ]	Reaction Rate [mol.m <sup>-2</sup> .s <sup>-1</sup> ]
Serra Maia (2018) [19]	50 nm Pt nano-powder	Concentration, pH	$1.17 \times 10^3$	$2.60 \times 10^5$	$3.252 \times 10^{-2}$
	20 nm Pt-‘black’ powder	Concentration, pH	$3.58 \times 10^3$	$3.30 \times 10^5$	$5.918 \times 10^{-3}$
Liu (2014) [73]	3 nm Pt	Concentration, pH	$(1.213 \times 10^{-3})^{*1}$	*1	$1.213 \times 10^{-3}$

\*1 Arrhenius exponential fit not used – no activation energy value specified.

\*2 Concentration not formally investigated, reaction order assumed to be 1.

### Catalyst Material Structure

The catalytic activity of the specific active material is important, however other properties affect the practical design and performance of a catalyst. Some of the more significant considerations include:

- The low melting point of certain catalysts, for example silver. This may result in the tendency to sinter or wash out the catalyst material or destroy the microstructure reducing the performance and lifetime [16], [74].
- Oxidation number, especially for metal oxide catalysts, for example manganese oxide ( $MnO_x$ ). This is thought to have a significant role on the activity, and a long residence duration at high-temperature, high oxygen environments, i.e. in an HTP catalyst bed, may reduce the catalytic activity [16], [65], [67]. While not investigated thoroughly, it may apply to any material that can oxidise, including platinum.

- The specific surface preparation of the active material. Given the surface area dependence, this can have a notable effect on the activity. Preparation methods include wash-coating [16], [70], [75], surface crystal growth [16], [19], [70], [75] and using high porosity active and support materials [16].

Most of the discussion on catalysts has focused on the active material, but the catalyst support material also plays a significant role in the activity of a given catalyst. This is a different material from the active phase in the majority of cases, and should be an inert, thermally and chemically stable material [16], [70], [76]. Ceramics are often used given many have ideal properties. Common materials include alumina, ceria, zirconia and silica, with a preference for higher porosity structural phases, such as  $\gamma$ -Alumina vs  $\alpha$ -Alumina, to promote higher surface areas [16], [70]. Metallic supports are also common, including refractory materials such as nickel and its alloys [16], [70]. In the case of catalyst beds manufactured using silicon MEMS techniques, monolithic structures are often etched out of the parent material, typically silicon [26]–[29], [77]. Some catalysts are self-supported, i.e. the catalyst material is solely composed of the catalytically active material, although this is less common since the material must be relatively low-cost which is prohibitive for many common catalysts. This may be less of a concern for microthrusters where the catalyst bed is small [30], [41], [42], [47], [78].

The type of catalyst may have an impact on the geometry of the bed. In general, there are two main types of catalyst bed macrostructure: packed beds composed of individual particles of catalyst material, and monolithic beds which are contiguous structures. Example sketches of the basic concepts of packed and monolithic catalysts structures are shown in Figure 2.5. Packed beds are most commonly composed of shaped pellets [16], [70], although meshes and screens may be used for metallic catalysts such as silver [16], [70]. Monolithic beds are conventionally extruded, resulting in axially aligned flow paths, illustrated in the figure. Packed bed catalysts are traditionally more common in monopropellant thrusters than conventional extruded monolithic structures since the random packing of the pellets provides a higher surface area and better propellant residence time [16], [79]–[82]. The flow path through an extruded monolith will be aligned along the straight channels so the diffusion of the reactant and product species to and from the catalyst surface will be relatively slow compared to the forced diffusion in a packed bed. In the packed bed, the propellant flows through a tortuous path between the pellets, so the propellant is forced into contact with the catalyst surface [81]. As a result, per unit mass of catalyst, packed beds have a higher catalytic activity. There is a lot of interest in novel manufacturing techniques for monolithic supports with more tortuous fluid paths. Approaches include AM manufacturing [79]–[82], using open cell foams [16], [70], and sintered pastes [76]. This is a promising field of research, although there are many complexities and parameters associated with these beds, and fine control of the support macrostructure at the small scales of a sub-newton thruster is difficult.

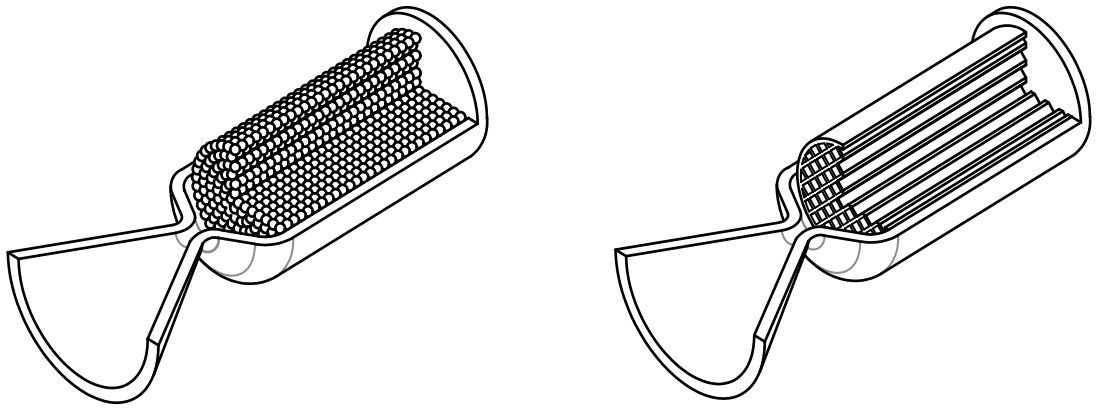


Figure 2.5 – Cutaway sketches of the axisymmetric packed bed (left), axisymmetric monolithic (right) catalyst bed architectures.

The structure of packed beds in monopropellant microthrusters is also a challenge at smaller scales. Since their performance is highly dependent on the active surface area in the flow, good packing of the bed is a critical factor. The catalyst packing is dependent on both the size and shape of the pellets. Different catalysts and catalyst beds can be compared simply using the void fraction, the ratio of voids to catalyst material in a bed [12], [16], [54], [83], [84]. This can be calculated either by inspection for example using commuted Tomography (CT) microscopy, or by using the density of the catalyst material and the volume of the bed. The void fraction is a mean volumetric measurement of the entire bed, but effects near boundaries affect the local packing density [16], [54], [83], [84]. These effects result in non-uniform packing and large channels that propellant will pass through more readily. The wall effects are directly related to the size of the pellet, and can be characterised using the non-dimensional distance from the wall:

$$z = \delta z / d_p = (R_c - \delta R) / d_p \quad (2.12)$$

Where  $\delta z$  is the distance from the wall and  $d_p$  is the length scale of the catalyst pellets, typically the diameter or minimum width. For a circular cross-section or radius  $R_c$ ,  $z$  is specified with respect to the radial distance  $\delta R$  from the centre of the cross-section such that  $\delta z = (R_c - \delta R)$ . For spherical particles, wall effects are expected for  $z \leq 4.5$ , or up to 4.5 pellet diameters into the bed [85]. These are large for 1 – 2 pellet diameters from any boundary [83], [84], [86] and a good design principle for a ‘well-packed’ bed is when the minimum geometric length is greater than 12 times the diameter of a pellet, i.e.  $D_c / d_p \geq 12$  [86]. This may be a challenge for microscale beds as they require very small catalyst pellets. The resulting small flow paths between these pellets will lead to microfluidic effects and high unit pressure drops. One significant microfluidic effect is the phase change of the propellant causing bubbles to form, potentially causing local choking of the fluid flow. This has been seen in some planar microthrusters where the size of the channels is small [26], [47], [87], and it is suggested that this has a significant effect on performance where the flow channel is of the order of  $20 \mu\text{m}$  [26]. Optimal sizing of monopropellant microthruster packed beds is therefore likely to be different to that of a conventional macroscale thruster and remains an open question.

The specific geometry of a catalyst bed is also an important parameter that can affect the choice of a monolith or packed bed. As with the design of the nozzle, in general larger scale thrusters ( $\geq 1 \text{ N}$ ) have axisymmetric catalyst beds, however the smaller nominally sub-newton thrusters are often

planar. Axisymmetric beds are similar to the sketches in Figure 2.5, and example sketches of planar catalyst beds are shown in Figure 2.6. The planar geometries are manufactured using the same techniques as the nozzles described in Section 2.1.1, and both packed pellet [30], [32], [33], [36], [47], [74] and monolith-type using packed wire or sintered paste [30], [41], [42], [78] catalyst beds have been successfully demonstrated. Another novel type of integrated monolithic catalyst bed, where the supporting structure is built into the main thruster body, is very common as it makes use of the etching process [26]–[29], [77]. These integrated beds afford the same fine control over the geometry of the catalyst, as with the nozzle, including accurately specifying the propellant flow path geometry. However, this geometry is still subject to the same manufacturing limits as the bed itself and the support geometry are etched pillars. In all literature, these integrated monoliths have a catalytically active material deposited on the surface of the pillars or channels.

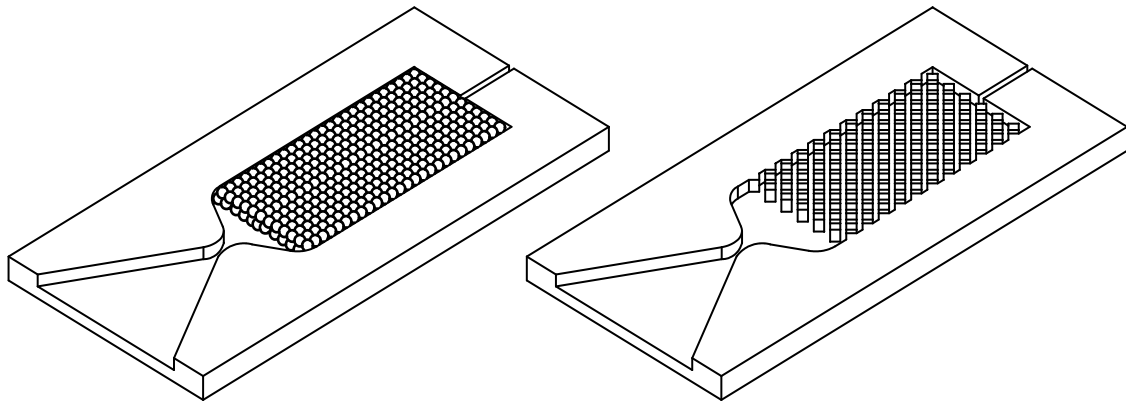


Figure 2.6 – Cutaway sketches of the two-dimensional packed bed (left) and integrated monolith (right) catalyst bed architectures.

The two-dimensional catalyst beds are subject to the same drawbacks as the planar nozzles. Critically, the greater surface area to volume ratios are expected to result in significant thermal losses, reducing the fluid temperature and causing a drop in the performance. The delamination of the thruster was also common, although this may be mitigated by regeneratively cooling the thruster with propellant flow channels in the thruster walls [36]. While this is effective at preventing the mechanical failure it greatly impacts the performance, highlighting the issue with thermal flux: In this particular study, the thrust decreased from 40.8 mN to 28.2 mN with the regenerative cooling, while the measured external temperature dropped from 154 °C to 65 °C.

Void fraction is also a concern with planar catalyst beds. Deep geometries are difficult to manufacture so void fraction wall effects may also be significant in this dimension. Packed beds have been used in several studies on planar microthrusters. The pellet shapes were non-uniform, manufactured from  $\gamma$ -alumina base material, ground and sized to 40 – 45 mesh size ( $355 \mu\text{m} \leq d_p \leq 425 \mu\text{m}$ ) [33]. While no specific packing calculations were presented, as the beds of these two thrusters are 2.25 mm and 4.5 mm deep, wall packing effects are expected throughout both beds, with non-dimensional wall distances of 2.15 mm and 4.30 mm respectively [33], [36]. These drawbacks suggest that conventional axisymmetric catalyst beds are superior to the planar designs, although manufacturing is still a challenge.

Since the catalyst bed geometry depends on the amount of catalyst required to support the propellant flow rate. The principal dimensions can be specified parametrically by the catalyst bed loading and the bed aspect ratio:

$$G = \dot{m}/A_c \quad (2.13)$$

$$AR = L_c/D_c \quad (2.14)$$

Where  $A_c$  and  $D_c$  are the geometric cross-sectional area and diameter, and  $L_c$  is the length of the catalyst bed. These parameters can be used to compare systems with different mass flow rates and therefore thrusts. The catalyst bed loading represents the propellant mass flux through the bed, and higher values correspond to a faster flow per unit length. A given aspect ratio will therefore only support a particular maximum bed loading while still fully decomposing the propellant [16], [70]. When the flow rate increases above the maximum loading, the bed will not support complete propellant decomposition. Equally, for a set mass flow rate, there is a minimum bed cross-sectional and length, below which the propellant will not be fully decomposed.

With respect to the simple model for the flow regimes above, this limiting condition is represented by the full decomposition front aligning with the end of the catalyst bed. As this moves further downstream, the performance will drop due to underutilisation of the propellant, since some chemical enthalpy will not be liberated. This will also break the frozen flow condition in the nozzle. In extreme cases, the liquid propellant will pass through the bed and will be entrained in the flow entering the nozzle. This is known as flooding and the entrained liquid may break the choked flow condition, heavily degrading the performance of the thruster [43], [76], [88]. This can be represented by the phase change pseudo-physical front moving beyond the end of the catalyst bed. The parametric geometry will affect the position of these fronts: high catalyst bed loading and low aspect ratios will move the fronts closer to the end of the bed for a given propellant flow rate, increasing the likelihood of underutilisation and flooding. Conversely, low bed loadings and high aspect ratios will move the fronts upstream in the bed. This will also decrease performance, since complete decomposition will occur earlier in the bed and the fluid will cool as it flows downstream. The geometry of the bed should be optimised for a specific catalyst, such that the bed is sufficiently large to avoid the underutilisation effect but limiting excessive thermal and viscous losses. This optimum size will be dependent on the specific decomposition rate, including the effects of the architecture, catalyst type and packing. Given the specific issues relating to microscale catalyst beds, this will be discussed later in a comparison between different monopropellant microthrusters from literature.

### 2.1.3. Propellant Microinjectors

Upstream of the catalyst bed is the propellant injector, which separates it from the PDS. The injector serves two main purposes: controlling the propellant flow rate into the bed and distributing it over the catalyst. Controlling the flow of the propellant into the bed is important for the stability and conditioning of the reacting flow in the bed, as any instabilities can lead to transient effects. These can lower performance and also create additional mechanical forces damaging the catalyst [11], [16], [89]–[91]. These transient effects are generally oscillatory and the low frequency components,

$10 \text{ Hz} \leq Fq \leq 400 \text{ Hz}$ , are especially detrimental to the thruster operation. These can couple across the injector and affect the mass flow rate, creating positive feedback further degrading the performance. This effect is known as 'chugging' and can result in unsteady flow conditions both in the catalyst bed and at the exit of the nozzle [11], [89]–[92]. The specific mechanism for this effect is not well documented for monopropellants but is related to both the injector and catalyst bed design. The other main purpose of an injector, the propellant distribution, affects the steady state performance of a thruster. Controlling the distribution of the fluid over the upstream of the bed will affect the usage of the catalyst in this region and reducing the required size of the catalyst bed. This can also help mitigate catalyst packing issues discussed in Section 2.1.2.

There are a broad range of injector architectures for liquid rocket engines. Many are more suited to larger thrust systems given their complex geometries, for example pintle and swirl injectors, which require large volumes for the propellant to mix and distribute upstream of a catalyst bed [11], [93]. These types of injectors are more typically associated with bipropellant thrusters where mixing is required. The main conventional injector types suitable for small monopropellant propulsion systems fall into two main categories:

- Venturi-type injectors – These use the venturi effect to cavitate the flow, causing liquid choking [11], [93]–[95]. There are two main categories: cavitating Venturi nozzles with converging-diverging geometry similar to the nozzle of the thruster, and orifice plates with much simpler straight-edged constrictions [12], [93], [95], [96]. In both cases, these can be single or multi-port showerhead designs which vary the propellant distribution.
- Poiseuille-type injectors – These use viscous losses to provide a resistance to the flow. They are generally small diameter tubes [78], [97], [98] or channels [26], [33], [36], [77], but their mode of operation is similar to that of swirl injectors [93]. As with Venturi injectors, they can also be single or multi-port injectors.

Controlling the propellant flow and preventing 'chugging' is the most critical purpose for an injector. Often the injector decoupling effect is tied to the pressure differential, or drop,  $dP_{inj}$ , across the injector. This may also be normalised with respect to the static pressure downstream of the injector to permits comparison between different systems [11], [12], [93], [95]. Most commonly, this fractional pressure drop uses the chamber pressure, and well-performing injectors from literature fall in the range  $0.05 \leq dP_{inj}/P_c \leq 0.20$  [12], [26], [36].

The pressure drop is a product of the resistance to the propellant flow in the injector, arising from the Venturi or Poiseuille effect, depending on the injector architecture, and can be described analytically. For the Venturi-type injectors, the flow can be characterised by a modified version of the Bernoulli equation:

$$|P_0 - P_1| = dP = \frac{1}{2} \frac{\dot{m}^2}{\rho} \left( \frac{1}{A_0^2} - \frac{1}{A_{orf}^2} \right) \quad (2.15)$$

Where  $P_0$  and  $P_1$  are the pre- and post-injector static pressures,  $A_0$  is the upstream cross-sectional area, and  $A_{orf}$  is the area of the throat.

This can be reduced further by assuming that the throat diameter is significantly smaller than the downstream diameter (i.e.  $A_{orf} \ll A_{in}$ ):

$$dP = \dot{m}^2 \frac{1}{C_d^2 A_{orf}^2} \frac{1}{2\rho} = \dot{m}^2 \frac{1}{C_d^2 \zeta_{orf}^2} \frac{1}{2\rho} \quad (2.16)$$

A coefficient of discharge  $C_d$  is included to account for losses resulting from cavitation, viscous effects, and flow around the sharp corners in the cases of orifice plate injectors. A well-designed cavitating Venturi nozzle should have  $C_d \sim 0.94$  [99], compared to  $0.61 \leq C_d \leq 0.90$  for orifice plates [11]. Note that as with the thermal rocket nozzle coefficient,  $C_d \equiv \dot{m}_{real}/\dot{m}_{ideal}$ , so that the exponent matches that of the mass flow rate. Equation (2.16) has also been recast with the parameter  $\zeta_{orf}$ , defined here as the geometric parameter. This is a collection of the key geometric parameters with the same exponent as the mass flow rate. While for Venturi-type injectors  $\zeta_{orf} \equiv A_{orf}$ , it is different for the Poiseuille architecture and can be used to compare the two.

An issue of small Venturi injectors is that the geometry will be very small of the low propellant flow rates in sub-newton thrusters. Manufacturing is difficult, and Venturi nozzle profiles are particularly challenging. All of the injectors from literature are axisymmetric orifice design, manufactured using conventional micromachining [12], [74] or etching processes [32]. As the thrust decreases into the sub-newton range, this size of the orifice becomes prohibitively small, and there are very few instances of this architecture. Only two examples of micro-injectors were found in literature at the time of writing, using on sub-newton thrusters targeting 0.7 N [74] and 0.13 N [32].

Poiseuille injectors are more common in small thruster literature than Venturi injectors. This is due to their mode of operation: the pressure drop arises from viscous losses acting along the length of the injector tube. As a result, the injector length can be chosen such that the cross-sectional area is larger relative to a comparable orifice injector. Manufacturing is easier and more tolerant to variability. For small-scale and microthrusters, Poiseuille injectors fall into two categories: axisymmetric injectors based on microbore tubes [43], [78], and planar injectors [26], [33], [36]–[38], [77], [100], using etching to create rectangular channels. These correspond to the rest of the thruster architecture. For the axisymmetric Poiseuille designs, the flow can be described using the Hagen-Poiseuille equation:

$$dP = \dot{m} \frac{L_{pos}}{C_d A_{pos}^2} \frac{8\pi\mu}{\rho} = \dot{m} \frac{1}{C_d \zeta_{pos}} \frac{8\pi\mu}{\rho} \quad (2.17)$$

Where  $L_{pos}$  is the length of the injector tube and  $\mu$  is the dynamic viscosity of the propellant. A coefficient of discharge is included to account for losses, and again the equation has been recast with the Poiseuille geometric parameter  $\zeta_{pos} = A_{pos}^2/L_{pos}$ . The Hagen-Poiseuille equation is derived from the incompressible and laminar Navier-Stokes equations, so is only valid for low Reynolds numbers. This is expected given that the injector functions through viscous forces, which must therefore be dominant compared to the inertial forces on the flow. The Reynolds number can be calculated using equation (2.9), using the inner diameter as the characteristic length in the circular cross-section derivation.

In general, for macro-scale laminar pipe flow  $Re < 2300$  [101], however for microscale flows turbulence transition occurs at lower values, i.e. lower flow velocities. From experimental research

on microscale flow through glass microbore tubes with diameters of 50  $\mu\text{m}$  – 247  $\mu\text{m}$  the turbulent transition region is  $1700 < Re < 2000$  so laminar flow is expected below this [102], [103]. It is important to highlight that the wetted surface of these microbore tubes was a relatively smooth glass, with surface variability of approximately  $\pm 2 \mu\text{m}$ . Depending on the manufacturing method the surface may not be this smooth which may result in turbulent flow at lower Reynolds numbers. It is expected that minor effects of turbulent transition should be captured in the discharge coefficient, but any significant turbulence will result in a breakdown of the analytical model. This should be apparent in any experimental characterisation of the flow for a given injector, where the  $dP \propto \dot{m}$  relationship will not be valid. Note that the majority of the microthrusters using Poiseuille injectors are planar, and the injector tubes are rectangular channels. Since equation (2.17) is for a circular cross-section, the flow will be described by a different equation. This may be derived for any arbitrary cross-section, although will not given here.

#### 2.1.4. A Survey of Existing Micro-Monopropellant Propulsion Systems

It is important to assess the current state-of-the-art microthrusters to lay the foundation for the current work. Table 2.2 lists the most significant research into sub-newton catalytic thrusters, detailing the overall design and reported key performance. Note that this also includes monopropellant thrusters with supplemental heaters, however there are a large number of similar microthrusters that add enthalpy either by purely resistively-heated vaporising liquid [38], [40], [100], [104]–[107] or electrolytic decomposition [37], [39]. These have not been included since their mode of operation is significantly different and they will have their own design challenges.

The overall systems performance is the most important metric, although this is dependent on the enthalpy of the propellants and the testing conditions. Neither are consistent across the range of thrusters. Most use varying concentrations of HTP as a propellant, likely due to the relative low toxicity and ease of handling, although there are two instances of hydrazine systems. As a reference figure, the ideal vacuum and atmospheric specific impulses for 87.5 %/wt. HTP ( $P_c = 10 \text{ bar}$ ) for a 0.1 N thruster are 109 s and 171 s respectively, although many of the studies use extrapolated results which closely match these values. The losses are attributed to significant thermal losses although viscous losses in the nozzle are expected. The thermal performance is not reported here: as discussed, it very challenging to instrument these small thrusters to directly measure the fluid temperature. Where provided, the studies report either speculative thermal results or the external surface temperatures.

It is notable that the thrusters fall into two categories: thrust  $> 0.1 \text{ N}$ , where the thrusters are axisymmetric, and thrust  $< 0.1 \text{ N}$  where the thrusters are planar. This is due to the difficulties with manufacturing small axisymmetric geometries, and it also suggests that the planar designs do not scale up well. This may be related to the challenges of controlling etching processes on relatively large scales, or that material and process costs become significant. Regardless, the range around a nominal thrust of 0.1 N is especially interesting since none of the demonstrated techniques appear particularly well-suited.

Table 2.2 – A list of the design architecture and nominal performance parameters of small and micro monopropellant thrusters, targeting thrusts  $\leq 1$  N, using catalytic decomposition as their primary source of enthalpy.

Source	Type	Propellant	Nominal Thrust [mN]	Nominal Specific Impulse * [s]	Nominal Mass Flow Rate [g.s <sup>-1</sup> ]
Hitt <i>et al.</i> (2001) [26]	Planar	HTP 90 %/wt.	0.5	160 <sup>vx</sup>	$3.50 \times 10^{-4}$
Platt (2002) [78]	Axisymmetric	HTP 85 %/wt.	2.8	150 <sup>v</sup>	$2.00 \times 10^{-2}$
Hebden <i>et al.</i> (2005) [43]	Axisymmetric	HTP 86 %/wt.	20	125	$1.00 \times 10^{-2}$
Takahashi <i>et al.</i> (2006) [27]	Planar	HTP 60 %/wt.	0.995	14-72	$3.87 \times 10^{-4}$
Kuan <i>et al.</i> (2007) [47]	Axisymmetric	HTP 92 %/wt.	182	101	$1.80 \times 10^{-1}$
Cen <i>et al.</i> (2010) [28]	Planar	HTP 75 %/wt.	5	90 <sup>v</sup>	$5.00 \times 10^{-3}$
Yuan <i>et al.</i> (2011) [29]	Planar	Hydrazine	1.01	162 <sup>v</sup>	Unknown
Lee <i>et al.</i> (2012) [32]	Axisymmetric	HPT 90 %/wt.	130	130	$3.00 \times 10^{-1}$
Miyakawa <i>et al.</i> (2012) [77]	Planar	Hydrazine	Not Tested	Not Tested	Not Tested
Chan <i>et al.</i> (2013) [74]	Axisymmetric	HTP 90 %/wt.	700	102	$7.02 \times 10^{-1}$
Kundu <i>et al.</i> (2013) [30]	Planar	HTP 50 %/wt.	1	100	$1.36 \times 10^{-3}$
Huh & Kwon (2014) [33]	Planar	HTP 90 %/wt.	0.0302	105	$3.28 \times 10^{-3}$
Khaji <i>et al.</i> (2016) [41]	Planar	HTP 30 %/wt.	0.084	92 <sup>v</sup>	$9.17 \times 10^{-4}$
Huh <i>et al.</i> (2017) [35], [36]	Planar	HTP 90 %/wt.	0.05	72	$6.98 \times 10^{-2}$
Khaji <i>et al.</i> (2017) [42]	Planar	HTP 31 %/wt.	0.084	92 <sup>v</sup>	$9.17 \times 10^{-4}$
Ryan <i>et al.</i> (2020) [12]	Axisymmetric	HTP 87.5 %/wt.	1000	160 <sup>v</sup>	$5.60 \times 10^{-1}$

\* Atmospheric test data, unless denoted:

<sup>v</sup> Vacuum test

<sup>vx</sup> Vacuum extrapolated

The nozzle designs of these thrusters are presented in Table 2.3. There are a variety of nozzle throat areas since the thrusters target a wide range of thrusts. While this is expected, the expansion ratios for these nozzles do not necessarily agree with the typical nozzle design values for atmospheric (1.123 – 36.1 vs 3 – 30) and vacuum (1.24 – 300 vs 200 – 300) conditions. This may be due to manufacturing constraints, for example the size or structural design of the planar thrusters limits the size of the nozzle, although this should not impact the atmospheric nozzles. The cross-sectional areas of these do not need to change much, so there is no reason for them to be oversized. In fact, as discussed under-sizing a nozzle may improve the performance of micronozzles due to the reduced nozzle wetted surface area and therefore viscous losses.

There is also a lot of variability in the nozzle divergent angles, between 24 ° and 56 ° (full-angle). As discussed, the computational studies on micronozzles identified the optimal divergent angles range from 50 ° to 60 ° (full-angle). This suggests that the majority of the experimental thrusters have micronozzle expansion angles that are below optimal and will therefore experience significant viscous losses. However, since the majority of the losses will occur in the high velocity flows in the throat and diverging sections of the nozzle, assuming that the nozzle is choked, the performance of the upstream elements (the catalyst bed and injector) should not be impacted by the conditions downstream of the throat or the external environment. In principle, a high-performance nozzle can be designed for either vacuum or atmospheric conditions, but the catalyst bed design should not be significantly impacted.

Table 2.3 – A list of the nozzle design parameters of small and micro monopropellant thrusters, targeting thrusts  $\leq 1$  N, using catalytic decomposition as their primary source of enthalpy.

Source	Nozzle Type	Throat Area [m <sup>2</sup> ]	Expansion Area Ratio	Expansion Full Angle [deg]
Hitt <i>et al.</i> (2001) [26]	Vacuum – Planar	$9.00 \times 10^{-9}$	1.24	30
Platt (2002) [78]	Vacuum – Axisymmetric	$1.14 \times 10^{-7}$	100	Unknown
Hebden <i>et al.</i> (2005) [43]	Ambient – Axisymmetric	$5.62 \times 10^{-7}$	36.1	28.19
Takahashi <i>et al.</i> (2006) [27]	Ambient – Planar	$6.00 \times 10^{-9}$	10.0	Unknown
Kuan <i>et al.</i> (2007) [47]	Ambient – Axisymmetric	$1.96 \times 10^{-7}$	1.96	30
Cen <i>et al.</i> (2010) [28]	Vacuum – Planar	$1.80 \times 10^{-8}$	11.7	28.19
Yuan <i>et al.</i> (2011) [29]	Vacuum – Planar	$1.10 \times 10^{-8}$	12.0	45
Lee <i>et al.</i> (2012) [32]	Ambient – Axisymmetric	$1.59 \times 10^{-7}$	1.23	2.86
Miyakawa <i>et al.</i> (2012) [77]	Unknown – Planar	$1.43 \times 10^{-8}$	13.3	Unknown
Chan <i>et al.</i> (2013) [74]	Ambient – Axisymmetric	$6.50 \times 10^{-7}$	2.16	30
Kundu <i>et al.</i> (2013) [30]	Ambient – Planar	$1.30 \times 10^{-8}$	5.00	28
Huh & Kwon (2014) [33]	Ambient – Planar	$6.05 \times 10^{-8}$	1.45	24
Khaji <i>et al.</i> (2016) [41]	Vacuum – Planar	$3.00 \times 10^{-8}$	6.50	56
Huh <i>et al.</i> (2017) [35], [36]	Ambient – Planar	$7.92 \times 10^{-8}$	1.54	24
Khaji <i>et al.</i> (2017) [42]	Vacuum – Planar	$3.00 \times 10^{-8}$	6.50	56
Ryan <i>et al.</i> (2020) [12]	Vacuum – Axisymmetric	$3.12 \times 10^{-7}$	300	30

Catalyst bed design is a very broad topic. Given this, the thrusters presented here are only a small subset of potential designs, although these thrusters capture the most common concepts that are easy to scale down to the small bed geometry. Table 2.4 contains the key catalyst bed design parameters. In addition to the mixture of planar and axisymmetric architectures, there is significant variation in the geometry of the beds. Considering the parameters introduced in 2.1.2, the catalyst bed loadings vary between  $0.04 \text{ kg.m}^{-2} \text{s}^{-1}$  and  $61.1 \text{ kg.m}^{-2} \text{s}^{-1}$ , and the aspect ratios between 0.40 and 5.36. This may suggest that there is no clear understanding of how the knowledge of the fluid and chemical processes has been or can be used to optimise the bed geometry. This is especially evident given the lower specific impulses. There are some comments that higher aspect ratio thrusters are oversized [12] and in many cases the low performance results in a steamy or wet plume, possibly without full decomposition indicating flooding of an undersized bed [26], [33], [36].

Despite this, the majority of the thrusters have catalyst bed loadings and aspect ratios in the ranges of  $1 \text{ kg.m}^{-2} \text{s}^{-1}$  –  $10 \text{ kg.m}^{-2} \text{s}^{-1}$  and 1 – 2 respectively, which is closer to larger catalyst beds [12]. This is likely to be nearer to an optimum design, but there have been a limited number of studies into the effect of different micro [42] and macro [12], [108], [109] thruster geometries. The tested geometries fall within the central range of the microthruster system literature survey, adding further support. However, none of these studies have highlighted an optimum catalyst bed design, and they have not tied the geometry selection to any of the underlying processes in the bed.

It is important to reiterate that while all of these systems use catalytic decomposition, some of them are thermo-catalytic. In these studies, the heaters are active during the thruster operation, supplementing the enthalpy of the beds with electrical power. Heaters are common on larger thrusters to preheat catalyst beds before firing. This is to decrease the thermal shock of the catalyst during start-up, improving the lifetime of the catalyst material [11], [16], not to improve the performance of the propellant unlike with the presented microthrusters. The additional enthalpy input raises the adiabatic temperature directly, as well as by preheating the propellant prior to injection. These thrusters should have higher relative performance compared to the purely catalytic systems. This obviously comes with the trade-off where additional electrical power input is required. It is reasonable to assume that the reason that so many of these small thrusters include this electrical heating is that the thermal issues of the bed mean that the chemical enthalpy isn't sufficient to achieve high performance. In many of these cases, a steamy plume has been observed. This is indicative of low mean chamber temperatures below the bulk boiling temperature of the propellant. Again, due to the lack of instrumentation, it is not possible to quantify the thermal performance, but the thermal losses are expected to be significant.

Table 2.4 – A list of the catalyst bed design parameters of small and micro monopropellant thrusters, targeting thrusts  $\leq 1$  N, using catalytic decomposition as their primary source of enthalpy.

Source	Type	Structure	Support Material	Active Phase Material	Catalyst Bed Loading [kg.s <sup>-1</sup> ]	Aspect Ratio
Hitt <i>et al.</i> (2001) [26]	Catalytic	Integrated Monolith	Si - Ti coated	Silver	1.59	1.97
Platt (2002) [78]	Catalytic	Packed Mesh	-	Silver	0.04	2.00
Hebden <i>et al.</i> (2005) [43]	Thermo-catalytic	Monolith	Silicon	Silver	0.23	0.57
Takahashi <i>et al.</i> (2006) [27]	Thermo-catalytic	Integrated Monolith	Silicon	Platinum	6.45	0.60
Kuan <i>et al.</i> (2007) [47]	Catalytic	Packed Pellets	-	Silver	9.17	1.10
Cen <i>et al.</i> (2010) [28]	Thermo-catalytic	Integrated Monolith	Silicon	Platinum	37.2	5.36
Yuan <i>et al.</i> (2011) [29]	Catalytic	Integrated Monolith	Silicon	Iridium *	Unknown	4.00
Lee <i>et al.</i> (2012) [32]	Catalytic	Packed Pellets	$\gamma$ -Al	Platinum	61.1	0.40
Miyakawa <i>et al.</i> (2012) [77]	Thermo-catalytic	Integrated Monolith	Silicon	Platinum *	Unknown	0.67
Chan <i>et al.</i> (2013) [74]	Catalytic	Packed Pellets	ceramic?	Silver	Unknown	Unknown
Kundu <i>et al.</i> (2013) [30]	Thermo-catalytic	Packed Wire	-	MnO <sub>2</sub>	4.53	2.33
Huh & Kwon (2014) [33]	Catalytic	Packed Pellets	$\gamma$ -Al	Platinum	0.41	1.59
Khaji <i>et al.</i> (2016) [41]	Thermo-catalytic	Monolith	Sintered Pt Paste	Platinum	0.71	1.74
Huh <i>et al.</i> (2017) [35], [36]	Catalytic	Packed Pellets	$\gamma$ -Al	Platinum	4.43	1.26
Khaji <i>et al.</i> (2017) [42]	Heated Catalyst	Monolith	Sintered Pt Paste	Platinum	0.71	1.77
Ryan <i>et al.</i> (2020) [12]	Catalytic	Packed Pellets	$\gamma$ -Al	MnO <sub>x</sub> / Platinum	16.9	2.85

\* Hydrazine propellant catalyst active phase is not necessarily applicable to HTP propellants.

The injector geometries used for the microthrusters are listed in Table 2.5, although unlike with other elements, there is significantly less documentation on the specific designs. In several cases there is apparently no injector included, although here all of the thrusters are planar, and use a simple actuated syringe pump rather than a flight-representative PDS. ‘Chugging’ and flow instabilities have not been investigated, but in some studies, there is transient pulsing behaviour consistent with the expected unsteady ‘chugging’ phenomenon [27], [28], [30], [41], [42]. Of the remaining known injectors, all of the orifice plate Venturi-type injectors are axisymmetric, and the majority of the Poiseuille-type injectors are planar. This is most likely a result of the manufacturing techniques but is it also apparent that there is a lack of formal injector design methodology for thrusters at these scales. Note that in all cases the injector architecture corresponds to the thruster architecture, i.e. axisymmetric or planar.

There is wide variability of the specific injector design throughout the studies. This includes number and position of ports, and specific cross-sectional areas and lengths. There is no detail on the specific design process, for example fractional pressure drop. Again, this highlights that there is no clear methodology for designing these injector elements, and that there is space for significant research into microinjectors. Some conclusions and assumptions may be drawn from other elements of the system: there may be a certain minimum size of catalyst bed channels of the order of 20  $\mu\text{m}$  that supports steady flow of propellant [26], [47], [87]. This is related to the expansion of the catalytic reaction, so this provides a minimum spacing of injector ports to prevent choking: if they are closer together, they will likely not improve the distribution through the bed.

Table 2.5 – A list of the injector design parameters of small and micro monopropellant thrusters, targeting thrusts  $\leq 1$  N, using catalytic decomposition as their primary source of enthalpy.

Source	Injector Architecture	Number of Ports	Cross-sectional Geometry <sup>*1</sup> [mm]	Length [mm]
Hitt <i>et al.</i> (2001) [26]	Poiseuille – Planar	1	$0.029 \times 0.2$	2.53
Platt (2002) [78]	Poiseuille – Axisymmetric	1	Unknown	Unknown
Hebden <i>et al.</i> (2005) [43]	Orifice – Axisymmetric	2	Unknown	(Unknown)
Takahashi <i>et al.</i> (2006) [27]			None	
Kuan <i>et al.</i> (2007) [47]	Unknown	Unknown	Unknown	Unknown
Cen <i>et al.</i> (2010) [28]			None	
Yuan <i>et al.</i> (2011) [29]	Unknown	Unknown	Unknown	Unknown
Lee <i>et al.</i> (2012) [32]	Orifice – Axisymmetric	1	0.05	(1)
Miyakawa <i>et al.</i> (2012) [77]	Poiseuille – Planar <sup>*2</sup>	7	$0.055 \times 0.2$	2
Chan <i>et al.</i> (2013) [74]	Orifice – Axisymmetric	Unknown	Unknown	Unknown
Kundu <i>et al.</i> (2013) [30]			None	
Huh & Kwon (2014) [33]	Poiseuille – Planar	1	$0.057 \times 0.25$	0.5
Khaji <i>et al.</i> (2016) [41]			None	
Huh <i>et al.</i> (2017) [35], [36]	Poiseuille – Planar	1	$0.05 \times 0.35$	0.5
Khaji <i>et al.</i> (2017) [42]			None	
Ryan <i>et al.</i> (2020) [12]	Orifice – Axisymmetric	1	0.19	(0.5)

<sup>\*1</sup> Presented as circular diameter or width  $\times$  depth.

<sup>\*2</sup> Includes Tesla valve geometry to limit backflow.

## 2.2. Characterising Propulsion Performance

It is important to introduce and discuss the different techniques for characterising thruster performance. Note that the metrics here require direct instrumentation of the internal fluid. As noted, this is a considerable challenge with instrumenting small thrusters. The performance metrics can be split into three main categories:

- Steady state – Metrics that are constant over a long duration of the thruster firing.
- Quasi-static – Metrics that appear constant over a long duration, but that capture effects that are transient in nature. These can be either oscillatory or random, but are of a high enough frequency (e.g.  $\geq 10$  Hz) such that they appear as constant stochastic phenomena.
- Transient and unsteady – Metrics or observations of transient phenomena that are of low frequency or non-repeating and affect to the steady state performance.

### 2.2.1. Steady State Performance

Most classical thruster performance metrics are steady state. These include the raw measured parameters such as static fluid conditions (pressure and temperature), as well as the mass flow rate and thrust. For larger thrusters these are easy to measure: instrumentation standpipes can be included in the thruster and PDS, allowing direct measurement of the static fluid conditions. The mass flow rate and thrust can be measured using instrumentation in the PDS and on the thruster mounting stand [11], [12]. Direct fluid measurements are much more challenging for microthrusters. Instead most temperature measurements are made indirectly using surface thermocouples [33], [36], [77] or thermal cameras [42]. Internal fluid temperatures are often modelled, assumed to be adiabatic [26], [28], or simply just ignored. Similarly, pressure can be challenging to measure, and values used are either the design parameter or an extrapolation from flow characterisation. In some cases, integrated instrumentation has been demonstrated, although it is clearly a non-trivial aspect of microthruster design [41], [42], [47].

Sub-newton thrust levels are not difficult to measure: significantly lower thrusts, for example for most EP systems, have been measured [11]. The thrust measurement for monopropellant engines is tied to the ambient environment and nozzle design. Since sub-newton microthrusters are intended for on-orbit operation, measuring the thrust is not particularly useful in lab-scale atmospheric engineering models: an optimal nozzle could be developed for any environment, and it should not have a significant impact on the rest of the propulsion system elements.

Measuring the mass flow rate for these small systems is more challenging due to the low flow rates. In many cases it is controlled volumetrically using a syringe pump rather than driven by a pressurant system [26], [28], [30], [33], [36], [41]. For some thrusters, it is possible to use very sensitive mass flow meters, for example Coriolis flow meters for low flow rates, for example down to  $0.30 \text{ g.s}^{-1}$  [12]. Alternatively, the mass flow can be lowered by transiently pulsing the flow valve reducing the mean flow rate [74], [78], although for these systems the transient mode of operation will change the behaviour of the thruster. The mass flow rate can also be estimated using a cavitating

Venturi in the PDS line. Similar to a propellant injector, a specific mass flow rate will result in particular pressure differential, measurable across the Venturi nozzle [32], [110]. As with direct fluid parameters, high precision conventional steady state mass flow rate measurements at these scales are non-trivial.

The raw steady state instrumentation can also be used in a number of derived steady state performance metrics. The specific impulse is an important parameter for the full propulsion system and is calculated using the instrumented parameters, either using the thrust or by using the nozzle flow to estimate the nozzle exit velocity. Like the thrust, it is dependent on the performance of the nozzle, so this is less useful when testing under atmospheric conditions. As discussed, the thermal performance of a monopropellant thruster is critical: the main system-level performance gained over a warm or cold gas thruster is due to the additional internal energy of the flow from the decomposition reaction.

The catalytic thermal efficiency of the bed characterises the balance between the thermal energy released from the catalytic decomposition and the heat flux lost through the thruster structure into the ambient environment [16]. It is the ratio of the measured temperature increase to the ideal adiabatic with respect to the inlet propellant temperature, calculated using:

$$\eta_{cat} = \frac{T_c - T_{in}}{T_{ad} - T_{in}} \quad (2.18)$$

Where  $T_{in}$  is the propellant inlet temperature. This is normally equivalent to the ambient temperature but may be higher in the case of preheated propellant. The catalytic thermal efficiency is a direct measurement of the efficiency of the fluid temperature rise due to the propellant decomposition, and represents the enthalpy balance in the thruster. For an ideal adiabatic thruster this will be unity. This requires measuring the steady state chamber temperature which may be difficult, however it does not require the nozzle choking condition. This makes it useful for measuring the performance when the propellant is not fully decomposed or even vapourised, including for a flooded catalyst bed.

A more common measure of the steady state performance of the catalyst bed is the characteristic velocity. Similar to the catalytic thermal efficiency, this captures the catalyst bed performance [11]. Despite being fundamentally a measure of the thermal performance, it can be derived in two ways, using either the chamber pressure and mass flow rate, or the temperature:

$$c_p^* = \frac{P_c A_t}{\dot{m}} \quad (2.19)$$

$$c_T^* = \frac{\sqrt{\gamma T_c R_{spec}}}{\gamma \sqrt{\left(\frac{2}{\gamma+1}\right)^{(\gamma+1)/(\gamma-1)}}} \quad (2.20)$$

While it has no strict physical meaning, it permits the direct comparison of different catalyst beds, regardless of the ambient environment. Both methods are derived from the isentropic nozzle equations presented in Section 2.1.1, and therefore it assumes frozen flow and nozzle choking conditions, unlike the catalytic thermal efficiency. The parameters in both methods are easy to measure on a larger thruster although, as described, they are more difficult to measure on sub-newton thrusters. For ideal adiabatic conditions they are both equal. As an example, the adiabatic

characteristic velocity, calculated using the temperature method for 87.5 %/wt. HTP ( $P_{in} = 25^\circ\text{C}$ ) is 915 m.s<sup>-1</sup>. Since the maximum value for ideal adiabatic conditions, the characteristic velocity can be recast into a characteristic velocity efficiency: the ratio of the real value to the ideal adiabatic value:

$$\eta_{c^*} = c^* / c_{ad}^* \quad (2.21)$$

This can be estimated from experimental measurements using either derivation of the characteristic velocity, where unity represents the ideal case. This is especially useful for characterising the significance of the losses [11], and also allows comparison between unlike propellants. Note that for all of these nozzle-independent catalyst bed performance parameters, while the external ambient pressure does not have any direct effect, the additional convective heat flux will increase the thermal losses, although this may not significantly impact the operation [12].

The nozzle performance can be characterised using the coefficient of thrust:

$$C_F = \frac{F}{P_c A_t} \quad (2.22)$$

This represents the thrust amplification due to the diverging section of the nozzle, and peaks for an ideally expanded isentropic nozzle [11]. This can be used to optimise a nozzle for a given ambient and it is independent from the performance of the injector and catalyst bed, although it also assumes frozen flow and the choked condition. It is expected that for a given catalyst bed, a suitable high-performance nozzle can be designed, but the performance of the two sections upstream and downstream of the nozzle throat are independent.

### 2.2.2. Quasi-Static Performance

The steady state metrics capture the most important performance of the system, although high frequency transient effects also provide information on the specific processes in the catalyst bed or injector. For example, this includes the stability of the decomposition reaction. The roughness of a signal is a statistical measure of the variability of data around the steady state value. It may be expressed as the standard deviation around the mean steady state [12], [111], or as the difference between absolute (peak-to-peak) signal values [28], [91], [92], [112]. Both of these are a combination of any instabilities in the actual conditions as well as the inherent noise of the instrumentation and Data Acquisition and Control (DAQC) hardware. The signal noise is expected to be considerably lower than the roughness. The absolute roughness may be normalised as a fraction of the mean steady state. Variation in the chamber pressure is a result of the reacting flow in the catalyst bed, so the chamber pressure roughness is a representation of the stability of the decomposition processes [12], [32], [91], [92], [111], [112].

It is common to see higher pressure roughness for unsteady flows with poorly performing catalyst beds, for example at lower thermal efficiencies [90], [91], and at high propellant flow rates [111], [112]. The proposed cause of roughness is the cyclical local diffusion of propellant and decomposition products respectively to and from the catalytically active surface area. The frequency and amplitude of the roughness are therefore expected to capture this effect. A relatively dense catalyst bed packing may reduce this source of roughness by limiting the expansion of the products, and the penetration of the liquid propellant into the packed catalyst [90], [112], although the smaller

flow channels may become transiently choked affecting the mass flow rate and pressure drop over the bed [26], [28].

The steady state roughness of the signals either side of the injector is a common method for measuring the injector decoupling effect and 'chugging' onset [32], [90], [91]. There should be no significant pressure roughness upstream of the injector, so comparing the magnitudes of the pre and post-injector roughness highlights any significant instabilities upstream of the injector [90], [91]. This flow coupling behaviour is oscillatory, as is the roughness in the catalyst bed. Some studies have used frequency analysis techniques to try and identify the significant frequency peaks using Discrete Fourier Transform (DFT) analysis [32], [90]–[92]. The specific frequency of 'chugging' is expected to fall between 10 Hz and 400 Hz [11], and some experimental studies with small macroscale thrusters have shown that there are significant frequency peaks between 28 Hz to 73 Hz, which are insensitive to the catalyst bed size and the propellant flow rate [90]. These preliminary results suggest that there is potential for using frequency analysis to provide further insight into the processes underpinning catalyst bed and injector performance.

### 2.2.3. *Transient Effects*

Microthrusters are well-suited for AOCS. These applications require short and repeatable start-ups for fine control, compared to systems for orbit raising which are generally more concerned with performance and thrust over a longer firing [11], [78]. The time to reach steady state operation is important for these applications, and is defined here as  $\tau_{90}$ , or the time between the actuation of the system and the internal conditions reaching 90 % of the steady state value [113].

### 2.3. Review Summary

This chapter presents an overview of monopropellant microthruster theory and current state-of-the-art. The main focus of the literature is on systems using HTP as a propellant since this is directly pertinent to the current work, although much of the discussion can be applied either directly or indirectly to other propellant systems. The discretisation of the system model into different elements: the nozzle, catalyst bed and propellant injector, permits modelling of each components' operation depending on the local conditions. This also implies that the design and performance of each element can be designed independently from the rest of the thruster system. Each element can therefore be studied in isolation of the rest of the system, assuming nominal performance in the rest of the thruster i.e. assuming steady flow, complete decomposition, choked nozzle etc.

The literature also highlights some key challenges with microthruster design. In terms of the overall thruster, most existing sub-newton thrusters have been based on two-dimensional planar architectures which support micro-manufacturing techniques that provide better control over the geometry and tolerances at these small scales. These techniques introduce other issues and challenges, including suffering from reduced performance due to increased thermal and viscous losses. Manufacturing these planar architectures is also challenging, and most of the techniques have limited controllability of the geometry in one or more dimensions and have a common delamination failure mode. Along with the challenge and cost of scaling these techniques up towards the target 0.1 N thrust, these suggest that planar thrusters, or at least the typical manufacturing methods used, are not particularly well suited. There are also some important conclusions that can be drawn from the literature and theory affecting the thruster elements. Notably, where possible axisymmetric designs should be considered.

Sub-newton micronozzles have additional losses resulting from the viscous boundary layer effects for smaller geometries. There has been significant computational work trying to understand and solve the issues on this topic. However, while the overall thruster performance will be significantly impacted by the nozzle design, the effect on the operation and performance of the upstream elements should not be affected, so long as the choked flow condition is valid. Since the scope of the current work only allows for atmospheric testing, the catalyst bed and injector components are the main research focus. In principle, the nozzle design can be optimised for a specific environment. The nozzle is still a critical component of the thruster design, for example the nozzle throat area must be sized with a suitable tolerance to control the mass flow rate. It is also used to calculate some of the derived metrics such as the pressure-derived characteristic velocity. However, not focusing on the nozzle design means that any of the overall system performance metrics such as thrust and specific impulse will not be optimal and are therefore not relevant in the current work.

There has been a lot of experimental and computational research into different aspects of catalyst bed design. This includes analysis of the underlying catalysis mechanism and the reaction fluid flow processes in a catalyst bed. However, the results of the number of monopropellant catalyst bed models illustrate that it is difficult to link these together into a holistic experimentally-validated model that can be used to design a catalyst bed. Instead designs must be optimised experimentally by trial and error. This is especially challenging for sub-newton thrusters given the difficulties with instrumenting the internal fluid. In addition, they also have increased thermal and viscous effects, as

well as the local fluid choking in the small fluid channels between the catalyst material, which may not be captured in models developed for larger thrusters. A better understanding of both the general mechanisms and those specific to the microthrusters would be a useful contribution to the field. It is also important to highlight that there has been little demonstration of high thermal performance of sub-newton thrusters. This is essential to justify their use over micro-EP or cold/warm gas propulsion systems, which are already widely used for this level of thrust.

There is a relative lack of documented knowledge on injector design for small-scale chemical thrusters, and much of the research appears to use rule-of-thumb metrics for good performance (e.g.  $dP = 10\% / P_c$ ). The cause of the flow coupling, and the onset of 'chugging' is not well-documented. Understanding how the different injector architectures prevent this is important for injector design and the optimisation of a propulsion system. This is a particular challenge for sub-newton microthrusters where the manufacturing of the injector geometry at the required scales is difficult, which is another area that would also benefit from extra attention.

There are clearly a number of potential research topics of interest. Given the scope of the current work, several particularly important goals are identified here. Firstly, as there has not been a clear demonstration of a high performing thruster targeting 0.1 N, demonstrating a high-performance thruster design is essential. This includes establishing whether there are any limitations that bound the maximum performance, for example thermal and viscous losses. As part of this, identifying suitable manufacturing techniques for 0.1 N -scale thrusters is critical: Techniques demonstrated for microscale thrusters (e.g. MEMS) or conventional machining are not well suited, and facilitating the instrumentation of the internal flow is critical to verify the performance. A 'baseline' thruster design provides the starting point for further work and demonstrates manufacturing techniques and experimental performance data. The second goal is investigating the design of the catalyst bed and injector elements, providing details on the optimisation process. This also helps underpin the current understanding of the fundamental physical processes in these beds, and validates the models presented in this chapter. A number of different designs, including variants of the catalyst, propellant and element architectures demonstrates the performance impacts. To support this, a third goal is identifying novel analysis techniques to characterise the performance of the thruster elements and wider system. An example that was preliminarily demonstrated in literature is the DFT frequency analysis, which can help to identify the injector coupling and also provide insight on the decomposition and phase change processes inside the catalyst bed.



# Chapter 3

## Experimental Methodology

This chapter will introduce the necessary methodology for the experimental testing of a sub-newton thruster. This includes detailing the design and operation of the PDS developed alongside this research, with a specific focus on the instrumentation used and associated measurement uncertainties. These are especially important given the relative lack of detailed data on the internal fluid conditions of a monopropellant microthruster in the wider literature. Demonstrating rigorous testing and high-quality results is crucial to support future research efforts, and the PDS and instrumentation underpin all of the analysis of the experimental results in the current work.

### 3.1. Chemical Micropropulsion Lab Development

The current research focuses on the design of the thruster components rather than developing a full flight-representative propulsion system. Therefore, as discussed a laboratory-scale PDS is required for propellant storage and flow control over the duration of testing. Since the PDS is laboratory equipment, the design challenges are greatly reduced and larger COTS components may be used. A purpose-built chemical micropropulsion laboratory was created including an HTP PDS, funded as part of a UKSA NSTP research project [12]. The PDS is composed of two main subsystems: the fluidic and DAQC subsystems. The fluidic subsystem is comprised of the components that contain the propellant and pressurant fluid used to drive the flow. It also provides valves to control the fluid flow through the PDS. The DAQC subsystem, encompasses all electronics and computational processing hardware required to support the control of the PDS and the instrumentation. The PDS provides all of the necessary functionality for testing thrusters targeting  $0.01 \text{ N} \leq F \leq 10 \text{ N}$  under atmospheric conditions. Photographs of the laboratory hardware and a schematic of the PDS fluidic system are given in Figures 3.1 and 3.2 respectively, with the key fluidic components listed in Table 3.1, highlighting their specification and usage.

The primary goal of the PDS is to deliver a steady and controllable fluid flow to the thruster under various conditions. The flow is driven by compressed dry nitrogen driving any fluid through the fluidic system to any open vent (including the thruster). The fluidic system is separated into four main sections:

- The dry line where only air, dry nitrogen and trace concentrations of HTP vapour are expected, with components primarily supporting the pressurant system and safety functions.

- The wet line, including the propellant storage tank some supporting fluid fittings and tubing for connectivity, safety and manual pressure control.
- The flow line, joining the tank to the thruster firing valve. This also incorporates the mass flow meter as well as components to support filling and draining of the PDS.
- The inlet line, downstream of the firing valve, including the thruster and the instrumentation for the inlet (upstream of the injector) and any thruster instrumentation.

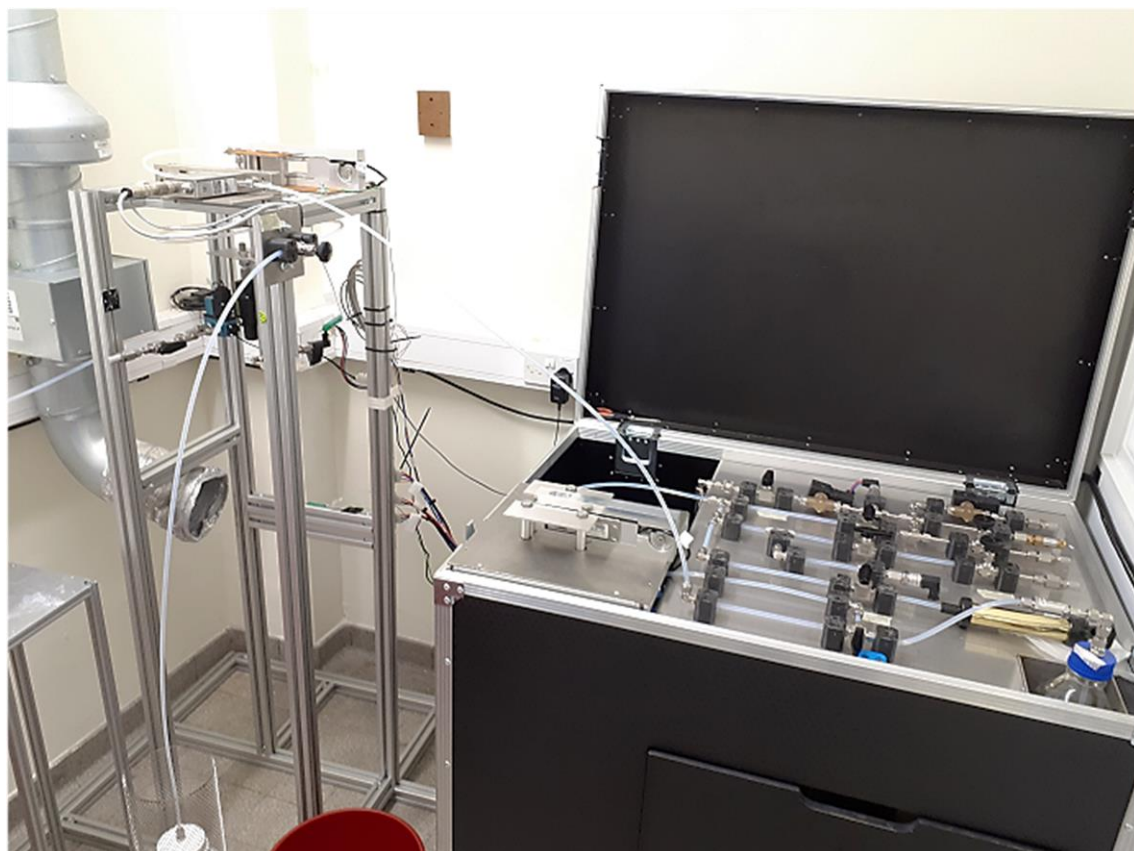


Figure 3.1 – A photograph of the chemical micropropulsion laboratory fluidic system, showing the thrust stand (downstream of MV5) on the left and the rest of the system on the right.

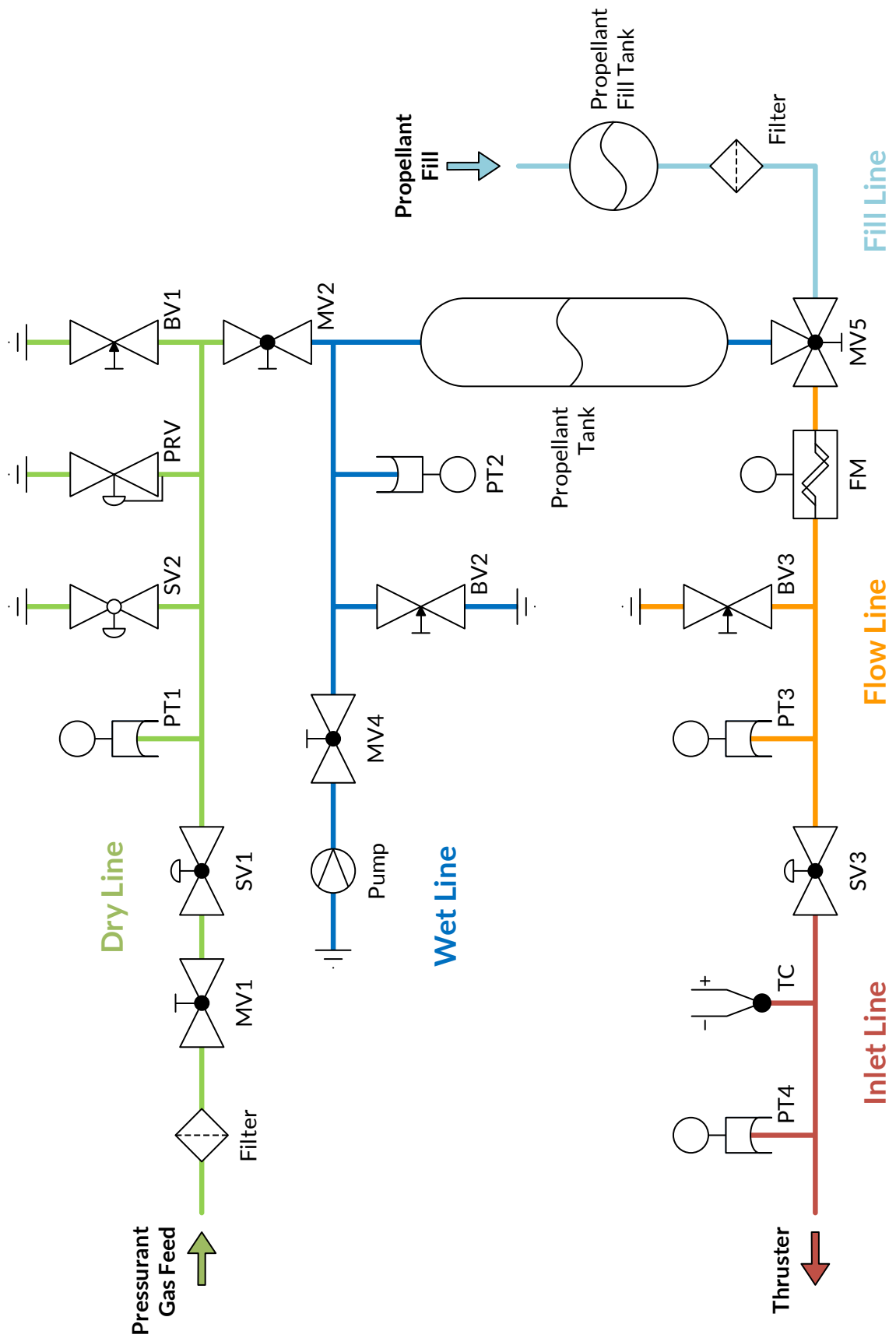


Figure 3.2 – A schematic of the chemical micropropulsion lab PDS and thrust stand.

Table 3.1 – The key fluid and instrumentation components in the micropropulsion lab PDS.

Component ID	Type	Specification	Usage
SV1	Valve (Solenoid)	ERA 2/2 NC 22011 Series, Brass body, Viton Seat Solenoid Valve	Pressurant Control
SV2	Valve (Solenoid)	ERA 2/2 NC 22011 Series, Brass body, Viton Seat Solenoid Valve	Emergency Dry Vent
SV3	Valve (Actuated)	Swagelok SS-43GS4-SC11, One-Piece Ball Valve, SS 316L, 2-Port L-Flow Path, Pneumatically-Actuated	Firing Valve
MV1	Valve (Manual)	Swagelok SS-43GS4-SC11, One-Piece Ball Valve, SS 316L, 2-Port L-Flow Path	N <sub>2</sub> Isolator
MV2	Valve (Manual)	Swagelok SS-43GS4-SC11, One-Piece Ball Valve, SS 316L, 2-Port L-Flow Path	Wet/Dry Isolator
MV3	Valve (Manual)	Swagelok SS-43GS4-SC11, One-Piece Ball Valve, SS 316L, 2-Port L-Flow Path	Wet Vent
MV4	Valve (Manual)	Swagelok SS-43GS4-SC11, One-Piece Ball Valve, SS 316L, 2-Port L-Flow Path	Fill Pump Isolator
MV5	Valve (Manual)	Swagelok SS-42GXS4-SC11, One-Piece Ball Valve, SS 316L, 3-Port L-Flow Path	Propellant Line Selector
BV1	Valve (Needle)	Swagelok SS-1RS4-SC11, Integral Bonnet Needle Valve, SS 316L, PFA Seat	Manual Dry Vent
BV2	Valve (Needle)	Swagelok SS-1RS4-SC11, Integral Bonnet Needle Valve, SS 316L, PFA Seat	Manual Wet Vent
BV3	Valve (Needle)	Swagelok SS-1RS4-SC11, Integral Bonnet Needle Valve, SS 316L, PFA Seat	Manual Drain
PRV	Pressure Release Valve	Brass Pressure Release Valve, 40 bar	Dry Safety Valve
PT1	Pressure Transducer	GEMS 3100 Series, 0-40 barG	Pressurant Control / Dry Pressure Measurement
PT2	Pressure Transducer	GEMS 3100 Series, 0-27 barG	Wet Line Pressure Measurement
PT3	Pressure Transducer	GEMS 3100 Series, 0-27 barG	Flow Line Pressure Measurement
PT4	Pressure Transducer	GEMS 3100 Series, 0-27 barG	Inlet Pressure Measurement
TC	Thermocouple	TC Direct Type K Mineral Instrumented Thermocouple, 0.25 mm SS321 Sheath	Inlet Temperature Measurement
FM	Mass Flow Meter	Bronkhorst M14 Mini Coriflow	Mass Flow Measurement
Filter	Inline Flow Filter	Swagelok SS-4F-40, 40 µm Mesh Filter	Inline Fluid Filter
Not Shown	Flow Arrestor	Swagelok 40 µm Mesh Filter	Vent Flow Arrestor

The system is segregated to group functional and fluid regions together. This is important for ease of reference but also for safety (discussed below). Under nominal operating conditions, all of the lines are connected together and sealed from the ambient environment. When the firing valve (SV3) is opened, the pressurant pushes the fluid through the lines and into the thruster. The system may operate in a passive blowdown mode, where an initial pressure is set which decreases throughout operation as fluid is vented. Alternatively, an active 'bang-bang' pressurant system, controlled by the DAQC, can be used to maintain the pressure at a particular set point. This briefly actuates the pressurant control valve (SV1) between the pressurant storage tank and the rest of the fluidic system, allowing additional high-pressure fluid to maintain the driving pressure. In the blowdown mode, SV1 is closed as the upstream pressure may be up to 300 bar, although the main fluid system is limited to 40 bar. The other valves in the system are for safety, or support the operation by providing filling and draining functionality. When in a passive state, i.e. at all times when not testing, the fluidic sections are isolated from each other and are all vented to atmosphere in case of any residual hydrogen peroxide in the PDS.

HTP poses a number of specific challenges as a propellant for a micropropulsion system: One significant issue with using HTP as a propellant is that it is relatively unstable. It will readily decompose or react with many chemicals, so material compatibility and stringent surface cleanliness is essential. This reduces the risk of decomposition inside the fluidic system which can lead to the build-up of pressure in a sealed region and potentially an explosion. In less extreme cases, slow decomposition inside the PDS lines will produce small oxygen bubbles. These present a number of issues as they will entrain in the flow, precluding consistent measurement of the mass flow rate. As discussed in Chapter 2, accurately measuring the low propellant mass flow rates for sub-newton thrusters is non-trivial, and is made even more difficult by any multiphase or non-homogenous fluid flow in the PDS.

The different lines in the fluidic subsystem define the potentially sealed regions in the PDS. Each of these sections has pressure instrumentation, providing real-time monitoring of the state of the sealed fluid. This is used procedurally to reduce the risk of pressure build-up since each line can be opened to relieve any pressure. One particular concern is the volume inside the ball valves: when closed, a normal ball valve will seal a small amount of propellant inside the valve. This may decompose and may cause the valve to rupture as the pressure increases. To mitigate this, the valve balls are all 'back-drilled', such that any internal volume will always be open to one of the fluidic line sections.

The segregation of the fluidic system affords control of HTP contact to the PDS materials. The decomposition risk is controlled by selecting materials appropriate to the potential exposure to HTP. Where possible, all materials have minimal incompatibility with hydrogen peroxide, i.e. not reacting with or encouraging decomposition. This is particularly important in the sections where the internal materials are in direct contact with liquid HTP. Wetted material selection is limited to only Class 1 HTP-compatible materials [16], [114], [115]. In general, every attempt was made to use only stainless steel grade 316/316L, Perfluoroalkoxy Alkane (PFA) plastic and virgin Polytetrafluoroethylene (PTFE) since the compatibility has been previously demonstrated at the University of Southampton (UoS) for concentrations of HTP up to 87.5% [12], [16]. The full list of wetted materials and their application is included in Table 3.2.

Table 3.2 – A list of the chemical micropropulsion lab PDS wetted materials and uses.

Material	Usage
SS 316/316L	<ul style="list-style-type: none"> <li>• Dry and Inlet line tubing</li> <li>• Tube compression fittings (wetted)</li> <li>• Ball valves (wetted)</li> <li>• Instrumentation (wetted surfaces)</li> </ul>
SS 304	<ul style="list-style-type: none"> <li>• Propellant Tank</li> </ul>
PFA (Clear)	<ul style="list-style-type: none"> <li>• Wet line tubing</li> </ul>
Viton <sup>*1</sup>	<ul style="list-style-type: none"> <li>• Solenoid valve seats</li> <li>• Bleed valve seats</li> <li>• Pressure transducer bonded washers</li> </ul>
PTFE <sup>*1</sup>	<ul style="list-style-type: none"> <li>• Thermocouple fitting thread sealant (tape)</li> <li>• Ball valve seat packing</li> </ul>
Brass <sup>*2</sup>	<ul style="list-style-type: none"> <li>• Pressurant system solenoid body</li> <li>• Dry line Pressure Release Valve (PRV)</li> <li>• Propellant fill pump</li> </ul>

<sup>\*1</sup> Usage limited given the potential for contamination resulting from mechanical attrition.

<sup>\*2</sup> Poor compatibility so only used in areas with low potential for HTP contact (i.e. pressurant lines without any expected contact with hydrogen peroxide liquid, and limited contact with hydrogen peroxide vapour).

In addition to controlling the materials, several other design choices have been made to improve the robustness and safety of the PDS operation:

- All liquid-wetted valves between the propellant tank and thruster are one-piece SS 316/316L ball valves with PTFE seat packing (rather than an elastomer to reduce risk of aging and PDS contamination). The valve balls have a ‘back-drilled’ flow path to prevent any enclosed propellant volume in the valve. These valves were also cleaned to the Swagelok SC-11 standard (ASTM G93) and assembled without lubricant to limit the risk of contamination.
- Clear PFA tubing is used for all cool liquid connections. This is compatible with hydrogen peroxide and allows inspection of the flow, including bubble entrainment. This is particularly important with HTP as they can result of decomposition in the lines.
- The tank fill and feed lines flow both flow through a 3-way ball valve (MV5) to reduce the risk of flow back into the propellant fill line since only one path may be open at one time. This reduces the likelihood of contamination of the propellant fill line, as well as reducing the risk of accidental pressure release.
- A system bleed line for flushing the PDS of propellant or water, post-test or for cleaning, is located close to the thruster inlet to enable flushing of the majority of the system without requiring the removal the thruster. This allows for the fluidic lines to be cleaned directly after testing when the thruster is hot.

- All isolatable sections of the propellant lines are pressure-instrumented to manage risk of propellant decomposition in the lines and to characterise dynamic pressure drops and losses through the system.

The propellant is not stored in the PDS for any long duration due to the possible compatibility issues. Instead, it is stored in surface-treated aluminium 7000 series vented containers at temperatures below 5 °C to minimise the rate of decomposition. Cleanliness is also important to prevent any contaminants from entering the PDS fluidic system. This is not only critical for preventing decomposition, but contaminants can cause blockages in the PDS lines and the small-scale geometries in the thruster, especially the injector. The fill line is nominally isolated from the rest of the system and has a 40 µm inline filter to remove any small particulates during filling. The propellant is filled by drawing the propellant up into the tank by reducing the dry line pressure below ambient with a pump. All vented ports, except the thruster inlet and drain, have inline flow arrestors to prevent ingress of any contaminants. The inlet and drain are also nominally covered to limit any contamination, however these regions are less critical than the rest of the system.

Contaminants may also arise from the materials in the PDS. While all of the wetted materials are Class A compatible, some of the materials are susceptible to damage over long-term usage. Notably, the elastomer PTFE and Viton valve seats can be degraded by both exposure to HTP and to the repeated mechanical wear of the valve actuation. In the extreme case some of this material can break off and become entrained in the flow. Apart from inspection of the components, this is mitigated by flushing the fluidic line with Deionised (DI) water and then dried with the dry N<sub>2</sub> pressurant gas. This clears the HTP from the system, and significantly reduces the concentration of any remaining hydrogen peroxide. In addition, this will flush any contaminants out of the system. Given the high enthalpy and reactivity of HTP, this is drained directly into water to massively dilute it below 2 %/wt. hydrogen peroxide for safe disposal. Note that in many cases DI water may be used instead of HTP, for example characterising the liquid flow through thruster components, for example the injector.

The chemical micropropulsion laboratory also has measures to improve safety and mitigate risk:

- The entire fluidic subsystem is in a test cell, physically isolated from the operation and control room, and access to the system is remote during operation. This limits exposure of personnel to any HTP liquid or vapour during testing. This also reduces the risk of injury in the case of any failure of the PDS or thruster.
- The test cell has a purpose-build Local Exhaust Ventilation (LEV) system for exhaust extraction for up to 10 N engines (using 87.5 %/wt. HTP). This extraction limits the risk of hydrogen peroxide vapour build-up in case of incomplete decomposition.
- Provision of Personal Protective Equipment (PPE), including class 1 compatible polyvinyl gloves, safety glasses and masks, respirator masks, and lab coats, for appropriate use in preventing personnel exposure. In addition, in the case of exposure, DI water eye wash and Diphtherine emergency rinsing solution is also included in the laboratory to limit injury.
- Stocking a minimum of 10 litres of DI water in the test cell for emergency dilution of HTP spills as required.

### 3.2. Instrumentation and Measurement Uncertainties

Besides providing the propellant flow control, the other main function of the PDS is to support instrumentation for measuring the conditions in the PDS and thruster. These data are important for safety, control of the propellant flow, and to measure the internal thruster conditions. There are four types of instrumentation used in the system, providing measurement of temperature, pressure, mass flow rate and force. The key parameters of the instruments are listed in Table 3.3, including the measurable range and uncertainties.

There are two pressure transducer variants with different full-scale ranges. These can be chosen depending on the required range and resolution: in most cases the 27 barG maximum transducer is suitable. The PDS pressurant system uses a 40 barG transducer, but the maximum pressure in the system is limited to 37 barG, below the pressure release valve set-point. While the pressure transducers report the gauge pressure, absolute pressure is used exclusively throughout the rest of this work; the signals are converted in the DAQC system. The Coriolis mass flow meter can measure within the full range of  $0 \text{ g.s}^{-1}$  to  $3 \text{ g.s}^{-1}$ , however the actual measurement range is limited to a subset, selectable based on the target measurement scale. For most testing here, it is set to the limits  $0 \text{ g.s}^{-1}$  to  $0.35 \text{ g.s}^{-1}$  since this captures the range of expected flow rates for the nominal operation of a 0.1 N thruster. A particular benefit of a Coriolis mass flow meter is that it is self-calibrating, and as part of this measures the fluid density. The density measurement is not reported in the current work, however it is used for the automatic calibration of the mass flow rate signal. It may also be used to test the concentration of the HTP.

Table 3.3 – A list of the chemical micropropulsion PDS and thrust stand instrumentation.

Instrument / Hardware	Signal Type	Signal Range	Uncertainty [%]	Response Rate [Hz]
Pressure Transducer, Sputtered Film	[barG] *1	0 – 27 0 – 40	0.25 †1	1000
Thermocouple, Type-k	[°C] *2	0 – 1260	1.0 †2	2.6
Coriolis Flow Meter	[g.s <sup>-1</sup> ] *1	0 – 3.0	0.20 †2	5
Thrust Load Cell, Full Bridge	[N] *3	0 – 5	0.05 †1	2000
Tank Load Cell, Full Bridge	[N] *3	0 – 20	0.02 †1	2000

\*1 Measured as voltage by a NI 9205 DAQ voltage input card.

\*2 As measured by a NI 9213 DAQ thermocouple card.

\*3 As measured by a NI 9237 DAQ bridge card.

†1 Uncertainty as percentage of full-scale.

†2 Uncertainty as percentage of measurement.

The accuracy of the mass flow meter is of particular concern to the current work, as any slight deviation from the actual value has a non-negligible impact on the performance results. The PDS propellant tank is fully supported by a load cell, which is intended to report the propellant tank fill. However, the time differential of the signal can be used to provide validation of the Coriolis mass flow rate measurement. Figure 3.3 shows example tank mass and mass flow rate data. Here the steady state data for the load cell are calculated using linear regression fitting to account for the signal noise and uncertainties. The steady state Coriolis mass flow measurement and the derived mass flow rate measurement from the tank mass are  $0.032 \text{ g.s}^{-1} \pm 0.003 \text{ g.s}^{-1}$  ( $1\sigma$ ) and  $0.037 \text{ g.s}^{-1} \pm 0.006 \text{ g.s}^{-1}$  ( $1\sigma$ ) respectively. Both of these are shown in the figure, including uncertainty bars which are the sum of the  $1\sigma$  measurement variability and the propagated uncertainty. This demonstrates that, for mass flow rates at least as low as  $0.04 \text{ g.s}^{-1}$ , the mass flow meter maintains a good mean accuracy over the length of a test.

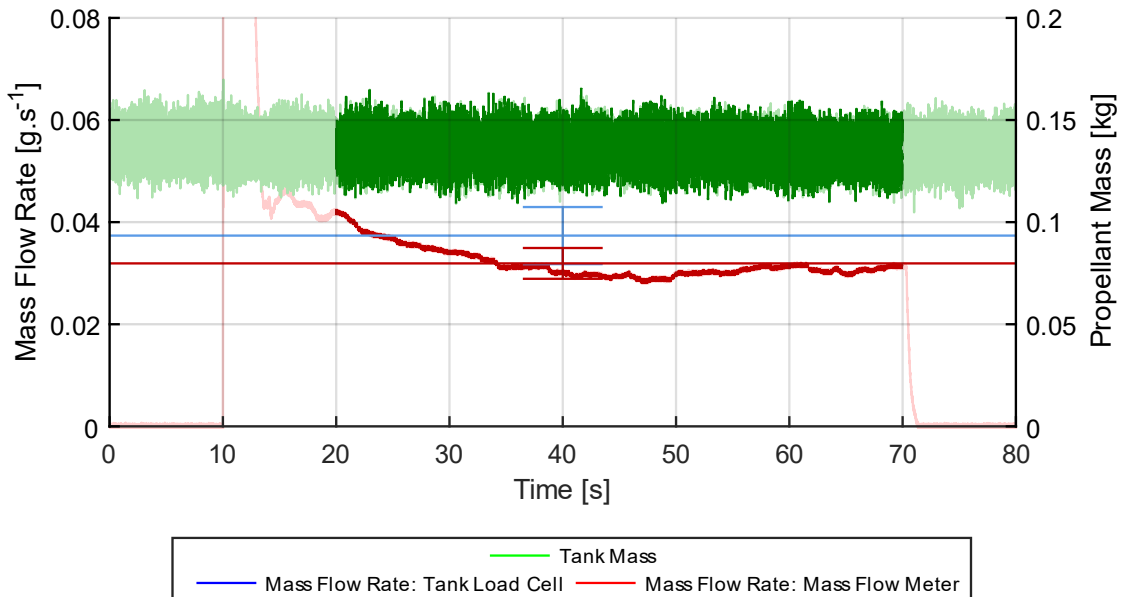


Figure 3.3 – Example time domain data for the propellant tank mass and steady state mass flow rates, showing good agreement between the Coriolis mass flow meter and the propellant tanks load cell data.

The DAQC acquisition and control loop is set at a 2000 Hz cycle frequency to capture any high frequency response in the signals. Note that the upper resolvable frequency is given by the Nyquist frequency, half the frequency of the sample rate. This is discussed in more detail in Appendix A, but the high sampling frequency also helps to reduce aliasing of the signal, where false frequency peaks are reported. It is important to note that while the DAQC sampling rate is 2 kHz, the specific instrument response rates vary. These are also listed Table 3.3, and are given as the maximum resolvable data rate. Most of the instrument sampling rates are lower than the acquisition rate. Data above the Nyquist frequency of each instrument is meaningless. This is not an issue for the steady state metrics but it impacts spectral analysis for quasi-steady metrics where high frequency responses are required.

It is essential to characterise the measurement uncertainties of the instruments and the derived performance metrics. This is particularly important for the mass flow rate given the low range and the relative importance of this parameter for analysis: it is used to calculate derived parameters such as the characteristic velocity and is required to compare different test conditions and components. The instrument uncertainties are also included in Table 3.3, as provided by the manufacturer. It should be noted that both the pressure transducers and load cell uncertainties are fractions of the full scale so higher measured values have a lower relative error. Conversely, the thermocouple and flow meter uncertainties are a constant fraction of the signal. For the derived parameters, for example the characteristic velocity, the instrumentation signal uncertainty propagation is a result of the specific equation used to calculate the data. For an equation  $f(x_1, x_2, \dots, x_n)$  of  $n$  independent variables  $x_i$  each with a standard deviation  $\sigma_i$ , the propagated error of the function can be calculated using the variance equation:

$$\sigma_f = \sqrt{\sum_{i=1}^n \left( \frac{\partial f}{\partial x_i} \right)^2 \sigma_i^2} \quad (3.1)$$

This is only valid for uncorrelated variables, but implicitly allows for non-linear combinations [116], [117]. Values for the typical propagated uncertainties resulting from the instrumentation are given in Table 3.4, based on the expected thruster conditions and calculated using the theory presented in Chapter 2. The uncertainty data are presented as percentages of the mean value, i.e.  $\sigma_f/f$ . Note that this assumes that the definition of the measurement uncertainty specification for each instrument maps directly to the implicit standard deviation in the signal. This means that these values constitute the lower uncertainty bound since there is an additional spread in the data from real thruster tests. Effects include run-to-run variability and signal roughness of the thruster and will be discussed in more detail with the experimental data.

Table 3.4 – Example expected measurement and propagated uncertainties from the instrumentation specification, expressed as a percentage of the signal value.

Parameter	Uncertainty Type	Inlet Pressure [bar]					
		5	10	15	20	25	30
$P_{in}$	Full-scale	1.35	0.68	0.45	0.34	0.27	0.23
$P_c$	Full-scale	1.42	0.71	0.47	0.35	0.28	0.24
$T_{in}^*$	Measurement	0.30					
$T_c^*$	Measurement	0.75					
$\dot{m}$	Measurement	0.20					
$c_P^*$	Propagated	1.42	0.71	0.47	0.35	0.28	0.24
$c_T^*$	Propagated	0.24					

\* Temperatures assumed constant,  $T_{in} = 25^\circ\text{C}$ ,  $T_c = 557^\circ\text{C}$  ( $\eta_{cat} = 0.8$ ).

### 3.3. Summary

This chapter describes the experimental setup of the PDS and instrumentation. The operation of the laboratory is critical both in terms of safety, and to ensure that the collected raw data is robust with known uncertainties. In particular, accurate measurement of the propellant flow rate and the instrumentation from the inlet and the thruster are important for the results and analyses presented in this work. Validation of the Coriolis mass flow meter measurements using the time differential of the propellant tank load cell shows good agreement with the Coriolis flow meter signal. The instrumentation of the thruster has not been described in detail here as the specifics of the implementation will be introduced in the next chapter. However, the instruments used on the thruster are the same pressure transducers and thermocouples used in the PDS fluidic system.



# Chapter 4

## Baseline Thruster Development

### 4.1. Aims and Scope

The theory presented in Chapter 2 is the basis for designing an arbitrary monopropellant thruster. The fluid flow through each of the system elements, the injector, catalyst bed and nozzle, is coupled by mass flow continuity. For a given thruster design, this is set by a target nominal thrust at a particular driving pressure. As discussed, a typical monopropellant propulsion system will operate in a blowdown mode over a range of driving pressures, corresponding to the changing pressure in the PDS over the lifetime. A thruster must be designed for an arbitrary nominal operating point and the performance will vary over this lifetime range. While this sets the mass flow rate, values of other parameters must be chosen, for example of the catalyst bed parametric geometry. These can be selected based on ranges from literature studies, although without experimental testing the performance is unknown, so the chosen design is unlikely to be optimal.

This Chapter outlines the design, manufacture, and characterisation of the baseline thruster used to underpin the following experimental research. As previously noted, the design is based on the analytic monopropellant theory and experimental data from literature. The manufacture is particularly important to document given the issues with other sub-newton thrusters, especially since this thruster architecture incorporates direct instrumentation of the internal fluid. The characterisation of the baseline thruster presented in this Chapter introduces some results from inspection and experimental testing. These results are used to describe the manufactured article, including the expected flow through the thruster elements which are important for the experimental testing in later Chapters.

## 4.2. Thruster Design

### 4.2.1. Blowdown System Model

It is important to select an appropriate nominal design point for the thruster to maximise the performance of the system over the full lifetime. The performance of a thruster is described by the analytic theory from Chapter 2. This can be extended to include the full system by modelling the PDS, and the lifetime performance can be calculated using an explicit forward difference scheme. This computational algorithm steps forward in time from an initial set of BoL conditions, updating the state of each of the elements in the system in turn. The result is a set of data describing the operation of the system over the full blowdown time period. A schematic of this algorithm is shown in Figure 4.1, indicating the data flow and equations used for each of the different calculation steps. By varying the input parameters, i.e. choosing the nominal design point, the model predicts the performance of the system.

Note that the model for the PDS requires additional parameters. The PDS is specified by the lifetime blowdown pressure range and propellant throughput. This assumes that the propellant is incompressible and the pressurant is an ideal gas, such that the tank volume is defined as:

$$V_t = V_{p,BoL} + V_{press,BoL} = M_p / \rho_p + \frac{M_p / \rho_p}{\left(\frac{P_{BoL}}{P_{EoL}}\right) - 1} \quad (4.1)$$

Where the BoL propellant volume  $V_{p,BoL}$  is the full propellant throughput, and the BoL pressurant volume  $V_{press,BoL}$  is defined by the tank lifetime pressure ratio  $P_{BoL}/P_{EoL}$  and the same propellant throughput volume. The propellant throughput is specified as a mass  $M_p$  and the density  $\rho_p$ .

The satellite mass is also provided so that the momentum transfer can simulate the change in velocity of the spacecraft. This is calculated using the rocket equation from Equation (1.3), for reference:

$$\Delta v = c \ln \frac{M_0}{M_1} = c \ln \frac{M_1 + M_p}{M_1} = c \ln \frac{1}{w} \quad (4.2)$$

This can be used to estimate the required propellant throughput since a specific mission will have a defined  $\Delta v$  budget. From discussion with SSTL, a  $\Delta v$  budget of 200 m.s<sup>-1</sup> is a good approximate estimate for start of life operations for an Earth observation microsatellite ( $M_0 \sim 50$  kg) in Low Earth Orbit (LEO), although more capable larger platforms may benefit from a higher budget ( $\geq 500$  m.s<sup>-1</sup>) [12]. The propellant throughput can be calculated using the exhaust velocity from equation (2.5) and the effective exhaust velocity in equation (4.2). For an adiabatic 87.5 %/wt. HTP thruster operating in vacuum, a 200 m.s<sup>-1</sup>  $\Delta v$  manoeuvre for a 50 kg satellite requires 5.102 kg of propellant. Note that this is obviously a gross simplification of the thruster design process: the ideal expansion to vacuum reduces the exhaust velocity calculation to equation (2.8). However, a 5 kg total propellant throughput is a good estimate for this scale of micropropulsion system.

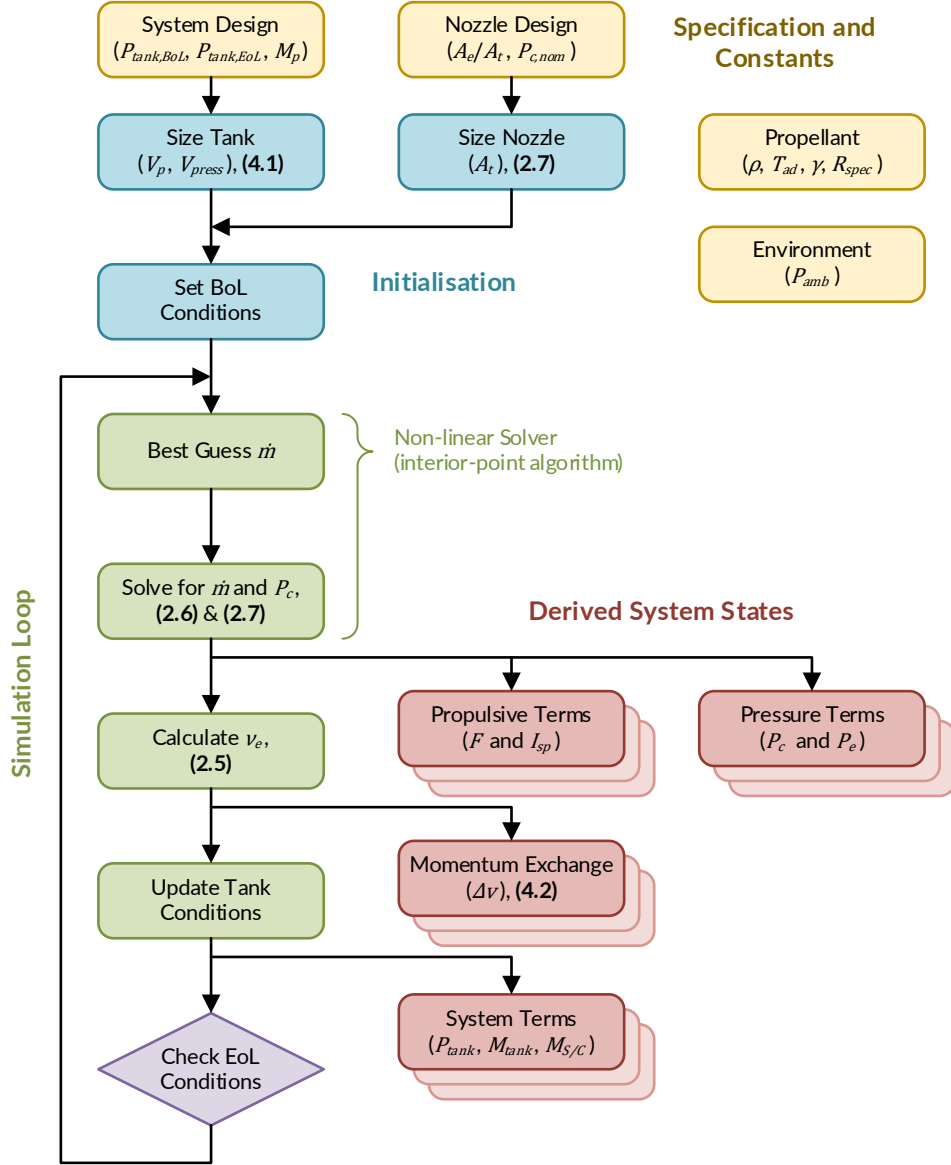


Figure 4.1 – A schematic of the blowdown thruster model algorithm, including parameters and analytic equations. Iterative outputs generated at each time step are shown in red.

The specific schema for selecting the optimal design is to pick the nominal chamber pressure such that the mean thrust over the blowdown lifetime is equal to 0.1 N, i.e. the nominal thrust of the system. The model outputs for this case are shown in Figure 4.2, with the additional parameters specified in Table 4.1. The resulting nominal chamber pressure is 8.053 bar, found through iterative simulations to solve for the mean lifetime thrust. Note that as the current work focuses on experimental testing under atmospheric conditions, values of  $P_{amb} = 1$  bar and the catalytic thermal efficiency,  $\eta_{cat} = 0.8$ . The catalytic thermal efficiency was defined in equation (2.18), and is the ratio of the real to the adiabatic chamber temperature rise. It is less than unity to account for thermal losses to the environment, although there is no data from literature studies to validate the value. The corresponding chamber temperature is 561 °C for the 87.5 %/wt. HTP which was considered to be higher than the expected temperatures when the thruster was designed.

Several other schemas were initially considered, including maximising the specific impulse and cumulative  $\Delta v$ . However, both of these have drawbacks: the specific impulse under vacuum conditions is insensitive to the varying chamber pressure, as discussed in Chapter 2. This is due to the invariable exhaust velocity since the pressure ratio  $P_e/P_c \sim 0$  as  $P_e \rightarrow 0$ . The specific impulse changes considerably under atmospheric conditions since the exhaust velocity varies with the pressure ratio. However, since the tank driving pressure decreases exponentially over the lifetime, the optimal design point to maximise the specific impulse is at BoL. Here the mass flow rate is highest and an ideally expanded nozzle will have the greatest impact. Optimising for the specific impulse is therefore not appropriate under either ambient condition, regardless, a good thruster design methodology should be equally applicable to a flight-representative system. The  $\Delta v$  is similarly affected by the exhaust velocity and pressure ratio and is also not appropriate.

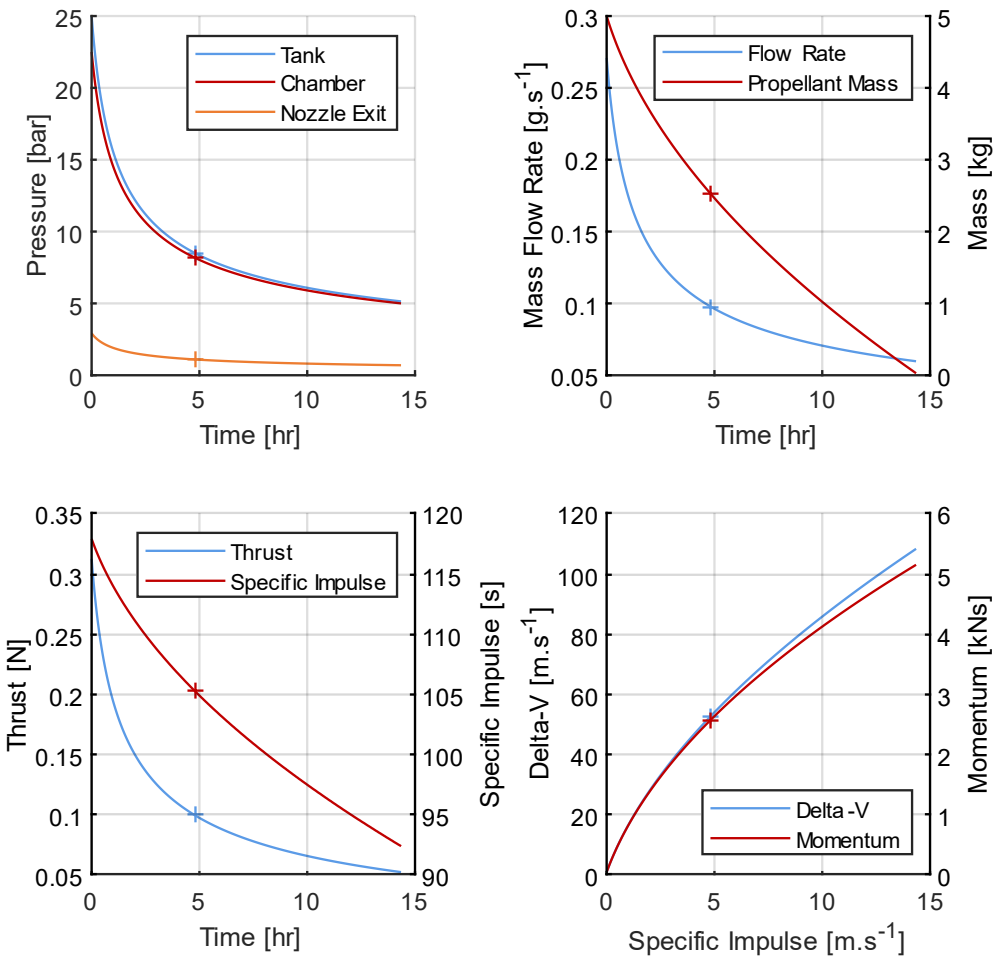


Figure 4.2 – Typical outputs of the blowdown model, generated using the example input parameters listed in Table 4.1. The nominal design point is indicated on each curve.

Table 4.1 – A list of the model parameters for the example simulation results in Figure 4.1.

Element	Parameter	Unit	Value
Satellite / Environment	S/C Wet Mass	kg	50
	Ambient Temperature	K	298.15
	Ambient Pressure	bar	1
Tank	BoL Propellant Mass	kg	5
	EoL Propellant Mass	kg	0
	Tank Volume <sup>*1</sup>	m <sup>3</sup>	4.549 × 10 <sup>-3</sup>
	BoL Tank Pressure	bar	25
	EoL Tank Pressure	bar	5
Thruster	Nominal / Mean Lifetime Thrust	N	0.1
	Nominal Chamber Pressure	bar	8.053
	BoL Injector Pressure Drop (/P <sub>c</sub> )	-	0.1
	Nozzle Area Ratio <sup>*1</sup>	-	1.823 (ideal)
	Nozzle Throat Diameter <sup>*1</sup>	mm	0.363
	Catalytic Thermal Efficiency <sup>*2</sup>	-	0.8

<sup>\*1</sup> Derived value calculated in the simulation initialisation step.

<sup>\*2</sup> Thermal performance is specified as a constant, although it will change over the lifetime.

#### 4.2.2. Baseline Thruster Design

The simulated blowdown model can specify the size of some of the thruster geometry to any arbitrary precision. The actual design values are appropriately rounded for manufacturing and are listed in Table 4.2. The table also includes other key parameters that are not defined by the model. These include the parametric geometry of the catalyst bed and the conical nozzle profile angles. Note that the values for these parameters were selected based on the ranges from the monopropellant microthrusters studies presented in the literature survey in Chapter 2, as well as previous experience on larger thrusters [12]. Importantly, since different propellants have very different reaction pathways, for example the two-step decomposition pathway of hydrazine [60], only literature using HTP propellant was used for these parameters.

Table 4.2 – Baseline thruster parameters including values from the model and literature, as well as the selected design.

Parameter	Unit	Design Value	Source Value	Parameter Type	Parameter Source
Nominal Chamber Pressure	bar	8	8.053	Specification	Model
Nominal Thrust	N	0.1	-	Specification	Specification
Nominal Mass Flow Rate	$\text{g.s}^{-1}$	0.096	0.097	Derived	Model
Nozzle Throat Diameter	mm	0.36	0.362	Specification	Model
Nozzle Exit Diameter	mm	0.49	0.494	Specification	Model
Nozzle Area Ratio	-	1.853	1.857 (ideal)	Derived	Model
Nozzle Convergence Half-Angle	degrees	60	-	Specification	Literature
Nozzle Divergence Half-Angle	degrees	25	25 – 30 *	Specification	Literature
Nominal Catalyst Bed Loading	$\text{kg.s}^{-1}.\text{m}^{-2}$	10	0.05 - 37.2 *	Specification	Literature
Catalyst Bed Aspect Ratio	-	2	0.2 – 2.0 *	Specification	Literature
Catalyst Bed Diameter	mm	3.50	3.504	Derived	Derived
Catalyst Bed Length	mm	7.00	-	Derived	Derived

\* Ranges from literature survey presented in Chapter 2.

An engineering drawing of the thruster design is shown in Figure 4.3. This shows the key dimensions from Table 4.2 and also highlights some important geometric features. Firstly, the thruster design includes integrated standpipes for instrumentation. These have a minimum diameter of 0.5 mm, allowing measurement of the internal temperature using 0.25 mm diameter mineral-insulated K-type thermocouples inserted into the flow and the pressure using externally attached pressure transducers. These instruments are described in Chapter 3. It was unclear whether the preliminary  $\eta_{cat} = 0.8$  was realistic, and where the maximum fluid temperature would be in the bed. To get more detail of the internal catalyst bed conditions, two variants of the thruster were designed with different levels of instrumentation: the standard and highly-instrumented variants. Both have standpipes to instrument the pre- and post-catalyst bed regions to characterise the thruster performance, however the highly-instrumented thruster includes a mid-bed standpipe to provide additional data on the inside of the catalyst pack. The engineering drawing in Figure 4.3 is for the highly-instrumented design, although the standard variant is identical except for the mid-bed standpipe. The instrumentation was expected to affect the thruster performance and operation. The main expected impact was to reduce the thermal performance due to the additional conductive thermal path for enthalpy to leave the thruster. The magnitude of this effect is discussed further in later Chapters. The additional internal volume of the standpipes and attached instrumentation was also expected to affect the quasi-steady and transient performance, including increasing the start-up

time of the thruster. Since this was not expected to have any direct effect on the steady performance of the thruster, this has not been investigated in detail.

Another possible effect arises from the standpipe in the converging section of the nozzle: Firstly, the flow expands in this region so the static pressure may not be the true chamber pressure. Secondly, since the flow is non-negligible, the angle of the standpipe may affect both the flow and the measurement. Notably, the flow may partially stagnate so the measured pressure may be higher than the static pressure of the flow. The design was considered acceptable given the challenges of instrumenting a thruster of this size and the expected issues with convective thermal losses. Improvements could be made in future iterations, for example extending the cylindrical profile downstream of the bed to move the standpipe out of the nozzle.

The second important feature is the bolted flange. To allow easy filling and reuse of the thruster it is manufactured from two parts: the thruster body which consists of the catalyst bed and nozzle, and the injector head which seals the thruster and provides the pre-bed instrumentation. These are held together by six M1.7 bolts, providing a compressive force to seal the components with a gasket. This is discussed further in Section 4.3. Finally, since the catalyst bed is composed of pellets, the pellets must be held in a stable packed structure. Catalyst retainer plates are included upstream and downstream, held in place by the surface of the injector head and integrated retainer support arches respectively. This is also covered in more detail in Section 4.3.

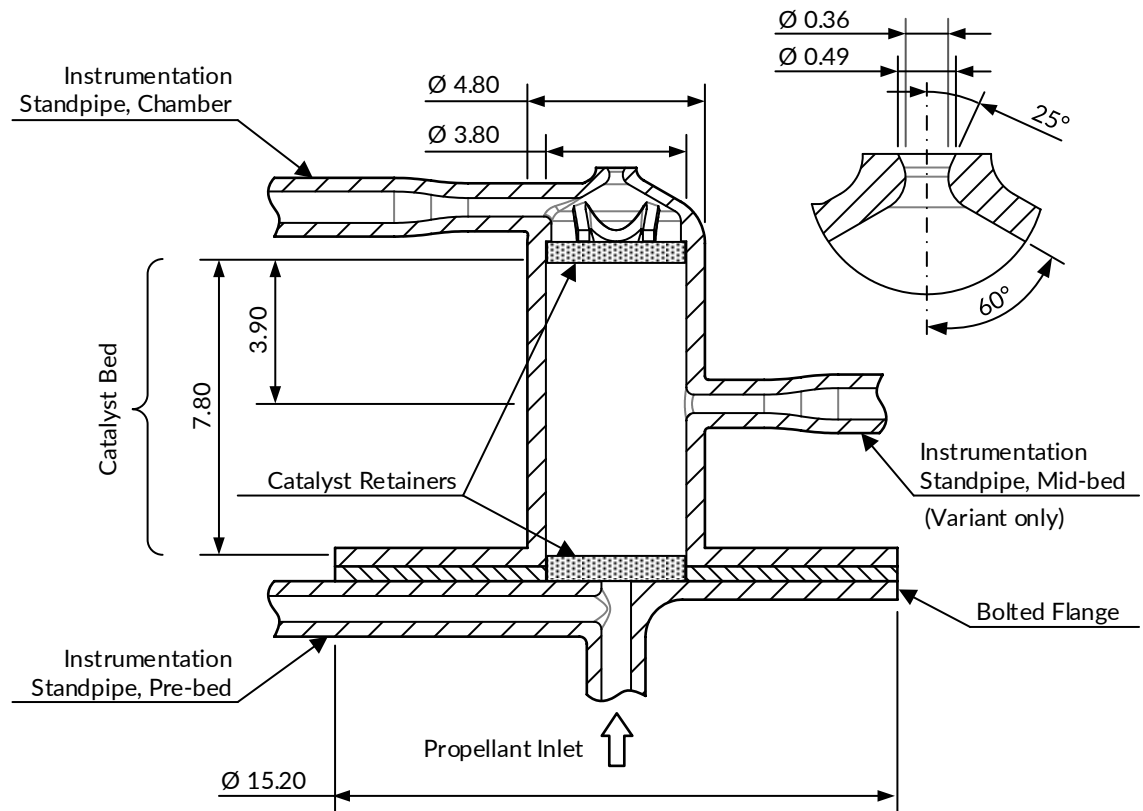


Figure 4.3 – An engineering drawing of the highly-instrumented baseline thruster variant, including a detail view of the nozzle.

## 4.3. Thruster Manufacture

### 4.3.1. Baseline Thruster Manufacturing and Components

The baseline thruster design is not suitable for any of the processes demonstrated for microthrusters: metal or glass etching, or co-fired ceramic forming. Additionally, the high complexity and scale of the geometry also means that conventional machining is not feasible. Instead, the baseline thruster components are additively manufactured using metal SLM. This process is well-suited to producing parts with complex geometries, including larger propulsion system components [44], [118], [119], although at the time of writing, this is the first application of the process to a sub-newton thruster below 0.5 N and is the only microthruster including integrated instrumentation standpipes.

The components were commercially manufactured by Metal Technics 3D from SS 316/316L on a Trumpf Truprint 1000 metal SLM machine with a 15  $\mu\text{m}$  diameter mean powder particle size. A minimum wall thickness of 0.30 mm was chosen to maintain the structural integrity while minimising the conductive thermal path through the propellant inlet and instrumentation standpipes. The SLM process parameters were defined as a layer thickness of 30  $\mu\text{m}$ , a 150 W beam power, a scanning speed of 675  $\text{mm}\cdot\text{s}^{-1}$  and a 100  $\mu\text{m}$  hatch spacing. The resulting energy density was 74.1  $\text{kJ}\cdot\text{mm}^{-2}$ . The thruster was oriented with the nozzle towards the base plate so that the internal nozzle surface and catalyst retainer supports could be printed without support. As a result, the outer surfaces were manufactured with support material to reduce distortion of the parts during the process. There was some minor distortion of the standpipes, however this did not affect the compression fitting seal. A photograph of the two baseline thruster variants as-printed is shown in Figure 4.4



Figure 4.4 – A photograph of the as-printed baseline thruster components.

The thruster body flange thickness was oversized by an additional 1 mm thickness to reduce the impact of any distortion. This excess was removed in a secondary grinding process. The injector head flange did not require any additional material to prevent distortion since the flange was printed in contact with the base plate. However, it was oversized by 0.3 mm to permit polishing of the mating face to improve gasket sealing. The thruster body flange was also polished as part of the grinding step. After the removal of the support, some post-processing was required on the nozzle exit to improve the surface quality. The final components have relatively high roughness on all non-post-processed surfaces compared to conventional machining. This is especially high on the outer surfaces of the thruster due to removal of the required support material, but this should not affect the performance of the thruster. It is worth highlighting that these flanges will not be present on a flight-representative thruster. Instead a thruster is typically sealed using a process such as welding or brazing [12]. A full list of the component specification for the thruster is given in Table 4.3, including all wetted components for instrumentation and assembly, along with the relevant sections discussing the components. A photograph of the assembled thruster (standard variant) is shown in Figure 4.5.

Table 4.3 – A full list of the baseline thruster components, including any ancillary items for instrumentation and sealing.

Component	Material	Manufacturing Method	Relevant Section
Thruster	SS 316	SLM, Polished	(4.3.1)
Injector Head	SS 316	SLM, Polished	(4.3.1)
Catalyst	Pt - $\gamma$ Al	Procured	4.3.5
Catalyst Retainer Plates	Ni	Punched, Compressed	4.3.5
Flange Sealing Gasket	Klinger C-4430 (bonded polyaramid-glass fibre)	Procured, Punched	(4.3.1)
Flange Bolts	SS A2, M1.6	Procured	-
Fluid Compression Fittings	SS 316	Procured	-
Instrumentation - Thermocouple	SS 321 (0.25 mm diameter sheath)	Procured	3.2
Instrumentation – Pressure Transducer	SS 316	Procured	3.2
Instrumentation - Thermocouple Compression Fitting (Ferrule)	Graphite	Procured	-
Instrumentation – Pressure Transducer Bonded Washer	SS 316 - Viton	Procured	-

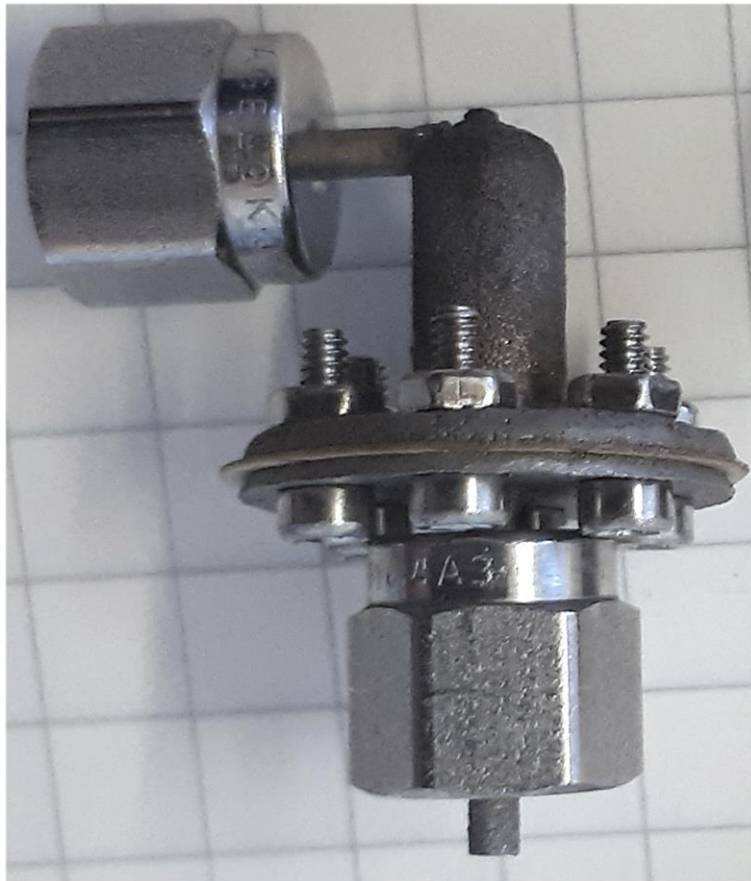


Figure 4.5 – A photograph of the assembled standard variant baseline thruster.

#### 4.3.2. Thruster Inspection

The roughness of the as-printed thruster surfaces compared to a machined surface raises concerns about the possible viscous losses. A metric to assess the significance of the surface roughness is the surface arithmetical mean height,  $S_a$ . This is estimated using 3D meshed geometry generated from x-ray CT scan data of the thruster. An example section of the CT micrograph is included in Figure 4.6 for reference.  $S_a$  measurements were made separately on the vertical and 60 ° converging nozzle walls with values of 13  $\mu\text{m}$  and 38  $\mu\text{m}$  respectively. These measurements are similar to the expected roughness resulting from the SLM mean particle size and layer thickness, 15  $\mu\text{m}$  diameter and 30  $\mu\text{m}$  thick respectively. This confirms that these parameters are the principal causes for the microscale surface geometry, and therefore represent a minimum limit to the as-printed roughness. Any further improvements without changing these requires additional post processing steps.

It should be noted that the voxel resolution of the CT data is 21  $\mu\text{m}$  and the complex geometry of the thruster results in x-ray shadowing and refraction on the raw images used to generate the CT data. As a result, there is some uncertainty in the  $S_a$  measurements. These effects are difficult to quantify without reference calibration geometry, which was not possible to manufacture and inspect to a suitable accuracy within the scope of this research.  $S_a$  measurements were also not possible for areas with complex geometry, such as the nozzle throat and catalyst retainer supports, as there is no clear contiguous geometry. Qualitatively, these regions appear to have a higher roughness.

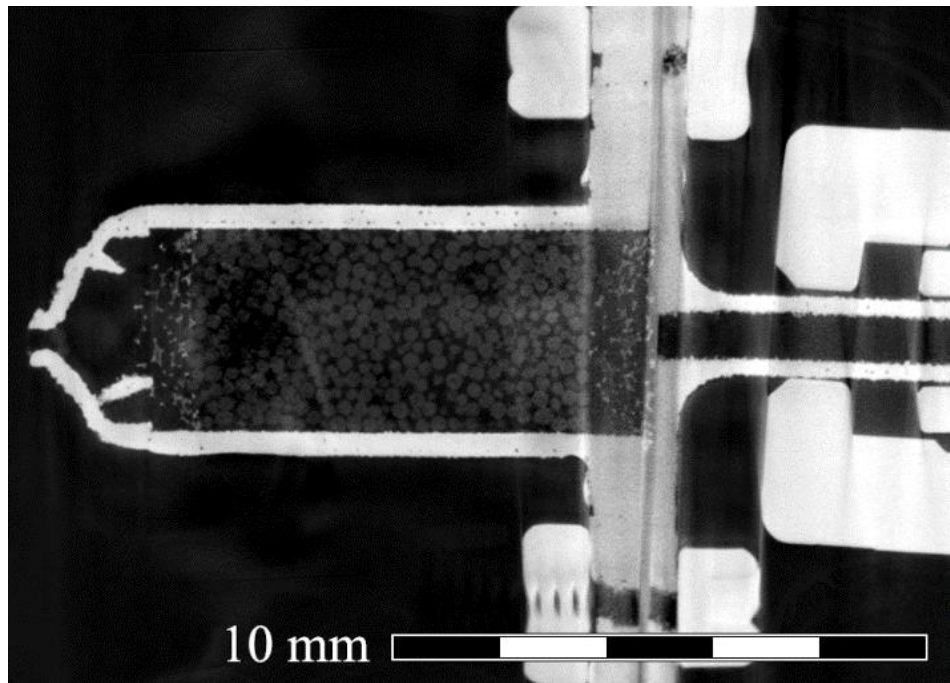


Figure 4.6 – A micrograph section through the central axis of the highly-instrumented baseline thruster variant CT scan. The absolute pixel brightness has been adjusted to better visualize the catalyst pellets, also increasing the relative effect of the x-ray shadowing artifacts.

There are some additional notable effects of the manufacturing process on the thruster:

- **Material Porosity:** AM components have some degree of porosity as a result of sintering/melting of the powder base material. There are noticeable small voids located at the intersection between the wall and infill paths, particularly in the cylindrical section walls, visible in Figure 4.6. They are at the limit of the resolution of the CT scan data, i.e.  $\leq 21 \mu\text{m}$ , but smaller pores are expected throughout the bulk of the material. While these will affect the material properties, the design took potential defects and porosity into account and the components were deemed satisfactory for testing under high temperature and pressure.
- **Thermal effects:** Given the large amount of localised thermal energy in the SLM process, thermal stresses are common in metal AM parts, and the localised heating can affect geometry during printing. The large thermal mass of the nozzle plenum standpipe has caused local distortion of the nozzle, pulling it off-centre during manufacturing. This is shown in the overlay of the 3D surface data from the CT scan and the Computer Aided Design (CAD) model in Figure 4.7. The distortion appears to be linear, only affecting the centre-centre offset, 297  $\mu\text{m}$ .
- **Throat geometry distortion:** As discussed, there is a surface roughness in regions with complex geometry. While no support material was on the internal faces (including the diverging nozzle section) this has resulted in deviation from the nozzle design. The nozzle cross-section is imperfect and there is some non-uniformity in the profile along the axial direction, illustrated in the CT micrograph sections in Figure 4.8 of the nozzle profile and the throat plane. Analysis of the CT scan data provides the profile circularity of the nozzle geometry, plotted in Figure 4.9. Note that the variability in the

profile diameter in this data is due to the plenum standpipe. This analysis gives the throat area,  $0.0754 \times 10^{-8} \text{ m}^2$ , corresponding to an effective diameter of 0.310 mm. This is smaller than the specified 0.36 mm diameter for the design and is due to the small 'bump' seen on the throat cross-section in the micrograph in Figure 4.8. Note that due to the shape of the thrusters and the optical diffraction around the rough surface, it was not possible to get a clear optical micrograph to measure the throat area of the AM thrusters.

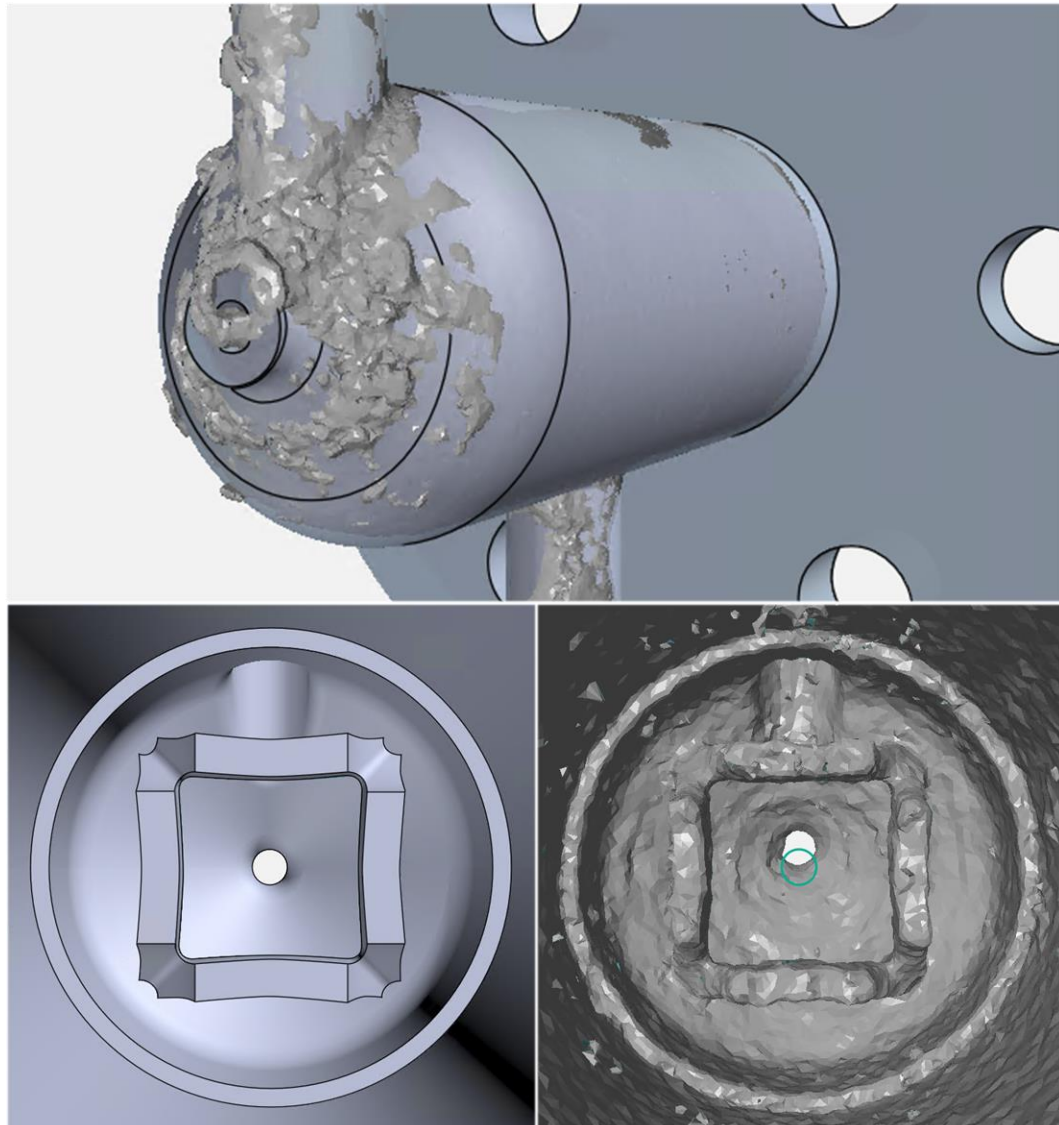


Figure 4.7 – 3D geometry of the CT scan surface data and the CAD design showing the distortion of the nozzle resulting from the inclusion of the plenum standpipe.

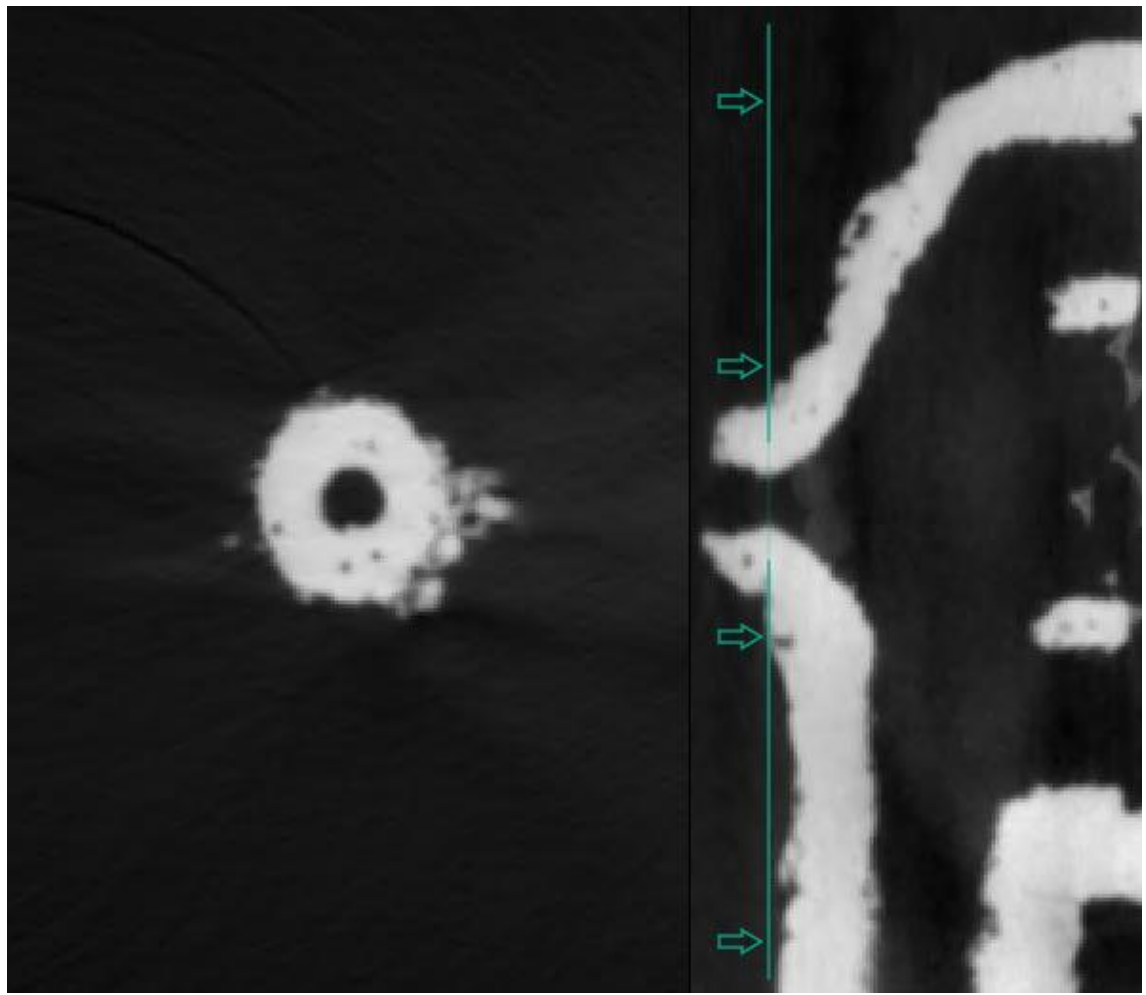


Figure 4.8 – Micrograph sections through the central axis and the plane of the nozzle throat of the highly-instrumented baseline thruster variant CT scan.

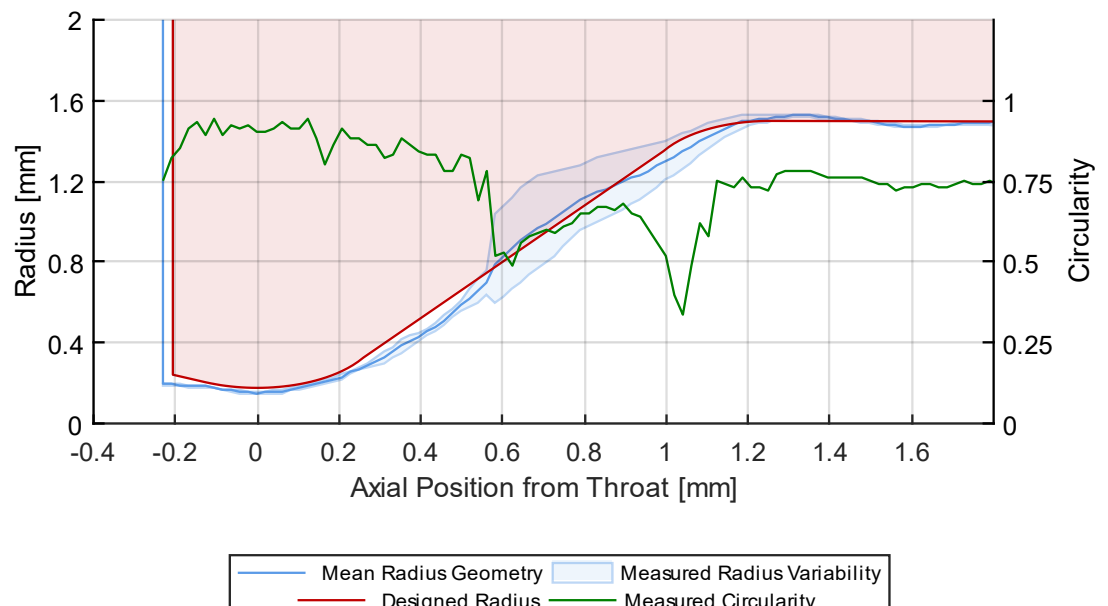


Figure 4.9 – Nozzle geometry parameters, extracted from the highly-instrumented baseline thruster variant CT scan.

### 4.3.3. Nozzle Characterisation

The x-ray CT scan data can be used to find the nozzle throat area, although acknowledging the issues resulting from x-ray refraction. However, x-ray CT scanning was only possible for a small number of the components in the current work, so another method of determining the throat area was needed. Since the mass flow rate through an ideal nozzle can be described by Equation (2.6), deviations from the design geometry are captured using the effective throat area,  $C_d A_t$ , where  $C_d$  is the nozzle discharge coefficient. This also includes any impacts of the viscous effects which are likely given the rough surface, as well as other non-isentropic effects, for example shock formation. Equation (2.6) therefore becomes:

$$\dot{m} = C_d A_t \frac{P_c \gamma}{\sqrt{\gamma T_c R_{spec}}} \sqrt{\left(\frac{2}{\gamma + 1}\right)^{\frac{\gamma+1}{\gamma-1}}} \quad (4.3)$$

The nozzle flow characterisation uses dry nitrogen gas, with known physiochemical parameters and assumes the choked flow condition. The mass flow rate and pressure inside the thruster are measured over a blowdown range, and the effective throat area is calculated using the gradient of the experimental data. Example flow characterisation data for the standard baseline thruster variant are shown in Figure 4.10, including the both the time and characterisation domain data. A quick validation check confirms the choking condition: the characterisation curve is linear so  $\dot{m} \propto P_c$ . Note that the in this instance, mass flow rate through this nozzle is limited to  $\dot{m} \leq 0.3 \text{ g.s}^{-1}$  by the Coriolis flow meter range.

The baseline thruster variant effective throat areas are listed in Table 4.4, along with the expected isentropic nozzle design for reference. These were calculated using linear regression to test data, illustrated in Figure 4.10. The two baseline nozzles have a large difference between their characterisation values, with  $C_d = 1.19$  and  $C_d = 0.89$  for the standard and highly-instrumented variants respectively. This is due to the variability resulting from the AM process and the lack of accurate inspection of the standard variant nozzle: the nozzle throat is estimated using the design value of 0.36 mm diameter; however the discharge coefficient is above unity so the actual area must be larger. The highly-instrumented nozzle is characterised using the CT inspection data so should only be considering non-isentropic effects: using the as-designed throat area, the discharge coefficient drops to  $C_d = 0.66$ , reflecting the smaller throat area compared to the design.

The expected discharge coefficients of nozzles with diameters  $\geq 0.2 \text{ mm}$  should be in the range  $0.9 \leq C_d \leq 1$ , assuming that the nozzle is well designed [48]–[53]. The highly-instrumented nozzle appears to fall just below this, which may be expected given the surface roughness. A dummy thruster with simplified micro-nozzle geometry was manufactured using conventional micromachining. The ‘nozzle’ geometry is an orifice plate with a 0.36 mm diameter throat in a 0.5 mm thick plate. Unlike the AM nozzles, the throat area could be optically inspected. The throat area was measured to be  $1.06 \times 10^{-7} \text{ mm}^2$ , corresponding to a 0.367 mm diameter. The inspection and characterisation data are also included in Table 4.4. The coefficient of discharge is calculated as 0.88, which agrees with the increased losses expected for gas flow through orifice plates [120]. A sharp-edged orifice has significant non-isentropic effects due to the gas flowing around the sharp corners of the throat, which may result in highly turbulent flow or shock formation. These effects should be larger than for those in a contoured nozzle, so the orifice characterisation provides a lower bound for the expected choked

flow coefficient of discharge. It also further corroborates that the standard variant thruster result is due to the as-manufactured geometry variability. Despite this, without accurate throat areas the non-isentropic effects cannot be decoupled from the manufacturing variability, therefore the effective throat area  $C_d A_t$  describes the flow regardless of the either of these effects and will therefore be used for all following analyses instead of the designed nozzle throat area.

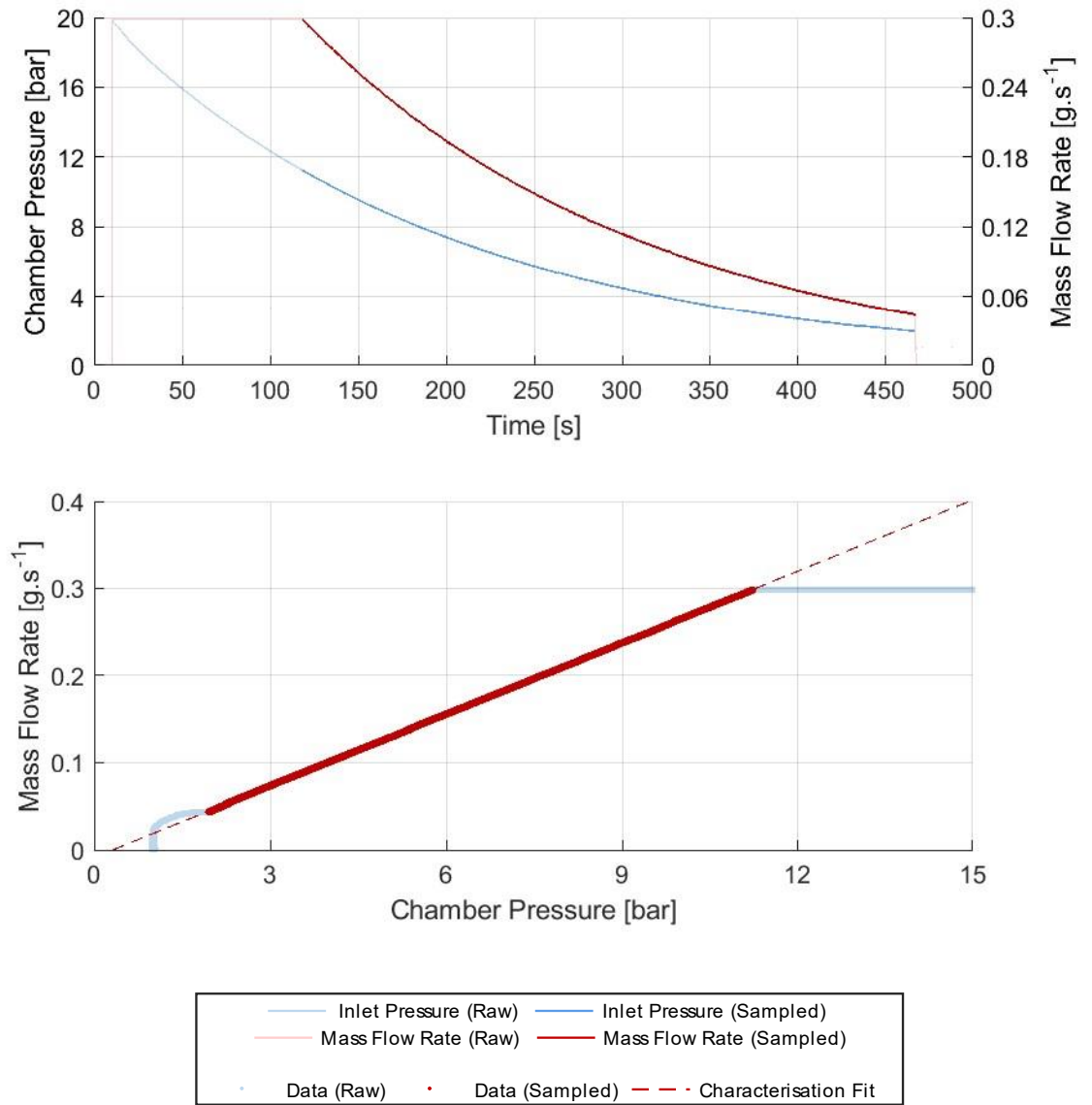


Figure 4.10 – Example nozzle characterisation for the standard baseline thruster variant, showing data in the time domain (top) and characterisation domain (bottom).

Table 4.4 – Baseline thruster nozzle characterisation table, including the additional model parameters.

Parameter	Unit	Thruster Variant			
		Design	Standard	Highly-Instrumented	Dummy Thruster
Effective Throat Area	$\text{m}^2$	$1.018 \times 10^{-7}$	$1.208 \times 10^{-7}$	$0.672 \times 10^{-7}$	$0.937 \times 10^{-7}$
Effective Throat Diameter	mm	0.36	0.392	0.292	0.345
Reference Throat Diameter	mm	-	(0.36) *1	0.310	0.367 *2
Reference Geometry Type	-	-	Design	X-ray CT Inspection	Optical Inspection
Nozzle Discharge Coefficient		1	1.19	0.89	0.88
Model Pressure Range	barG	N/A	1.02 – 10.14	1.80 – 15.53	3.88 – 14.03
Model Mass Flow Rate Range	$\text{g.s}^{-1}$	N/A	0.046 – 0.296	0.035 – 0.248	0.083 – 0.298
Model x-Intercept	barG	N/A	-0.71	-0.48	-0.14

#### 4.3.4. Injector Selection

A preliminary injector selection was carried out to identify a suitable design for the baseline thruster. Based on the surveyed literature in Chapter 2, Poiseuille injectors are extensively used in micro-thrusters and were expected to be robust to pressure instabilities. A number of cold-rolled SS 304 microbore tubes were procured, and the liquid flow was characterised similarly to the nozzles. In this case deionised water was used as the working fluid, where the pressure drop and mass flow rate are related through the modified Hagen-Poiseuille in Equation (2.17), for reference:

$$dP = \dot{m} \frac{L_{pos}}{C_d A_{pos}^2} \frac{8\pi\mu}{\rho} = \dot{m} \frac{1}{C_d \zeta_{pos}} \frac{8\pi\mu}{\rho} \quad (4.4)$$

As this equation is only valid for low  $Re$  numbers, i.e. low flow velocities, the flow should be unchoked and therefore the exit pressure is assumed to be ambient  $\sim 1$  bar. The full results of the characterisation will be discussed in Chapter 7, which details the investigation into injector design and performance. Instead, this section presents the characterisation of the selected baseline Poiseuille injector, a 100 mm  $\times$  254  $\mu\text{m}$  tube with an expected  $10.6\% / P_c$  pressure drop. This was anticipated to be insensitive to flow instabilities since it falls within the demonstrated range for well-performing injectors from literature,  $0.05 \leq dP_{inj}/P_c \leq 0.20$  [12], [26], [36].

Figure 4.11 shows plots of the injector characterisation data. Note that due to the low flow rates of liquid and the size of the pressurant head in the PDS tank, the pressure is varied in steps rather

than allowed to blowdown as with the nozzle. The effective geometric parameter,  $C_d A_{inj}^2 / L_{inj}$  is calculated by linear regression fitting to the mass flow rate and pressure drop. The pressure drop is calculated assuming the ambient downstream pressure, i.e.  $dP = P_{in} - P_{amb} = P_{in} - 1$  bar. The effective geometric parameter was calculated as  $2.46 \times 10^{-14} \text{ m}^3$ , compared to the expected  $2.57 \times 10^{-14} \text{ m}^3$  from the design geometry, yielding a coefficient of discharge of 0.96. The model has a non-zero intercept, but as the offset is greater than the propagated instrumentation uncertainty, it is suggested that this is due to some effect not captured by the model. There are several possible causes, although the most likely is are the result of the non-axial flow components in the regions around the ends of the injector; this is discussed in more detail later in Chapter 7.

As a check to ensure that the flow is laminar and the effective geometric parameter is valid, the Reynolds number can be estimated using Equation (2.9) for the circular cross-section channel:

$$Re = \frac{4\dot{m}}{\pi D \mu} \quad (4.5)$$

The highest expected Reynolds number occurs at the maximum mass flow rate ( $0.3 \text{ g.s}^{-1}$ ). For this baseline injector, this 'worst case' (most likely to be turbulent) flow has a  $Re = 1290$ , which is below the expected turbulent transition for microbore tubes of  $1700 < Re < 2000$  from literature [102], [103]. The model is therefore expected to be valid, although this turbulent transition range considers smooth tubes while the injectors have some surface roughness which may reduce the transition point further. This is also discussed in more detail in Chapter 7.

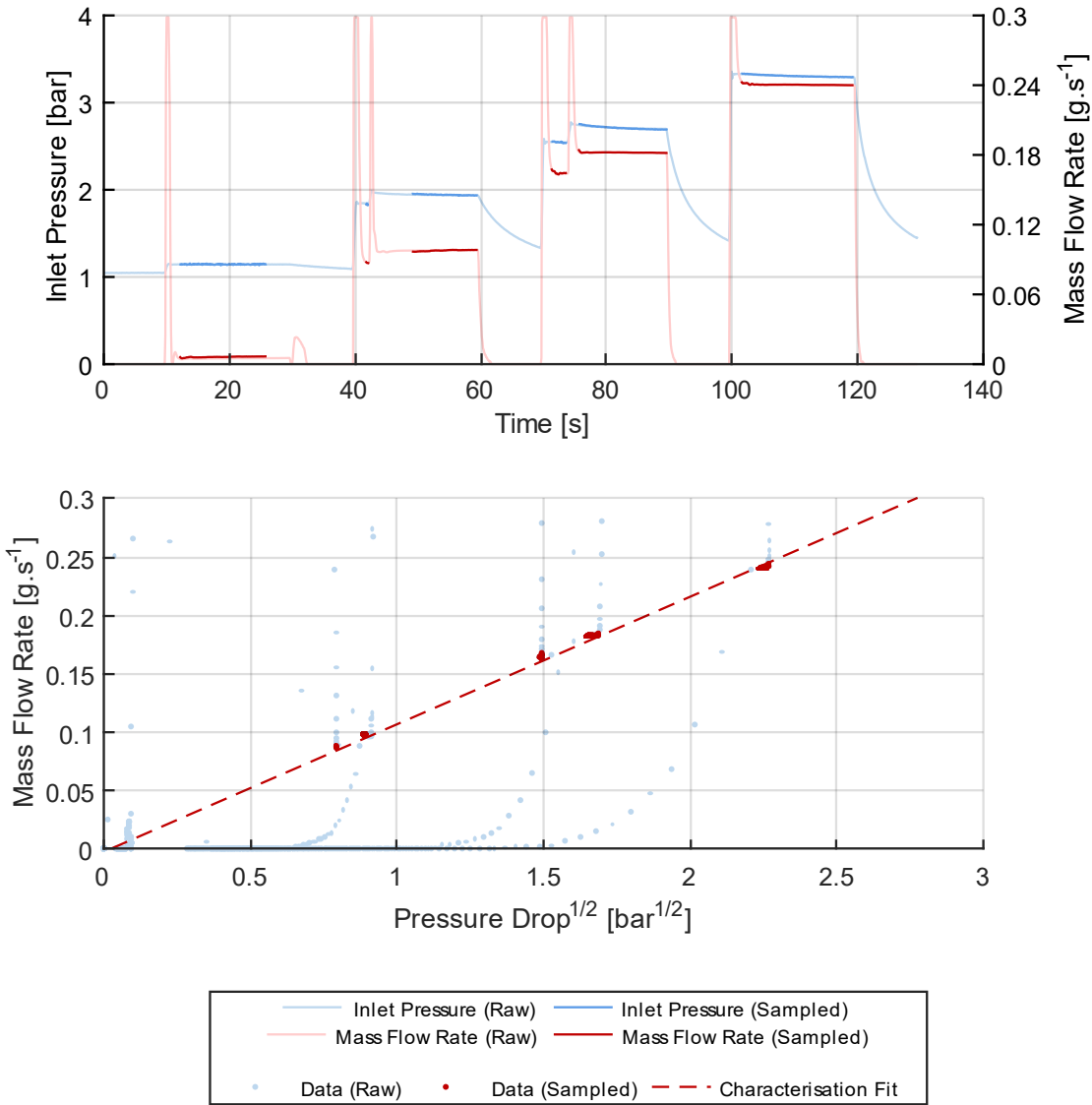


Figure 4.11 – Baseline Poiseuille injector characterisation showing the time-series data (top) and the characterisation curve (bottom).

#### 4.3.5. Catalyst Bed Material and Retention

The current work is not intending to investigate the design of catalyst material. Therefore, a suitable high performance commercially available catalyst was selected as the baseline material. This catalyst has a platinum active phase supported on nominally 300  $\mu\text{m}$  diameter spherical  $\gamma$ -alumina pellets, supplied by Alsys France. A series of optical micrographs were taken to perform an assessment of the catalyst material geometry. An example Extended Focal Image (EFI) micrograph from this series is included in Figure 4.12, showing the surface detail over the depth of the pellets. While the catalyst is approximately spherical, there is some variability in shape and surface texture. The statistical distributions of some key geometric parameters of the pellets, the area and circularity, shown in Figure 4.13.

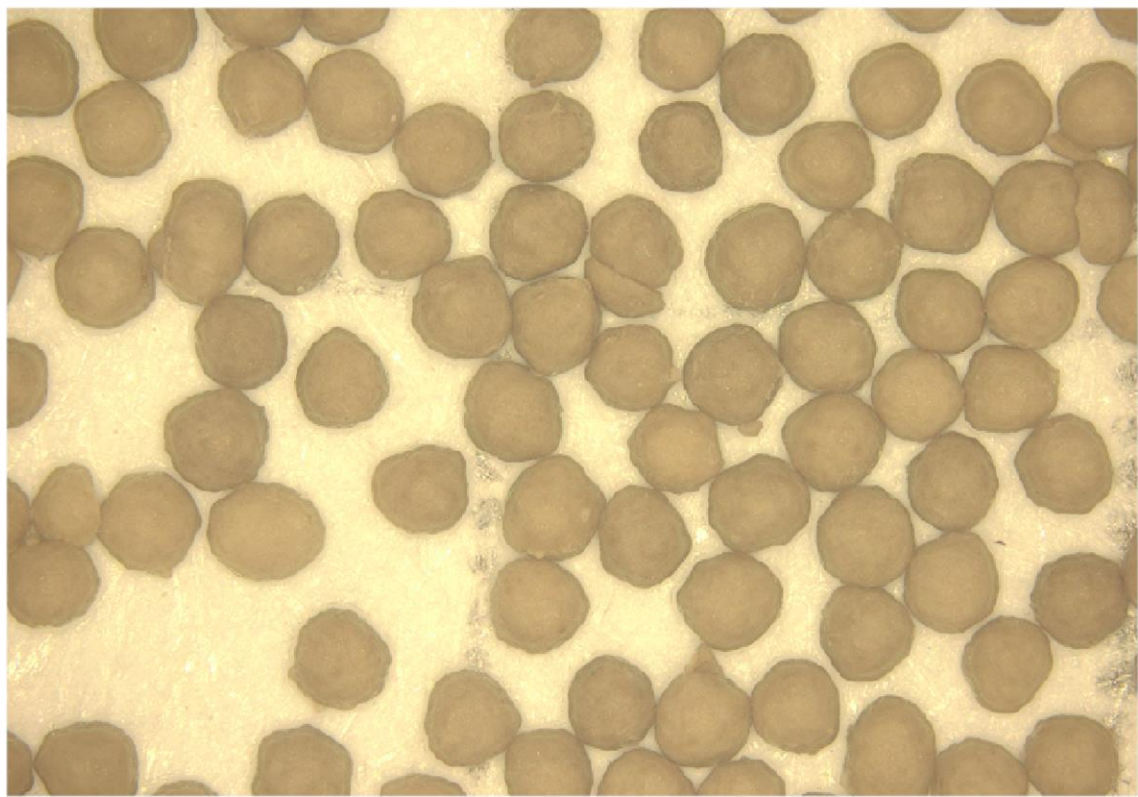


Figure 4.12 – A example optical EFL micrograph of the catalyst material.

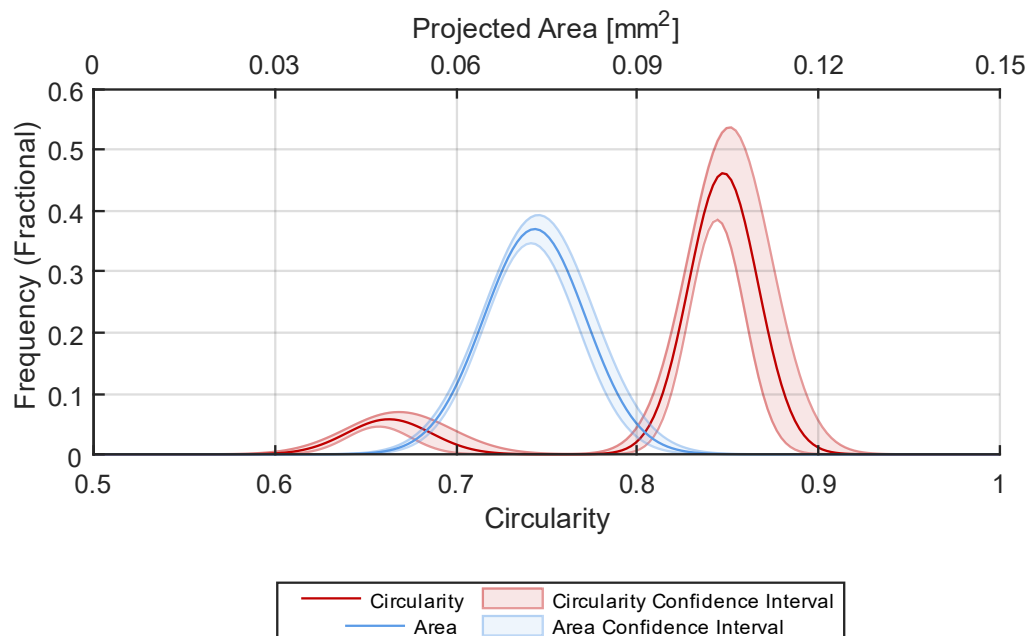


Figure 4.13 – Statistical distribution of some of the geometric parameters of the catalyst material.

The cross-sectional areas of the pellets are measured as  $7.30 \times 10^{-2} \text{ mm}^2 \pm 0.84 \times 10^{-2} \text{ mm}^2$  ( $1\sigma$ ), corresponding to diameters of  $305 \mu\text{m} \pm 104 \mu\text{m}$  ( $1\sigma$ ). The mean is close to the specified value however there is a significant spread in the data. This is attributed to the irregularity of some of the pellets: The circularity is calculated using  $c = 4\pi(A/p^2)$  where  $p$  is the perimeter of each particle. The

two peaks seen in Figure 4.13 correspond to the roughly spherical particles with some surface variation ( $c = 0.85$ ) and particles with a consistently elongated shape ( $c = 0.66$ ). Several examples of this latter particle shape can be seen in Figure 4.12, for example in the top-left quadrant, and this is an apparent non-uniformity of the manufacturing process. Despite this, as the distributions show, the majority of the catalyst is approximately spherical. Note that these estimations are all made using the optically projected area and therefore assume that the pellets don't have a bias to their shape that make them more likely to settle in a specific orientation, although this is not expected in this case.

Since these pellets are very small compared to rest of the geometry, they are retained in a mechanically stable catalyst pack. This is achieved with two retainer discs at either end of the bed. As listed in Table 4.3, these are made of open-cell Ni foam, nominally 1.6 mm thick with an approximate pore size of 300  $\mu\text{m}$ . The discs were pressed out of the foam sheet material using a 3.6 mm die on a punch press, oversized with respect to the 3.5 mm diameter thruster body to provide an interference fit with the walls. The size of the open-cell pores was an issue since some of the smaller pellets could pass through the material. To prevent this, the discs were compressed to approximately 0.6 mm thickness to reduce their axial pore size to better retain the 300  $\mu\text{m}$  diameter catalyst pellets, while still allowing an unimpeded fluid flow. The compressibility of the retainer discs also has the benefit of providing a static force to the catalyst bed during and after assembly. This is similar to other larger thruster designs where springs are included to help maintain the shape of the catalyst bed, especially over the lifetime as pellets may fragment [12].

The catalyst material was manually filled by completely filling the thruster bed cavity and gently agitated to settle the pellets into a stable and more dense pack. This was repeated until the bed is filled to approximately 0.3 mm to 0.4 mm below the mating flange plane. When the thruster is assembled, the upstream retainer compresses against the catalyst pack providing a force to keep the material in the stable configuration.

The CT scan of the thruster in Figure 4.6 also shows the catalyst material in the bed, with a random but qualitatively close packing. The mass of catalyst in the standard and highly-instrumented catalyst beds were measured as 0.162 g and 0.158 g respectively. This was determined by taking the difference of the measured weights of each thruster before and after assembly, i.e. with and without catalyst. The respective mean packing densities are roughly estimated as 0.53 and 0.52 using the volume of the bed and estimating the catalyst density as  $4540 \text{ kg.m}^{-3}$  (5 %/wt. Pt loading with  $\rho_{Pt} = 21450 \text{ kg.m}^{-3}$ ,  $\rho_{\gamma-Al} = 3650 \text{ kg.m}^{-3}$ ). This is smaller than the expected maximum limit of 0.634 for random spherical packing [121], although this may be due to the irregularities in particle shape, non-ideal packing technique, or an incorrect estimation of the catalyst material density.

A more rigorous estimation of the packing was taken from the CT scan itself. The packing density with respect to the axial and radial dimensions in the catalyst bed are shown in Figure 4.14. While the same distortion effects preclude a direct scale measurement, as void fraction is a fractional measurement of local packing, distortions should not have a significant impact on the results. These data were extracted from the CT scan by convolving multiple slices in the bed. Therefore, the curves are smoother than for a single slice, however this shows the radial wall effects better since is averages out the random nature of the pellets in any given slice.

Along the length of the bed, the packing is roughly uniform, with a value of  $0.442 \pm 0.066 (1\sigma)$ . The large variability is due to the significant wall effects at ends of the catalyst bed near the planar retainer boundary. Despite the variability, this seems to confirm that the catalyst material density is  $4319 \text{ kg.m}^{-3}$ , rather than the estimated  $4540 \text{ kg.m}^{-3}$ , suggesting that the  $\gamma\text{Al}$  support material is more porous. Note that the end of the bed is non-discrete given the open-cell pores in the Ni foam retaining some of the pellets in the surface cells, although this did not appear to have a significant effect on the packing. There was also no apparent effect of the mid-bed standpipe, but this was not unexpected since no thermocouple was inserted into the bed for this scan. It is suggested that the thermocouple in the bed might introduce some local variation in packing, although the thermocouple diameter is only 0.25 mm, similar to the catalyst pellets, so any impact is unlikely to be significant.

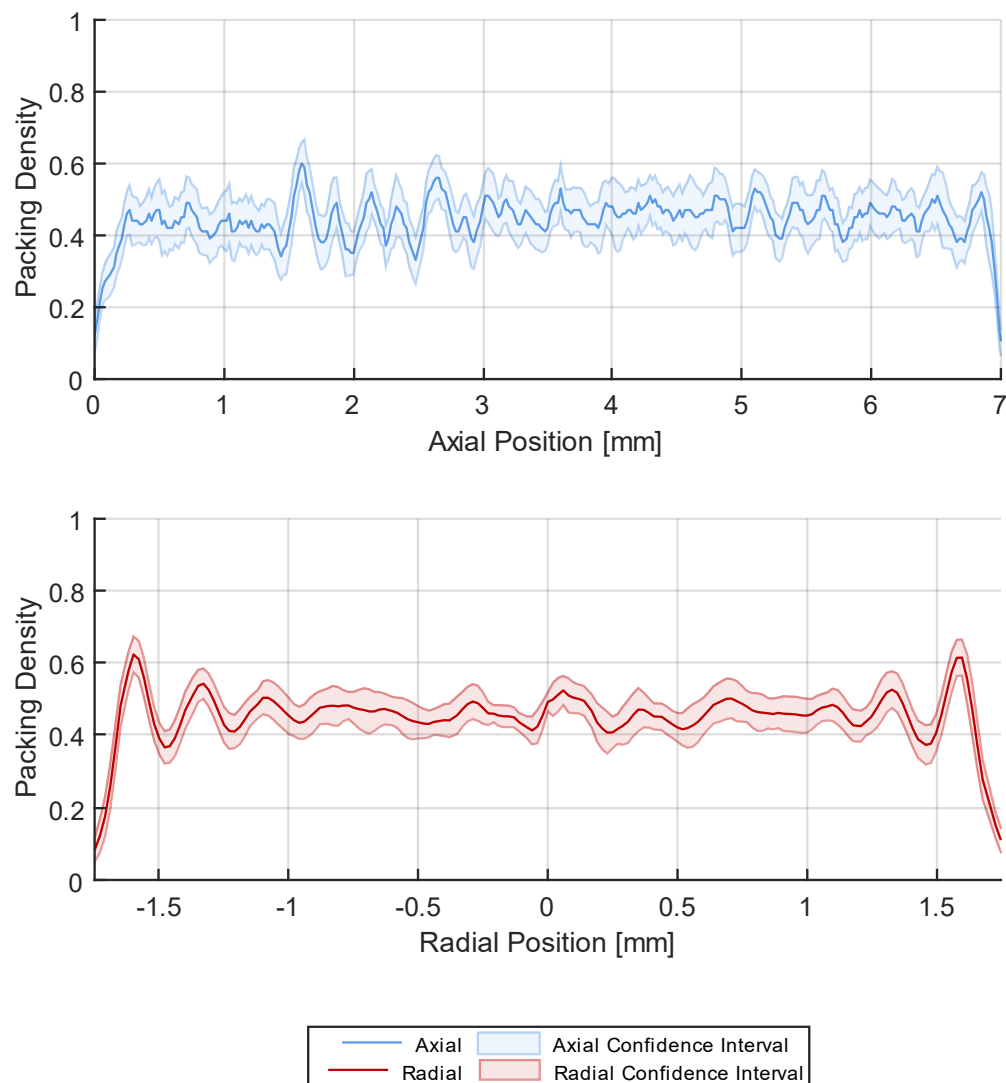


Figure 4.14 – Baseline catalyst bed packing data taken from x-ray CT scan data, including the  $1\sigma$  confidence interval. Packing is shown with respect to the axial (top) and radial (bottom) positions in the bed.

The radial packing is similarly uniform in the middle of the bed:  $0.445 \pm 0.047$  ( $1\sigma$ ), however there is significant variability in the packing close to the walls. The data shows an oscillating pattern of high and low packing, consistent around the bed. This is expected and the specific pattern is related to the diameter of the pellets, as pellets on the outside 'ring' have a structured position which becomes more random deeper into the bed [16], [54], [85], [86]. The wall effects are directly related to the size of the pellets, and can be characterised using the non-dimensional distance from the wall, described by Equation (2.12), for reference:

$$z = \delta z/d_p = (R_c - \delta R)/d_p \quad (4.6)$$

The circular cross-section formulation is appropriate here, where  $z$  is specified as a distance  $\delta z$  from the wall radius  $R_c$  or with respect to the radial distance  $\delta R$  from the centre. For spherical particles, wall effects are expected for  $z \leq 4.5$ , or approximately  $1.37 \text{ mm} \pm 0.47 \text{ mm}$  into the bed for the baseline catalyst material [85]. This matches the observed oscillatory pattern in the radial data. The significant wall effects with  $1 - 2$  pellet diameters from the boundary also agree with the data [83], [84], [86]. In this region, the packing density oscillation period is approximately  $0.25 \text{ mm}$ , which is similar to an estimated  $0.25 \text{ mm}$  for a  $z$ -pitch hexagonal close pack crystal structure ( $\text{pitch}_z = \sqrt{6} \frac{d}{3}$ ). Also worth noting is that the design principle for a 'well-packed' bed,  $D_c/d_p \geq 12$  is approximately satisfied [86]: The bed is  $3.5 \text{ mm}$  in diameter, compared to the suggested  $3.66 \text{ mm} \pm 1.25 \text{ mm}$  diameter. However, it is worth highlighting that the packing data from the CT scan confirms that the bed appears to be well packed through the bulk of the volume.

#### 4.4. Thruster Design Summary

This Chapter presents the design and manufacturing methodology for the baseline thruster. The thruster is designed for atmospheric operation with nominal and mean (over the lifetime blowdown range) thrusts of 0.1 N. This assumed 5 kg of 87.5 %/wt. HTP propellant, over the driving pressure range of 25 bar  $\geq P_{tank} \geq$  5 bar. The nominal design point, i.e. for an ideally expanded nozzle, has  $P_c = 8$  bar and a predicted  $\dot{m} = 0.096$  g.s $^{-1}$ . The full operational range assumes a fractional injector pressure drop of 0.1 / $P_c$ , so the propellant mass flow rates should vary between 0.270 g.s $^{-1}$  and 0.059 g.s $^{-1}$ , corresponding to chamber pressures between 22.5 bar and 4.90 bar, at BoL and EoL respectively. The numerical model used to select this design does not account for several important geometric parameters, including the catalyst bed loading and aspect ratio, and the converging-diverging nozzle profile. These were chosen based on the literature survey presented in Chapter 2 as a baseline for further experimental studies but were not expected to be optimal. Two design variants were manufactured with different degrees of instrumentation: both have pre- and post-catalyst bed instrumentation standpipes, facilitating direct measurement of the internal fluid conditions. The highly-instrumented variant includes a mid-bed port to provide insight into the catalyst bed conditions.

The scales of the geometry required for this preclude either conventional micromachining or Microelectromechanical Systems (MEMS) manufacturing techniques. Instead, the thrusters were additively manufactured from SS 316/316L using metal SLM. Some minor post-processing steps improved the surface finish of critical sealing surfaces. While the AM process allows flexible and low-cost manufacture of small complex geometries, there is significant variability in the as-manufactured parts. Flow characterisation of the nozzles showed that the discharge is at the lower end of the expected  $0.9 \leq C_d \leq 1$  range, indicating significant non-isentropic effects. These are likely due to the relatively high surface roughness of the as-printed parts, determined from x-ray CT scan data. The flow characterisation also captures the variability in the nozzle throat area, so direct inspection is not required. Note that this variability and the surface roughness are not important in the current work but will need further development for use on flight-representative thrusters.

The additional components and materials have also been characterised. The baseline injector is a cold-rolled SS 304 microbore tube, selected from a number of procured articles. This injector has a fractional pressure drop of 10.6 %/ $P_c$ . This was selected as a conservative design, to be insensitive to flow instabilities based on the results in the literature survey. The packed bed catalyst was also chosen from commercially available materials. The pellet geometry and bed packing were investigated and suggest that this bed is 'well-packed'. The packing densities estimated from the catalyst mass are 0.53 and 0.52 for the standard and highly-instrumented variants, while the CT scan results yield  $0.443 \pm 0.060$  ( $1\sigma$ ) for the highly-instrumented variant. This indicates that the catalyst material density is actually 4319 kg.m $^{-3}$ .

The analysis of the baseline design presented in this Chapter suggested that it would perform well under hot firing with 87.5 %/wt. HTP propellant. The integrated instrumentation is also a key feature, improving on other microthruster designs from literature. They permit direct measurement of the internal fluid conditions to characterise the thruster performance, and also validate the parameters used in the analytical design model.



# Chapter 5

## Baseline Thruster Testing and Performance

### 5.1. Aims and Scope

The main goal of the study in this Chapter is to experimentally test the performance of the baseline microthruster detailed in Chapter 4. This also validates the chosen design parameters, as well as the specific implementation including the manufacturing processes, instrumentation, and flow characterisation methodologies. A secondary goal of the testing is to define a baseline performance of a thruster to support the optimisation and assessment of some of the fundamental design parameters for microthrusters in later Chapters.

#### 5.1.1. *Test Campaign Methodology*

The thruster hot-firing test campaign was intended to capture the performance of the thruster over the full design blowdown range. Test runs were conducted at several steady state inlet pressures based on the nominal  $5 \text{ bar} \leq P_{in} \leq 25 \text{ bar}$  range. The test pressures were set by the PDS driving pressure at approximate 5 bar increments, and also included a 30 bar test point to investigate the higher performance region. The control of the PDS was discussed in Chapter 3. To capture the steady state performance, each test was nominally 60 s in duration. Run-to-run uncertainties were expected, so each test point was repeated. The performance of the bed is tied to the adiabatic decomposition temperature. This is affected by the preheating temperature of the propellant, so between runs, the bed is brought below 50 °C for repeatability.

### 5.1.2. Example Test Run

An example run of the standard baseline thruster variant is shown in Figure 5.1, illustrating the typical time domain data for the pressure, temperature, and mass flow rate channels. Note that while the thrust was measured, the data is not included here or in any future results since optimising the nozzle design was not a research goal. As discussed in Chapter 4, the effective throat area from characterisation sufficiently describes the flow and confirms the choking condition. The plots include an initial 10 s of pre-firing data, which is used to establish an instrumentation baseline. This is followed by a nominal 60 s firing and a further 10 s of post-firing to capture the shutdown transients. These segments are identified by the actuation of the inlet valve and are also indicated in the figure. The specific method for identifying these in the raw experimental data is discussed in Appendix A.

The data in this example shows a good performance, representative of the majority of the baseline thruster tests: After the thruster firing valve (SV3) is opened, there is a rise in chamber pressure and temperature, up to the steady state. This main operational period is stable, with a constant mean steady state performance, although there is high frequency roughness in the pressure data due to the decomposition processes. The statistical mean and  $1\sigma$  spread of the steady state performance data are extracted using the algorithm also detailed in Appendix A.

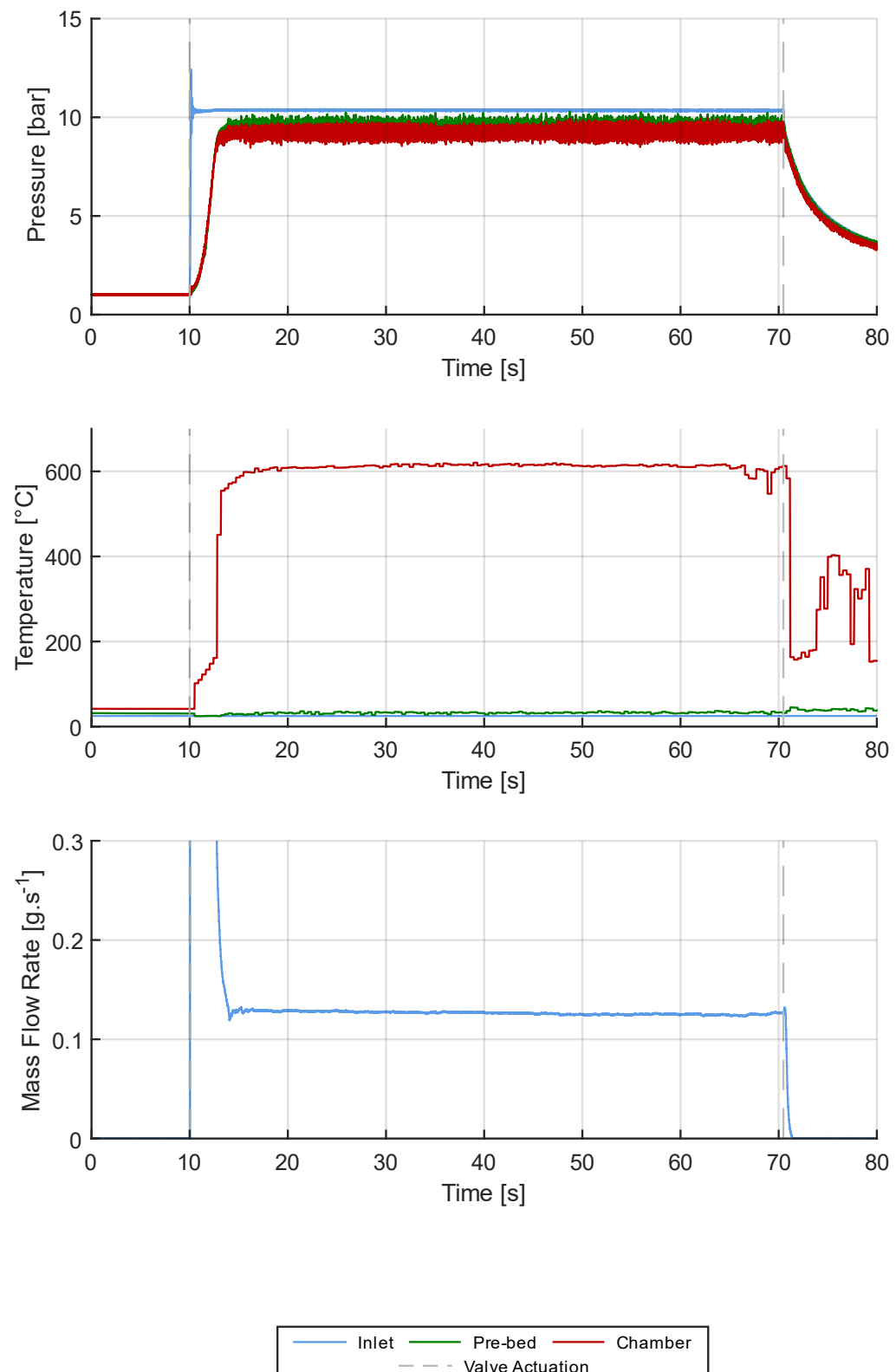


Figure 5.1 – Example time domain test data of the standard baseline thruster variant, with a target inlet pressure of 10 bar. Firing valve actuation times are indicated.

## 5.2. Steady State Performance

### 5.2.1. Temperature and Thermal Performance

The high decomposition temperature in the chamber is the mechanism that elevates monopropellant thruster performance above that of a cold gas thruster with comparable chamber pressures and mass flow rates. This is illustrated in Equations (2.5) and (2.20) for the exhaust velocity and characteristic velocity efficiency respectively. Here  $v_e \propto c^* \propto \sqrt{T_c} (\propto I_{sp})$ . Characterising the thermal performance is therefore essential. The steady state temperatures from the baseline test campaign are plotted in Figure 5.2 for each thermocouple with respect to the steady state propellant mass flow rate for each test. These thermocouples were visually aligned with the central axis of the bed. It is also important to note that the mass flow rate ranges differ between the variants due to the different nozzle throat areas.

In general, the chamber and mid-bed temperatures are high, all above 500 °C, with most tests in excess of 600 °C. The key conclusion here is that both variants of the baseline thruster appear to perform well, in line with the  $\eta_{cat} = 0.8$  corresponding to 561 °C using for the thruster design. The chamber temperature increases with the propellant mass flow rate, while the mid-bed temperature measured on the highly-instrumented variant decreases slightly. The latter matches the trend in the cool ( $T_{prebed} < 70$  °C) pre-bed temperature data for both variants, indicating that the propellant preheating strongly affects the decomposition temperature in the bed. The temperatures converge with the increasing mass flow rate: the pre-bed temperature approaches in ambient inlet as the higher mass flow rates cool the upstream regions of the bed, while the downstream high temperature regions approach the corresponding adiabatic decomposition temperature, calculated using the ambient temperature, i.e.  $T_{in} = 25$  °C.

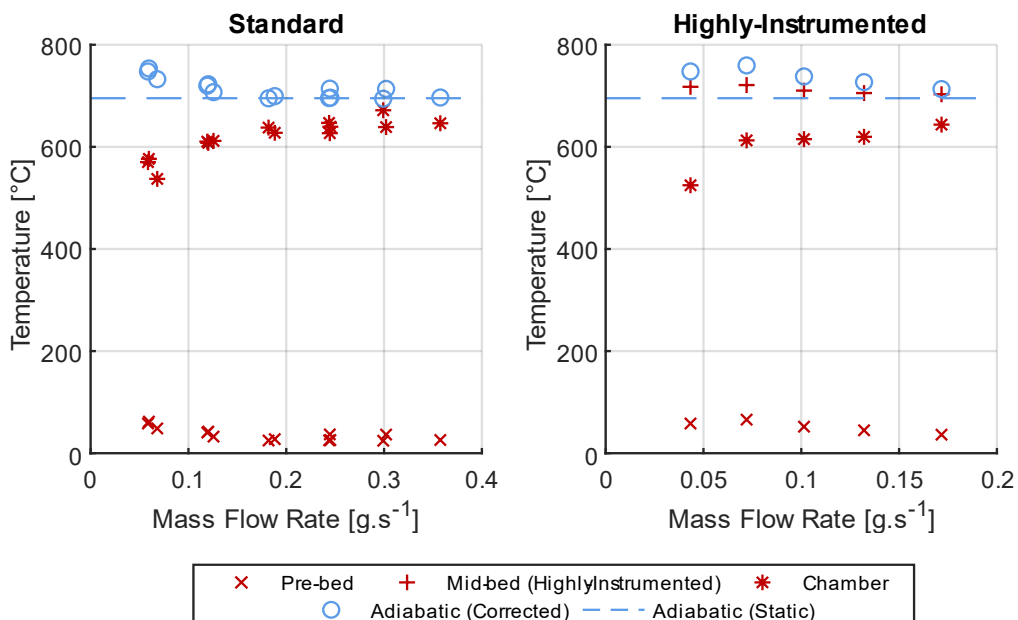


Figure 5.2 – Steady state temperatures for the standard and highly-instrumented baseline thruster variants. Static ( $T_{in} = 25$  °C) and preheat-corrected adiabatic temperatures are included.

The data from the highly-instrumented variant shows that the mid-bed temperature is consistently above the chamber temperature, shown in Figure 5.3. This suggests that the decomposition is complete before the end of the bed: the chemical enthalpy has been fully liberated inside the bed, and since the only thermal flux is through the thruster walls, the chamber temperature is reduced. It also explains the convergence of the mid-bed and chamber temperatures with increasing propellant flow rates: As the pseudo-physical full decomposition front moves downstream towards the end of the bed, the axial distances between the front and both thermocouples will approach each other.

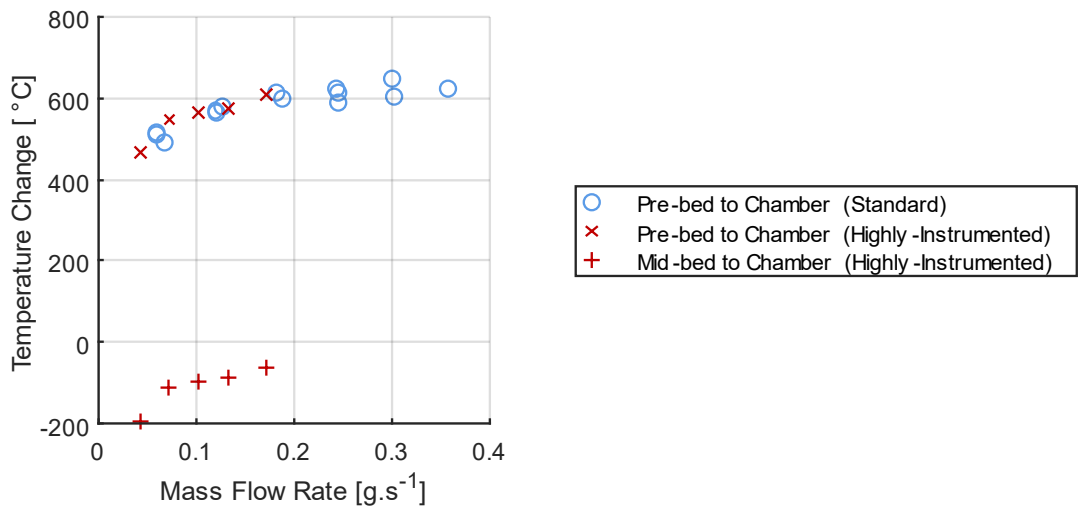


Figure 5.3 – Steady state temperature differences in the baseline thruster variant catalyst beds.

The thermal performance of a bed is relative to the ideal adiabatic case, i.e. the maximum temperature of the decomposition reaction where there is no thermal flux through the walls. Figure 5.2 shows a constant reference adiabatic decomposition temperature,  $T_{ad} = 695.3\text{ °C}$ , for the 25 °C inlet conditions of the 87.5 %/wt. HTP propellant. The measured steady state mid-bed data is above adiabatic, which is not possible. However, the adiabatic decomposition temperature varies with the initial propellant temperature. The propellant is preheated by the hot catalyst bed, so the adiabatic temperature is corrected using the measured pre-bed fluid thermocouple measurement. Note that the data approach the static reference value as the mass flow rate cools the pre-bed. All further analyses use this corrected adiabatic temperature.

The relative thermal performance can be described by the catalytic thermal efficiency, calculated using Equation (2.18). This parameter is the ratio of the measured temperature increase in the bed to the adiabatic temperature rise. It captures the net enthalpy input from the propellant, accounting for thermal losses. The catalytic thermal efficiency of both baseline thruster variants is plotted with respect to the mass flow rate in Figure 5.4. Both variants show increasing efficiency with mass flow rate, from 0.68 to 0.96, i.e. as the enthalpy input increases. The catalytic thermal efficiencies of the two variants are similar, implying that there is no significant difference in the net enthalpy flux. This was unexpected since the mid-bed instrumentation was anticipated to add a large thermally

conductive path. Instead, the thermal performance is governed by the enthalpy from the propellant and the position of the full decomposition front with respect to the end of the catalyst bed.

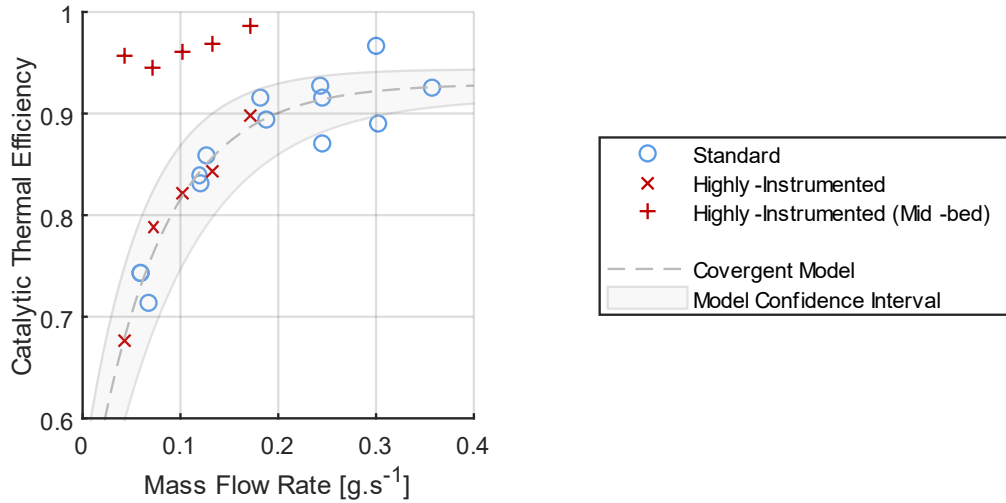


Figure 5.4 – The catalytic thermal efficiency of the baseline thruster variants. A convergent model is fit to the data. The  $1\sigma$  confidence interval of the model and the mid-bed thermal efficiency are included.

Since these data appear to converge to a maximum, which represents the peak thermal equilibrium of the system, a simple convergent analytical model can be fit to the data. The model is detailed in Appendix A, but takes the form:

$$\eta_{cat} = a(1 - \exp(-cm)) \quad (5.1)$$

Where the coefficients  $a$  and  $c$  are the asymptotic value and rate of convergence respectively. The y-intercept is constrained to  $\eta_{cat} = 0$  for  $\dot{m} = 0$ , since there should be no temperature rise without any propellant flow. The model is fitted to the data from both variants, with a good correlation ( $R^2 = 0.926$ ). The model and  $1\sigma$  confidence interval are overlaid on Figure 5.4. The maximum equilibrium catalytic thermal efficiency given by  $a$  is  $0.929 \pm 0.014$  ( $1\sigma$ ). This confirms that the thermal performance is high and is above the design condition,  $\eta_{cat} = 0.8$ . The thruster could be designed with a smaller nozzle throat corresponding to the higher thermal performance, however since  $A_t \propto \sqrt{T_c}$  from the modified choked flow Equation (4.3), the change is negligible compared to the variability in the nozzle manufacture.

The data from the two variants were also independently fitted to confirm that they have the same performance: The maximum equilibrium catalytic thermal efficiencies are  $0.931 \pm 0.019$  ( $1\sigma$ ) and  $0.908 \pm 0.055$  ( $1\sigma$ ) for the standard and highly-instrumented catalyst beds respectively. The mid-bed instrumentation standpipe may cause a slightly reduced performance, but this is insignificant with respect to the run-to-run variability in the data.

### 5.2.2. Characteristic Velocity

The characteristic velocity is another metric that describes the thermal performance of a catalyst bed. As discussed in Chapter 2, it is more commonly used than the catalytic thermal efficiency, but relies on the choked nozzle condition. It can be calculated using the two methods: either using the mass flow rate and chamber pressure, or using the chamber temperature, respectively Equation (2.19) or (2.20). For reference:

$$c_p^* = \frac{P_c A_t}{\dot{m}} \quad (5.2)$$

$$c_T^* = \frac{\sqrt{\gamma T_c R_{spec}}}{\gamma \sqrt{\left(\frac{2}{\gamma+1}\right)^{(\gamma+1)/(\gamma-1)}}} \quad (5.3)$$

Note that the pressure-based method uses the effective nozzle throat area to account for the manufacturing variability and the non-isentropic flow. Both methods should be equivalent. The data derived using both methods is plotted in Figure 5.5, and converge with increasing propellant mass flow rates to around 900 m.s<sup>-1</sup>, although there is considerable difference between the two trends. For the thermal characteristic velocity, the data has a relatively low spread and follows a similar shape as the chamber temperature and catalytic thermal efficiency. Here performance increases with mass flow rate from a minimum  $c_T^* = 832.7$  m.s<sup>-1</sup>. Conversely, the pressure-derived data has a much wider spread for a low propellant flow rate, between 760.0 m.s<sup>-1</sup> and 993.3 m.s<sup>-1</sup>, with the main trend decreasing with flow rate. This was not expected given the catalytic thermal efficiency results.

The adiabatic characteristic velocity is also included on both plots. It is calculated using the preheat-corrected adiabatic decomposition temperature and is equivalent between both methods. These data are the ideal maximum characteristic velocity, i.e. with no thermal losses. In this case the trend is downwards, again towards 900 m.s<sup>-1</sup>, with little spread. For this ideal performance, the trend is driven by the preheating of the propellant, however the real performance is not expected to match since the thermal performance is poor at low propellant flow rates. The pressure-derived characteristic velocity also seems to neglect these losses, and the widespread in the data suggests that there is some error. In several of the tests the pressure-derived performance is above the maximum adiabatic data which is not physically possible.

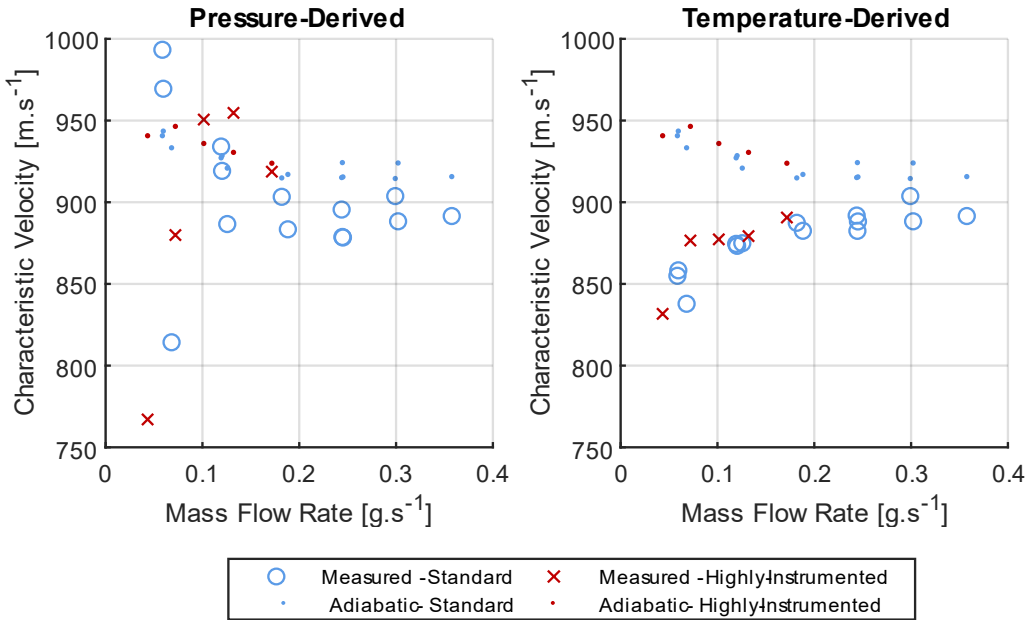


Figure 5.5 – Steady state characteristic velocities of the baseline thruster variants using the pressure and temperature methods. Adiabatic characteristic velocities are also included.

Taking the ratio of the two methods,  $c_p^*/c_T^*$ , confirms that in the majority of cases the pressure-based value is higher than the temperature-based data. This is plotted in Figure 5.6, and shows that the results of both methods approach each other at higher flow rates. The error is unlikely to be due to the instrumentation: The thermocouples, pressure transducers and Coriolis mass flow meter were well within their operational range, and the flow rate measurements were also verified using the PDS propellant tank load cell. These uncertainties were discussed in Chapter 3. To confirm this, the propagated instrumentation uncertainties in the pressure-derived data are shown as tails on each data point in Figure 5.6. This does not affect the overall trend in the data and several measurements are still above the adiabatic maximum. The implication is that there is either some larger systematic offset, or there is an unexplained phenomenon at the lower flow rates. It is suggested that the effect may be due to the scale of the micronozzle: Since the viscous forces and relatively large boundary layers are not common for larger thrusters, these may affect the pressure-derived data. Note that this effect is also present regardless of whether the nozzle throat area is taken from design, inspection, or characterisation since  $c_p^* \propto A_t \propto C_d A_t$ . The discrepancies in the pressure-derived characteristic velocity mean that it cannot be reliably used to assess the catalyst bed performance, so the thermal characteristic velocity is the main metric for further analysis.

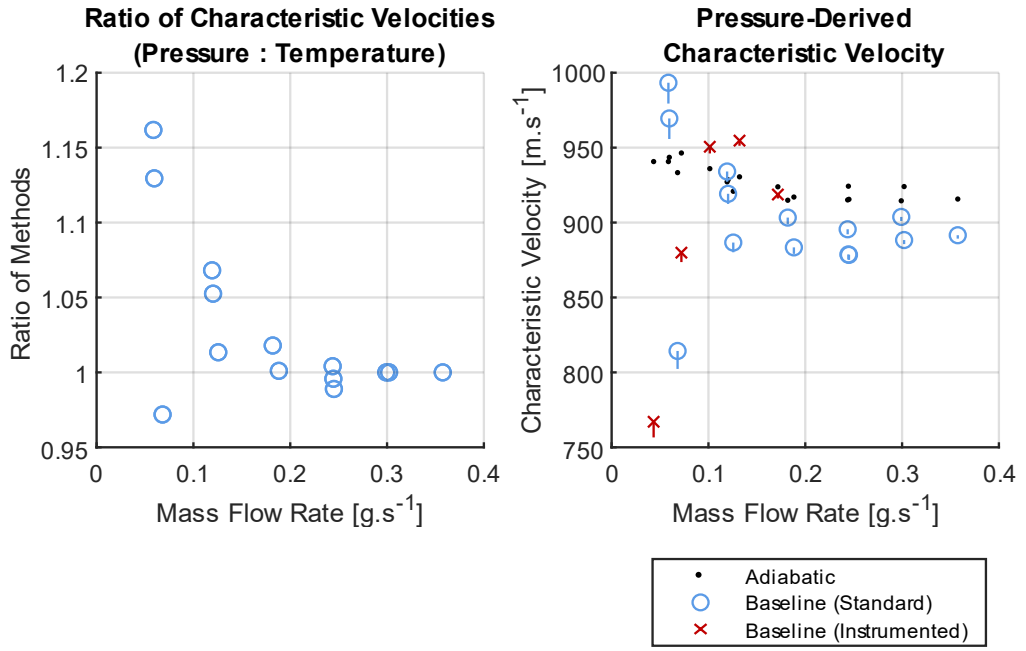


Figure 5.6 – The ratio between the values of the two steady state characteristic velocity methods (left), and the pressure-derived characteristic velocity efficiency with tails showing the propagated instrumentation uncertainty (right).

The characteristic velocity can be normalised with respect to the adiabatic performance to give the characteristic velocity efficiency,  $\eta_{c^*}$ , according to Equation (2.21). This metric describes the performance relative to the maximum ideal case and permits direct comparison between runs, regardless of the different propellant preheating. The thermal characteristic velocity efficiency,  $\eta_{c_T^*}$ , is plotted with respect to the mass flow rate in Figure 5.7, with the performance falling in the  $0.884 \leq \eta_{c_T^*} \leq 0.988$  range. These results are comparable to similar but larger 87.5 %/wt. HTP monopropellant thrusters [12], [16], and suggests that microscale catalyst beds have similar relative thermal losses to larger scale thrusters. It is not possible to compare these results to the sub-newton thrusters from literature, since the characteristic velocity efficiencies are not stated, most likely due to a lack of data.

The thermal characteristic velocity efficiency follows a similar convergent trend to the catalytic thermal efficiency. It can be fitted with a constrained convergent exponential model of the form:

$$\eta_{c^*} = a - \left( (a - \eta_{c_0^*}) \exp(-cm) \right) \quad (5.4)$$

As with the catalytic thermal efficiency model fit (Equation (5.1)) the coefficient  $a$  is the maximum equilibrium limit of  $\eta_{c^*}$  and  $c$  represents the rate of convergence to this value. In this case,  $\eta_{c_0^*}$  is the boundary condition where there is no mass flow rate. This specific derivation is also discussed in Appendix A. The boundary condition is set as  $\eta_{c_0^*} = c_{T_{298.15K}}^* / c_{T_{ad}}^* = 0.5548$ , i.e. the characteristic velocity efficiency for no temperature rise. It is important to note that  $\eta_{c_0^*}$  has no real physical meaning, since at low non-zero propellant flow rates the nozzle choking condition will break and characteristic velocity is meaningless. However, the boundary condition is analytical, and constraining the model improves the regression algorithm stability. It is also worth highlighting that the coefficients  $a$  and  $c$  are relatively insensitive to the specific value of the constraint.

The model is fitted to the aggregated data from the standard and highly-instrumented variants, and is plotted in Figure 5.7 along with the  $1\sigma$  confidence interval. The model is well-correlated ( $R^2 = 0.821$ ) with values for coefficients  $a$  and  $c$  calculated as  $0.963 \pm 0.004$  ( $1\sigma$ ) and  $32.7 \pm 1.98$  ( $1\sigma$ ) respectively. The maximum equilibrium again demonstrates that the baseline thruster is high performance, however the rate of convergence metric  $c$ , is not especially useful in isolation. It is more useful when comparing the performance for different catalyst beds in the study in Chapter 6.

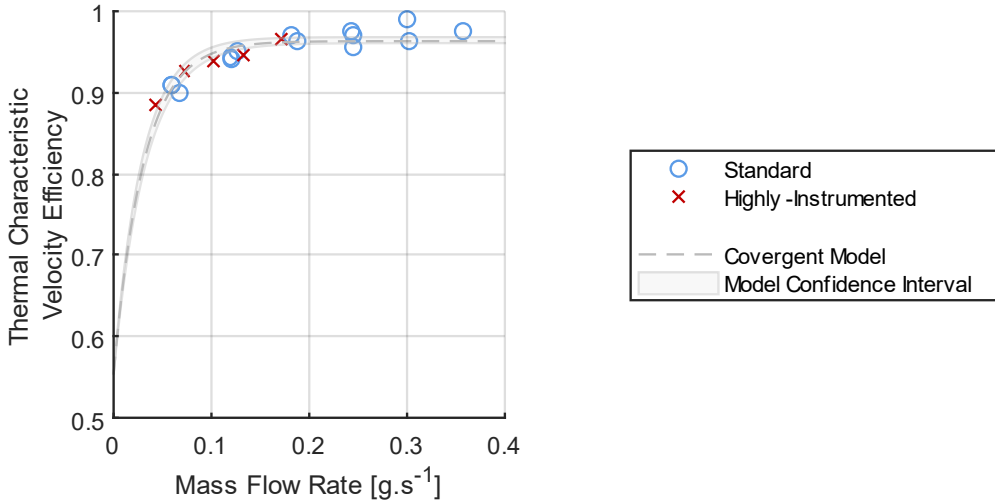


Figure 5.7 – Steady state thermal characteristic velocity efficiency of the baseline thruster variants. The  $1\sigma$  confidence interval of the model is included.

### 5.2.3. Pressure

The thermal performance of the bed was critical to demonstrate, however the steady state pressure results are also important. The measured pressures from the different regions of both baseline thruster variants are shown in Figure 5.8. In general, the run-to-run steady state pressures are tightly clustered for each variant, however they do not match. This is due to the significant difference in their nozzle  $C_d A_t$  values:  $1.208 \times 10^{-7} \text{ m}^2$  vs  $6.716 \times 10^{-8} \text{ m}^2$  for the standard and highly-instrumented versions respectively. The mass flow rate is not directly comparable for a given driving pressure, which was briefly discussed with the thermal data. Instead, the two variants can be compared to their cold flow characterisations, presented in Chapter 4.

The experimental nozzle characterisations show the proportionality between mass flow rate and chamber pressure. This is also clearly present in the chamber pressure data in Figure 5.8. In both the hot and cold flow characterisation, the effective nozzle area  $C_d A_t$  is different between the two variant thrusters: The standard variant discharge rate is expected to be  $\sim 1.79$  that of the highly-instrumented thruster. The standard and highly-instrumented effective throat areas are  $1.177 \times 10^{-7} \pm 0.059 \times 10^{-7} \text{ m}^2$  ( $1\sigma$ ) and  $0.657 \times 10^{-7} \pm 0.045 \times 10^{-7} \text{ m}^2$  ( $1\sigma$ ) respectively, compared to the dry nitrogen characterisation values of  $1.208 \times 10^{-7} \text{ m}^2$  and  $0.672 \times 10^{-7} \text{ m}^2$ . These data show good agreement despite the different physiochemical parameters of the gases. The hot flow

characterisation uses the NASA CEA code [17], [18] to predict the exhaust physiochemical parameters. Since the CEA results are for fully decomposed HTP, these results are another confirmation that the fluid in the nozzle is fully decomposed before entering the nozzle, i.e. frozen flow is a valid assumption.

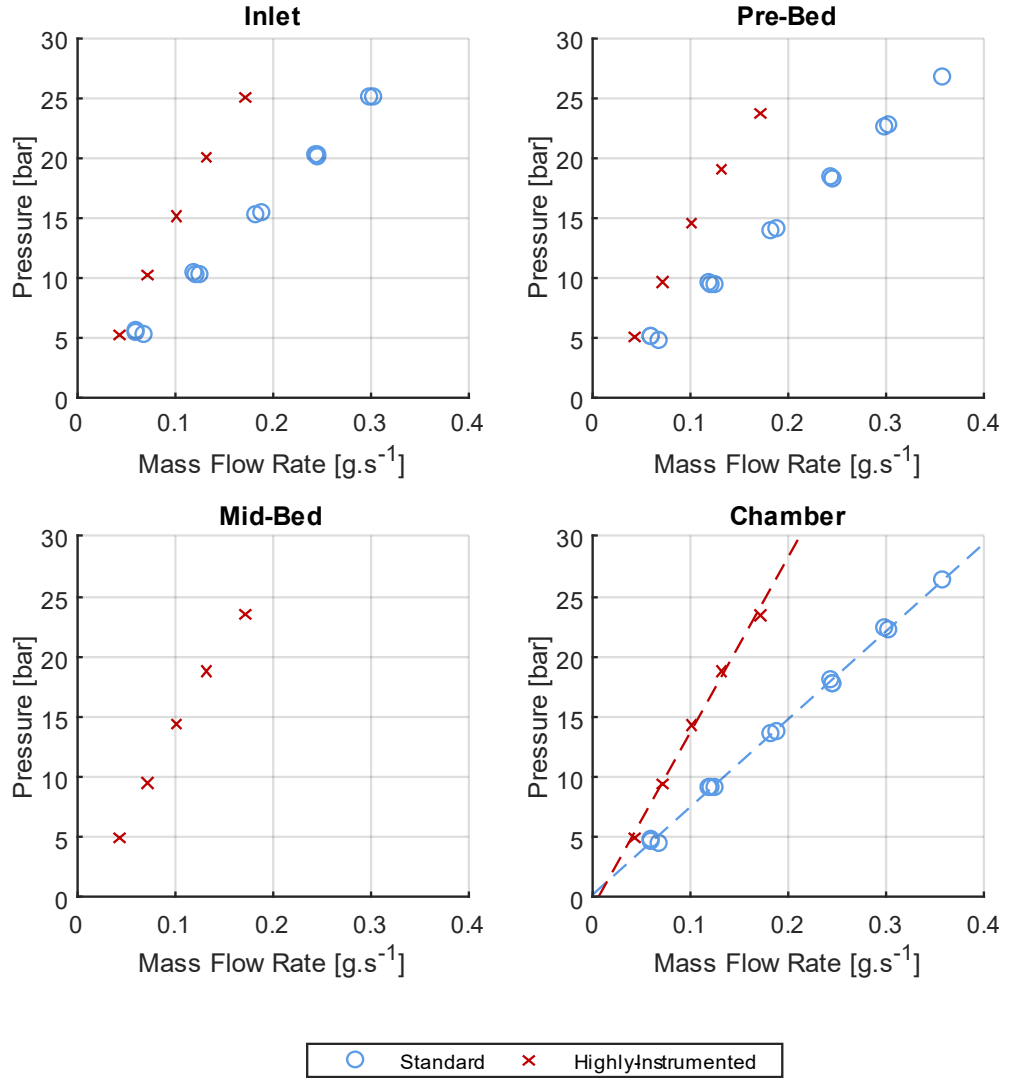


Figure 5.8 – Steady state pressures for the baseline thruster variants at different instrumentation positions.

Viscous losses affect the flow through the other elements of the thruster: the catalyst bed and injector. Maximising the chamber pressure improve the thruster performance, so minimising the pressure drops over these upstream elements is essential. The propellant mass flow through the injector was characterised in Chapter 4 showing a linear relationship between the pressure drop and flow rate, described by the modified Hagen-Poiseuille equation (2.17). The measured injector pressure drops are shown in Figure 5.9, showing good correlation with the overlaid linear fit ( $R^2 = 0.975$ ). The geometric parameter of this fit model is  $2.25 \times 10^{-14} \pm 2.00 \times 10^{-15} \text{ m}^3$ , compared to the DI water characterisation value of  $2.46 \times 10^{-14} \text{ m}^3$ . This is just outside of the  $1\sigma$  confidence bounds

of the HTP data, but it is close enough to suggest that the injector characterisation model is unaffected by the working fluid. The results demonstrate that the cold flow Poiseuille is valid with the different physiochemical parameters of HTP. A full investigation of injector design and performance will be covered in Chapter 7.

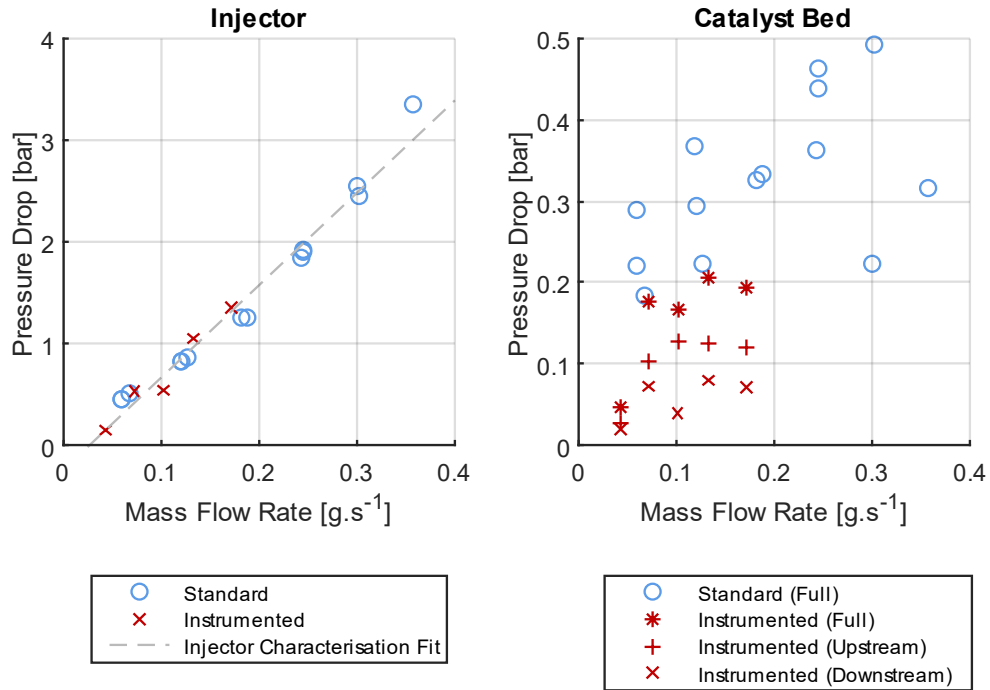


Figure 5.9 – Steady state pressure drops for the baseline thruster variant tests across the injector and the catalyst bed.

The viscous effects in the catalyst bed result in a pressure drop. This also reduces the chamber pressure and therefore the thruster performance, so these losses should be minimised. The pressure drops across the bed are also shown in Figure 5.9, and the data from the highly-instrumented variant also includes the pressure drops over the upstream and downstream regions. As expected, the pressure drop increases with the mass flow rate, although the correlation is lower than for the injector ( $R^2 = 0.407$ ). The lower correlation is a result of the relative spread of the data: The absolute variability is of the same order of magnitude as for the injector data, however since the absolute catalyst bed pressure drop is lower, the variability is relatively more significant. Additionally, these values are approaching the pressure transducer uncertainty of 0.0675 bar so the data is close to the minimum resolvable resolution. Even accounting for the instrumentation and run-to-run uncertainties, the pressure drop across the highly-instrumented catalyst bed is lower than that of the standard variant. This might be expected if the mid-bed thermocouple reduced the packing efficiency. However, the mean packing densities were similar, calculated in Chapter 4. It is also important to note that there is only one set of data from the highly-instrumented variant, and the results are within the full spread of the standard variant data. Regardless, since the pressure drop through the catalyst bed is smaller than across the injector, optimising the injector design will have a greater impact on the thruster performance.

The mid-bed instrumentation gives insight into how the pressure drop is distributed through the catalyst bed. The computational models from literature also predicted this distribution. The ratio of the upstream to downstream pressure drops is shown in Figure 5.10. The data show that the pressure drop in the upstream region is consistently higher in the downstream, the opposite result to that predicted by the one-dimensional models [57]–[59]. In the models, the high velocity gas-dominated phase towards the end of the bed had a higher pressure drop. The likely cause is the local formation of gaseous bubbles of decomposition products in the liquid phase, locally choking the flow through the small cross-section channels. This effect was visually identified in some planar microthrusters [26], [47], [87]. The proposed mechanism is the same cyclical expansion of decomposition products resulting in roughness. The mechanism was not modelled in the literature studies and is only expected for small flow channels with sizes of the order of 20  $\mu\text{m}$  [26]. Therefore, this effect will only be present for small-scale catalyst beds such as the one in the current work.

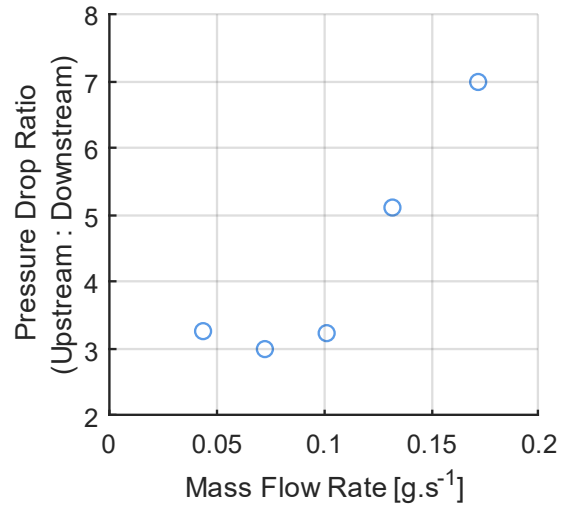


Figure 5.10 – Highly-instrumented baseline variant catalyst bed pressure ratio,  $dP_{upstream} / dP_{downstream}$ .

### 5.3. Quasi-Steady Performance

The quasi-steady phenomena in the thruster are important to characterise the stability of the catalyst bed operation. As discussed in Chapter 2, these are random or high frequency effects, and are closely related to the decomposition reaction. They not only affect the performance but are also indicative of the fundamental processes in the catalyst bed. The quasi-steady behaviour can therefore be used to investigate the decomposition reaction and local flow effects in the thruster.

#### 5.3.1. Steady State Pressure Roughness

The steady state pressure roughness, defined here as the  $1\sigma$  variation from the mean steady state pressure, is a common metric for characterising the catalyst bed stability. There are several potential effects influencing the magnitude of the roughness: localised expansion of decomposition products, acoustic resonance within the internal volumes, flow coupling across the injector ('chugging'), and instrumentation phenomena including instrument resonance and noise. In general, it was assumed that roughness was primarily driven by the unsteady reaction kinetics, specifically the localised expansion of the decomposition products that also cause the high liquid-phase pressure drops. The pressure roughness can therefore be used to investigate the decomposition reaction mechanism.

Figure 5.11 shows the steady state roughness for the four pressure channels with respect to the mass flow rate. Note that the data are plotted on the same scales to allow for direct comparison of the magnitudes. In general, the absolute roughness increases linearly with mass flow rate, with little difference between the thruster variants. This suggests that the roughness is tied to the enthalpy input into the bed. Here the additional energy will result in more violent or frequent expansion of the decomposing propellant: The increase in roughness magnitude may also be accompanied by an increase in the frequency, although this will be discussed in a later section.

There is little apparent difference in the absolute pressure roughness of the measurements inside the thruster body: the pre-bed, mid-bed and chamber, however the inlet data are significantly lower. This confirms that roughness is due to the decomposition inside the catalyst bed, since very little decomposition is expected upstream of the injector. The inlet conditions are therefore driven by the conditions in the bed propagating upstream through the injector, which attenuates the magnitude. This may explain the onset of the 'chugging' phenomenon: when the roughness in the bed is sufficiently high, it will affect the flow of propellant, resulting in the coupled flow instability. 'Chugging' was not observed with the baseline injector and is investigated further in Chapter 7. The similar magnitudes of pressure roughness throughout the catalyst bed suggest that the catalyst pack does not attenuate the instabilities, since the phase and species composition of the fluid varies axially. Pressure variations are therefore free to propagate through the bed.

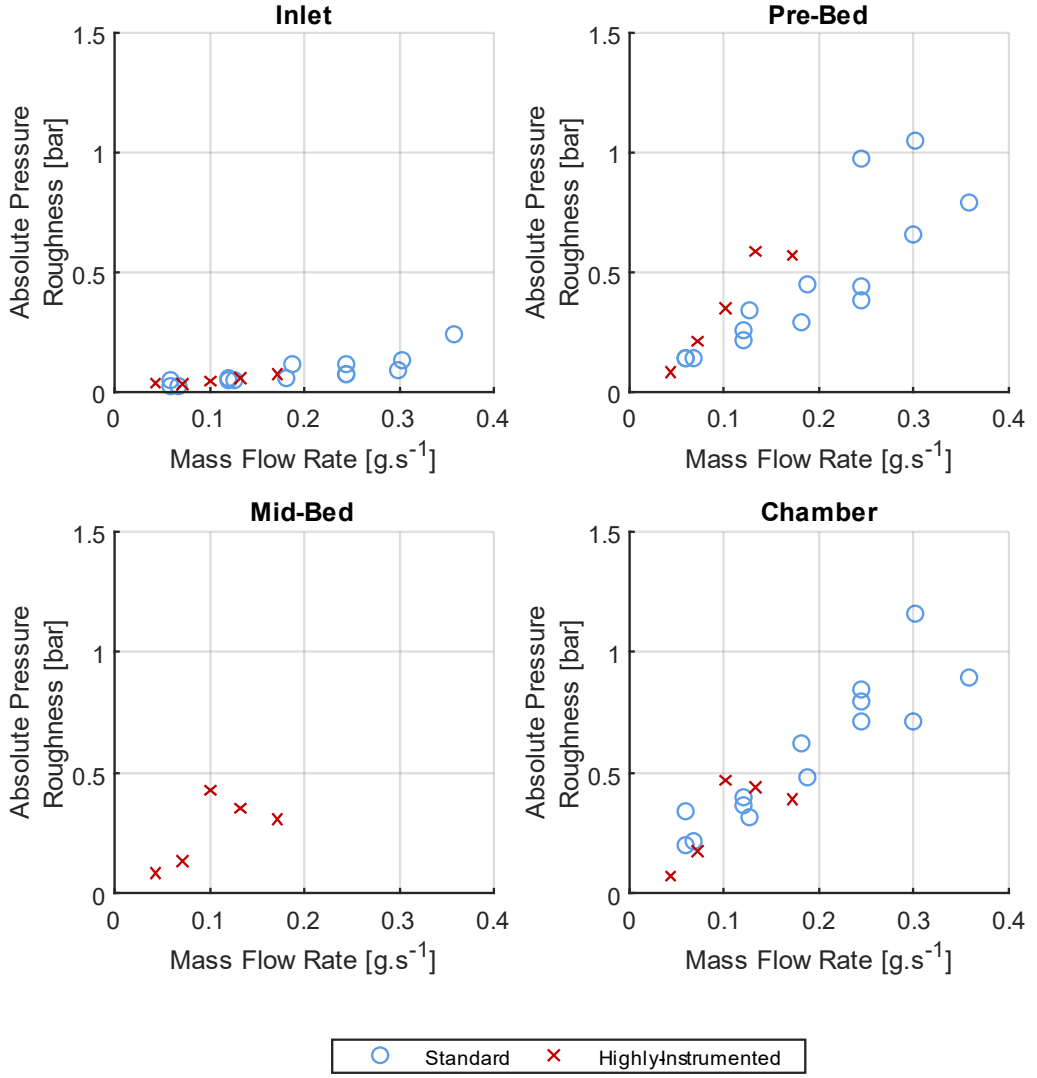


Figure 5.11 – Absolute  $1\sigma$  steady state pressure roughness for the baseline thruster variants at different instrumentation positions.

### 5.3.2. Pressure Roughness First Significant Peak

The steady state pressure roughness provided insight into the underlying reaction kinetics in the bed, suggesting that it is tied to the local expansion of decomposition products. This process should be cyclical: the expansion of the decomposition products transiently limits the reactant diffusion to catalytically active surface. Since this prevents further local decomposition the expansion stops, and the reactants diffuse back to the surface. The result is an oscillating diffusion to and from the catalytically active surface, and the pressure roughness should have a high frequency spectral response. It was suggested that this effect is tied to the enthalpy and therefore propellant mass flow rate.

The high frequency data were extracted from the pressure channels using the Fast Fourier Transform (FFT) algorithm detailed in Appendix A. The resolvable frequency range of the pressure channel DFT is  $10 \text{ Hz} \leq Fq \leq 500 \text{ Hz}$  with a resolution of 0.25 Hz, set by the limits of pressure

transducers and the algorithm. An example of typical DFT spectrograms is shown in Figure 5.12. This figure shows data from the highly-instrumented thruster variant, including the time domain and spectral data for each of the four pressure channels. The magnitude of the response, represented by the colour, has been normalised with respect to the maximum chamber pressure value.

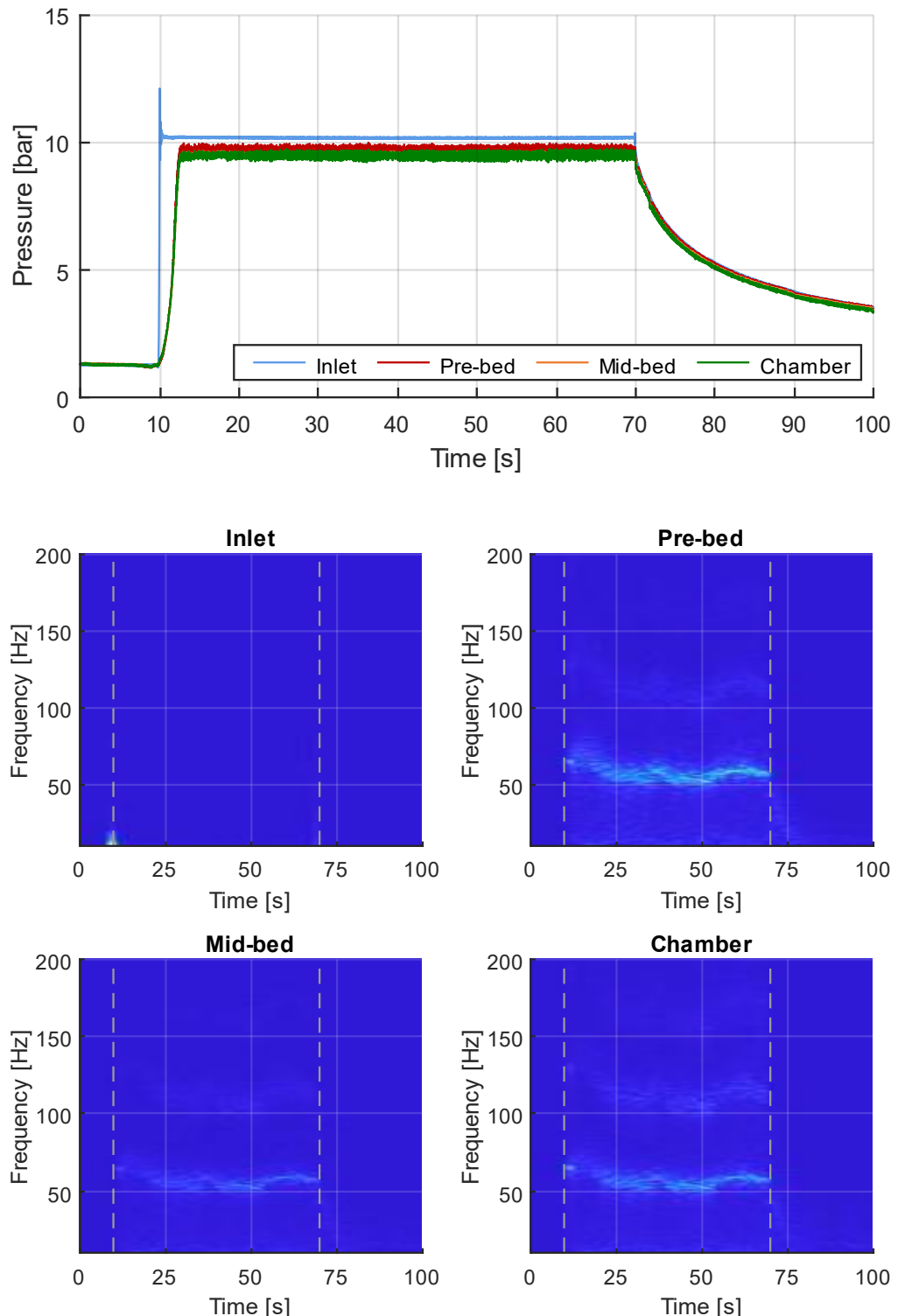


Figure 5.12 – Example time domain (top) and spectral response (bottom) data for the four pressure channels of the highly-instrumented baseline thruster. The thruster firing valve actuation times are indicated.

There are clear peaks visible in the spectrograms: in the example data in Figure 5.12 the first significant peak falls between 50.4 Hz and 58.0 Hz. This peak represents the main oscillatory mode, i.e. the frequency components with the highest energy. However, less significant peaks can be seen at higher frequencies. The relative magnitude of the peaks for each pressure signal follows the same trend as the absolute pressure roughness, where the responses in the thruster are significantly stronger than those upstream from the injector. Note that extracting more specific information from the amplitude of a DFT is non-trivial, and so is not considered further.

The spectrogram was decomposed using a Gaussian Mixture Model (GMM) to identify the central frequency and spread of these peaks. The method is described in Appendix A. The steady state central frequency of the first significant peak is easily determined using the same method as extracting the regular steady state performance data. These central first significant peak frequencies are plotted in Figure 5.13 for each pressure channel. The data for each of the channels follow the same trend and are of similar magnitudes, increasing with mass flow rate but appearing to approach a maximum. The frequency of the mechanism driving the pressure roughness is therefore dependant on the local conditions in the bed. Assuming that the suggested cyclical decomposition process is correct, a higher propellant flow rate results in a faster diffusion. Possible mechanisms may include the higher forces diffusion to the catalyst bed or the higher local fluid pressure more easily overcoming the bubble expansion.

The centre frequency of the first significant peak increases with the mass flow rate. This agrees with the proposed expansion process since higher flow rates should correspond to a shorter period. The data also appear to converge towards the higher flow rates, which might suggest that there is some limit to the rate of this process, such as a maximum diffusion rate of either propellant to or products from the catalytic surface area. Note that this conclusion is speculative and there is insufficient supporting data to strongly confirm it. However, frequency analysis might provide a method of characterising whether the catalyst bed is approaching a reaction rate limit. This would therefore be related to the flooding condition, where the catalyst bed cannot support a particular mass flow rate and will be investigated further in Chapter 6.

There may be other causes for the oscillatory behaviour, for example an acoustic resonance effect in the bed. In this case the frequency is tied to the fluid conditions in the bed, i.e. the pressure and temperature. Varying the catalyst bed geometry will test this, since different catalyst bed geometries will have a different spectral response. This will also be tested in the catalyst bed study presented in Chapter 6.

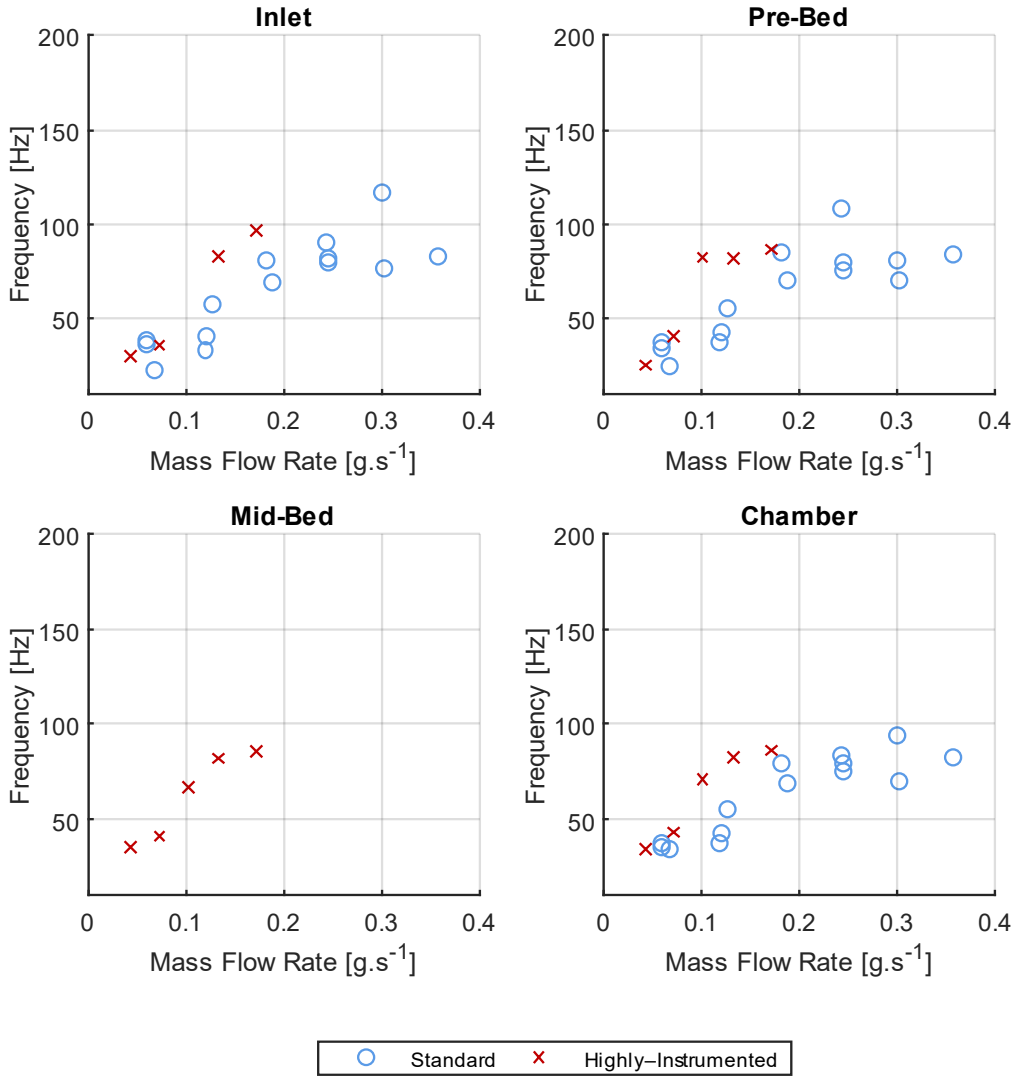


Figure 5.13 – First significant peak centre frequencies for the four pressure transducer channels.

### 5.3.3. Pressure Coupling

The spectral response for each DFT time window can be correlated. The method is discussed in detail in Appendix A, however correlating two data from two channels characterises the extent to which the trends of two datasets match, i.e. whether two pressure signals have similar spectral responses. A value of 0 indicates no correlation, i.e. that the two channels have completely independent frequency responses, while a value of 1 implies that the two channels have exactly the same frequency components and are likely fully coupled. Figure 5.14 shows the variation of the correlation across the injector and the full catalyst bed with respect to the mass flow rate for both catalyst bed variants.

The coupling across the injector was expected to indicate the onset of 'chugging'. The baseline injector was specifically chosen with a conservative fractional pressure drop to avoid the condition, and no coupled flow instabilities were observed in the baseline thruster testing. Therefore, correlation is expected to be low. The data are spread between 0.133 and 0.990, with a weak trend

of increasing correlation with propellant flow rate. Since 'chugging' was not observed, some other conditions must be required for the onset, since some data demonstrate a very high degree of correlation. This is attributed to the increased magnitude of the pressure signal roughness, which is a further demonstration that the pressure roughness is driven by the conditions in the catalyst bed: Higher roughness downstream of the injector will correspond to an increased upstream signal after the attenuation since it provides a greater driving force. Note that the low correlation at low flow rates may also be due to the noise floor of the DFTs: the inlet pressure signal has a much less distinct response. Further investigations of the injector will be conducted in the microinjector study in Chapter 7, although the baseline Poiseuille injector demonstrates stable performance.

The frequency correlation across the bed is more consistent and closer to unity ( $\geq 0.906$ ). This agrees with the pressure roughness observations that there is little flow resistance and acoustic attenuation in the bed: the fluid throughout the bed is well coupled. There is a trend of increasing coupling approaching 0.99 with propellant mass flow rate. As with the injector, this is attributed to the increased signal roughness. This will not be investigated further since the catalyst bed appears to provide little attenuation to the pressure roughness.

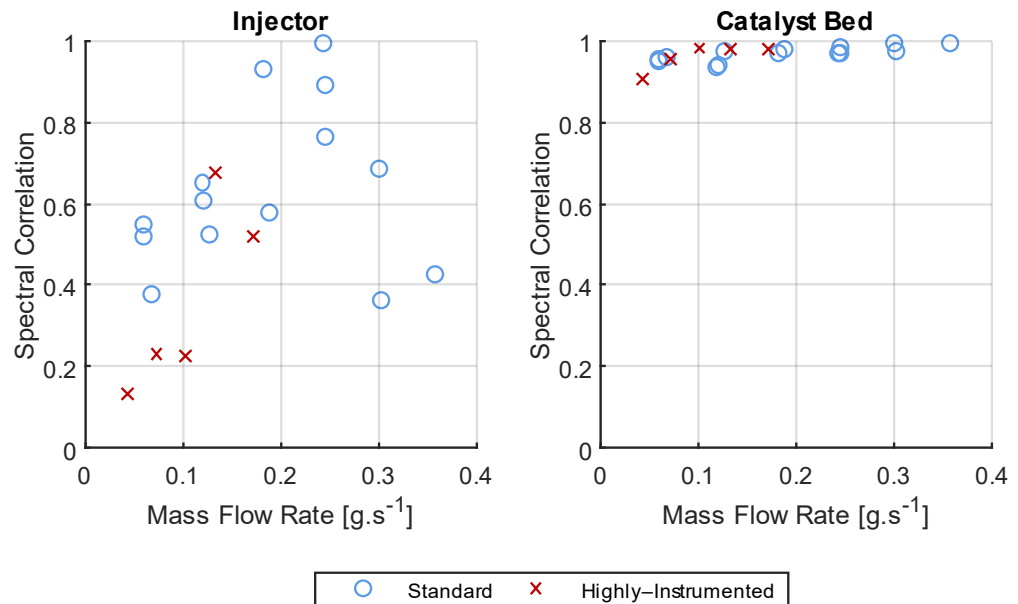


Figure 5.14 – Baseline quasi-steady pressure correlation of the DFTs across the injector (left) and the full bed (right).

## 5.4. Summary of the Baseline Thruster Performance

The goal of this chapter was to test the thruster design outlined in Chapter 4. This was both to test the performance of the thruster, as well as to provide a baseline set of data for further studies into the catalyst bed and injector design. The general performance of both thruster variants is good, demonstrating high temperatures and thermal efficiencies of the thruster: The steady state chamber temperatures reached in excess of 500 °C in all cases and above 600 °C at higher propellant flow rates. The design assumed an  $\eta_{cat} = 0.8$ . At the time, it was not known whether this overestimated the thermal performance under atmospheric conditions. However, the results here demonstrate efficiencies above 0.68 and approaching 0.98, which is similar to larger HTP monopropellant systems. This high performance was also confirmed using the characteristic velocity, with efficiencies approaching  $0.963 \pm 0.004$  ( $1\sigma$ ). Demonstration of these results was only possible given the direct fluid measurements afforded by the integrated instrumentation standpipes and AM techniques. The AM process is well-suited to thrusters designed to operate at 0.1 N.

Validating the cold flow characterisation data from Chapter 4, was also important, since direct inspection of a large number of components is difficult. The flow through the injector and nozzle components shows good agreement with the characterisation models. The performance of the system was stable, with relatively low-pressure roughness and no sign of flow coupling across the injector. This is indicative of a well-designed thruster, although the elements are unlikely to be optimal. The impact of the design of specific elements will be investigated in more detail in the catalyst bed and injector studies in Chapters 6 and 7 respectively.

While not solely an issue for sub-newton monopropellant thrusters, validation of the pseudo-physical front model for the catalyst bed is useful to understand the fundamental processes. The temperature measurements in the highly-instrumented thruster variant were especially valuable as they show the relative movement of the maximum fluid temperature through the bed with respect to different propellant mass flow rates. From the model, the maximum decomposition temperature coincides with the full decomposition of the hydrogen peroxide, i.e. when the maximum enthalpy has been liberated. The data suggest that this front also moved downstream with the increasing propellant flow, agreeing with the model. Direct measurement of the completeness of decomposition and phase of the fluid is not possible given the scale, but these data provide preliminary validation which will be expanded upon in the catalyst bed study.

The pressure drop in the liquid-dominated upstream region was expected to be lower than in the gas phase downstream. This was predicted by the computational models in literature. However, the data here disagrees with this: From the highly-instrumented catalyst bed variant, the upstream bed has a consistently higher pressure drop than the downstream region. The catalyst bed itself does not appear to cause a significant resistance to the flow, with a high degree of coupling and low roughness attenuation between the different pressure transducer locations. Instead, it is suggested that this is due to the formation of decomposition bubbles in the small channels, locally choking the flow. These bubbles have been observed in other micropropulsion literature, and are suggested to result from the cyclical process of species diffusion to and from the catalytically active surface. The varying magnitude and principal frequency of the pressure roughness data support this. Regardless, this confirms that small flow channels negatively impact the catalyst bed performance.

# Chapter 6

## Catalyst Bed Study

### 6.1. Aims and Scope of the Study

The baseline thruster design, detailed in Chapter 4 and tested in Chapter 5, shows promising performance. Testing with 87.5 %/wt. HTP demonstrated stable operation and high chamber temperatures above 500 °C and in most cases in excess of 600 °C. The catalyst bed for this thruster was sized using catalyst bed loading and aspect ratio values chosen based on literature studies. The target thrusts from these sources are between 0.05 mN and 1 N. Despite the large number of studies there is a relative lack of comparative research on catalyst bed geometry and no clear methodology for optimising a design. This Chapter will investigate the effect of varying the parametric geometry has on the performance of the system and identify the optimum design for the thruster presented here. This is enabled by the flexibility of the AM process, allowing a large number of catalyst bed designs to be manufactured at relatively low cost.

An initial investigation into the decomposition processes in the baseline catalyst bed was also presented in Chapter 5. Notably, these include the axial position of the decomposition reaction with respect to mass flow rate and the local oscillatory diffusion process causing roughness and higher liquid-phase pressure drops. Varying the catalyst bed geometry provides further insight into these processes, and provides additional validation of the simplified pseudo-physical front model of the complete decomposition and phase change. It is implied that the optimum catalyst bed length is linked to the axial position of the full decomposition front within the bed. This is dependent on the propellant flow rate, the activity of catalytic material, and the geometry of the bed. To investigate this, a number of under- and oversized catalyst beds will be tested. It is expected that thermal losses and incomplete decomposition will have a marked effect on the performance and operation across the range of catalyst bed designs.

In addition to the research outlined, testing other catalyst-propellant pairs also provides further data in support of the model. Changing the catalyst or propellant is not the primary goal of this research, however a variant catalyst and propellant are available for testing. The variant catalyst is another platinum-based pellet material used on other projects at UoS [12], and will be discussed in detail later in the Chapter. The additional propellant is a higher concentration 98.0 %/wt. HTP blend with considerably more enthalpy. Both of these variants are similar enough to the baseline materials to permit a direct comparison. This not only simplifies the analysis, but should also not affect the assumptions made about the catalytic processes and reaction rates. Also, the 98.0 %/wt. HTP is the highest commercially available concentration of hydrogen peroxide, so the results of this testing will

demonstrate the maximum performance of this thruster without using a different propellant chemical composition.

This Chapter is split into three main sections:

- A study on the catalyst bed geometry. This will investigate the effect of varying the diameter and length of the catalyst bed. This section will also include the design, manufacturing and characterisation of the thrusters.
- A study on the effect of the catalyst material. This investigation will compare the catalyst bed performance using the baseline material with a different Pt- $\gamma$ Al pellet catalyst using 87.5 %/wt. HTP. Several different catalyst bed variants will be tested, to be selected following the bed geometry study.
- A study on the effect of propellant enthalpy. This will compare the performance of the baseline thruster with 87.5 %/wt. HTP against the higher enthalpy 98 %/wt. HTP propellant.

## 6.2. Catalyst Bed Geometry Study

### 6.2.1. Catalyst Bed Design

The catalyst bed geometries are defined in terms of the catalyst bed loading,  $G$ , and aspect ratio,  $AR$ . As discussed in Chapter 2, these directly correspond to the diameter and length of the bed for a given propellant mass flow rate, related through Equations (2.13) and (2.14). For reference:

$$G = \dot{m}/A_c \quad (6.1)$$

$$AR = L_c/D_c \quad (6.2)$$

The catalyst bed loading and aspect ratio specify the parametric catalyst bed design, taking into account different propellant flow rates. This allows the direct comparison of systems with different target thrusts. From the monopropellant microthruster literature presented in Chapter 2, the catalyst bed loadings fall between  $0.04 \text{ kg.m}^{-2}.\text{s}^{-1}$  and  $61.1 \text{ kg.m}^{-2}.\text{s}^{-1}$ , with most within the range  $1 \text{ kg.m}^{-2}.\text{s}^{-1} - 10 \text{ kg.m}^{-2}.\text{s}^{-1}$ . The catalyst bed aspect ratios vary between 0.40 and 5.36, with a majority between 1 – 2 (see Table 2.4). The baseline thruster design was chosen at the approximate mid-point in these ranges, with a selected bed loading and aspect ratio of  $10 \text{ kg.m}^{-2}.\text{s}^{-1}$  and 2 respectively. The catalyst bed geometries in this study are selected considering the good baseline thruster performance as well as the ranges from literature. However, there are some limits to the possible geometry that are imposed by the rest of the system.

A minimum constraint on the bed diameter and length is imposed by the catalyst: It is suggested that for a relatively uniform catalyst packing, the bed should be approximately 12 times the diameter of a spherical catalyst pellet for the mean packing density to approach the ideal bulk value [86]. This is due to the packing effects near the bed walls, which can be assessed by considering the non-dimensional wall distance, defined in Equation (2.12), for reference:

$$z = \delta z/d_p = (R_c - \delta R)/d_p \quad (6.3)$$

Radial wall effects for spherical pellets are expected to affect the packing for  $z \leq 4.5$ , and significant effects are likely for  $z \leq 2$  [85]. These effects were observed in the CT scan data for the baseline catalyst bed in Chapter 4. The baseline catalyst spherical pellets have diameters of  $d_p = 305 \mu\text{m} \pm 104 \mu\text{m}$  ( $1\sigma$ ), so the minimum bed diameter and length,  $R_c$ , should be at least  $3.6 \text{ mm} \pm 1.2 \text{ mm}$  to minimise the wall effects. The relatively large variation in the pellet size and shape should improve the packing density and may reduce the impact of poor packing at lower sizes. A minimum bed diameter and length is chosen at 2.5 mm. This should still perform relatively well, but the reduced packing will hopefully capture the performance effect of more significant wall effects. For the nominal 8 bar chamber pressure, this sets the maximum nominal catalyst bed loading as  $19.6 \text{ kg.m}^{-2}.\text{s}^{-1}$  (for the 2.5 mm diameter bed), assuming ideal nozzle flow through the baseline nozzle design,  $D_t = 0.36 \text{ mm}$  and  $C_d = 1$ .

The geometry of the catalyst bed also impacts the performance by changing the thermal mass and wetted surface area. To limit this, the nozzle and sealing flange designs are fixed. This imposes an upper limit on the maximum catalyst bed diameter of 6.6 mm. Any larger and the flange cannot be sealed using the M1.7 fasteners. A 6.6 mm diameter bed defines the minimum catalyst bed loading at  $2.82 \text{ kg.m}^{-2}.\text{s}^{-1}$  under nominal operating conditions.

Table 6.1 lists the selected catalyst bed designs, including the absolute and parametric geometry. The catalyst bed loading is calculated for the operational pressure range,  $5 \text{ bar} \leq P_{in} \leq 25 \text{ bar}$ . The designs are split into two blocks: the first block focuses on designs close to the baseline to investigate the optimum design condition, including the baseline thruster results from Chapter 5. The second block of catalyst beds has more extreme designs. These investigate the catalyst bed model and proposed pseudo-physical phase change and full decomposition fronts. As the diameter limits have already been reached in the first block, the catalyst bed loading cannot be varied further, so instead aspect ratios are changed. The absolute lengths are greater than 3.5 mm to avoid axial wall effects on packing. The  $6.6\varnothing2.2\text{L}$  catalyst bed is the exception with a 2.2 mm length, but the wall effects are not expected to have as much of an impact in the axial direction given the axial packing for the baseline thruster, presented in Chapter 4.

Table 6.1 – Absolute and parametric geometry for the selected catalyst bed designs.

Thruster Notation	Bed Geometry			Catalyst Bed Loadings [ $\text{kg}\cdot\text{m}^{-2}\cdot\text{s}^{-1}$ ]		
	Diameter [mm]	Length [mm]	Aspect Ratio	BoL, $P_{in} = 25 \text{ bar}$	Nominal, $P_c = 8.0 \text{ bar}$	EoL, $P_{in} = 5 \text{ bar}$
$2.5\varnothing5.0\text{L}$	2.5	5.0	2	58.9	19.6	11.8
$3.5\varnothing3.5\text{L}$	3.5	3.5	1	30.0	10.0	6.01
$3.5\varnothing7.0\text{L}^*$	3.5	7.0	2	30.0	10.0	6.01
$3.5\varnothing10.5\text{L}$	3.5	10.5	3	30.0	10.0	6.01
$6.6\varnothing13.2\text{L}$	6.6	13.2	2	8.45	2.82	1.69
$2.5\varnothing10.0\text{L}$	2.5	10.0	4	58.9	19.6	11.8
$2.5\varnothing15.0\text{L}$	2.5	15.0	6	58.9	19.6	11.8
$3.5\varnothing14.0\text{L}$	3.5	14.0	4	30.0	10.0	6.01
$6.6\varnothing2.2\text{L}$	6.6	2.2	0.33	8.45	2.82	1.69
$6.6\varnothing6.6\text{L}$	6.6	6.6	1	8.45	2.82	1.69

\* Baseline thruster.

Varying the bed diameter impacts the performance of the catalyst bed by changing the surface areas of the bed and the converging nozzle section. Considering the thermal effects, larger diameter beds reduce the external surface area of the flange exposed to the atmosphere. Any effect from this should be minor as the flange is small and this region of the thruster is cooled by the incoming propellant flow. The thermal mass of the thruster increases for larger thrusters, although allowing the system to converge to steady state mitigates any transient effects of heating this mass. Smaller diameter beds have a higher external surface area-to-volume ratio, so the relative thermal flux is higher. In addition, the central core flow of these thrusters is closer to the walls which may reduce the temperature of the flow. The performance impacts are assessed by experimental testing.

The viscous losses in the beds are driven by the cross-sectional area and catalyst packing, although the slow flow rate through the bed means that these are minimal compared to the losses in the high velocity regions in the nozzle throat and diverging section. The nozzle geometry parameters are the same as for the baseline thruster, using the conservative  $\eta_{cat} = 0.8$  and a nominal 8 bar chamber pressure. The throat diameter, area ratio, and convergent and divergence section half-angles are  $D_t = 0.36$  mm,  $A_e/A_t = 1.853$ ,  $60^\circ$ , and  $50^\circ$ , respectively. Changing the diameter of the catalyst bed affects the convergent section of the nozzle: for a fixed convergent section angle, a larger diameter bed requires a larger volume and surface area. This is unavoidable although the flow will be subsonic in this region so the impact will be minimal. The bed diameter also directly changes the catalyst retainer plates but this does not have any significant impact.

### 6.2.2. Catalyst Bed Manufacture

The selected designs listed in Table 6.1 were manufactured using the same AM and post-processing techniques detailed in Chapter 4. A photograph of the thrusters after post-processing is included in Figure 6.1. It was not possible to accurately inspect the nozzle throat area using optical or x-ray CT techniques. Instead, experimental characterisation using dry nitrogen was used to compare the effective throat areas. These are given in Table 6.2, along with the updated bed loadings calculated using the updated expected mass flow rate, accounting for the non-isentropic flow. The resulting range in bed loadings is  $62.7 \text{ kg.m}^{-2}.\text{s}^{-1}$  to  $1.61 \text{ kg.ms}^{-2}.\text{s}^{-1}$ , which also considers the mass flow rates over the range of driving pressures.



Figure 6.1 – A photograph of all of the manufactured thruster variations, labelled with their corresponding notation. A 1 EUR coin is included for scale.

Table 6.2 – Catalyst bed experimental nozzle flow characterisation results and updated catalyst bed loadings.

Thruster Notation	Nozzle Flow Characterisation			Modelled Bed Loadings, $\text{kg.m}^{-2}.\text{s}^{-1}$		
	Effective Throat Area $[\text{m}^2]$	Effective Throat Diameter $[\mu\text{m}]$	Nozzle Discharge Coefficient	BoL, $P_{in} = 25 \text{ bar}$	Nominal, $P_c = 8.0 \text{ bar}$	EoL, $P_{in} = 5 \text{ bar}$
2.5Ø5.0L	$1.155 \times 10^{-7}$	383.5	1.07	62.7	20.9	12.6
3.5Ø3.5L	$1.498 \times 10^{-7}$	436.7	1.21	36.4	12.1	7.29
3.5Ø7.0L	$1.208 \times 10^{-7}$	392.2	1.09	32.7	10.9	6.55
3.5Ø10.5L	$1.038 \times 10^{-7}$	363.5	1.01	30.3	10.1	6.07
6.6Ø13.2L	$9.520 \times 10^{-8}$	348.2	0.97	8.17	2.73	1.63
2.5Ø10.0L	$1.020 \times 10^{-7}$	360.4	1.00	59.0	19.6	11.8
2.5Ø15.0L	$1.058 \times 10^{-7}$	367.0	1.02	60.1	20.0	12.0
3.5Ø14.0L	$7.520 \times 10^{-8}$	309.4	0.86	25.8	8.60	5.17
6.6Ø2.2L	$1.269 \times 10^{-7}$	402.0	1.12	9.43	3.15	1.89
6.6Ø6.6L	$9.290 \times 10^{-8}$	343.9	0.96	8.07	2.69	1.61

The coefficient of discharge is used to compare the manufactured nozzles. These are also included in Table 6.2, and were calculated assuming the 0.36 mm throat diameter, corresponding to an expected throat area of  $1.018 \times 10^{-7} \text{ m}^2$ . The discharge coefficients include the manufacturing variability as well as the non-isentropic flow effects, although noting that the viscous losses should be similar across the nozzles. The nozzle throats are as-designed, with the mean and  $1\sigma$  variation of the nozzle discharge coefficients is  $1.03 \pm 0.10$ . There is some variability, but this is expected to be due to effects on the nozzle throat profile that were discussed for the baseline thruster variants in Chapter 4. It is reasonable to expect that manufacturing can be improved with further iteration, or with secondary processes to improve the repeatability of this critical geometry, for example wire electro-discharge machining. However, for the current work the nozzle flow will choke, and therefore the catalyst bed performance should not be affected.

### 6.2.3. Catalyst Bed Test Campaign

The experimental setup and test procedure is nearly identical to the baseline testing methodology presented in Chapter 5. The only significant difference is in handling the onset of catalyst bed flooding. This is important since many of these beds are undersized, and it was essential to capture the flooding onset to a reasonable resolution for analysis. The flooding condition can either occur at the start of a test or after some period of steady operation. In the former case, no steady state performance parameters can be measured or calculated. However, in the latter case the steady

state pre-flooding period can be analysed. Each thruster was tested, as previously described, over the  $5 \text{ bar} \leq P_{in} \leq 30 \text{ bar}$  range in 5 bar increments. Once a bed has flooded the thruster was retested from the last operational test pressure, stepping up in 1 bar increments until flooding was observed again. This provides a 1 bar resolution of the onset.

Experimentally, flooding was clearly identified by a multiphase flow which is visibly ‘steamy’ due to the entrained liquid droplets. The onset was also easily distinguishable in the test data since it was accompanied by a rapid increase of propellant flow rate which further cooled the bed. This resulted in a sharp drop in chamber pressure and temperature. A full discussion about these phenomena, focusing on the data post processing and analysis is included in Appendix A. The nominal test duration was 60 s, but in the case of flooding it was ended early. Many of the beds were expected to perform poorly and not reach steady state in the nominal period. In these cases, the test was extended up to a maximum of 180 s.

#### 6.2.4. Catalyst Bed Performance

The recorded steady state signal ranges for each catalyst bed are shown in Table 6.3. These are the absolute minimum and maximum steady state values for pressures, temperatures and mass flow rates, as well as the observed flooding onset to the nearest 1 bar. The results from the test campaign highlight some interesting results. Firstly, the mass flow rate under nominal steady state operation of each thruster agrees with the nozzle flow characterisation model using the modified choked flow Equation (4.3), the measured chamber pressure, effective nozzle throat area, and physiochemical parameters for fully decomposed HTP from the NASA CEA code [17], [18]. This is shown in the plot in Figure 6.2, comparing the modelled mass flow rate to the measured. This is unsurprising given the result for the baseline thruster in Chapter 5, although this further demonstrates the validity of the nozzle characterisation technique. In addition, it shows the flow effects for a specific exhaust gas are described fully by the gas physiochemical parameters  $\gamma$  and  $R_{spec}$ . It is therefore likely that the reaction is complete by the time the gases enter the exhaust for all of the tested thrusters, right up to the point of flooding. Considering the simplified model of the catalyst bed, this would suggest that the gas phase decomposition occurs very quickly after the phase transition.

Table 6.3 – Catalyst bed test campaign steady state results over the full tested range.

Thruster Notation	Pressure [bar]		Temperature [°C]		Mass Flow Rate [g.s <sup>-1</sup> ]	Flooding Onset, $P_c$ [bar]
	Inlet	Chamber	Pre-bed	Chamber		
2.5Ø5.0L	3.52 – 10.37	3.14 – 9.26	24.8 – 79.3	150.8 – 627.9	0.030 – 0.297	4
3.5Ø3.5L	5.30 – 14.25	3.68 – 13.03	24.1 – 80.0	141.7 – 592.5	0.044 – 0.151	4
3.5Ø7.0L	5.29 – 30.05	4.59 – 26.39	24.4 – 61.9	537.3 – 671.7	0.059 – 0.358	18
3.5Ø10.5L	5.27 – 25.14	4.51 – 22.76	25.2 – 79.1	344.9 – 647.2	0.043 – 0.263	N/A
6.6Ø13.2L	5.21 – 25.15	4.68 – 22.79	25.6 – 49.0	411.5 – 637.4	0.051 – 0.251	N/A
2.5Ø10.0L	5.29 – 20.13	4.37 – 17.78	25.7 – 93.2	414.4 – 613.4	0.053 – 0.222	17
2.5Ø15.0L	5.27 – 30.10	3.75 – 26.84	21.6 – 75.8	493.2 – 650.0	0.055 – 0.318	N/A
3.5Ø14.0L	5.34 – 30.17	4.61 – 28.05	24.0 – 117.6	147.5 – 599.8	0.043 – 0.250	N/A
6.6Ø2.2L	5.22 – 10.32	4.93 – 9.76	31.3 – 42.9	490.3 – 537.7	0.051 – 0.101	N/A
6.6Ø6.6L	5.29 – 20.21	4.86 – 19.06	37.2 – 50.9	501.5 – 593.9	0.055 – 0.195	N/A

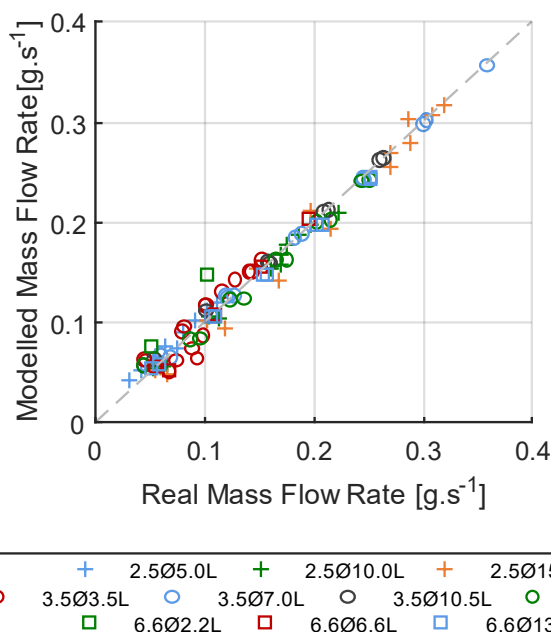


Figure 6.2 – Modelled vs measured mass flow rate for each thruster. The expected equivalence line is plotted.

The assumption of complete decomposition is also supported by the thermal performance of the full set of thrusters. The mean chamber temperature for the full set of thrusters is  $549\text{ }^{\circ}\text{C} \pm 112\text{ }^{\circ}\text{C}$  ( $1\sigma$ ). Ideally a catalyst bed should reach chamber temperatures close to the adiabatic condition. The steady state chamber temperature varies based on the geometry beyond the expected impact from the mass flow rate, but in the majority of cases the steady state chamber temperature is greater than  $400\text{ }^{\circ}\text{C}$ . This is considerably higher than the boiling point of 87.5 %/wt. HTP and is indicative of the gas phase decomposition. To visualise the variability, Figure 6.3 shows the mean catalytic thermal efficiency from equation (2.18) for each thruster, with vertical bars indicating the absolute spread of the results. The baseline thruster performs particularly well, with a relatively narrow range of high thermal efficiencies. Several other thrusters have similarly good performance, with comparable steady state performance as the baseline catalyst bed.

From inspection it appears that longer beds generally perform better since the mean and absolute spread of performance improve, although the set of 3.5 mm diameter beds also suggest that there is an optimum aspect ratio. It is important to note that the flange design affected the data collection for the 6.6 mm diameter beds: The gasket could not be fully compressed for the 6.6Ø2.2L and 6.6Ø6.6L thrusters, which resulted in the seal failing above 10 bar and 20 bar respectively. There is less data from these catalyst beds and the flooding onset was not captured. This limited data also explains the much narrower absolute range of catalyst thermal efficiencies for these two thrusters.

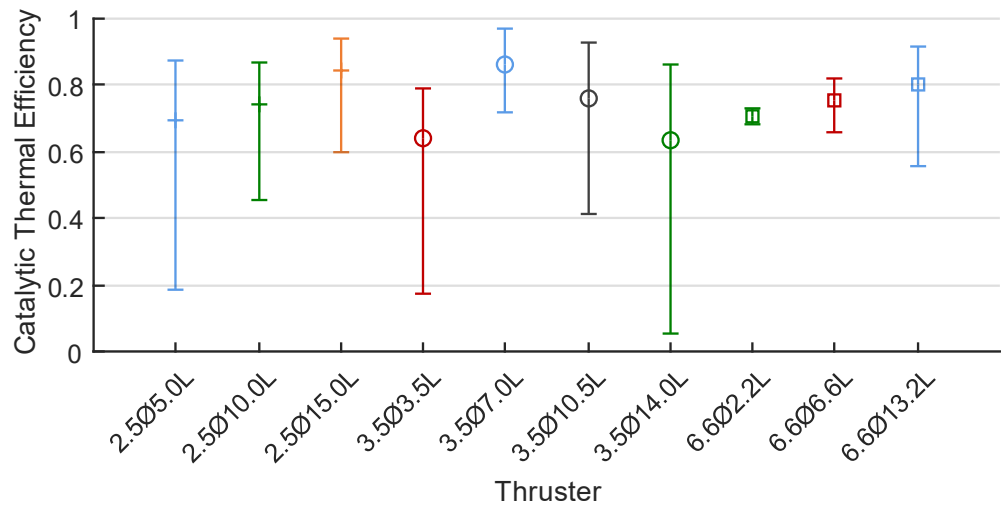


Figure 6.3 – Mean and absolute spread of the catalytic thermal efficiencies for the different catalyst bed geometries.

While the mean catalytic thermal efficiency of all of the thrusters is  $0.746 \pm 0.172$  ( $1\sigma$ ), many of the deliberately under- and over-sized thrusters have reduced thermal performance. The larger, high aspect ratio catalyst beds, i.e.  $AR \geq 3$ , often have very protracted start-up transients, with a low temperature steady state period. In this mode the temperature of the chamber is below  $200\text{ }^{\circ}\text{C}$ , which indicates incomplete decomposition. The majority of the liberated enthalpy is used to boil the propellant and the excess is needed to heat the thermal mass of the thruster. Once the thruster material is sufficiently hot, the temperature quickly rises to the true steady state. An example of the

time domain data for a 5 bar test of the  $3.5\varnothing14.0L$  thruster is included in Figure 6.4. The ‘steady state’ also exhibits very unsteady flow characteristics. Smaller beds do not have this long thermal start-up transient but still perform poorly, also shown in an example 5 bar test of the  $3.5\varnothing3.5L$  thruster in Figure 6.4. Unlike the larger variants, these small catalyst beds cannot sustain the higher propellant flow rates and flood, while at lower flow rates they have reduced thermal efficiencies. These observations agree with the simplified catalyst bed model: an optimum thruster should be sized such that the decomposition is complete, but without having excessive catalyst material to cool the decomposed gases prior to the nozzle.

The sub optimal designs still show moderate maximum thermal performance prior to flooding, with all beds reaching  $\eta_{cat} \geq 0.8$  (ignoring the  $6.6\varnothing2.2L$  thruster with a maximum 10 bar chamber pressure). Overall, the performance demonstrates that this catalyst material is very active and well-suited to this scale of catalyst bed. Coincidentally, Figure 6.3 appears to suggest that the baseline parametric geometry is close to optimal: it performs consistently better than any other design. This might be expected since it is informed by a large number of thruster studies, although the largest diameter beds do not provide enough data to demonstrate their maximum performance. Qualitative observations of the unsteady channels also appear to be tied to the thermal performance. Note that the lifetime of the catalyst material has not been investigated, which will also affect the optimal bed geometry (i.e. the catalyst bed loading) for a flight-representative thruster.

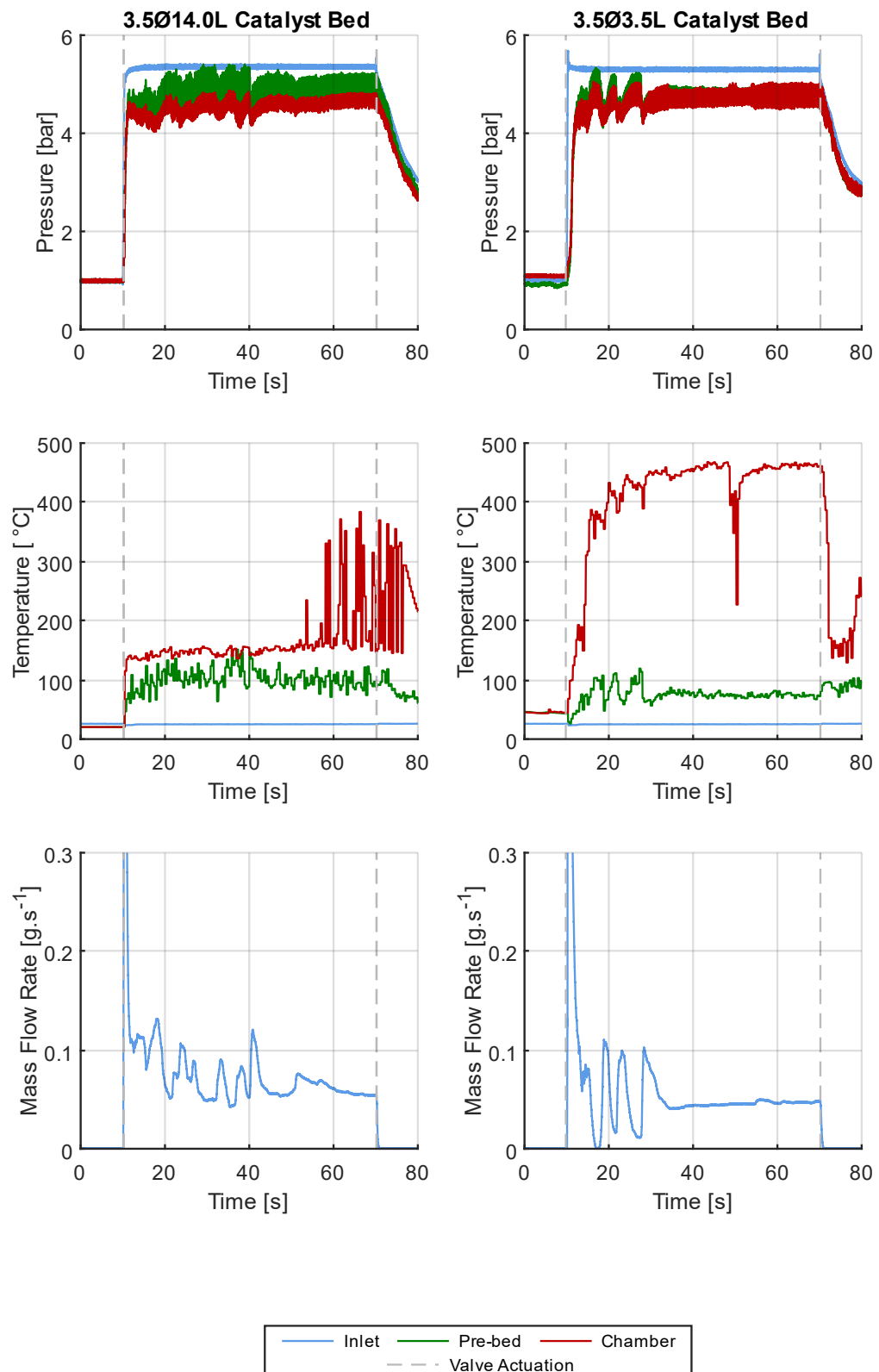


Figure 6.4 – Example time domain data for thruster tests with poor thermal performance. These tests are for the 3.5Ø14.0L – high aspect ratio bed, and the 3.5Ø3.5L – low aspect ratio bed.

The catalytic thermal efficiency is a good measure of the thermal performance of the bed; however the characteristic velocity is a more widely accepted performance metric for a thruster. This requires the choked nozzle condition and is therefore only applicable to non-flooded data, but it can be calculated using the two methods: either using the mass flow rate and chamber pressure, or using the chamber temperature, respectively Equation (2.19) or (2.20). For reference:

$$c_p^* = \frac{P_c A_t}{\dot{m}} \quad (6.4)$$

$$c_T^* = \frac{\sqrt{\gamma T_c R_{spec}}}{\gamma \sqrt{\left(\frac{2}{\gamma+1}\right)^{(\gamma+1)/(\gamma-1)}}} \quad (6.5)$$

The efficiency may then be calculated by normalising these data with the ideal adiabatic characteristic velocity, again using the pre-bed temperature to correct for the propellant preheating. These two methods should provide a degree of validation of the result, although given the discrepancies and unrealistic above-unity pressure-derived efficiencies demonstrated in Chapter 5, the temperature-derived data is more reliable here.

Figure 6.5 contains plots of the data derived using both methods against the propellant mass flow rate. The thermal characteristic velocity efficiency follows the same trend as for the baseline results. The majority of the tests have performance above 0.75. Similarly, the pressure method has a large spread in the data, with the same higher-than-unity discrepancies as demonstrated in Chapter 5. In this case, there is no apparent trend in the erroneous pressure-derived data with respect to the catalyst bed geometry, so the cause cannot be tied to the catalyst bed. This reinforces the previous suggestion that micronozzle effects may be the cause, although this is still unconfirmed. Again, the thermal characteristic velocity efficiency is exclusively used going forward.

The thermal performance of the catalyst beds was expected to be affected by convective and radiative thermal losses from the thruster walls. The different catalyst bed designs have a range of outer surface areas, so significant variability in the characteristic velocity efficiency was anticipated. Instead, the different temperature-derived data sets in Figure 6.5 all follow similar trends, and any difference between the catalyst bed geometries is qualitatively within the run-to-run variation. Therefore, the propellant flow rate dominates the performance: the size of the catalyst bed sets the maximum supported flow rate through the catalyst bed loading. The difference between supported flow rates can be linked to the completeness of the decomposition with respect to the end of the bed. While it is not possible to directly measure this, the simplified model of the pseudo-physical fronts can provide insight.

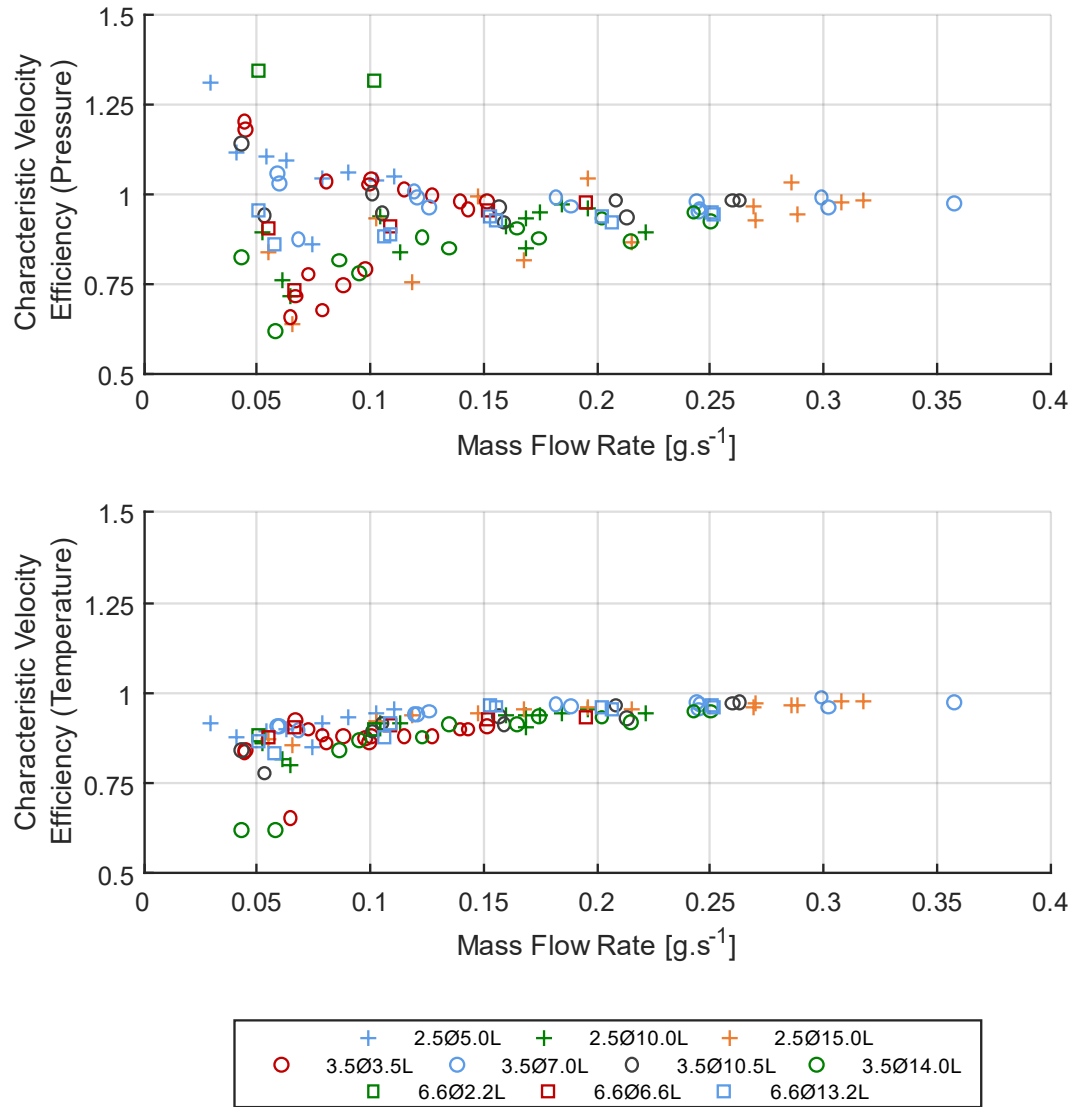


Figure 6.5 – Pressure and thermal characteristic velocity efficiencies plotted against propellant mass flow rate.

The position of the pseudo-physical phase-change and complete-decomposition fronts within the bed will affect the chamber temperature and fluid composition. This is fundamentally controlled by the amount and distribution of the catalyst material and catalytically active surface area with respect to the propellant flux. A smaller bed will require a comparatively larger volume of the catalyst material to support a specific propellant flow rate. Therefore, both fronts will be comparatively further downstream than in a larger bed. The maximum temperature should occur at the axial position of the complete decomposition front. This should be measurable as a peak in the characteristic velocity efficiency when the front reaches the end of the catalyst bed. When the front passes beyond the end, i.e. for an undersized bed, the performance will drop due to propellant underutilisation. Conversely, for an oversized bed, when the decomposition is complete upstream in the catalyst pack, the enthalpy input will be lower relative to the heat loss.

There was no apparent decrease in the characteristic velocity efficiency data for any of the nominally operating catalyst beds as the propellant flow rate increased, i.e. the performance does not

peak prior to the onset of flooding. If flooding occurs when the phase transition front approaches the end of the bed, then this result confirms that the phase-change and complete-decomposition fronts are very close together. This agrees with the computational models from literature, where the gas phase decomposition rate is much higher than the liquid phase [55], [57]–[59]. The bed operation just prior to the onset of flooding therefore coincides with complete decomposition and the maximum performance. This is an interesting result from the perspective of the fundamental processes but does not provide any particularly useful information for the design of an optimum bed: a larger bed should always perform better as it can support a higher enthalpy input. Instead, the inefficiencies of different bed designs must be assessed.

The losses of a particular catalyst bed geometry can be investigated by considering the maximum theoretical performance in the case where there is no flooding. The characteristic velocity efficiency should approach a maximum, below the adiabatic condition and the differences between these represent the inefficiencies of each bed. The pre-flooding experimental data follow this expected convergent trend, which was also demonstrated in Chapter 5. The performance of each bed is fitted with a constrained convergent exponential model of the form:

$$\eta_{c^*} = a - \left( (a - \eta_{c_0^*}) \exp(-cm) \right) \quad (6.6)$$

Where the coefficients  $a$  and  $c$  are the maximum equilibrium value and rate of convergence respectively, and the y-intercept is constrained to  $\eta_{c,0}^* = c_{T_{298.15K}}^* / c_{T_{ad}}^* = 0.5548$  for  $G = 0$ . This was introduced in Chapter 5 and discussed in more detail in Appendix A. The fitted models are plotted in Figure 6.6 against the catalyst bed loading. This qualitatively shows that the smaller aspect ratios converge faster to the maximum with increased catalyst bed loading. The pseudo-physical front model also predicts this: for a larger diameter bed (lower aspect ratio) the axial positions of the fronts should converge at lower catalyst bed loadings and therefore vary less over the range of mass flow rates. The fluid temperature in the chamber will be consistently closer to the maximum equilibrium state.

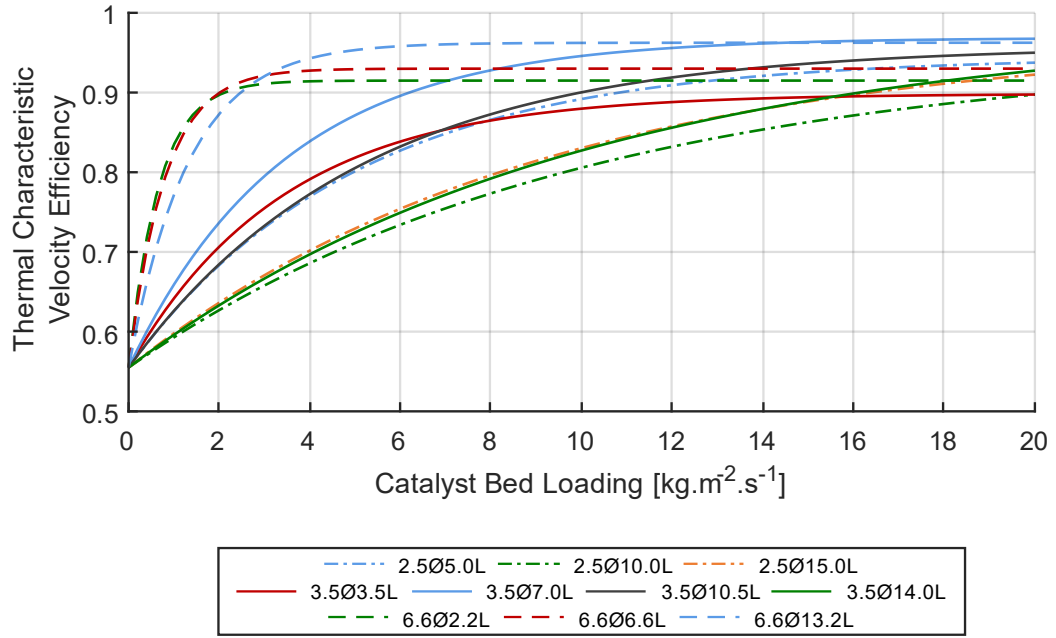


Figure 6.6 – Thermal characteristic velocity efficiency regression-fitted models plotted against catalyst bed loading.

The predicted maximum equilibrium characteristic velocity efficiency is plotted with respect to the catalyst bed cross-sectional area and aspect ratio in Figure 6.7. In isolation, the effect of the cross-sectional area is insignificant compared to the run-to-run variability, agreeing with the observation that the thermal losses are insensitive to the surface area of the bed. The maximum theoretical performance shows a clear increasing trend with the aspect ratio. This implies that a larger bed can sustain a higher mass flow rate and therefore greater enthalpy input. However, since the goal of this work is to optimise a system with a specific target thrust. The propellant mass flow rate is fixed by the thrust of the system, so the maximum performance is capped by the operational range of flow rates. This metric is therefore not particularly useful for optimising a thruster.

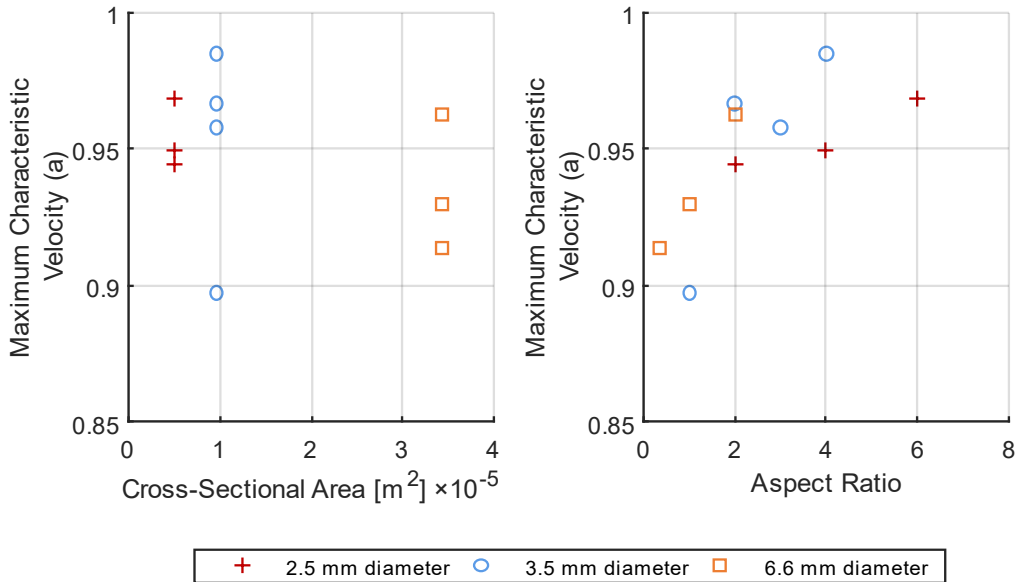


Figure 6.7 – Variation of the fit coefficient  $a$  (maximum characteristic velocity efficiency) for the analytical model with respect to the area (left) and aspect ratio (right) of the beds.

The rate of convergence to the maximum theoretical characteristic velocity efficiency is a better metric to assess a bed designed for a specific target thrust. Higher values of the coefficient  $c$  represent faster convergence to the predicted maximum equilibrium state. The variation of  $c$  with respect to the parametric geometry is shown in Figure 6.8. In general, the convergence rate increases with larger cross-sectional areas and lower aspect ratios, i.e. short and wide catalyst beds. This is also consistent with the pseudo-physical decomposition front model: The axial position of the fronts in a low aspect ratio bed will be closer to the end over the range of mass flow rates. Therefore, maximising the cross-sectional diameter and minimising the length to support the highest mass flow rate will result in a higher characteristic velocity efficiency over the operational range.

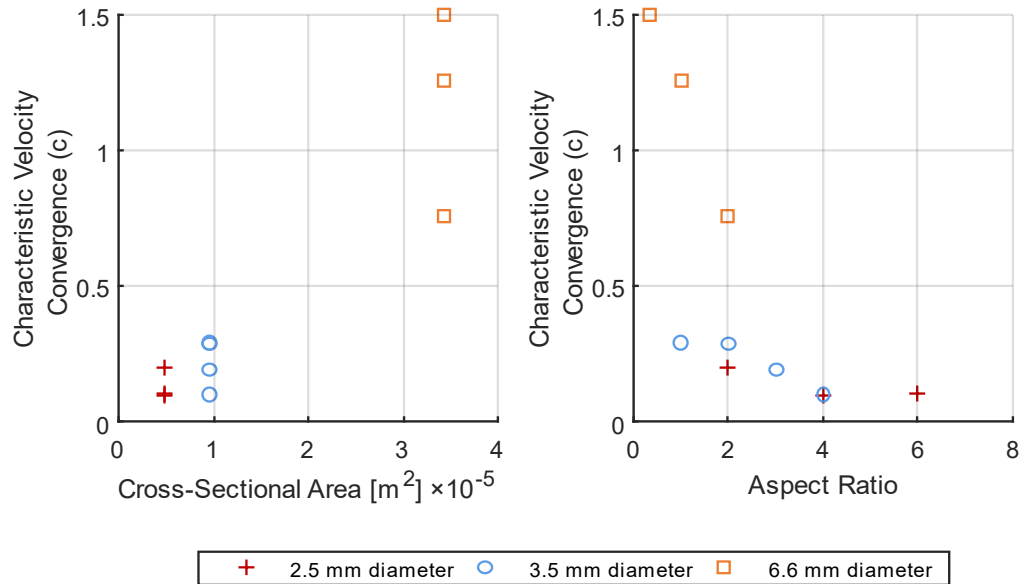


Figure 6.8 – Variation of the fit coefficient  $c$  (rate of convergence to maximum characteristic velocity efficiency) for the analytical model with respect to the area (left) and aspect ratio (right) of the bed.

An optimum catalyst bed design will be volumetrically sized by the maximum propellant flow rate, with a low aspect ratio to increase the performance of the operational range. By definition, a lower aspect ratio corresponds to a lower catalyst bed loading for a particular mass flow rate. Lower bed loadings are also beneficial for other reasons: firstly, high bed loadings result in increased thermal and mechanical stresses on the catalyst material, which can limit its lifetime. This is due to thermal shock and mechanical attrition in the bed. Secondly, higher loadings will also correspond to faster fluid velocities in the bed which will result in greater viscous losses and therefore a higher pressure drop over the catalyst bed. Neither are ideal for an on-orbit thruster which should minimise losses and limit degradation of the catalyst.

However, a catalyst bed with a low catalyst bed loading and aspect ratio has issues. For extreme low aspect ratios, propellant distribution at the start of the bed will impact the upstream catalyst utilisation since the propellant must spread out further radially in the bed. The catalyst material axially close to, but radially far from the injector will be underutilised, which implies a minimum catalyst bed length is required to support the decomposition. The underutilised volume will increase with the bed diameter since the propellant radial diffusion rate will not change. The thermal losses will also start to affect performance in the extreme cases, as with the planar microthrusters from literature. There must therefore be an optimum minimum aspect ratio, although the incomplete datasets of the 6.6Ø2.2L and 6.6Ø6.6L thrusters, due to the flange sealing issues, do not provide enough data to confirm if these are better than the baseline 3.5Ø7.0L.

There is a more fundamental issue that is not captured by this analysis in optimising the design by maximising  $c$ . This optimisation schema seeks to minimise the distance between the full decomposition front and the end of the catalyst pack. As the axial position of the phase-change is very close to the complete-decomposition front, the lower the aspect ratio, the more liable the bed is to flooding. This is because the turbulent environment in the catalyst bed may transiently push the

liquid into the nozzle, breaking the choking condition and causing flooding. In the extreme case for some low aspect ratio, the catalyst bed will be liable to flood at any operational condition.

Neither  $a$  nor  $c$  can be used in isolation to optimise a catalyst bed geometry. Instead, the bed should be sized by the maximum propellant mass flow rate. This is fundamentally tied to the activity of the catalyst material. While the specific parametric geometry affects the performance over the operational range, in most cases the catalyst beds in this study performed well, with mean characteristic velocity efficiencies of all beds approaching  $0.947 \pm 0.027$  ( $1\sigma$ ). Identifying the specific conditions that affect the onset of flooding are therefore an important aspect to appropriately size a catalyst bed.

### 6.2.5. Decomposition Plane Analysis

The steady state results align well with the expected behaviour of the pseudo-physical front model of the catalyst bed. The conditions describing the flooding onset should provide additional information to further validate the model. Determining the specific volume of catalyst material that supports a specific propellant flow rate will also help optimise the bed design. This condition is tied to the reaction kinetics of the propellant and catalyst.

For the assumed first order catalytic decomposition of hydrogen peroxide, the rate is limited by the diffusion of the propellant species to the catalytically active surface. This process must be time-dependant and is related to a particular length scale. Neither of these can be readily derived, but assuming that a reaction must be complete for non-flooded operation, the catalyst bed loading can be recast as a superficial velocity. This is the mean velocity of the liquid phase propellant in an empty catalyst bed volume and is an abstracted representation of the diffusion process. It is calculated as the ratio of bed loading to fluid density  $v_{bed} = G/\rho_{HTP}$ , assuming mass continuity and constant cross-sectional area of the bed. This is related to the macroscale bulk decomposition over the length of the catalyst bed, and can therefore be used to calculate the superficial propellant residence time, or a representative time taken for the liquid phase propellant to pass through the bed:

$$t_{bed} = \frac{L}{v_{bed}} = \frac{L\rho_{HTP}}{G} = \frac{LA_c\rho_{HTP}}{\dot{m}} \quad (6.7)$$

This is different from the actual bed residence time, as the fluid is multiphase and a large volume of the bed will be catalyst pellets, but this simplification avoids having to measure or estimate the catalyst bed packing density or the fluid phase fraction in the catalyst bed.

The superficial residence time for each catalyst bed with respect to the catalyst bed loading is shown in Figure 6.9. The figure also details the data in the  $0.2 \text{ s} \leq t_{bed} \leq 0.5 \text{ s}$  range to highlight the flooding onset times. As expected, the likelihood of flooding increases as the residence time decreases. The flooding onset also appears to be consistent across the designs for residence times below  $0.341 \text{ s} \pm 0.047 \text{ s}$  ( $1\sigma$ ). This confirms that flooding is determined by the specific propellant-catalyst pairing and is insensitive to the geometry of the catalyst bed. It is worth reiterating that the superficial residence time is not the true decomposition timescale but is a representative measure of the minimum timescale needed to achieve vaporisation in the bed. As this timescale is consistent

across a range of bed geometries, it may be used to size a near-optimum thruster catalyst bed, independent of the specific geometric parameters and with minimal experimental testing. In this case, capturing the flooding onset for an arbitrary bed would provide the minimum bed residence time. This corresponds to the maximum performance of the system since the phase change and full decomposition fronts are close together. The bed loading and aspect ratio may then be selected to maximise performance and stability over the operational range.

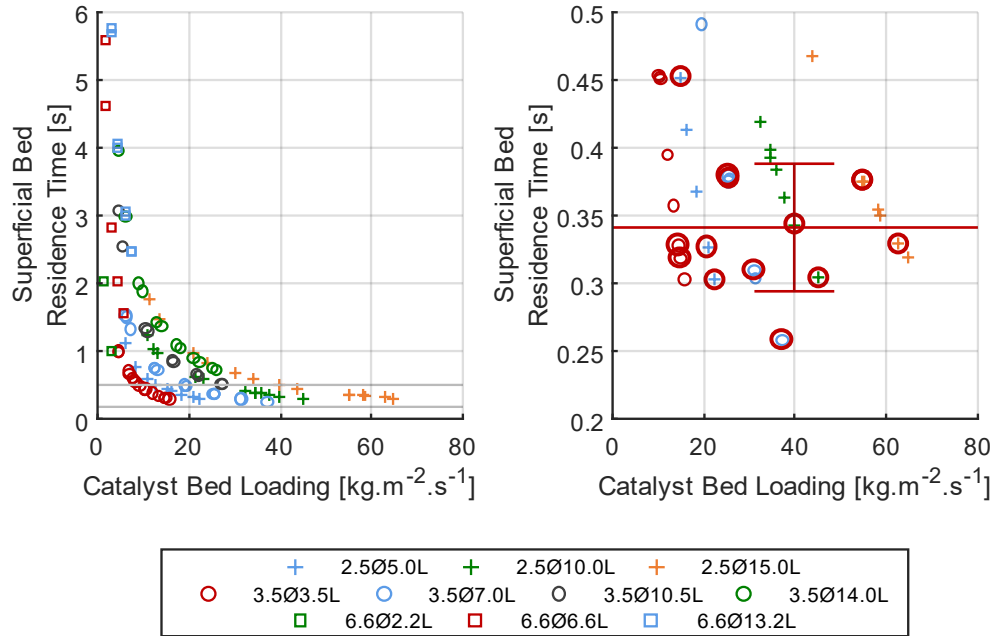


Figure 6.9 – Catalyst bed superficial residence time vs respect to catalyst bed loading. A subset (right) of the full dataset (left) is included to highlight  $t_{bed} \leq 0.50$  s. Flooded tests are highlighted (circled) and the mean flooding onset time is shown with  $1\sigma$  uncertainty bar.

The relationship between the maximum supported propellant mass flux and the flooding onset superficial catalyst bed residence time, is related to the decomposition rate of the propellant. This can be formalised by combining the mass transport and chemical reaction rates or representative timescales into a Damköhler number  $Da$ , defined here using two methods:

$$Da_{rate} = \frac{\text{decomposition rate}}{\text{mass transport rate}} \quad (6.8)$$

$$Da_{timescale} = \frac{\text{diffusion timescale}}{\text{decomposition timescale}} \quad (6.9)$$

The Damköhler number gives an estimation of the completeness of the decomposition reaction: Around unity the decomposition and mass flux rates are similar, and neither process is dominant. For  $Da \gg 1$ , decomposition is faster than the reactant mass transport so the reaction will be more complete than when  $Da \ll 1$ , i.e. where propellant passes through the bed faster than the catalyst can support. Therefore, for full decomposition the Damköhler number must be greater than unity and flooding is expected as this approaches unity. It may be possible to design an optimal catalyst bed without testing using knowledge of the specific propellant and catalyst reaction rate.

Both formulations of the Damköhler number require the propellant decomposition rate. As discussed in Chapter 2, this is outside of the scope of the current work: the decomposition rate is not trivial to calculate or measure. The rate will vary throughout the bed with the local conditions and is a combination of the relative catalytic and thermolytic reaction rates. Both reaction mechanisms will vary with temperature, concentration, fluid phase and proximity to the catalyst material. Instead, the decomposition rate of the limiting process can be used to simplify the analysis. The liquid-phase catalytic decomposition rate is suggested to be this critical step. At these low temperatures,  $< 200$  °C, catalysis is the dominant reaction pathway. The liquid-phase catalysis rate of Pt- $\gamma$  alumina material is estimated using the Arrhenius Equation (2.10), and data from the studies into the hydrogen peroxide catalysis by platinum presented in the literature in Chapter 2 (see Table 2.1). This also uses the steady state pre-bed temperature, between 21.6 °C and 117.6 °C, to correct for propellant preheating. The resulting expected range for chemical decomposition rate is  $1.295 \times 10^{-5} \text{ kg.s}^{-1}.\text{m}^{-2} \leq k \leq 1.201 \times 10^{-2} \text{ kg.s}^{-1}.\text{m}^{-2}$ . The range of values is kept deliberately large as this is an oversimplification of the process.

The main source of the uncertainty in the reaction rates from literature studies is that the reaction rate is dependent on the catalytic surface area. This varies between the different materials in these studies, which are also different to the catalyst material used in the current research. The reaction rates must be converted to a range of specific reaction rate,  $k_{spec}$  for each bed. This uses the catalyst SSA,  $A_{spec}$ , calculated from the catalyst mass  $M_{cat}$  and unit catalytic surface area,  $A_{unit}$ :

$$k_{spec} = kA_{spec} = kA_{unit}M_{cat} \quad (6.10)$$

Table 6.4 – Catalyst bed packing parameters and estimated specific reactivities.

Thruster Notation	Catalyst Mass, $M_{cat}$ [g]	Packing Density * <sup>1</sup>	Mean (Spread) SSA, $A_{spec}$ [m <sup>2</sup> ]	Mean (Spread) Specific Decomposition Rate, $k_{spec} \times 10^{-3}$ [kg.s <sup>-1</sup> ]
2.5Ø5.0L	0.048	0.46	10.9 (9.7 – 12.1)	4.32 (0.16 – 12.0)
2.5Ø10.0L	0.095	0.45	21.3 (18.9 – 23.7)	8.48 (0.31 – 23.6)
2.5Ø15.0L	0.120	0.38	27.0 (24.0 – 30.0)	10.74 (0.40 – 29.9)
3.5Ø3.5L	0.061	0.42	13.7 (12.2 – 15.2)	5.45 (0.20 – 15.2)
3.5Ø5.2L	0.113	0.55	25.4 (22.6 – 28.2)	10.10 (0.37 – 28.1)
3.5Ø7.0L	0.162	0.443 * <sup>2</sup>	36.5 (32.4 – 40.6)	14.52 (0.54 – 40.4)
3.5Ø10.5L	0.200	0.46	45.0 (40.0 – 50.0)	17.92 (0.66 – 49.8)
3.5Ø14.0L	0.275	0.47	61.9 (55.0 – 68.8)	24.64 (0.91 – 68.5)
6.6Ø2.2L	0.139	0.43	31.3 (27.8 – 34.7)	12.43 (0.46 – 34.6)
6.6Ø6.6L	0.448	0.46	100.8 (89.6 – 112.0)	40.11 (1.48 – 111.5)
6.6Ø13.2L	0.934	0.48	210.2 (186.9 – 233.6)	83.64 (3.08 – 232.5)

\*<sup>1</sup> Packing density is calculated using the catalyst bed mass and the density of the catalyst material, 4319 kg.m<sup>-3</sup>, estimated in Chapter 4.

\*<sup>2</sup> Packing density calculated from CT scan inspection.

The rate formulation of the Damköhler number in equation (6.8) can be calculated using the estimated specific decomposition rates:

$$Da_{rate} = \frac{k_{spec}}{\dot{m}} \quad (6.11)$$

The propellant mass flow rate is taken as the mass transport rate of the reaction. This assumes complete decomposition of propellant within the bed and can be related to the known limit: the flooding onset. A plot of the resulting steady state Damköhler numbers with respect to the catalyst bed loading is included in Figure 6.10. The plotted data are calculated using the mean specific decomposition rates. As expected, the trend between the Damköhler number and the catalyst bed loading is similar to that of the superficial residence time from Figure 6.9. The Damköhler number for the mean flooding onset is 56, with a propagated uncertainty between 2.6 and 159.9. Even

considering the spread of possible reaction rates, flooding occurs when the mass transport rate approaches the decomposition rate, i.e. as the order of  $Da \rightarrow 1$ . This agrees with the first order reaction kinetics proposed for HTP-Pt catalyst from literature.

The large, propagated uncertainty in the decomposition rates preclude detailed analyses of the specific value for  $Da$ . Despite this, the data are all above unity, so the decomposition rate must be higher than the mass transport rate for nominal operation. The implication is again that flooding occurs when the propellant mass transport is the limiting step in the decomposition process. In this case, the propellant will not diffuse to the catalyst surface quickly enough to be catalysed. The onset data for the different beds are clustered around the mean  $Da = 56$  with a  $1\sigma$  spread of  $\pm 17.47$ . This low relative spread of the data confirms that while the knowledge of the specific reactivity of the catalyst is not known, there is a strong relationship between the catalyst reactivity and the flooding onset. This may permit analytical catalyst bed design only using the specific propellant-catalyst pair reaction rates.

There is an apparent negative trend in the Damköhler numbers indicating flooding with respect to the catalyst bed loading, i.e. at higher bed loadings (thinner beds) flood at lower values for  $Da$ . This is likely because a higher catalyst bed loading corresponds to a higher aspect ratio for a given maximum mass flow rate. The tortuous flow path forcing the propellant into the catalytically active surface is longer for a longer catalyst bed, so and this effectively increases the diffusion timescale. This also agrees with the conclusion from the characteristic velocity efficiency analyses: that beds with higher aspect ratios are less sensitive to flooding.

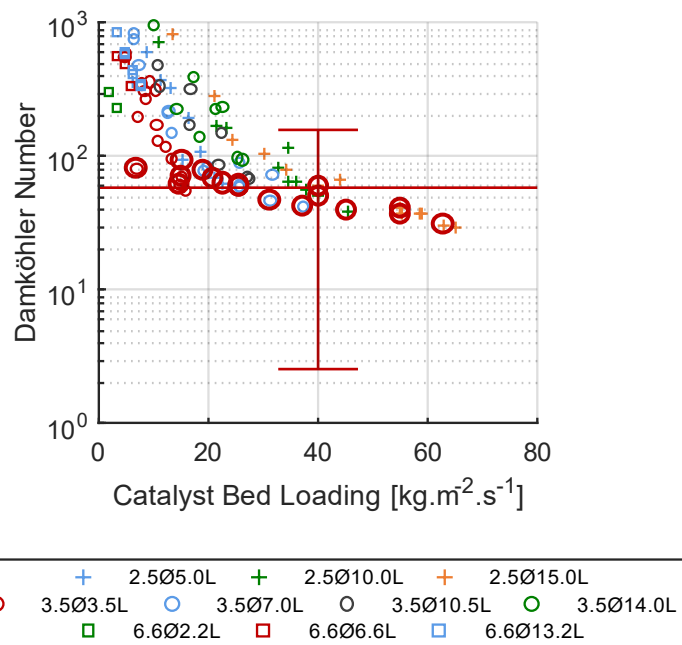


Figure 6.10 – Calculated Damköhler numbers from testing, highlighting flooded runs (circled). The mean flooding onset Damköhler number is shown with a propagated uncertainty bar, determined from the estimated parameter ranges.

### 6.2.6. Catalyst Bed Roughness and Quasi-Steady Performance

The impact of the quasi-steady behaviour on the catalyst bed is important for stable operation. Based on the steady state analysis, instabilities affect the maximum sustainable propellant flow rate, since they may push sufficient liquid into the nozzle, breaking the choking condition. Understanding how the turbulent processes impact the flooding onset condition is therefore important for optimising the performance of a thruster. Investigating the high frequency transient phenomena may also provide further insight into the fundamental fluid and chemical processes in the bed.

A plot of the  $1\sigma$  roughness for the full set of catalyst beds is shown in Figure 6.11. There is significant variability and overlap in the data, and there are no obvious differences from qualitative inspection. However, there is an apparent linear correlation between the roughness and the mass flow rate. This was expected from the observations on the baseline thruster variants in Chapter 5. Therefore, the data from each catalyst bed is regression fitted with a linear model, also in Figure 6.11. For clarity, the raw data have not been shown, but the goodness of fit for each catalyst bed is moderately high (mean  $R^2 > 0.72$ ). The data are still very cluttered, however the gradients of these fit models show the growth of the roughness as the propellant flow increases: Steeper gradients indicate a faster growth in the instabilities over the operational range. In general, the larger catalyst beds have lower gradients and therefore lower pressure roughness over the full operational range.

The roughness in the catalyst beds has been attributed to the oscillatory localised expansion of decomposition products. It is therefore proposed that the lower roughness in the larger catalyst beds is due to the larger fluid volume for the transient gas bubbles to expand into. This attenuates the magnitude of the roughness by distributing the energy over a bigger region. The bubbles are the same phenomenon that cause local choking in the small channels in the catalyst bed. These were discussed in Chapter 5 with relation to the liquid phase pressure drop and the pressure roughness, but have also been directly observed in literature studies on small MEMS catalyst beds [26], [47], [87]. The catalyst beds from literature are considerably smaller than the geometries in the current work, however the phenomenon appears to affect the beds investigated here. Given this, it is suggested that the minimum size of the microscale catalyst beds may also be constrained by the growing absolute magnitude of the pressure roughness, in addition to the local choking effect. This means that smaller beds should be more sensitive to flooding due to the pressure roughness. Note that the effect on the size of a catalyst bed on the decomposition stability is also true for macroscale catalyst beds, where larger beds are more robust to the transient effects [90].

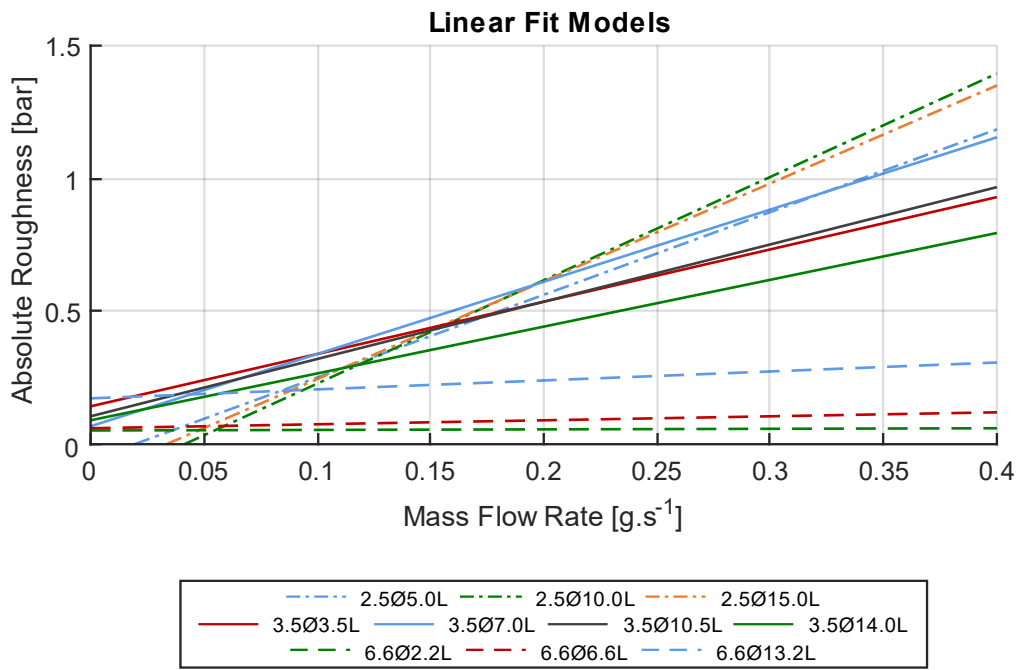
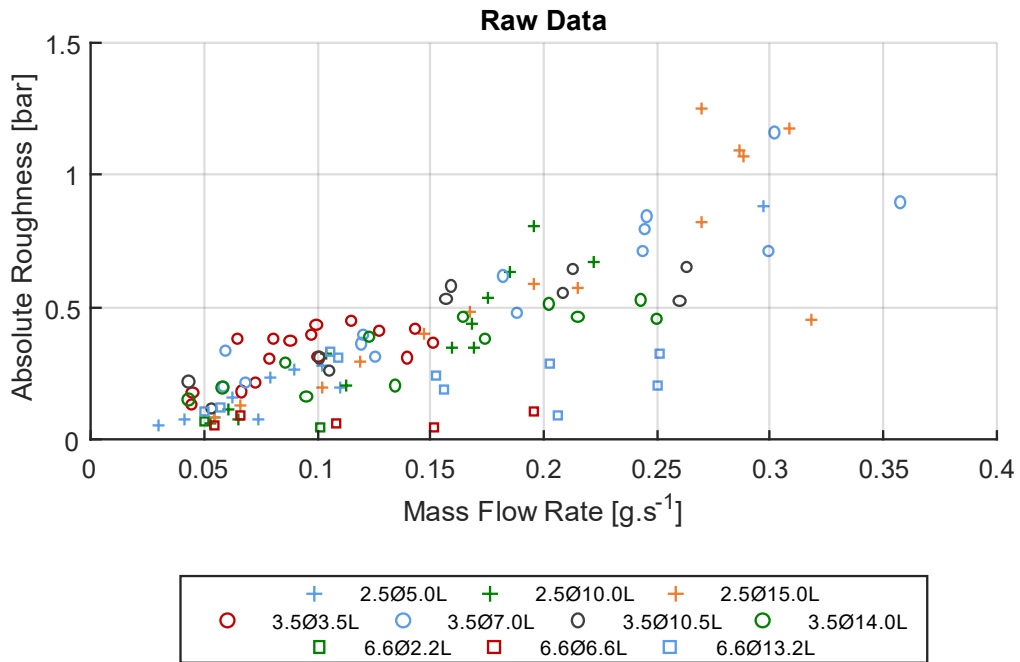


Figure 6.11 – The  $1\sigma$  pressure roughness for the full dataset of catalyst beds. Raw data and linear fit models (per catalyst bed) are both shown.

The frequency of the pressure roughness was also investigated in Chapter 5. The baseline bed exhibited an increasing first significant frequency in the pressure signals with the propellant mass flow rate. While it was suggested that the oscillatory behaviour was due to the cyclical diffusion/decomposition process, it was noted that it could also be tied to a resonant frequency of the catalyst bed. In this latter case, different catalyst beds should have clearly differentiated spectral responses for the different volumes and aspect ratios. The steady state first significant frequency peak of the chamber pressure for the full set of catalyst beds is plotted in Figure 6.12. There is

significant spread in the data, and each thruster exhibits the expected increasing trend with propellant flow rate. Importantly, there is no clear distinction between the different catalyst bed geometries. This implies that there is little to no effect of resonance in the bed, and that the frequency of the roughness is principally due to the reaction kinetics.

Another open question from Chapter 5 was whether the apparent converging first significant peak frequency of the pressure roughness indicated a maximum reactant diffusion limit. Unfortunately, the variability in the data, even between tests with the same catalyst bed mean that the converging trend cannot be confirmed so this is still speculative. It is clear that frequency analysis provides data on the internal conditions in a catalyst bed, but there is insufficient clarity in the data presented here to draw any further conclusions.

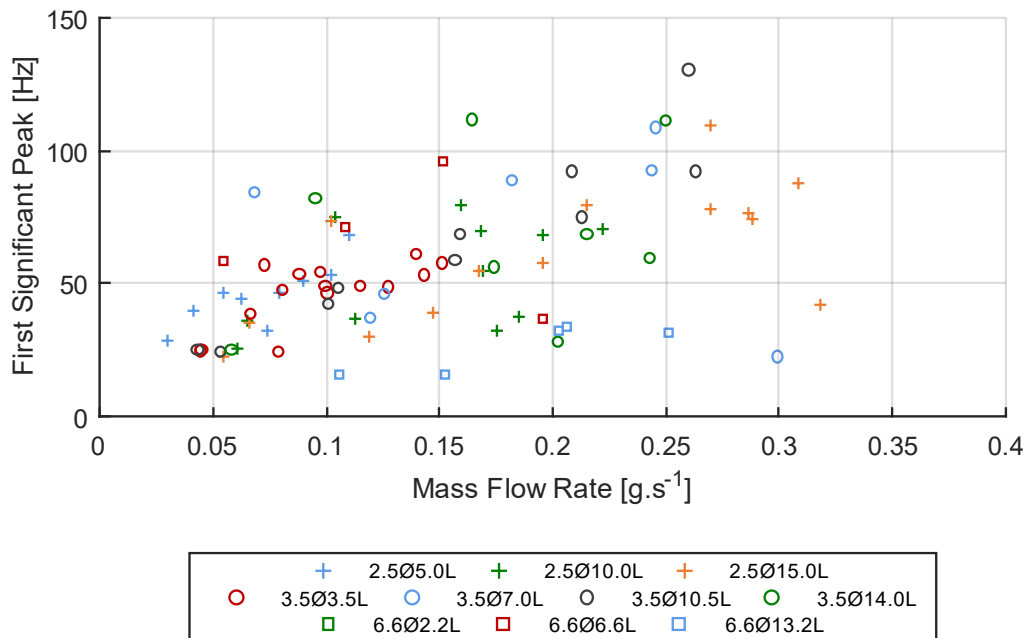


Figure 6.12 – First significant peak centre frequencies for the chamber pressure channel for the full catalyst bed dataset.

### 6.3. Catalyst Material Study

The study into the performance effects due to different bed geometries suggests that the catalytic activity of the propellant-catalyst pair is the most critical component of a high-performance catalyst bed. A key parameter of the activity is the specific reaction rate, which is dependent on the SSA of the bed: the surface area of the catalyst that in contact with the propellant. The first order reaction kinetics of hydrogen peroxide with a platinum catalyst mean that the rate is governed by the diffusion of the reactant species to this catalytically active surface area. Different catalyst geometries will affect the bed packing, so the performance should be directly affected by altering the pellets in a packed bed. Decreasing the size of the pellets will increase the SSA and therefore rate of decomposition, although this may result in a significant increase of the viscous losses and the localised liquid choking effect. Larger catalyst pellets will have a decreased specific decomposition rate so will not be able to sustain as high a propellant flow rate, although they will have a lower pressure drop. This study seeks to investigate these effects by using a different catalyst geometry in a number of the beds tested in section 6.2.

#### 6.3.1. Catalyst Material Comparison

The scope of the study is limited by the available catalytic materials suitable for the scale of the beds. As discussed in Chapter 2, the design space for packed bed pellets is immense, although many are not suitable for the small size of microthrusters. Achieving sufficiently high packing densities in the microscale catalyst beds to sustain any meaningful propellant flow rate is a particular challenge. Only one additional suitable catalyst was available for testing to provide a direct comparison. The catalyst variant is another commercial catalyst, H1820, supplied by Heraeus GmbH. The main difference between the catalysts is the pellet geometry: the variant catalyst pellets are larger with a non-uniform shape. The specified size of the pellets is mesh number #18 – #20, corresponding to a size range of between 850  $\mu\text{m}$  and 1000  $\mu\text{m}$ , which is the upper limit for the size along the smallest dimension of the particles.

The difference between the two materials can be seen in the photograph in Figure 6.13, and Figure 6.14 shows the distribution of the geometric circularity and projected area, calculated in a similar fashion as with the baseline catalyst using image processing of EPI optical micrographs. For reference, the baseline catalyst parameters were plotted in Figure 4.13. As expected, the H1820 variant is much larger than the baseline catalyst material, with a mean projected area of  $1.05 \text{ mm}^2 \pm 0.23 \text{ mm}^2$  compared to  $0.07 \text{ mm}^2 \pm 0.01 \text{ m}^2$ . Neither pellets are completely circular: the mean circularity of the non-uniform H1820 variant is  $0.83 \pm 0.16 (1\sigma)$ , slightly lower than the spherical baseline catalyst,  $0.85 \pm 0.02 (1\sigma)$ , but with a much wider spread. The wider spread in the variant circularity data captures the non-uniform pellet geometry. The size difference is clear by calculating the effective diameter, i.e. assuming that both catalyst variant pellets are perfectly circular. The H1820 variant has an effective diameter of  $1.16 \text{ mm} \pm 0.55 \text{ mm} (1\sigma)$  compared to the baseline's  $0.305 \text{ mm} \pm 0.104 \text{ mm} (1\sigma)$ .

The H1820 variant has the same catalyst mass loading as the baseline variant, 5 % Pt, and the microstructure of the catalytically active material should be similar. The direct measurement of the

catalyst surface area was not within the scope of this research and a value of the unit surface area was not provided. Despite this, the catalysts should have a similar range of areas, although the variant material unit surface area will likely be slightly lower than for the baseline catalyst since the pellets are larger.



Figure 6.13 – A photograph for comparison of the variant (left) and baseline (right) catalysts.

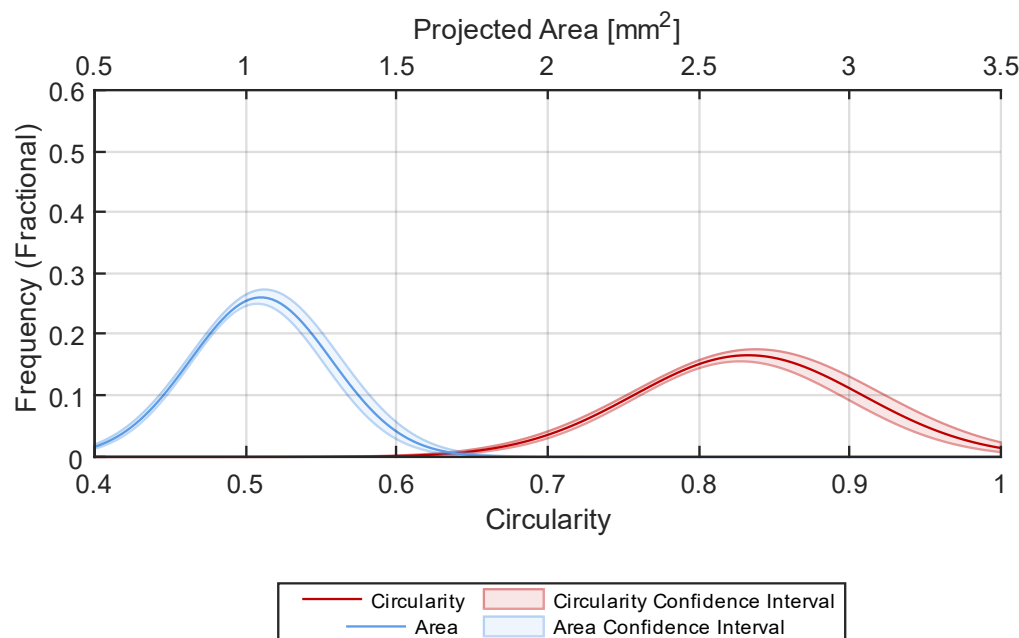


Figure 6.14 – The mean and  $1\sigma$  confidence of the distribution of key variant catalyst geometric parameters.

Different sizes and shapes of the pellets will result in different packing densities. As the baseline catalyst pellets are spherical, their packing is much easier to estimate. The design principle for a ‘well-packed’ bed is where the bed diameter is greater than 12 pellet diameters, i.e.  $D_c/d_p \geq 12$  [85], [86]. Considering the best-case minor length of the variant catalyst pellets,  $0.947 \text{ mm} \pm 0.114 \text{ mm}$  ( $1\sigma$ ),  $D_c/d_p$  is 2.64, 3.70 and 6.97 respectively for the 2.5 mm diameter, 3.5 mm diameter and 6.6 mm

diameter beds. The beds are all below the suggested limit and are expected to have low packing densities below ideal, with significant impact from wall effects. In the extreme, the 2.5 mm diameter bed can only fit  $\sim 3$  pellets over the circular cross section.

X-ray CT scanning of a thruster packed with this catalyst material was not possible for this study, however the catalyst has been tested in previous work on the development of a 1 N thruster with a 13.0 mm diameter 17.5 mm long catalyst bed [12]. A CT micrograph of the catalyst bed of this thruster is shown in Figure 6.15 with the void fraction in the radial and axial directions shown in Figure 6.16. Note that the length of the bed of this thruster is actually  $\sim 20$  mm due to over-filling of the bed and compression of the catalyst retainer plate spring. The bulk variant catalyst packing density is calculated as  $0.459 \pm 0.024$  ( $1\sigma$ ) from the 1 N thruster packing density data presented in Figure 6.16. Wall effects impact packing approximately 1.3 mm to 2.0 mm into the bed in both dimensions. The corresponding non-dimensional wall distance is  $1.4 \leq z \leq 2.1$ , calculated using Equation (2.12). This is considerably lower than the expected  $z_x = 4.5$  for spherical particles [85], although as these pellets are not spherical or uniform, a better packing density and less significant wall effects are expected.

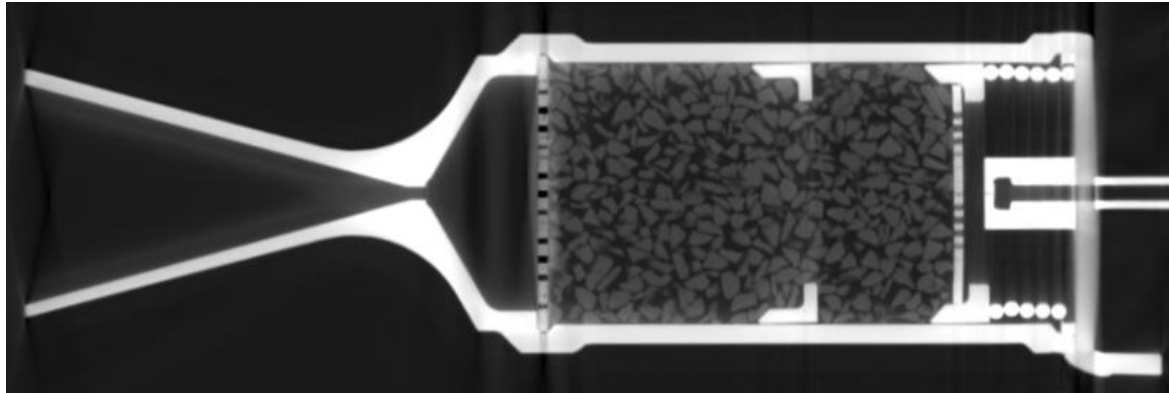


Figure 6.15 – A CT scan section through the central axis of the 1 N thruster to show the packing of the variant catalyst. The absolute pixel brightness has been adjusted to better visualize the catalyst pellets, also increasing the relative effect of the x-ray shadowing artifacts.

The results from the larger thruster are beneficial for the sub-newton catalyst bed packing: the centre of the 2.5 mm, 3.5 mm, and 6.6 mm diameter beds have non-dimensional wall distances of 1.3, 1.8, and 3.5. This suggests that significant wall effects will be present in the 2.5 mm and 3.5 mm diameter beds, but the 6.6 mm diameter bed should have relatively good catalyst packing. Note, the 1 N packing data does not show the expected oscillating packing density seen with the baseline catalyst in Chapter 4. This is because the pellet non-uniformity reduces the regularity of the distribution. In addition, the data here is from the single CT scan slice in Figure 6.15, rather than the convolved data from the full three-dimensional baseline 0.1 N data set, so it is not possible to extract the statistical data. The packing is estimated for the chosen beds by using the measured mass and estimated design of the catalyst material.

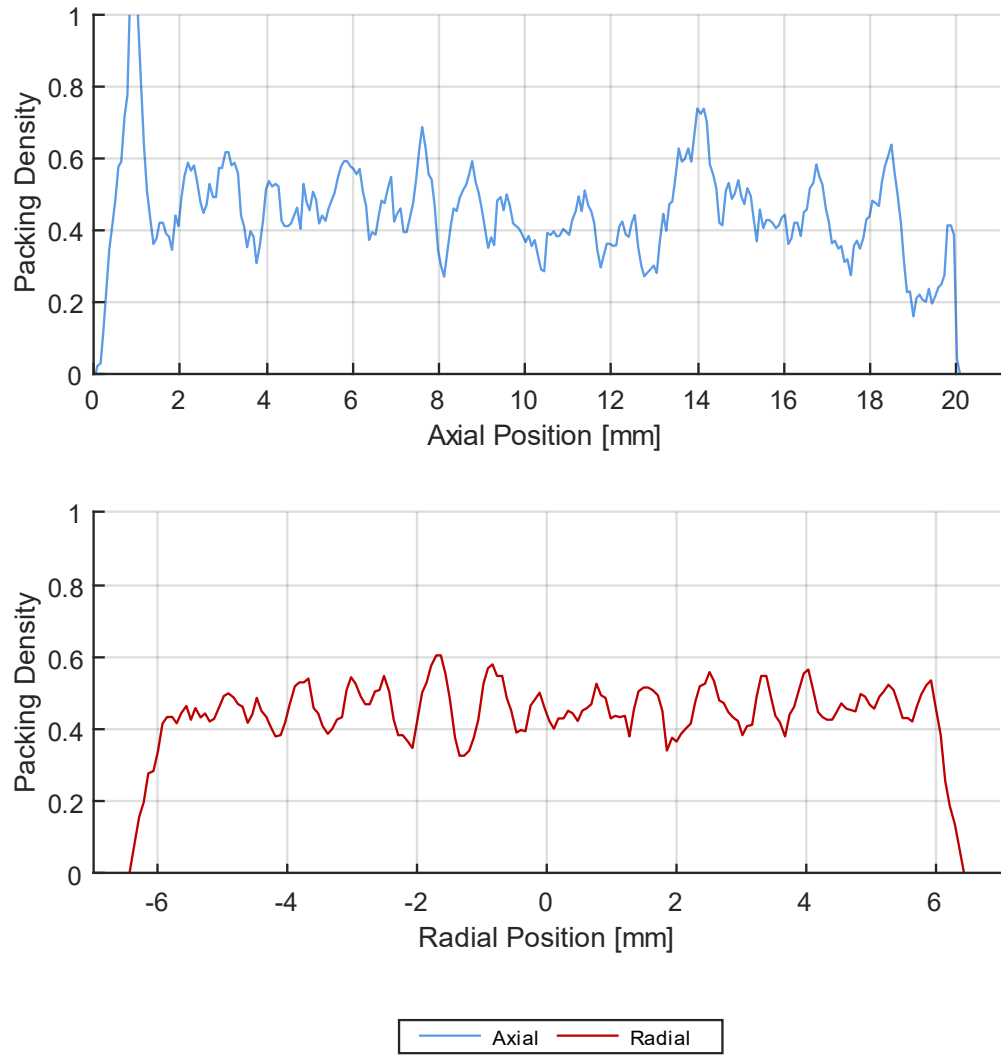


Figure 6.16 – 1 N catalyst bed packing with the variant catalyst, with data taken from x-ray CT micrograph. Packing is shown with respect to the axial (top) and radial (bottom) positions in the bed.

### 6.3.2. Test Campaign

Different catalyst beds were selected for testing the H1820 variant catalyst material based on their likelihood of capturing flooding within the test range. They are listed in Table 6.5 with their estimated packing with both the baseline and variant catalysts. The variant catalyst mass was measured by taking the difference between pre- and post-assembly masses of each thruster. The resolution of the mass balance was only 10 mg rather than 1 mg used for measuring the baseline catalyst. In most cases the mass of the variant catalyst is below that of the corresponding baseline bed. The predicted packing densities of the beds explicitly shows the expected trend: packing is worse for the smaller beds. The bulk packing density of the 1 N catalyst bed is  $0.459 \pm 0.024$  ( $1\sigma$ ), compared to a minimum 0.1 N catalyst bed packing of 0.30 for the  $2.5\text{Ø}10.0\text{L}$  bed. Despite this, the  $6.6\text{Ø}6.6\text{L}$  0.1 N bed design appears to have a similar packing to the larger 1 N thruster, with a value of 0.47, indicating that the wall effects are minimal. The packed bed of the  $6.6\text{Ø}6.6\text{L}$  also has a higher

mass of variant catalyst than the baseline material. This agrees with the previous statement that the random pellet shapes pack better than spheres.

Table 6.5 – A comparison of the catalyst bed packing parameters and estimated specific reactivities for the baseline and variant catalyst material

Thruster Notation	Catalyst Parameters						
	Baseline Catalyst			Variant Catalyst			Projected Flooding Onset Mass Flow Rate, $\times 10^{-4}$ [g.s $^{-1}$ ] <sup>*2</sup>
	Mass [g]	Packing Density <sup>*1</sup>	SSA [m $^2$ ]	Mass [g]	Packing Density <sup>*1</sup>	Estimated SSA [m $^2$ ]	
2.5Ø10.0L	0.095	0.45	21.3	0.06	0.30	21.3	0.151 (0.002 – 9.030)
3.5Ø5.2L	0.113	0.52	25.4	0.08	0.36	25.4	0.180 (0.002 – 10.756)
3.5Ø7.0L	0.162	0.4550	36.5	0.13	0.43	36.5	0.259 (0.003 – 15.467)
6.6Ø6.6L	0.448	0.46	100.8	0.47	0.47	100.8	0.716 (0.009 – 42.719)

<sup>\*1</sup> Packing density is calculated using the catalyst bed mass and the density of the catalyst material, 4319 kg.m $^{-3}$ , estimated in Chapter 4.

<sup>\*2</sup> Flooding onset condition calculated using the mean onset  $Da = 56$ , bounded by the propagated uncertainty range,  $2.61 \leq Da \leq 159.94$ .

All of the thrusters using the variant catalyst pellets, including the 6.6Ø6.6L thruster, are expected to have a lower catalytic performance, compared to the baseline, due to the reduced SSA and therefore reactivity. Smaller beds should have a considerably lower activity as they also have less catalyst material by mass. In the absence of specific data on the H1820 variant, the range of baseline unit surface areas can be used to predict the range of mass flow rates where flooding should occur. The projected propellant mass flow rates for the onset condition are also listed in Table 6.5. These are calculated from the flooding onset Damköhler number range from section 6.2.5 (mean: 56, propagated uncertainty spread: 2.6 - 159.9), using a rearrangement of Equation (6.11):

$$\dot{m}_{flood} = \frac{k_{spec}}{Da_{rate,flood}} \quad (6.12)$$

Note that these calculations assume that the liquid phase catalytic decomposition rate is the same for the two catalysts, and that it dictates the catalyst bed performance, i.e. the position of the phase change and full decomposition fronts and therefore the flooding condition. Unsurprisingly, these flow rates are lower than for the baseline catalyst with the exception of the 6.6Ø6.6L thruster, although as discussed, this is a result of using the same unit surface area range.

For a direct comparison of experimental results, the nominal test pressure range and steps are the same ( $5 \text{ bar} \leq P_{in} \leq 30 \text{ bar}$ ,  $dP_{in} = 5 \text{ bar}$ ). Flooding should occur at lower flow rates, but the procedure for capturing the onset to a 1 bar resolution will follow the previous methodology. The data analysis will differ given the issues with the estimated SSA; the onset mass flow rates will be directly compared instead of calculating the Damköhler number.

### 6.3.3. Results

The general steady state performance of the H1820 variant catalyst beds is good, with high performance at the lower propellant mass flow rates. In these tests the chamber temperatures are equivalent to the baseline catalyst testing and demonstrate that both catalyst variants are both effective. However, the performance drops at the higher flow rates and the majority of these tests exhibit ‘very steamy’ multiphase plumes and very rough chamber temperatures. This can be seen in the example time domain data comparing both catalyst materials in the baseline thruster, shown in Figure 6.17. Here, the difference in the data between the well-performing baseline catalyst and an equivalent lower thermal performance run with the H1820 variant catalyst is clear: the steady state chamber temperature is  $\sim 150 \text{ }^{\circ}\text{C}$  lower for the test with the variant.

The mode of operation appears similar to flooding – a multiphase exhaust plume with unvapourised propellant, and a higher mass flow rate – it is a stable mode of operation and there are only minor differences in the chamber pressure and mass flow rates. For the previous data capturing flooding, these are very different compared to the nominal conditions. It is suggested that this previous transient flooding represents the catastrophic failure of the nozzle choking condition, where the bed is overwhelmed by the incoming cool propellant flow. This is in contrast to the condition here, where the exhaust is sufficiently dispersed to only partially affect choking. One possible cause for this is propellant channelling: where propellant has a relatively short and wide flow path, often along the walls of the catalyst bed. The liquid propellant may not be forced into contact with the catalyst surface and will remain liquid. To mitigate this, larger thrusters may use baffles in the catalyst bed to interrupt the propellant flow [12], [16]. Despite the slightly different mode of operation, in this case the steamy plumes are considered to be flooded as the bulk propellant phase change front is clearly not within the catalyst bed. Despite this, it is still clear that the nozzles are choking, even if they are operating with a degraded performance.

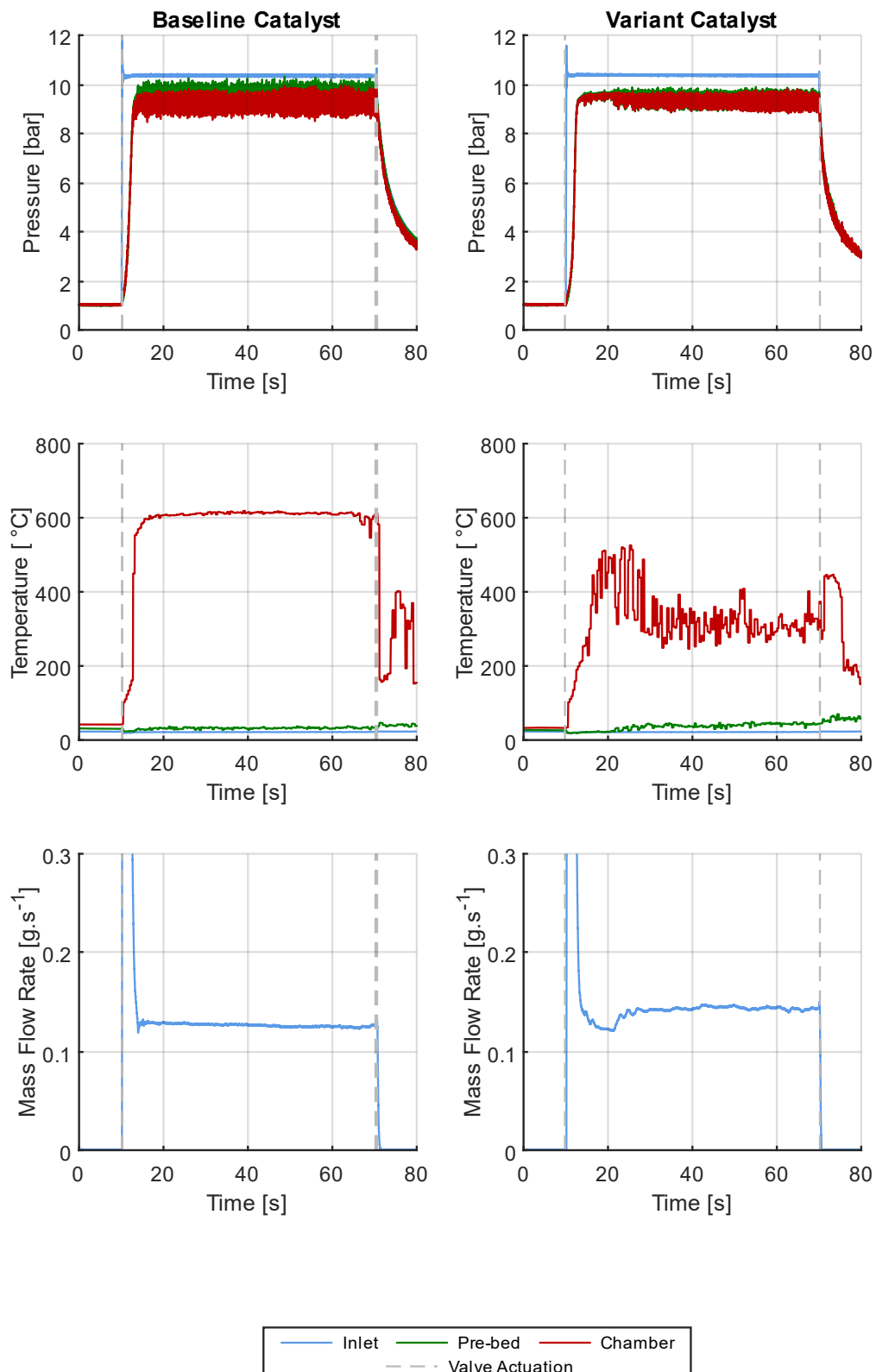


Figure 6.17 – Example time domain test data for 3.5Ø7.0L thruster with a target inlet pressure of 10 bar, for both baseline and H1820 variant catalysts. Firing valve actuation times are indicated.

The thermal characteristic velocity efficiency shows the performance of both modes. The results are plotted against the propellant mass flow rate in Figure 6.18. For the larger catalyst beds, especially the 6.6Ø6.6L design, the performance approaches that of the baseline catalyst, with characteristic velocity efficiencies in excess of 0.90. However, many tests, especially with the smaller beds (2.5Ø10.0L and 2.5Ø5.2L), stay in the steady low temperature multiphase exhaust mode. The steady state performance is considerably lower, between 0.6 and 0.8, and in some cases only just above the theoretical minimum limit,  $\eta_{c_0^*} = 0.5548$ .

The same constrained convergent fit model from Equation (6.6) is used to characterise the maximum equilibrium performance, and the rate of convergence to this. Note that this maximum condition assumes that the beds do not flood. The flooded results are omitted from the data used to fit the model, although this limits the number of data points and increases the impact of run-to-run uncertainties. The model fit parameters for both the baseline and variant catalysts are listed in Table 6.6, showing good agreement between the baseline and variant catalyst predicted equilibrium characteristic velocity efficiency. There is greater difference between the rates of the convergence to the maximum, but these are broadly similar. Despite the limited run to run variability and the limited data for fitting, both catalysts can therefore be described as having similar performance characteristics. This again implies that the performance of a well-packed catalyst bed, appropriately sized for a specific pellet geometry, is principally driven by the catalytic activity. It also confirms that the specific reactivities of the two catalyst materials are similar, although the lower flooding onset is indicative of a lower unit catalytic surface area and the increased size of the flow channels through the bed.

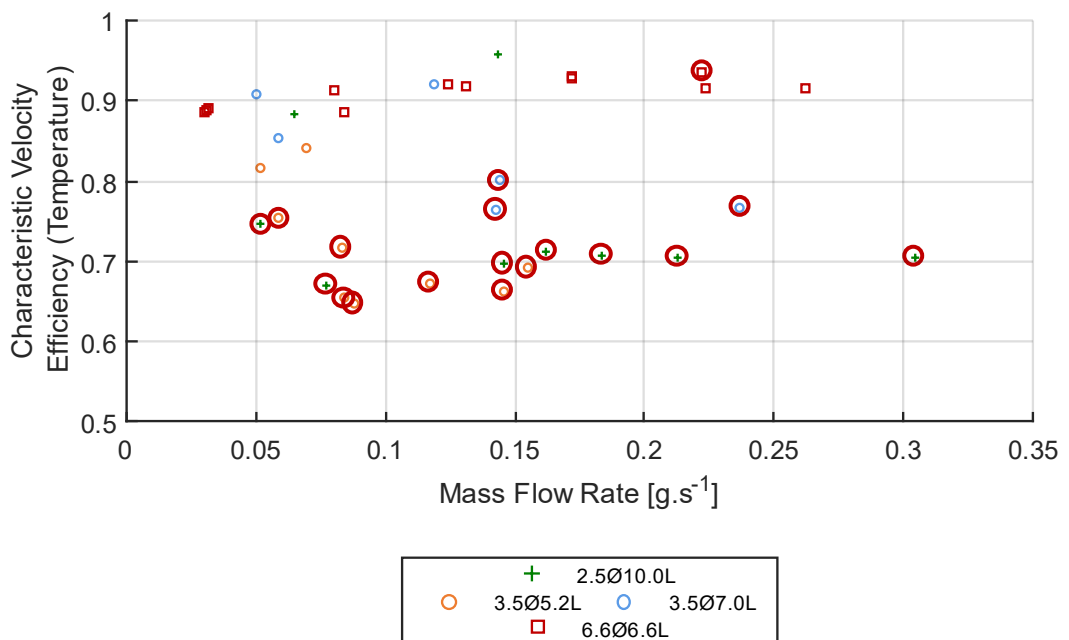


Figure 6.18 – Thermal characteristic velocity efficiencies of the variant thruster plotted against propellant mass flow rate. Flooded tests are highlighted (circled).

Table 6.6 – Steady state performance comparisons of the baseline and variant catalyst materials.

Thruster Notation	Baseline $\eta_{c^*}$ Model Parameters		Variant $\eta_{c^*}$ Model Parameters		Flooding Onset Mass Flow Rate [g.s <sup>-1</sup> ]	
	Maximum $\eta_{c^*}, a$	Convergence Rate, $c$	Maximum $\eta_{c^*}, a$	Convergence Rate, $c$	Predicted	Measured
2.5Ø10.0L	0.949	0.101	0.970	0.118	0.151 (0.002 – 9.030)	0.144
3.5Ø5.2L <sup>*2</sup>	–	–	0.901	0.205	0.180 (0.002 – 10.756)	0.055
3.5Ø7.0L	0.967	0.290	0.958	0.336	0.259 (0.003 – 15.467)	0.127
6.6Ø6.6L	0.930	0.758	0.916	0.807	0.716 (0.009 – 42.719)	0.136

<sup>\*1</sup> Flooding onset condition calculated using the mean onset  $Da = 56$ , bounded by the propagated  $1\sigma$  uncertainty ( $2.61 \leq Da \leq 159.94$ ).

<sup>\*2</sup> The 3.5Ø5.2L thruster was not successfully tested with the baseline propellant so the baseline characteristic velocity efficiency data is not available. The flooding onset should still be predictable if the  $Da$  data is consistent across the

The predicted and actual flooding onset mass flow rates are also included in Table 6.6. Both are of the same magnitude which suggests that the Damköhler number does indeed predict flooding, and can therefore be used for modelling the processes in the bed. This is despite the wide range of specific decomposition rates and the expected discrepancies between the unit catalytic surface areas. Of particular interest is that the absolute predicted onset range is very wide given the propagated parameter ranges, while the mean values are close to the measured mass flow rate. This is another confirmation that the specific reactivities of the two catalyst materials are not too dissimilar. It is proposed that this is because the difference between the macroscopic surface areas, i.e. the pellet geometry, is minor compared to the microscale surface area of the catalytically active platinum. This makes intuitive sense as the macroscale surface areas of 300  $\mu\text{m}$  diameter and 947  $\mu\text{m}$  spheres, representative of the baseline and variant catalysts, are  $2.83 \times 10^{-7} \text{ m}^2$  and  $28.17 \times 10^{-7} \text{ m}^2$  respectively. This is approximately only one order of magnitude difference, but even accounting for a large number of pellets in a bed, the surface areas are considerably lower than the estimated SSAs which are all above  $20 \text{ m}^2$ .

An important difference between the two variant catalysts is that the baseline catalyst onset mass flow rates increase with the SSA while the H1820 variant has an approximately constant onset regardless of the catalyst bed geometry. This may be another demonstration of the propellant channelling phenomenon: The wider and less-tortuous flow channels in the H1820 catalyst bed will not force the propellant into the catalyst active surface as much as in the baseline catalyst bed. This will reduce the decomposition rate of the propellant, and in extreme cases some propellant may rely on the thermolytic decomposition.

In some thrusters from literature, channelling along the catalyst walls is mitigated by forcing the propellant back towards the centre axis of the catalyst bed using baffles [12], [16]. However, in the current thruster, the poorly-packed H1820 catalyst beds have wide flow paths throughout, so the decomposition cannot be sustained. This leads to the conclusion that a bed will also have a maximum channel dimension i.e. a maximum pellet size for a given scale catalyst bed. For pellets larger than this, the propellant will channel, so the bed will not effectively sustain decomposition, and will exhibit the low performance steady flooding condition exhibited by some of the H1820 variant tests.

The minimum and maximum limits of the catalyst channels may converge as the target thrust and therefore mass flow rate decreases. This is because the catalyst material and bed must both decrease in size for lower propellant flow rates, which also reduces the size of the channels. This convergent point, where the size of the channels for local choking and the channelling condition are the same, provides a lower bound for the minimum size of a sub-newton monopropellant thruster that is based on the catalyst material and the bed architecture.

## 6.4. Propellant Enthalpy Study

The specific decomposition rate for the liquid catalysis in a catalyst bed is not only affected by the SSA and bed macrostructure, but also by the reaction rate of the propellant-catalyst pair. Changing the propellant or the catalytically active material can test the impact of the decomposition rate on the processes in the bed. In this study, a 98.0 %/wt. HTP propellant will be tested to assess the impact of the decomposition rate on performance. This change in the decomposition rate  $k$  should be proportional to the change in molar concentration given the first order reaction kinetics, illustrated by Equation (2.11), for reference:

$$k = k_1[H_2O_2]^1 \quad (6.13)$$

The fundamental processes in the bed may vary for different propellants or with a different catalyst. A key benefit of using a different hydrogen peroxide propellant is that the decomposition processes should be consistent, allowing for direct comparison between the results of the different propellants.

The primary goal of this study is to attempt to confirm the relationship between the liquid phase catalysis rate and the conditions in the bed, including presenting any further validation of the simple pseudo-physical front model. This is also an opportunity to demonstrate the maximum possible performance of an HTP monopropellant microthruster using 98.0 %/wt. HTP – the highest enthalpy aqueous hydrogen peroxide propellant available.

### 6.4.1. Propellant Comparison

A direct comparison between the baseline 87.5 %/wt. and variant 98.0 %/wt. HTP propellants is included in Table 6.7. This lists the adiabatic temperature and expected characteristic velocity, along with the minimum characteristic velocity efficiency for no temperature rise. These values take into account the difference in exhaust composition resulting from the higher molar fraction of oxygen in the exhaust for 98.0 %/wt. HTP. The parameters are derived using NASA CEA for the physiochemical properties [17], [18].

The higher performance of 98.0 %/wt. HTP also corresponds to an increased liquid phase decomposition rate and therefore higher projected propellant flow rate supported by a catalyst bed before flooding. This was calculated using the Arrhenius Equation (2.10), and data from the studies into the hydrogen peroxide catalysis by platinum presented in the literature in Chapter 2 (see Table 2.1) Note that this assumes the propellant temperature is 25 °C. The flooding onset is calculated as before using Equation (6.12), the Damköhler number and the estimated SSA for the baseline catalyst bed and material. This method results in a higher mean onset propellant mass flow. Note that this is close to the expected upper bound for the 5 bar  $\leq P_{in} \leq$  25 bar range.

Table 6.7 – A comparison of the 87.5 %/wt. and 98.0 %/wt. HTP propellant, showing key ideal performance metrics for the baseline catalyst bed and material.

Propellant	Ideal Performance			Liquid-Phase Catalysis Rate [kg.s <sup>-1</sup> .m <sup>-2</sup> ] * <sup>1</sup>	Flooding Onset Mass Flow Rate [g.s <sup>-1</sup> ]
	$T_{ad}$ [°C]	$c_{ad}^*$ [m.s <sup>-1</sup> ]	$\eta_{c_0^*}$		
87.5 %/wt. HTP	695.3	915.0	0.5548	0.40 (0.016 – 0.996)	0.259 (0.003 – 15.467)
98.0 %/wt. HTP	952.6	1021.2	0.4932	0.43 (0.016 – 1.077)	0.280 (0.003 – 16.729) * <sup>2</sup>

\*<sup>1</sup> Decomposition rate calculated using the empirical literature models as per the values for 87.5 %/wt. HTP listed in Table 2.1.

\*<sup>2</sup> Projected onset calculated using the mean flooding onset  $Da = 56$ , bounded by the propagated uncertainty range,  $2.61 \leq Da \leq 159.9$  using the baseline catalyst bed.

#### 6.4.2. Test Campaign

This study compares the performance of the baseline 3.5Ø7.0L catalyst bed, using the baseline 300  $\mu$ m spherical pellet catalyst material using 98.0 %/wt. HTP and 87.5 %/wt. HTP. A particularly important aspect to consider for this test campaign is safety: The higher enthalpy of the variant propellant corresponds to an increased adiabatic decomposition temperature, 952.6 °C. This is above the maximum intermittent service temperature for the SS 316/316L, 870 °C [122], [123], the material for the thruster body. Assuming that the thruster operates with a similar catalytic thermal efficiency to the baseline propellant, approaching  $\sim 0.95$ , the maximum chamber temperature may be in excess of 906.2 °C. A higher temperature is expected to have a lower thermal efficiency due to the increased thermal gradient, although the catalyst bed must have  $\eta_{cat} \leq 0.91$  for the chamber temperature to be within the safe material limits. Due to the risk of mechanical failure additional safety measures are required.

Physical safety measures include 5 mm thick polycarbonate shielding around the thruster and a large volume of water below the thrust stand to catch any material and propellant. Procedural safety measures limit testing to the nominal operational range (i.e. excluding the 30 bar test), assuming that there are no anomalous readings or any signs of mechanical failure. The expected mean mass flow rate for the flooding onset of 0.280 g.s<sup>-1</sup>, corresponding to an inlet pressure of 25.1 bar ( $\eta_{cat} = 0.95$ ). The upper 25 bar tests will therefore hopefully capture flooding due to run-to-run variation and the anticipated higher roughness.

#### 6.4.3. Results

The absolute steady state chamber temperature data are shown in Figure 6.19 along with the data from the 87.5 %/wt. HTP for direct comparison. As expected with a higher enthalpy propellant, the thermal performance of the bed is considerably greater, with chamber temperatures approaching 800 °C for increasing propellant flow rates. Fortunately, the maximum temperature of the thruster is comfortably below the maximum safe service temperature for the SS 316/316L material. The flooding onset was not captured in the tests, and there was no apparent drop in performance at the maximum flow rates. The latter is expected as the reaction mechanisms should be the same between the propellant concentrations. Unlike with the baseline propellant tests, during testing the external thruster temperature was high enough to visibly glow. This is common for many high-performance commercial propulsion systems using hydrazine or ionic liquid propellants, but HTP monopropellant thrusters do not typically achieve the necessary temperatures. At the time of writing this had not been demonstrated for a sub-newton system.

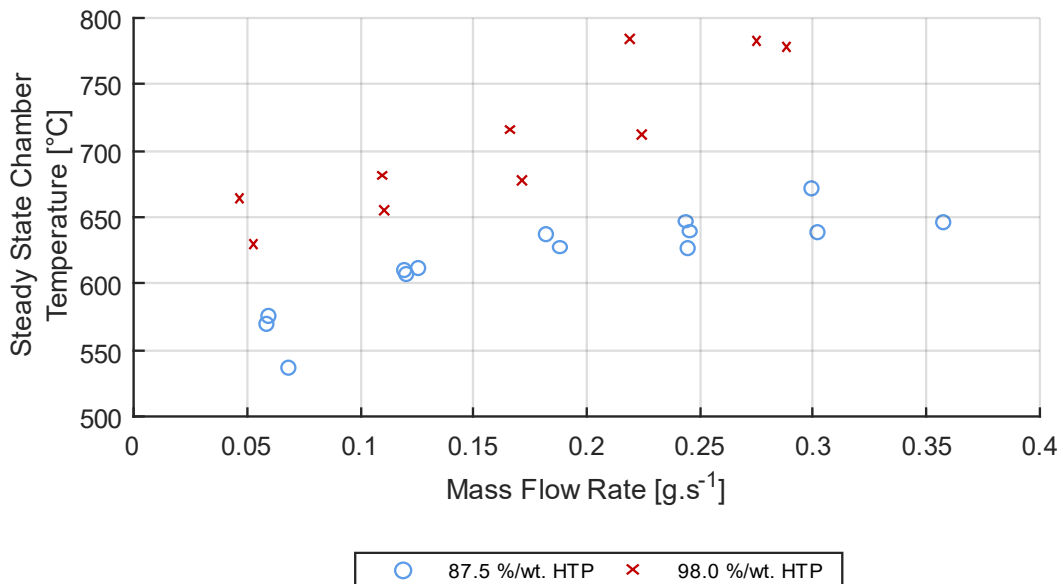


Figure 6.19 – A direct comparison of the steady state chamber temperatures for the baseline thruster with the different concentration HTP propellants.

The increased temperatures mean that the absolute thermal performance is higher than for the lower concentration propellant. However, the efficiency of the system is reduced. This is shown by the thermal characteristic velocity efficiency in Figure 6.20, and is an expected result given the higher thermal gradient between the fluid and external environment: This results in an increased heat flux, cooling the bed more. Note that this is an effect of the atmospheric testing. Since there was little appreciable difference between the thermal performances for the standard and highly-instrumented catalyst beds in Chapter 5, the convective losses are expected to be the dominant cause of thermal losses. Convection is not present in a vacuum environment so the thermal efficiencies of both propellants should be higher and more similar. Note that the convex trend in the 98.30 %/wt. HTP data in Figure 6.20 is due to a greater degree of propellant preheating due to the higher temperatures.

Since flooding was not observed it is not possible to directly compare the reactivity of the propellant concentrations, however a lower catalytic thermal efficiency reduces the expected onset conditions as the decomposition rate is lower. The maximum recorded catalytic thermal efficiency is 0.808 for a recorded steady state 25.2 bar inlet pressure. By definition the mass flow rate for a flooding onset assuming  $Da = 56$  is constant, however for  $\eta_{cat} = 0.8075$  the predicted inlet pressure for flooding is 23.8 bar. This driving pressure is calculated for the mass flow rate through the nozzle (the modified choked flow Equation (4.3)), and assuming a  $0.086 / P_c$  injector fractional pressure drop from the baseline 10-50 Poiseuille injector, accounting for the physiochemical parameters of the 98.0 %/wt. propellant. This suggests that the fundamental decomposition process changes with the propellant concentration. It is proposed that the higher temperatures in the bed increase the thermolytic decomposition rate and the rate of boiling. This will shift the pseudo-physical phase change front further upstream. Therefore, a more energetic propellant requires a smaller catalyst bed to support a specific propellant flow rate.

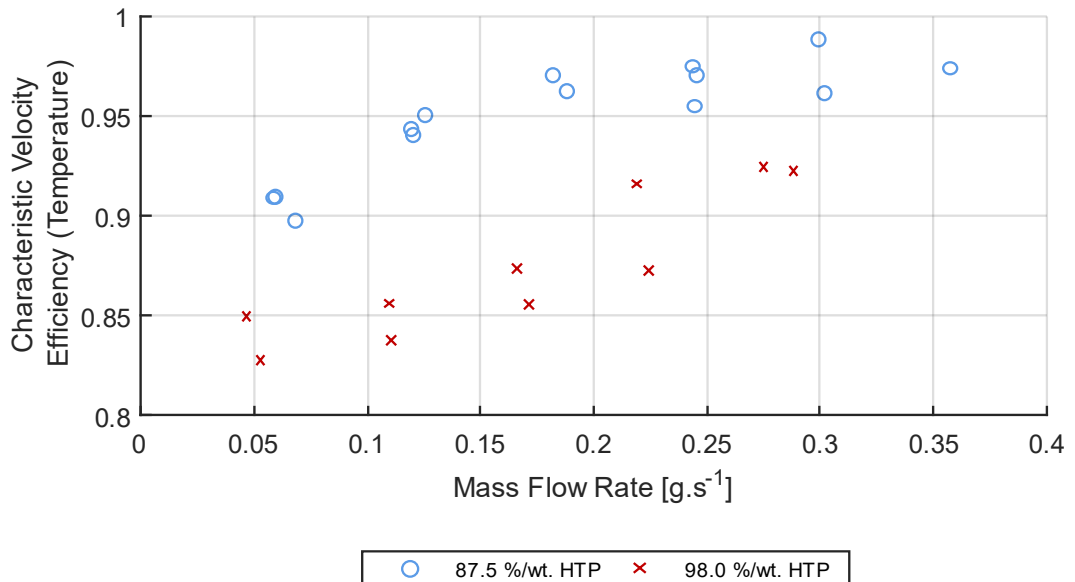


Figure 6.20 – Thermal characteristic velocity efficiencies of the baseline thruster with the two HTP propellant concentrations, plotted against propellant mass flow rate.

The roughness and quasi-steady effects have been tied to the reaction kinetics and the expansion of the decomposed species from the catalytically active material in the bed. This should be affected by the decomposition rate of the propellant, so a difference in both the magnitude and frequency of the driving instabilities is expected. The absolute  $1\sigma$  steady state chamber pressure roughness is plotted for the two propellants in Figure 6.21, showing a slight increase in the absolute roughness for the higher enthalpy propellant. However, there is no difference in the spectral response: the first significant peak centre frequencies are strongly correlated between the two propellant variants. The higher enthalpy of 98.0 %/wt. HTP was expected to result in shorter period oscillations in the bed given the proposed cyclical diffusion process. However, since the magnitude of roughness increases, this suggests that the expansion is more violent but takes approximately the same time.

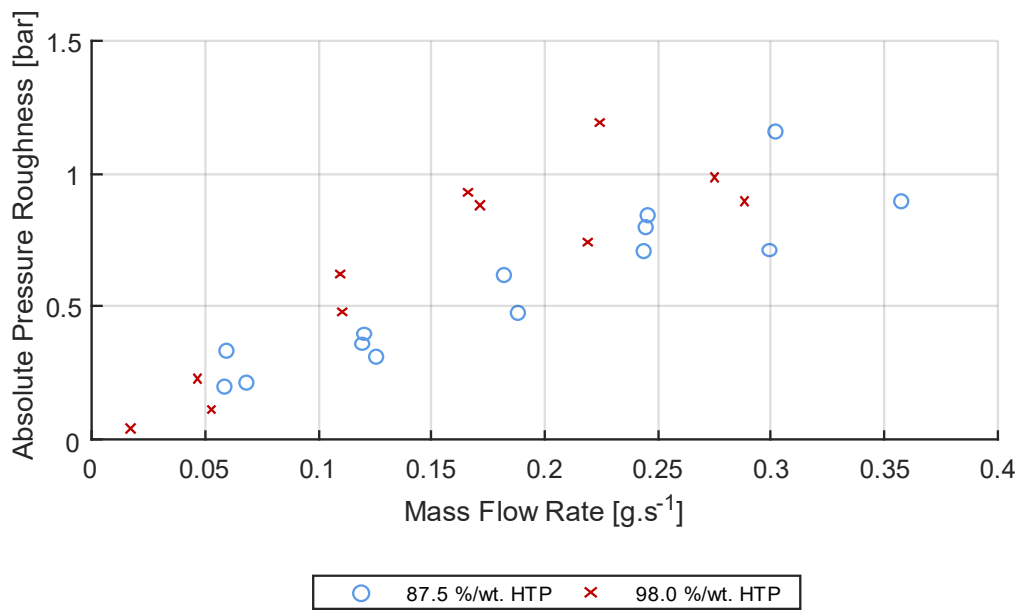


Figure 6.21 – Steady state chamber pressure roughness of the baseline thruster with the two HTP propellant concentrations, plotted against propellant mass flow rate.

## 6.5. Summary of the Catalyst Bed Study

This chapter presented a study into HTP monopropellant microthruster catalyst beds, tackling three topics: the influence of the catalyst bed geometry, the effect of varying the catalyst material, and the impact of different propellant enthalpies. The main goals were to identify an optimum for this thruster design, providing additional insight into the underlying bed processes, and further validating the simplified decomposition model. Broadly, these have all been achieved, although there are still several open questions.

The general performance of the catalyst beds is good, with relatively high thermal performance regardless of the geometry. In the majority of tests for the geometry study, the steady state chamber temperatures are greater than 400 °C, with a mean chamber temperature of the full data set of 549 °C  $\pm$  112 °C (1 $\sigma$ ). The corresponding mean catalytic thermal efficiency of these beds is 0.746  $\pm$  0.172 (1 $\sigma$ ). The characteristic velocity efficiencies of all beds are approaching 0.947  $\pm$  0.027 (1 $\sigma$ ), calculated using a regression fitted convergent exponential model. These performance values indicate that the baseline catalyst material, the 300  $\mu\text{m}$  spherical Platinum –  $\gamma$ -Alumina pellets, is high performance and well-suited to this scale of thruster.

As expected, changing the catalyst pellet geometry has a significant impact on the performance: beds using the larger non-uniform H1820 variant catalyst material, demonstrate a much more variable performance. The tested beds exhibit two modes of operation depending on the size of the catalyst material: nominal high performance with  $\eta_c^*$  approaching 0.918  $\pm$  0.040 (1 $\sigma$ ), and a low performance steady state flooding mode with a mean  $\eta_c^* = 0.723 \pm 0.068$  (1 $\sigma$ ). This is attributed to a propellant channelling effect through the relatively larger flow path in the variant catalyst beds, i.e. where the diffusion of the propellant to the catalytically active surface is not driven by the propellant flow. Despite this, when operating nominally, the larger H1820 catalyst material has comparably high thermal performance, and therefore has a similar specific reactivity.

Increasing the enthalpy of the propellant by switching from 87.5 %/wt. HTP to 98.0 %/wt. HTP also has the expected effect of increasing the absolute thermal performance. The mean chamber temperature for the higher enthalpy propellant is 672.1 °C  $\pm$  130.0 °C, with the maximum values approaching 800 °C. However, this higher temperature increases the thermal losses under atmospheric test conditions, so performance efficiency values are lower: 0.643  $\pm$  0.146 and 0.856  $\pm$  0.067 for the catalytic thermal and characteristic velocity efficiencies respectively. For reference the respective baseline thruster performance values with 87.5 %/wt. HTP are 0.859  $\pm$  0.077 and 0.950  $\pm$  0.028.

The large number of different parametric bed geometries show a wide range in performance. The maximum equilibrium thermal performance, derived from the regression fitting to the thermal characteristic velocity efficiency suggests that an optimal bed geometry will have a low catalyst bed loading and aspect ratio, i.e. a short and wide catalyst bed. This was not demonstrated in the data due to sealing issues with the 6.6 mm diameter catalyst beds. This is tied to the propellant decomposition process: Using a superficial residence time, flooding occurs for  $t_{\text{bed}} \leq 0.341 \text{ s} \pm 0.047 \text{ s}$  (1 $\sigma$ ). By taking some assumptions about the catalyst microstructure and reactivity, a similar analysis using the Damköhler number suggests that the flooding onset occurs when  $Da \leq 56$ , i.e. as the liquid phase catalytic decomposition rate approaches the diffusion rate.

This result must be taken with a caveat since there are significant uncertainties in the parameters used to derive the specific decomposition rate. There was also insufficient data from either the variant catalyst or propellant studies to confirm this: For the variant catalyst material, the channelling effect means that the diffusion rate is not equivalent to the mass flow rate, while for the 98.0 %/wt. HTP, the overall reactivity is expected to be higher due to the increased temperature and therefore thermolytic decomposition.

The catalytic reactivity was previously described in Chapter 5 using the simplified pseudo-physical front model of the decomposition process. The results presented here further validate that the complete decomposition occurs just after the phase change: there is no clear distinction between the maximum performance and the flooding onset. This confirms that the optimum bed design will be sized by the flooding condition, and will seek to locate the phase change front close to the end of the bed to minimise catalyst underutilisation. This may increase the sensitivity of the bed to flooding due to turbulence although this was not observed. Analysis of the quasi-steady effects also provided further evidence for the oscillatory local diffusion process as the source for the roughness in the bed.

To summarise the proposed optimum catalyst bed design, the volume of the bed is tied to the catalytic reactivity. For a known propellant-catalyst pair, this may be determined from a single bed capturing the flooding condition or could be derived from the specific reactivity of the catalyst. Further research investigating the Damköhler number analysis is warranted to confirm the conclusions. With a defined size of the catalyst bed the shape should be chosen to minimise the catalyst bed loading and aspect ratio. This will improve the thermal performance over the range of flow rates.

Despite the open questions and suggested future research topics, this study presents the testing of a significant range of microscale catalyst bed geometries. At the time of writing this is unique for monopropellant microthrusters and broader than many of the similar studies for larger thrusters. Validation of the simplified decomposition model and its applicability to the optimisation problem is also significant as this is an important step to move away from iterative experimental design. This work suggests that it is possible to use more fundamental chemistry and decomposition theory to create high performance monopropellant propulsion systems.

# Chapter 7

## Micro-Injector Study

### 7.1. Introduction and Scope

#### 7.1.1. Aims and Scope

This chapter is a study into the design and performance of different microinjectors. Up to this point all testing has used the baseline Poiseuille-type injector, a 50 mm long, 254  $\mu\text{m}$  inner diameter microbore tube. This was initially chosen given the ease of implementation and its apparent robustness, demonstrated in Chapters 4, 5, and 6. Preliminary testing showed predictable performance based on the Hagen-Poiseuille equation and experimental flow characterisation. This is important since low frequency roughness ( $10 \text{ Hz} \leq Fq \leq 400 \text{ Hz}$ ) is expected to couple with the propellant flow into the bed, resulting in oscillatory unsteady operation known as 'chugging'. This effect results in pulsed operation and degraded performance of the thruster. The baseline injector, used for all testing up to this point, demonstrated no apparent 'chugging' despite measurable coupling of roughness across the injector. Poiseuille injectors operate through viscous forces acting along their length, but there is little discussion on their governing processes in literature. The other common monopropellant injector architecture, Venturi-type injectors, operate through the principle of the cavitating Venturi effect, but are also not widely documented for microscale propulsion systems. Investigating the operational principles and assessing the suitability of these architectures for sub-newton monopropellant thrusters is important for the wider field.

This chapter presents a study into the design, manufacture, and experimental performance of the two architectures, Poiseuille-type and Venturi-type. Typically, injector design is driven by 'rule-of-thumb' metrics such as the fractional pressure drop (see Chapter 2). As a result, significant experimental testing is required to optimise an injector. Therefore, the primary goals of this study are to investigate key parameters that impact the injector performance, and to identify the conditions at which the 'chugging' phenomenon occurs. This is a particular challenge for microinjectors given that their size precludes direct instrumentation or observation. This study will also include some computational fluid simulations to provide insight into the underlying microfluidics, supplementing the experimental testing. Another supplementary goal is to assess the novel frequency analysis techniques used in previous Chapters and their use in characterising microinjector performance.

### 7.1.2. *Study Methodology*

The study is split into three main sections:

- Injector design and manufacture, including post-manufacture inspection and the specific integration of the injectors into the test setup.
- Cold flow testing, encompassing all analysis and testing of the injectors without a catalyst bed.
- Hot firing testing, demonstrating the performance of selected injectors with a catalyst bed, in this case using the standard baseline thruster variant introduced in Chapters 4 and 5.

The experimental testing will broadly use the same techniques as described in previous chapters: flow characterisation, roughness attenuation, DFT coupling and start-up transients. However, the cold flow testing will also include steady state computational simulations to provide insight into the flow field during nominal operation. A full discussion on the model methodology and implementation is described in Appendix B.

## 7.2. Injector Design and Manufacture

An introduction to the analytical theory and some of the challenges of injectors was presented in Chapter 2. The baseline Poiseuille injector was described in Chapter 4, however the specific design and manufacturing of Venturi-type injectors has not been discussed in detail. The goal of this work is to investigate the effect of different injector architectures and designs on the performance. This section covers the analytical design, manufacture, and inspection of sets of both injector architectures for testing.

The operation of Poiseuille-type and Venturi-type injectors are analytically described using the modified Hagen-Poiseuille Equation (2.17) and a simplified derivation of Bernoulli's Law (Equation (2.16)). For reference, these are:

$$dP_{pos} = \dot{m} \frac{L_{pos}}{C_d A_{pos}^2} \frac{8\pi\mu}{\rho} = \dot{m} \frac{1}{C_d \zeta_{pos}} \frac{8\pi\mu}{\rho} \quad (7.1)$$

$$dP_{orf} = \dot{m}^2 \frac{1}{C_d^2 A_{orf}^2} \frac{1}{2\rho} = \dot{m}^2 \frac{1}{C_d^2 \zeta_{orf}^2} \frac{1}{2\rho} \quad (7.2)$$

The geometries of the two architectures are defined in terms of a geometric parameter  $\zeta$ , which captures the key injector geometry. These are the cross-sectional area  $A_{pos}$  and length  $L_{pos}$  for the Poiseuille-type, and the throat area  $A_{orf}$  for the Venturi-type, such that  $\zeta_{pos} = A_{pos}^2/L_{pos}$  and  $\zeta_{orf} = A_{orf}$ .

### 7.2.1. Poiseuille Injectors

The Poiseuille injectors used in this work were procured from commercially available cold-rolled SS 304 microbore tube stock, detailed in Chapter 4. These tubes are typically used as COTS components in gas chromatography and are widely available in a range of inner diameters and lengths. An injector can be sized for a target fractional pressure drop  $dP/P_c$  by selecting the diameter and length of a tube using Equation (7.1). The standard range of COTS available microbore tube diameters are 127  $\mu\text{m}$ , 178  $\mu\text{m}$ , 254  $\mu\text{m}$ , 508  $\mu\text{m}$ , and 762  $\mu\text{m}$ . Table 7.1 lists the expected pressure drops over the nominal operational propellant mass flow rate range. These are calculated for a length of 100 mm to give an indication of the expected pressure drops from these different geometries. The fractional pressure drops of Poiseuille injectors are constant over the pressure range since  $dP_{pos} \propto \dot{m}$ . For the smaller cross-sectional microbore tubes, the pressure drops are a large fraction of the chamber pressure ( $> 0.2 / P_c$ ), reducing the performance of a thruster. In the case of the larger tube, the pressure drop is expected to be negligible. A subset of these diameters was selected for testing based on the range of fractional pressure drops over the 5 bar to 25 bar pressure range. Note that as discussed in Chapter 2, the Hagen-Poiseuille equation assumes laminar flow. This is expected for most microbore tubes, although smaller diameter injectors will have a higher Reynolds number for a given mass flow rate and may be turbulent. This was tested using cold flow characterisation.

Table 7.1 – Ideal Poiseuille absolute and fractional pressure drops for 87.5 %/wt. HTP, considering the standard diameters of available microbore tubing, with a length of 100 mm.

Injector Cross-sectional Geometry		Absolute Injector Pressure Drop [bar], (Mass Flow Rate [g.s <sup>-1</sup> ])			Fractional Injector Pressure Drop $/P_c$
Diameter [ $\mu\text{m}$ ]	Area, $\times 10^{-7}$ [m <sup>2</sup> ]	BoL, $P_{in} = 25$ bar	Design, $P_{in} = 8$ bar	EoL, $P_{in} = 5$ bar	
127	0.127	16.67 (0.119)	5.33 (0.038)	3.33 (0.024)	1.999
178	0.249	8.53 (0.234)	2.73 (0.075)	1.71 (0.047)	0.518
254	0.507	2.78 (0.316)	0.89 (0.101)	0.56 (0.063)	0.125
508	2.027	0.19 (0.353)	0.06 (0.113)	0.04 (0.071)	0.008
762	4.560	0.04 (0.355)	0.01 (0.114)	0.01 (0.071)	0.002

There are several practical limitations on the design that affect the possible selection of pressure drops. Firstly, these injectors are sealed into the system using compression fittings, which require a minimum length of 20 mm. Additionally, injectors longer than 200 mm are impractical to use in the PDS and are not representative of the size of flight-representative hardware. This limits the range of pressure drops for a given diameter, however the pressure drop is less sensitive to changes in the length than the cross-sectional diameter:  $\Delta P/\dot{m} \propto L_{pos}$  while  $\Delta P/\dot{m} \propto D_{pos}^4$ . Therefore, changing the inner diameter will have a much larger impact on the performance than the length. The limited number of standard COTS diameters mean that there are a number of gaps in possible pressure drops. For example, the fractional pressure drop of the shortest 254  $\mu\text{m}$  diameter injector ( $L_{pos} = 20$  mm) is 0.025  $/P_c$ . Matching this pressure drop with the next available injector diameter, 508  $\mu\text{m}$ , would require a 400 mm long tube.

Despite the discontinuities in the possible fractional pressure drops, a number of different Poiseuille injector designs were selected to cover a range of  $0.016 \leq dP/P_c \leq 1.999$ . This is larger than the range in fractional pressure drops for the baseline thruster ( $0.051 \leq dP/P_c \leq 0.137$ ), and the suggested design range from literature,  $0.05 /P_c$  to  $0.20 /P_c$ . This was intended to capture the ‘chugging’ phenomenon at low pressure drops and any non-linearities effects (e.g. turbulence) at high pressure drops. The selected injector designs are listed in Table 7.2. This includes the baseline injector design. Note that a number of identical articles of each specification were procured to test the manufacturing repeatability. The total number of Poiseuille injectors procured for testing is 45, including the replicated designs.

Table 7.2 – Selected Poiseuille injector designs, including the number procured, including their expected fractional pressure drop and highest (BoL) expected Reynolds numbers.

Injector ID	Injector Geometry			Expected Performance with HTP 87.5 %wt.	
	Diameter [μm]	Length [mm]	Cross-sectional Area, $\times 10^{-7}$ [m <sup>2</sup> ]	Fractional Pressure Drop	Worst case (BoL) Reynolds Number * (Mass Flow Rate [g.s <sup>-1</sup> ])
5-50	127	50	0.127	1.000	1446 (0.178)
5-100	127	100	0.127	1.999	964 (0.119)
7-20	178	20	0.249	0.104	1869 (0.322)
7-50	178	50	0.249	0.259	1638 (0.282)
7-100	178	100	0.249	0.518	1359 (0.234)
7-200	178	200	0.249	1.036	1013 (0.175)
10-20	254	20	0.507	0.025	1410 (0.347)
10-50	254	50	0.507	0.062	1360 (0.335)
10-100	254	100	0.507	0.125	1285 (0.316)
10-200	254	200	0.507	0.25	1156 (0.284)
20-200	508	200	2.027	0.016	712 (0.350)

\*  $Re$  numbers are calculated using the mass flow rate from the BoL condition from the lifetime model in Chapter 4, assuming ideal injector flow ( $C_{d,inj} = 1$  in Equation (7.1)).

The validity of the characterisation model relies on laminar flow in the injector. Table 7.2 also lists the estimated worst case (highest) Reynolds number at BoL. In all cases  $Re < 1870$  and in most cases it is below the microchannel turbulent transition range,  $1700 \geq Re \geq 2000$  [102], [103]. The injector flow is therefore expected to be laminar over most of the operational range but may enter the transition region at the highest mass flow rates. As discussed in Chapter 2, this transition range is experimentally determined using smooth glass microtubes. Surface roughness will lower the turbulent onset so quantifying the internal roughness of the cold-rolled microbore tubes is important. An x-ray CT scan of the end section of a nominally 254 μm diameter injector is shown in Figure 6.13. The voxel resolution is 4.398 μm.voxel<sup>-1</sup> and the scan includes a standard compression fitting ferrule to investigate any impact of the sealing. From inspection, the internal surface roughness is higher compared to the outer rolled finish. Note that the compression fitting front ferrule cut into the tube material, causing some deformation of the internal geometry.

Figure 7.2 shows the cross-sectional area, circularity and internal surface roughness of the inner profile of this section. The mean internal cross-sectional area is  $5.166 \times 10^4 \mu\text{m}^2 \pm 0.205 \times 10^4 \mu\text{m}^2 (1\sigma)$ , close to the  $5.067 \times 10^4 \mu\text{m}^2$  for a 254 μm diameter profile. For reference, the corresponding effective diameter is  $256.5 \mu\text{m} \pm 51.1 \mu\text{m} (1\sigma)$ . This suggests that there is good manufacturing repeatability, although this cannot be confirmed with the single CT scan. There is a

slight change in the internal cross-section due to the compression fitting, reaching a minimum area of  $3.267 \times 10^4 \text{ } \mu\text{m}^2$  or an effective diameter of  $204.0 \text{ } \mu\text{m}$ . This is not expected to have a significant impact on the overall pressure drop as the length of this region is small ( $< 1 \text{ mm}$ ). The sealing methods used on a flight-representative thruster, e.g. welding or brazing, should prevent this deformation. The cross-sectionalal profile is also slightly non-circular, with a consistent circularity of  $0.767 \pm 0.037$  ( $1\sigma$ ) along the length of the section. This should have minimal impact on the performance of the injector, but this may suggest that the cold-rolling process does not have fine control over the internal profile.

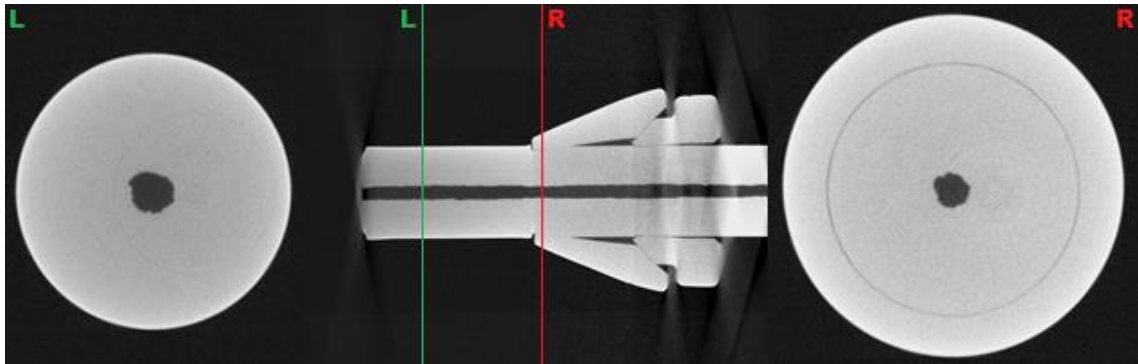


Figure 7.1 – CT micrograph of the end section of a  $254 \text{ } \mu\text{m}$  diameter Poiseuille injector. Sections showing the cross-sectional profile have been included.

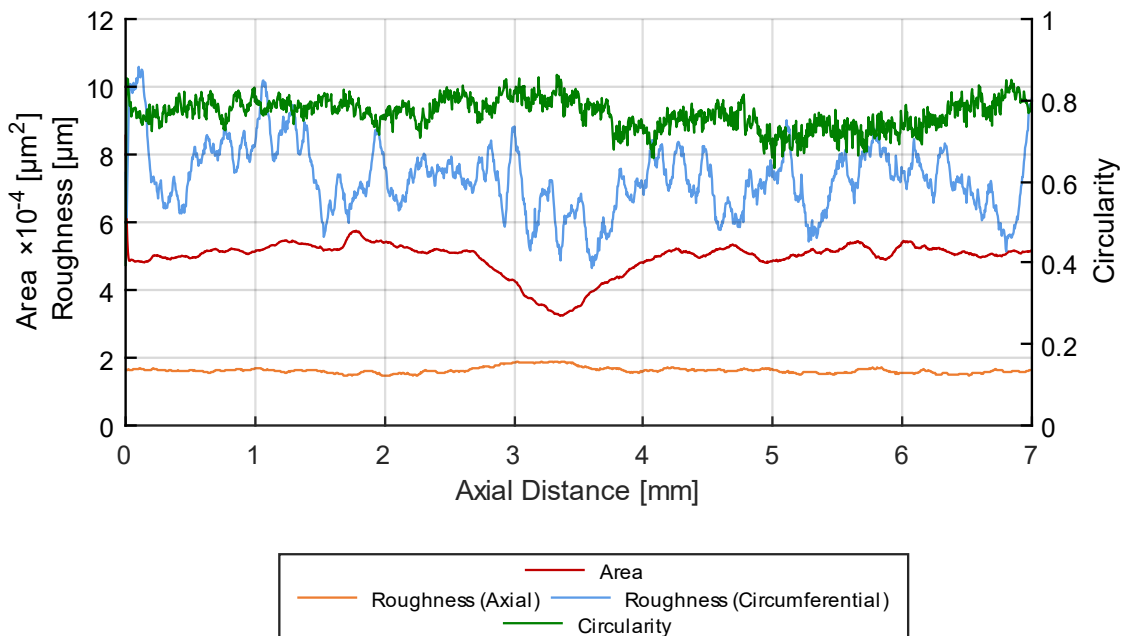


Figure 7.2 – Cross sectional area, circularity, and roughness (axial and circumferential) of the internal wetted surface, measured along the axial direction of the injector CT scan section from Figure 6.13.

Since the Poiseuille injector analytic model assumes laminar flow, surface roughness is important to consider. The roughness varies depending on the directionality, either axially or circumferentially, which is to be expected given that the manufacturing process will not affect the material isotropically. Figure 7.2 shows the variation of both axial and circumferential roughness along the length of the CT scan section. These are consistent along the length and are  $1.7 \mu\text{m} \pm 0.0 \mu\text{m}$  ( $1\sigma$ ) and  $7.3 \mu\text{m} \pm 1.1 \mu\text{m}$  ( $1\sigma$ ) respectively. These are lower than the voxel resolution as they are statistical measures. The direction of the fluid flow is axial, so the axial roughness is the important parameter for assessing the viscous effects and the circumferential roughness can be ignored. Given the standardised manufacturing process, the  $1\sigma$  axial surface roughness is expected to be similar for all of the injectors. The mean surface roughness of the microbore tubes from the literature studies on the turbulence onset were stated as  $1.71 \mu\text{m}$  [102], [103]. Since this is similar to the axial roughness of the SS 304 tubes in the current work, this confirms that the turbulent transition region should be equivalent, i.e.  $1700 \geq Re \geq 2000$  range.

### 7.2.2. Venturi Injectors

Venturi-type injectors operate by accelerating the liquid flow, reducing the local static pressure below the liquid vapour pressure, causing the liquid to boil. This results in quasi-steady cavitation, choking the flow. This is the mechanism that decouples the flow across a Venturi-type injector and was discussed in Chapter 2. Cavitating Venturis may be used as injectors or flow control devices in larger flow rate thrusters [11], [110], but the specific geometries are challenging to manufacture at the scales required for the range of mass flow rates for a sub-newton thruster. A simpler but functionally similar geometry is an orifice plate. These are components with one or more sharp-cornered orifices in a thin plate in the flow. The advantage of an orifice microinjector is that manufacturing orifices is considerably easier than accurately controlling the nozzle profile of a cavitating Venturi at the small scales. These are often used as injectors for small monopropellants [12], [90], [96] and will be considered exclusively in this study to simplify manufacturing.

The geometry of an orifice injector is sized by considering the pressure drop through the throat cross-sectional area, described analytically by Equation (7.2). The fractional pressure drop with respect to chamber decreases with the driving pressure since  $dP \propto \dot{m}^2$ , so the EoL operational condition corresponds with a minimum fractional pressure drop. As low fractional pressure drops can cause ‘chugging’, flow instabilities are more likely to occur towards EoL. The EoL condition is therefore typically used to size the injector. The variable fractional pressure drop also means that it will be higher than necessary at BoL, so optimisation is important to reduce the performance degradation from an overly conservative injector design. For an EoL pressure drop equivalent to the baseline Poiseuille injector ( $0.051 /P_c$  to  $0.137 /P_c$ ), an ideal Venturi-type orifice injector with a single port would have a throat diameter between  $102.7 \mu\text{m}$  to  $78.7 \mu\text{m}$ . These calculations assume ideal flow through the injector, i.e.  $C_d = 1$ , but a real injector will have non-isentropic losses that reduce the mass flow rate. Typical orifice plate discharge coefficients have  $0.61 \leq C_d \leq 0.90$  [11], so these example throats are undersized.

Orifice plates have been successfully machined using conventional drilling, although orifice diameters have generally only been demonstrated for 0.2 mm or larger [12]. Conventional machining of smaller orifices required here is not feasible within the scope of this study. Instead, two suitable techniques were identified: laser microdrilling and chemical etching. Unlike conventional drilling which results in a sharp-cornered, straight-walled orifices, these processes result in variable cross-section wall profiles as shown in the sketches in Figure 7.3. Laser microdrilling is a process where the material is thermally ablated with a rapidly pulsing laser. This creates a roughly conical orifice, although the taper angle can be low. Chemical etching uses a chemical photoresist to coat the metal surface except at the orifice location. The unprotected material is then etched using a chemical resulting in an orifice with profile shaped by the etching rate and hole depth. The etching technique presented here is double-sided wet etching, where both faces of the orifice plate are coated with a patterned photo resist before being submerged in the etchant. The result is that the orifice is created from both directions, resulting in the profile shape shown in Figure 7.3.

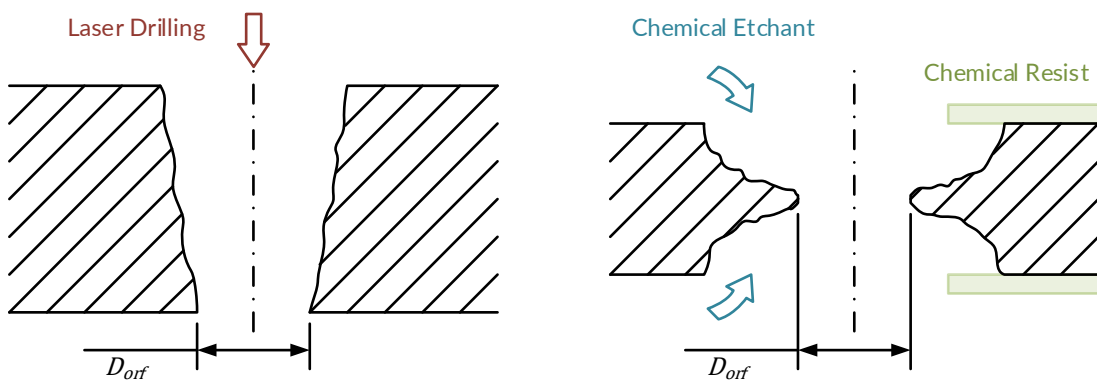


Figure 7.3 – Drawings of the expected orifice injector radial wall profiles, manufactured using laser microdrilling (left) and double-sided chemical etching (right).

A number of designs were selected for manufacture, with the parameters listed in Table 7.3. The designs include single and multi-port (showerhead) injectors to demonstrate the feasibility with both techniques. Laser microdrilling has a relatively high process cost compared to the chemical etching technique so only one injector was manufactured with this technique. From discussion with the supplier, the variability in the geometry was expected to be low and the technique is suited to high aspect ratio holes. A small orifice diameter multi-port design ( $6 \times 36 \mu\text{m}$ ) was therefore selected. Conversely the etching technique was expected to have a high variability for orifice sizes below 50  $\mu\text{m}$ . This makes the process more suitable for larger orifices with lower plate thicknesses. All injector designs in Table 7.3 have a plate thickness of 50  $\mu\text{m}$ .

Table 7.3 – Selected orifice plate injector design, including selected manufacturing process.

Injector ID	Orifice Diameter [ $\mu\text{m}$ ]	Orifice Number	Total Orifice Area, $\times 10^{-9} [\text{m}^2]$	Manufacturing Method
1-50-50	50	1	1.96	Etching
1-80-50	80	1	5.03	Etching
1-100-50	100	1	7.85	Etching
1-120-50	120	1	1.13	Etching
3-60-50	60	3	8.48	Etching
5-50-50	50	5	9.82	Etching
6-36-50	36	6	6.11	Laser Microdrilling

The expected absolute and fractional pressure drops for the different orifice injectors are given in Table 7.4. Since decoupling of the flow over the injector and therefore the onset of ‘chugging’ is tied to the pressure drop, it should also be related to the Venturi cavitation effect. The local cavitation occurs when the local static pressure drops below the vapour pressure of the liquid propellant. The bulk pressure change through the injector is estimated using Bernoulli’s law, and is equivalent to the pressure drop across the injector, i.e. Equation (7.2). For pure DI water and hydrogen peroxide at 25 °C, the vapour pressures are  $31.69 \times 10^{-3}$  bar and  $6.67 \times 10^{-3}$  bar respectively [124]. For cold flow characterisation, the DI water vapour pressure will be used. Since HTP is a mixture of hydrogen peroxide and water, the propellant vapour pressure can be modelled using Raoult’s Law:

$$P_{vap,mix} = \sum P_{vap,i} = \sum \chi_i P_{vap,i}^0 \quad (7.3)$$

Where the vapour pressure of an ideal mixture is the sum of the partial vapour pressures  $P_{vap,i}$ , of the mixture component  $i$ , which is given by the product of the pure vapour pressure  $P_{vap,i}^0$  and its molar fraction  $\chi_i$ . This method assumes an ideal mixture with equally volatile components. For 87.5 %wt. HTP, the vapour pressure is estimated as  $7.32 \times 10^{-3}$  bar. There is an order of magnitude difference between the pure vapour pressures of water and hydrogen peroxide, and HTP has a low concentration of non-volatile stabilisers. This value is therefore not exact, but it is a closer estimate than either pure liquid chemical vapour pressures.

The estimated pressure drops in Table 7.4 are all at least one order of magnitude higher than the vapour pressure. The equivalence condition where the bulk static pressure after the injector is equal to the vapour pressure may be calculated. However, the fractional pressure drop will always decrease with increasing mass flow rates, so equivalence will be when  $P_{in} \sim P_{vap} = 7.32 \times 10^{-3}$  bar. This condition will never be reached in the system so the bulk flow in the orifice will not cavitate. However, small local regions of the flow field in the injector throat will accelerate considerably more than the bulk flow. Cavitation initiates in these regions where local static pressure will reach the liquid vapour pressure and the resulting expansion of these bubbles as they flow downstream chokes the flow [99]. This means that the bulk fluid flow cannot be used to predict the cavitation effect, hence the injector pressure drop is only an approximate metric for predicting decoupling.

Table 7.4 – Ideal orifice plate absolute and fractional pressure drops for 87.5 %/wt. HTP, considering the selected injector designs

Injector ID	Injector Pressure Drops: Absolute [bar], Fractional $/P_c$ , (Mass Flow Rate $[\text{g.s}^{-1}]$ )		
	BoL ( $P_{in} = 25$ bar)	Design ( $P_{in} = 8$ bar)	EoL ( $P_{in} = 5$ bar)
1-50-50	15.88, 1.741 (0.130)	3.64, 0.833 (0.062)	1.87, 0.598 (0.045)
1-80-50	8.21, 0.489 (0.239)	1.31, 0.195 (0.095)	0.57, 0.129 (0.063)
1-100-50	4.85, 0.241 (0.287)	0.65, 0.088 (0.105)	0.27, 0.056 (0.067)
1-120-50	2.83, 0.128 (0.315)	0.34, 0.044 (0.109)	0.14, 0.028 (0.069)
3-60-50	4.36, 0.211 (0.294)	0.57, 0.076 (0.106)	0.23, 0.049 (0.068)
5-50-50	3.52, 0.164 (0.305)	0.44, 0.058 (0.108)	0.18, 0.037 (0.069)
6-36-50	6.65, 0.362 (0.261)	0.97, 0.139 (0.100)	0.41, 0.091 (0.065)

Three duplicates of each etched injector design were manufactured to check the repeatability of the processes. Only one laser drilled injector was manufactured. Each article was inspected using optical microscopy to measure the orifice geometry. Examples of these micrographs are shown in Figures 7.4 and 7.5 for the etched and laser microdrilled processes respectively. The numerical inspection results are listed in Table 7.5, showing that the spread of the area is low, although the circularity is more variable. This implies that the process is relatively repeatable, however none of the orifices created by either process have as-designed geometry. Most of the injector throats are over- or under-sized, and their cross-sectional profiles are non-circular. It is suggested that both manufacturing techniques could be controlled to create the intended geometry, although this would require further refinement of the processes.

The micrographs also show the wall profiles resulting from the manufacturing processes. While not apparent in the EPI micrograph, the discoloured annulus around the central orifice on the etched injector in Figure 7.4 has a variable profile matching the expected surface geometry in the sketch in Figure 7.3. This is not axisymmetric about the orifice, which is a result of misalignment between the photoresist layers on the two sides, which is the likely cause for the variability in the inspected circularities. The expected tapering of the laser microdrilled orifices is not visible in the micrograph, but the micrograph shows some sputtering on both surfaces of the injector from the laser ablation process. Some of the orifices are partially covered and it was not clear how this may affect the flow through the injector.

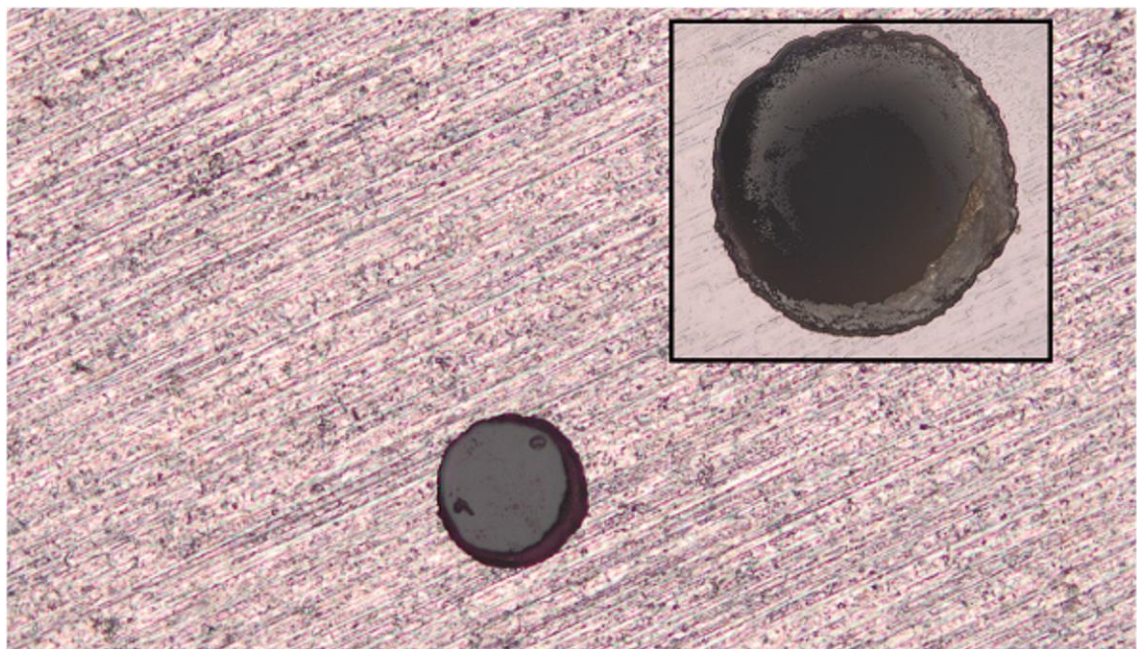


Figure 7.4 – A composite EFI reflection micrograph of a 1-120-50 etched orifice injector, showing the plate surface and the orifice. A higher resolution overlay is included. There is no appreciable difference on the reverse side, as expected due to the double-sided technique.

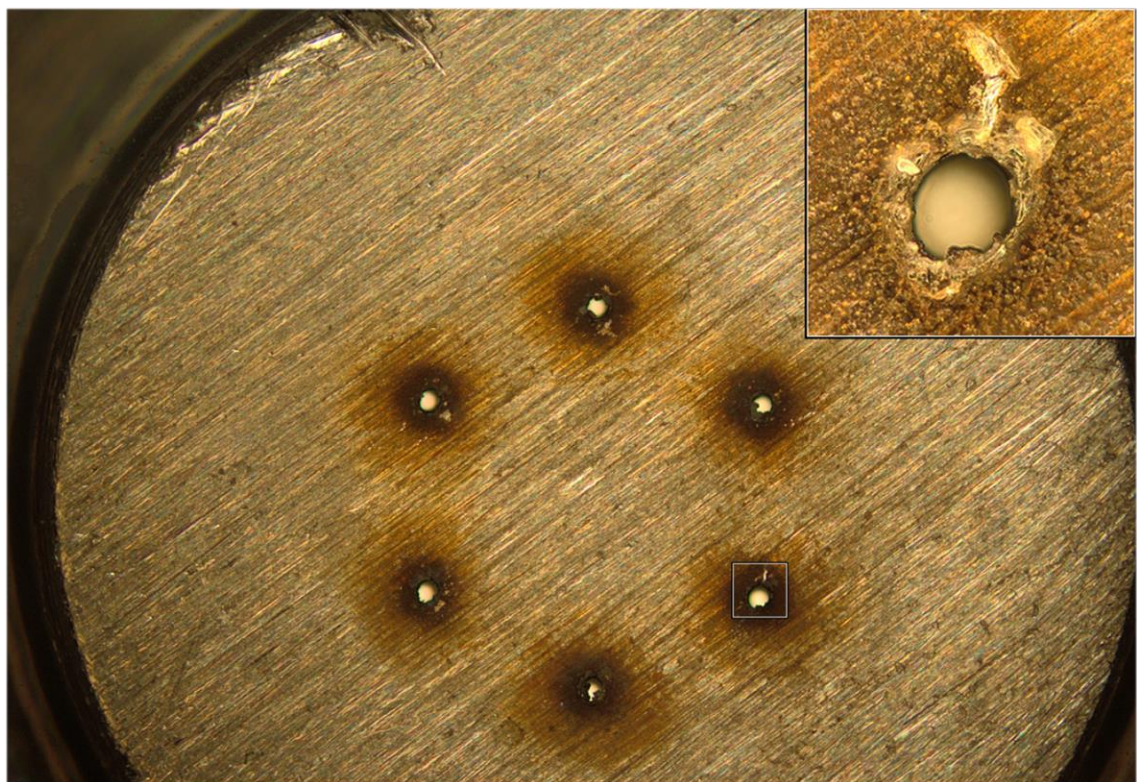


Figure 7.5 – A composite EFI reflection micrograph of the 6-36-50 etched orifice injector, showing the plate surface and the orifices. A higher resolution overlay shows the detail of a single orifice. This is imaged from the 'upper' surface with respect to the laser.

Table 7.5 – A list of the manufactured orifice plate injectors, by design, including the orifice geometry measured using optical inspection.

Injector ID	Designed Geometry		Inspected Geometry		
	Total Orifice Area, $\times 10^{-9}$ [m <sup>2</sup> ]	Mean Orifice Diameter [μm]	Total Orifice Area, $\times 10^{-9}$ [m <sup>2</sup> ]	Mean Orifice Diameter * [μm]	Orifice Circularity
1-50-50	1.96	50	$0.82 \pm 0.22$	$32.3 \pm 4.0$	$0.695 \pm 0.212$
1-80-50	5.03	80	$1.90 \pm 0.50$	$49.2 \pm 6.4$	$0.626 \pm 0.172$
1-100-50	7.85	100	$8.04 \pm 0.90$	$101.2 \pm 5.9$	$0.876 \pm 0.025$
1-120-50	11.3	120	$9.16 \pm 0.31$	$108.0 \pm 1.8$	$0.660 \pm 0.105$
3-60-50	8.48	60 (x3)	$7.04 \pm 0.22$	$54.7 \pm 6.5$	$0.873 \pm 0.017$
5-50-50	9.82	50 (x5)	$14.82 \pm 0.03$	$61.4 \pm 0.8$	$0.776 \pm 0.023$
6-36-50	6.11	36 (x6)	$3.15 \pm 0.10$	$25.9 \pm 11.2$	$0.699 \pm 0.188$

\* Diameter from inspection assumes perfectly circular orifices.

### 7.2.3. Thruster Integration

A wide range of injector designs and geometries were manufactured or procured. The injectors were mounted upstream of the thruster, attached to the injector head using standard compression fittings. An illustration of the injector-thruster integration for both injector architectures is shown in Figure 5.1. Like the baseline injector, all Poiseuille-type injectors are directly integrated with the fluid system using compression fittings. However, Venturi-type injectors require ancillary components: An injector is sealed between two bolted flanges using Viton o-rings. Permitting any injector port geometry, so long as the wetted surfaces are within the inner diameter of the o-rings. The Venturi injector stack components are manufactured using AM SLM. The ends of the stack are connected to the rest of the fluid system using standard compression fittings.

There are several other benefits of this implementation: Firstly, it keeps the fluid conditions over the injector consistent, regardless of the specific design: The physical separation between the catalyst bed and the injector means that the injectors had comparable thermal conditions, which is important for direct comparison of the results since the temperature affects the fluid physiochemical parameters. Separating the injector and catalyst bed also permits easy cold flow characterisation without additional components. The thermal isolation also improves the stability of the seal materials. The propellant preheating at the thruster sealing flange damaged all tested sealing materials, including the Viton o-rings and polyaramid-glass fibre gaskets. This degradation caused small fragments to break off and entrain in the flow, which frequently blocked the microscale geometries of Venturi-type injectors during testing. This issue also highlights the important issue that small injector geometries are prone to blockage, which may limit their usability in monopropellant microthrusters.

There are some drawbacks with this method. There is a fluid ullage volume between the injector and catalyst bed which will affect the flow field of the propellant entering the bed. This also prevents the assessment of multi-port injectors for propellant distribution. A flight-representative model system is likely to have the injector directly integrated with the body of the thruster to minimise the ullage volume for a faster start-up transient, and to reduce the size and thermal mass of the engine. Here, the high temperatures near the injector resulting from the close proximity to the catalyst bed will affect the flow. In extreme cases there may be decomposition in the injector. An integrated injector will therefore require additional testing beyond the scope of this study to validate the conclusions presented here. Despite this, testing injectors in isolation and under controlled conditions provides the best insight into the fundamental processes, which is important given that there is limited published research into the principles of microinjector operation.

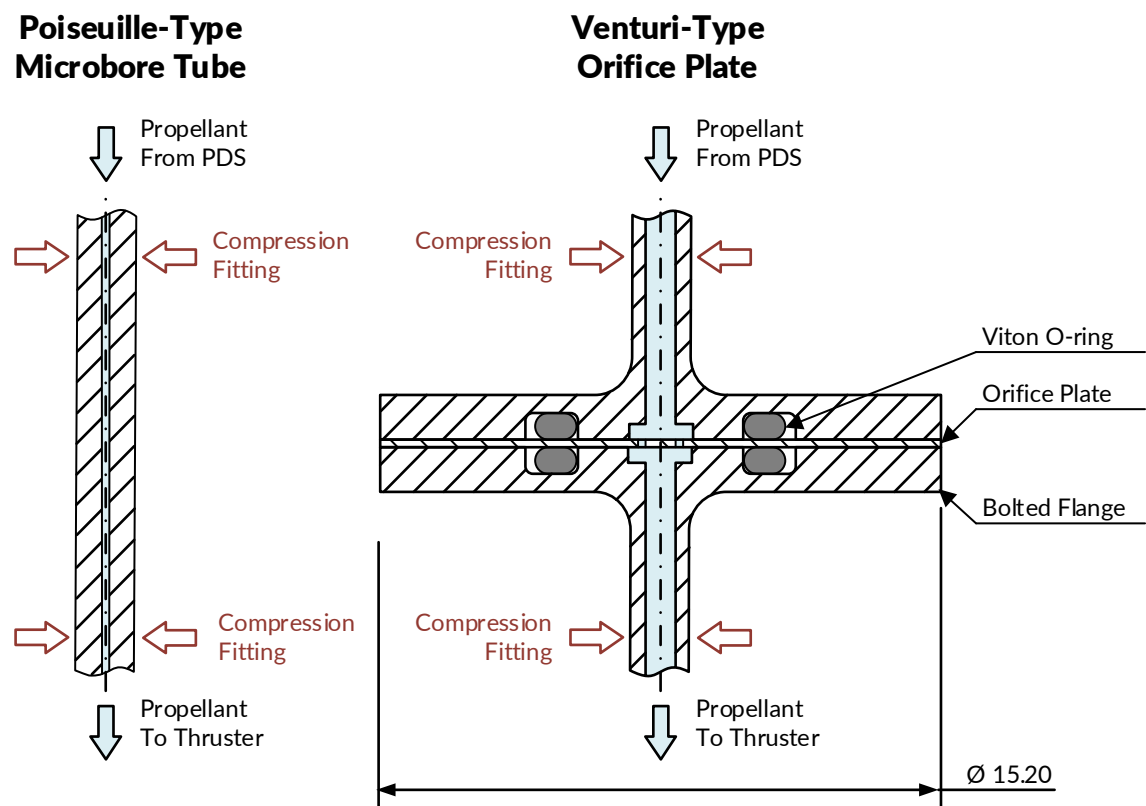


Figure 7.6 – A drawing illustrating the two methods for integrating both the Poiseuille (left) and Venturi (right) injector architectures into the system.

## 7.3. Cold Flow Characterisation

### 7.3.1. Scope and Test Campaign

Cold flow characterisation of the manufactured injectors is necessary to validate the analytical models of the steady state operation, from Equations (7.1) and (7.2). This flow characterisation is the same process demonstrated in Chapter 4, to measure the effective geometric parameter for the baseline injector. DI water is used as the working fluid, and the variation of upstream fluid pressure and mass flow rate are measured over a range of conditions. The nominal range of mass flow rates is  $0.05 \text{ g.s}^{-1} \leq \dot{m} \leq 0.3 \text{ g.s}^{-1}$ , set by choosing appropriate driving pressure in the PDS and venting the downstream of the injector directly to ambient conditions. As before, the pressure drop over the injector is  $dP = |P_{in} - P_{amb}|$ . The injector characterisation is calculated by regression fitting the pressure drop and discharge coefficient to the appropriate trend ( $\Delta P_{orf} \propto \dot{m}^2$  and  $\Delta P_{pos} \propto \dot{m}$ ), and the respective discharge coefficients are derived from the optically inspected and specified design geometry for the two architectures. Note that the geometry of some of the injectors imposes a limit on the full range. Highly resistive injectors require driving pressures above the 30 bar maximum for the higher mass flow rates, while low pressure drop injectors are limited by the instrumentation resolution given the low range of driving pressures.

This experimental characterisation is supported by computational analyses of flow through idealised injectors. The goals of the computational modelling are to replicate the experimental flow characterisation and to provide high resolution flow field data of both injectors. The model uses simplified axisymmetric geometry and assumes single-phase laminar flow, since turbulent flow was not expected. Any turbulence would be captured by discrepancies between the two datasets. An example of the ideal injector geometry is given in Figure 7.7, and is equivalent for both the orifice and Poiseuille injectors: the fluid region is defined by the injector diameter and length (50  $\mu\text{m}$  for the orifice injectors). A full description of the model and further details of the methodology are included in Appendix B.

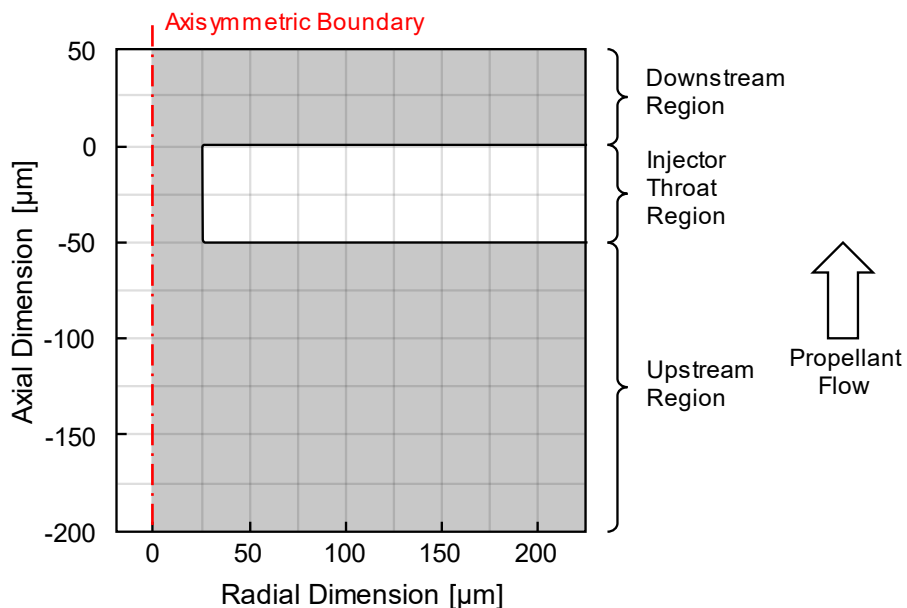


Figure 7.7 – An example of the ideal computational model geometry of the 1-50-50 orifice injector, with the main regions and propellant flow indicated. The grey area is the fluid domain.

### 7.3.2. Poiseuille Injector Cold Flow Characterisation

The full set of injectors was characterised, including several retests after hot firing to check for any performance degradation. In all cases the characterisation curves followed the expected linear analytic model ( $dP_{inj} \propto \dot{m}$ ), with repeatable performance between tests. Figure 7.8 shows two example experimental characterisation curves for two different injectors: 7-50 and 10-100 variants. In both examples the data is well correlated to the linear trend: the respective effective geometric parameters  $C_d \zeta$ , and discharge coefficients of these two examples are given in Table 7.6. This linearity is present in the rest of the characterisation data for the other Poiseuille injectors. The experimental results are lower than ideal flow based on the design geometry and assuming  $C_d = 1$ , suggesting that there are either additional losses or some other issue with the injector geometry that isn't accounted for by the laminar Hagen-Poiseuille equation.

The computational results for these two example injectors are plotted in Figure 7.8. These also demonstrate the expected linear  $dP \propto \dot{m}$  trend. The discharge coefficients are below unity, confirming that even idealised laminar flow rate is below the predicted analytical value. It is suggested that this is due to the flow around the sharp corners at the entrance and exit of the microbore tube: Since the fluid must accelerate around the corners, there are non-axial velocity components to the flow which are expected to reduce the discharge rate. The non-axial flow velocities in these regions should be proportional to the bulk fluid velocity, so the effect should be more pronounced for higher pressure differentials. This agrees with the divergence of the analytical and computational characterisation curves, since the Hagen-Poiseuille model assumes a constant profile of the cylindrical channel and therefore does not capture non-axial flow components.

Figure 7.8 also includes the microtube turbulent transition region,  $1700 \geq Re \geq 1900$ . This confirms that the flow was highly likely to be laminar over most of the tested range. However, in the 7-50 injector example, the conditions at the higher flow rates are above this transition point, and the characterisation data show some non-linearities. This provides some validation that the flow may transition in the expected range, and that turbulence reduces the discharge rate. Poiseuille-type injectors should therefore be designed with a maximum  $Re < 1700$ , although the surface roughness will also need to be assessed.

Table 7.6 – A comparison of the different characterisation method results for the 7-50 and 10-100 Poiseuille injectors, including the resulting coefficients of discharge and model goodness of fit.

Injector	Ideal Geometric Parameter, $\times 10^{-15} [\text{m}^3]$	Experimental			Computational		
		Geometric Parameter, $\times 10^{-15} [\text{m}^3]$	Discharge Coefficient	$R^2$	Geometric Parameter, $\times 10^{-15} [\text{m}^3]$	Discharge Coefficient	$R^2$
7-50	12.33	$7.08 \pm 0.02$	$0.574 \pm 0.001$	0.98	$10.70 \pm 0.21$	$0.868 \pm 0.017$	1.00
10-100	25.68	$20.72 \pm 0.07$	$0.807 \pm 0.003$	0.99	$22.32 \pm 0.48$	$0.869 \pm 0.018$	1.00

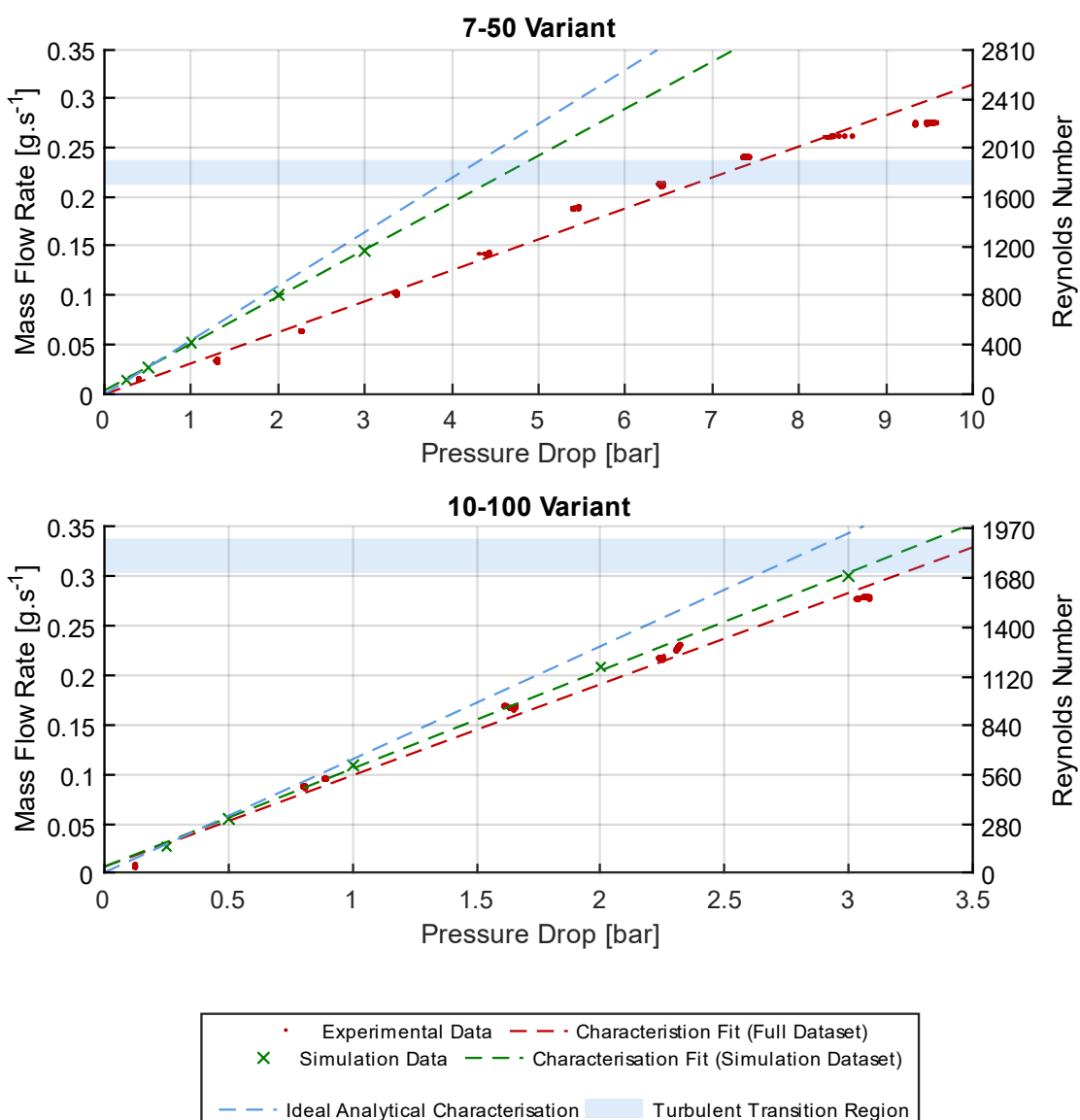


Figure 7.8 – Example Poiseuille cold flow characterisations for 7-50 and 10-100 variants. The mass flow rate recast as the Reynolds number is shown, along with the turbulent transition region ( $1700 \geq Re \geq 1900$ ) highlighted.

Figure 7.9 shows the full set of experimental and computational Poiseuille injector discharge coefficients plotted against the geometric parameter. While the computational results are similar, there is a large spread in the experimental results. There are data in the full range between 0 and 1, however there are several tests with discharge coefficients greater than unity. Despite the apparent control and repeatability in the manufacturing process from the CT data presented in Figures 7.1 and 7.2, this indicates that there is likely wide variation in the geometry between different injectors. There is also variability between different injectors with the same design, i.e. matching geometric parameters. Although not plotted, the variance has no dependence on either the specified area or length.

Since the Poiseuille injector CT scan data shows low axial roughness, and the as-manufactured injector lengths are similar to their specification, it is suggested that the variability is due to differences in the cross-sectional areas. Additional x-ray inspection of other microbore tubes was not possible to confirm this, although the significant variation is likely an issue with the manufacturing processes. This precludes selecting a specific pressure drop by injector design. However, the effective geometric parameter  $C_d\zeta_{pos}$  still repeatably describes the flow through an injector over multiple cold flow characterisations, including after hot fire testing with HTP. Therefore, Poiseuille injectors can be selected based on experimental characterisation. It is also worth highlighting that the manufacturing techniques may be improved to reduce the variability.

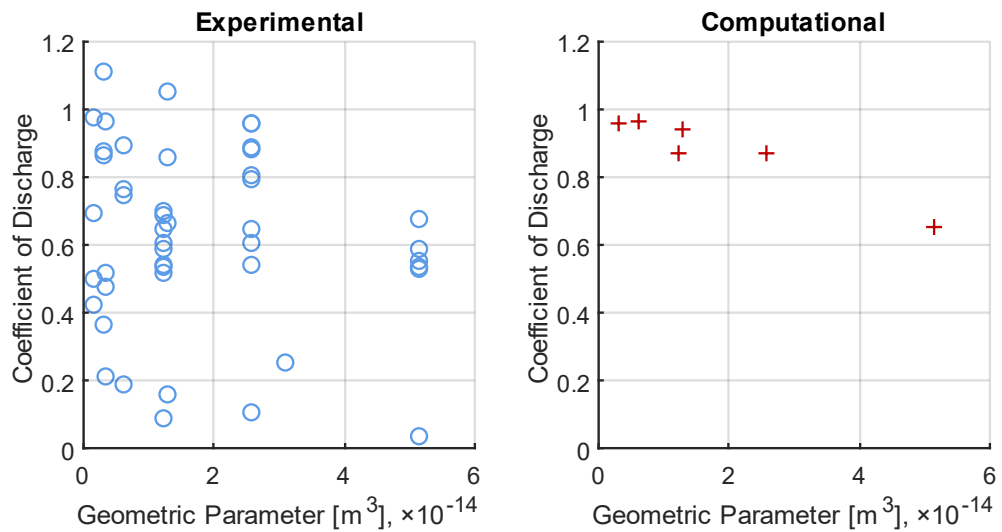


Figure 7.9 – Variation of the experimental (left) and computational (right) coefficients of discharge with respect to the Poiseuille injector geometric parameter,  $\zeta_{pos}$ .

### 7.3.3. Orifice Injector Cold Flow Characterisation

An example of the flow characterisation a 1-80-50 injector with a  $56.5\text{ }\mu\text{m}$  diameter is shown in Figure 7.10. Note that the characterisation procedure is identical to the Poiseuille injector, except that since  $dP_{orf}^{1/2} \propto \dot{m}$ , the linear characterisation fit takes the square root of the pressure drop. As expected, the linear characterisation curve is highly correlated with the data and passes close to the origin, matching the expected analytic model from Equation (7.2). However, the effective geometric parameter  $C_d\zeta_{orf} = 7.035 \times 10^{-9}\text{ m}^2 \pm 0.004 \times 10^{-9}\text{ m}^2 (1\sigma)$ , is much higher than the expected  $2.808 \times 10^{-9}\text{ m}^2$  from inspection assuming the measured  $56.5\text{ }\mu\text{m}$  orifice effective diameter. This corresponds to a discharge coefficient of 2.81, above unity. This expected characterisation curve is also plotted in Figure 7.10.

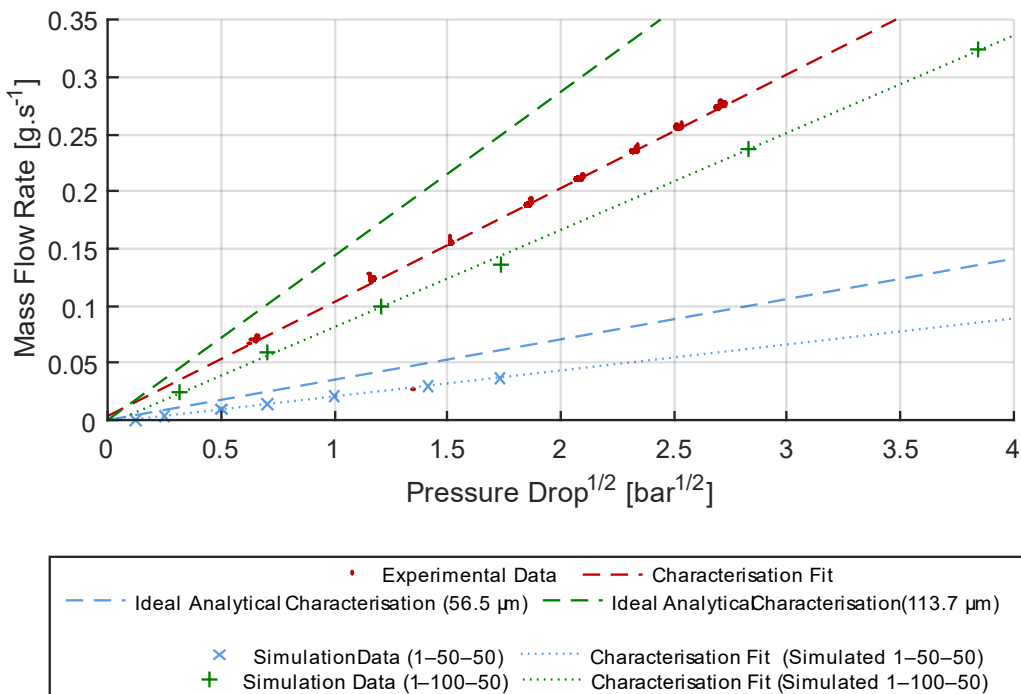


Figure 7.10 – Example Venturi-type 1-80-50 orifice injector characterisation showing the time-series data (top) and the characterisation curve (bottom).

Figure 7.11 shows optical micrographs of the injector, pre and post flow characterisation. These images clearly indicate a change in the throat area: the effective diameter has nearly doubled from  $56.5\text{ }\mu\text{m}$  to  $113.7\text{ }\mu\text{m}$ . Recalculating the coefficient of discharge for this new throat area results in  $C_d = 0.693$ , and the flow characterisation curve is also plotted in Figure 7.10. This updated value is much more reasonable, and corresponds to the lower end of the typical  $0.61 \leq C_d \leq 0.90$  range for orifice plates [11]. The change in area is due to damage to the thin material of the orifice plate resulting from the pressure differential. This is likely a result of the annulus of thin material around the throat, left by the double-sided etching process illustrated in Figure 7.3. This is a significant issue for the orifice injectors in the current work, although further improvements to the manufacturing process may be possible. Unfortunately, this effect was not noticed until considerably later, and it was not possible to reinspect all of the injectors to determine their post-testing orifice areas.

However, the full set of experimental discharge coefficients is plotted in Figure 7.12. All injectors show an increased discharge coefficient, indicating that they have been damaged, although the larger orifices were typically less affected given the lower coefficient values. Despite the damage to the experimental injectors, their effective geometric parameter  $C_d\zeta_{orf}$  still captures the propellant flow.

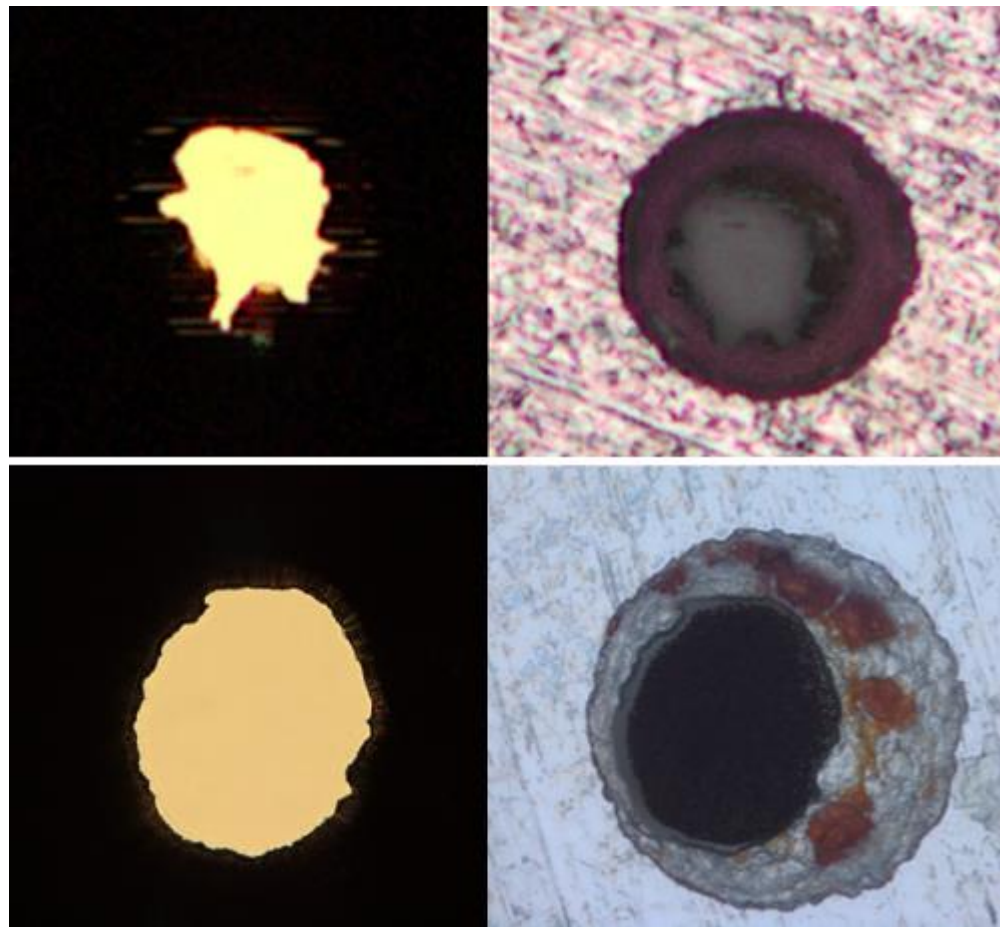


Figure 7.11 – Optical micrographs (transmission and reflection) of an orifice injector pre and post cold flow characterisation showing the change in orifice throat geometry during testing.

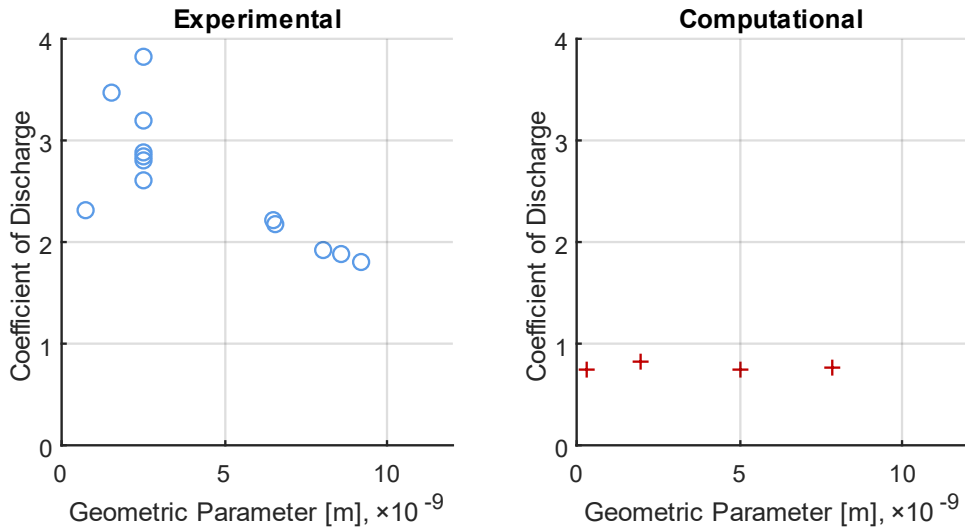


Figure 7.12 – Variation of the experimental and computational coefficients of discharge with respect to the Venturi-type orifice injector geometric parameter,  $\zeta_{\text{orifice}}$ .

The computational flow characterisation data for the 1-50-50 and 1-100-50 orifice injectors are also plotted in Figure 7.10. These simulated injectors were selected since they have similar throat areas to the ideal analytic characterisations based on the pre- and post-testing geometry of the example 1-80-50 injector. The effective geometric parameters from the characterisation are similar to the experimental data which suggests that the analytical, experimental and simulated characterisations are equivalent. There are some differences between the simulation and experimental data since the sizes are not identical.

The full set including simulated discharge coefficients is plotted in Figure 7.12. These include the 1-50-50 and the 1-100-50, as well as additional 1-80-50 and 1-120-50 injectors. These all show the same high degree of linearity and the simulated discharge coefficients appear relatively insensitive to varying the geometry:  $0.77 \pm 0.03$  ( $1\sigma$ ), within the expected  $0.61 \leq C_d \leq 0.90$  range. Since the computational model appears to capture the bulk flow processes in orifice injectors, the flow field can be used to investigate the local conditions, i.e. to confirm whether cavitation is captured. Figure 7.13 shows the simulated flow field at the entrance to a  $100 \mu\text{m}$  diameter orifice for flow rates approximately equivalent to the EoL, nominal and BoL operational conditions. The data shown is the static pressure flow field, overlaid with streamlines, indicating a region of high-speed, low-pressure flow around the inlet corner. The surface plot is clipped at  $31.69 \times 10^{-3}$  bar, the vapour pressure of DI water, indicating regions where cavitation will occur. Note that these regions are not the expected size of the cavitation bubble, instead this represents the region of the bubble formation, which will expand as they propagate downstream [99].

The size of the low-pressure region at the throat entrance in Figure 7.13 is very small for the low flow rates but increases significantly with the flow rate. At very high rates the region extends throughout the flow, detaching and propagating downstream. These regions are not cavitation bubbles, but their size is tied to the size of the bubbles that form. The size also implies the higher sensitivity to 'chugging' at lower mass flow rates: the lower the flow rate, the less absolute pressure fluctuation is required to stall the flow around the inlet corner. This will increase the local static

pressure above the vapour pressure preventing the formation of the cavitation bubble, breaking the choking condition.

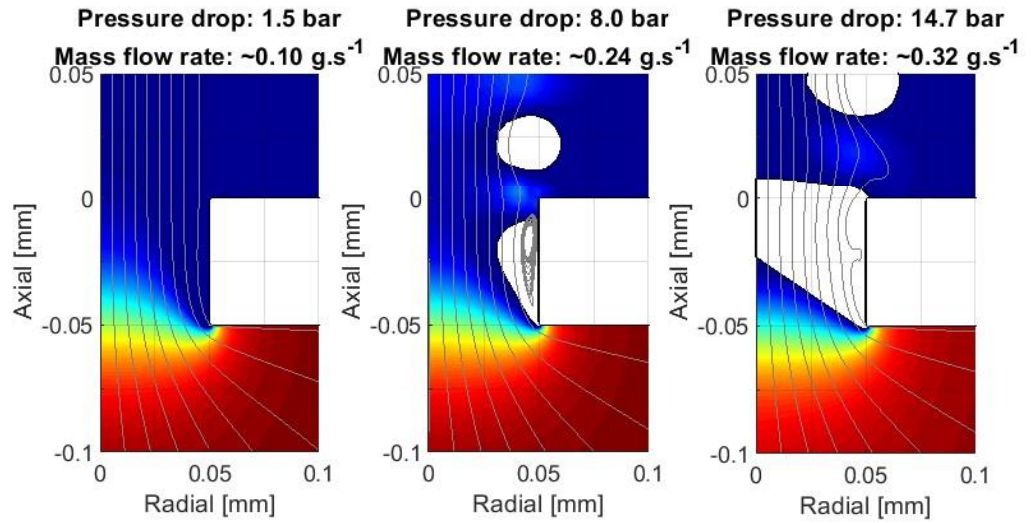


Figure 7.13 – Static pressure field of different flows through the 1-100-50 orifice injector. The colour field is the static pressure, with colours normalised between  $P_{amb}$  and  $P_{in}$ , and clipped for  $P \leq P_{vap,H_2O} = 31.69 \times 10^{-3}$  bar. Streamlines are included to show the expected flow path, with the flow moving in the positive I direction (from bottom to top).

A list of the successfully tested orifice injectors and their parameters is included in Table 7.7. Unfortunately, many of the smaller injectors with a specified throat diameter below 80  $\mu\text{m}$  did not have consistent flow and many blocked. This includes all of the multi-port designs, and may be due to contamination from either the propellant or PDS, although this was not obvious from inspection of the DI water passed through the system. These blockages highlight the issues with these small geometries, and it is suggested that orifice plate and other Venturi-type injectors may not be suitable as microinjectors for low thrust monopropellant systems below 0.1 N. This is in addition to the demonstrated challenges with the manufacturing processes used here, although in this case further iteration or other techniques, e.g. those used for MEMS, may result in more accurate orifice throat geometry.

Table 7.7 – A list of the successfully cold flow-tested orifice plate injectors.

Injector ID	Number of Injectors		Total Discharge Area, $\times 10^{-9} [\text{m}^2]$		Mean Orifice Diameter [ $\mu\text{m}$ ]	Effective Geometric Parameter, $C_d \zeta_{orf} \times 10^{-9} [\text{m}^2]$
	Produced	Successfully Tested	Designed	Inspection		
1-50-50	3	1	1.96	$0.82 \pm 0.22$	$32.3 \pm 4.0$	1.72
1-80-50	3	2	5.03	$1.90 \pm 0.50$	$49.2 \pm 6.4$	$6.59 \pm 1.38$
1-100-50	3	3	7.85	$8.04 \pm 0.90$	$101.2 \pm 5.9$	$14.67 \pm 0.72$
1-120-50	3	3	11.31	$9.16 \pm 0.31$	$108.0 \pm 1.8$	$14.85 \pm 0.92$

## 7.4. Hot Firing Testing

### 7.4.1. Scope and Test Campaign

A subset of the injectors was tested to validate their performance under representative conditions, and to identify the 'chugging' coupled flow phenomenon. The standard baseline thruster variant was used: 3.5 mm diameter, 7.0 mm long catalyst bed, with the baseline 300  $\mu\text{m}$  diameter spherical Pt- $\gamma$  alumina catalyst. Another important aspect of the injector operation is the start-up transient of a thruster, or the time for the thruster to reach steady state operation. Understanding how the different architectures impact this is important for small attitude-control thruster systems, which typically need fast and predictable start-up performance.

This test campaign captures the performance of the injectors over the nominal  $5 \text{ bar} \leq P_c \leq 30 \text{ bar}$  test range. Each injector was tested with a new catalyst bed, with pre-firing temperatures controlled below 50  $^{\circ}\text{C}$  for consecutive runs. As with the previous testing, a set of repeat tests at each pressure captured run-to-run changes. The Poiseuille injectors with the lowest expected range of fractional pressure drops were selected, aiming to capture the 'chugging' condition since the baseline injector demonstrated stable operation. The range of orifice injectors was limited by the blockages, so geometries were chosen to capture the widest range of pressure drops, predicted from the cold flow characterisation results. A list of the injectors tested is included in Table 7.8, indicating the predicted pressure drops across the injector in the nominal operational range. Note these assume physiochemical parameters for 87.5 %/wt. HTP. The table also notes the range of inlet pressures that were successfully tested. In some cases, this did not cover the full intended range due to blockages.

Table 7.8 – A list of the hot fire-tested injectors and their expected performance from the cold flow characterisation results over the nominal  $0.05 \text{ g.s}^{-1} \leq \dot{m} \leq 0.3 \text{ g.s}^{-1}$  range.

Injector ID	Number Tested	Architecture	Predicted Pressure Drop over Operational Range [bar]		Successful Testing Range, $P_{in}$ [bar] *
			Absolute [bar]	Fractional, $/P_c$	
7-20	1	Poiseuille	1.43 – 8.61	0.408	5 – 15
7-50	1	Poiseuille	1.77 – 10.65	0.505	5 – 30
10-20	1	Poiseuille	0.26 – 1.58	0.075	5 – 30
10-50	5	Poiseuille	0.33 – 1.95	0.093	5 – 30
10-100	4	Poiseuille	0.56 – 3.35	0.159	5 – 30
10-200	1	Poiseuille	0.63 – 3.78	0.179	5 – 30
1-80-50	1	Orifice	0.17 – 6.27	0.050 – 0.297	5
1-100-50	2	Orifice	0.04 – 1.60	0.013 – 0.076	5 – 27
1-120-50	1	Orifice	0.03 – 1.20	0.009 – 0.057	5 – 26

\* The successful testing range consists of tests with near nominal/expected flow rates, i.e. where there is no obvious sign of degradation or blockage.

#### 7.4.2. The Flow Coupling Condition

'Chugging', or the flow coupling phenomenon, is an oscillatory effect. From literature the expected frequency range is  $10 \text{ Hz} \leq Fq \leq 400 \text{ Hz}$  [11], and is a result of the mass flow rate through the injector being affected by the turbulent catalyst bed environment downstream. In the previous chapters the baseline Poiseuille injector performed well with no apparent instabilities. The baseline thruster was tested without an injector to demonstrate unstable operation and the need for an injector in a thruster of this scale. These hot firing tests were performed at a range of inlet pressures starting at 2 bar (for safety), incrementing up to a maximum of 10 bar. Data from the minimum and maximum test conditions are shown in Figure 7.14.

The data in these examples is very atypical: there is negligible pressure drop across the injector but a significant drop over the catalyst bed. In the 2 bar case, the chamber pressure is at ambient indicating that the nozzle is unchoked. In addition, the chamber temperatures are low ( $< 400^\circ\text{C}$ ) but there are very high pre-bed temperatures up to the limit set by the latent heat of vaporisation, shown in the 10 bar example in Figure 7.14. However, since 'chugging' is fundamentally a flow coupling phenomenon, the mass flow rate is very unsteady. At the lower flow rates, including in the 2 bar example in the Figure, there is negligible mass flow rate with periodic flow bringing fresh propellant into the bed. This is similar cyclical process to the effects in the catalyst bed with choking and pressure roughness, however here the mass transport is the bulk mass flow rate rather than the localised diffusion to the catalyst material. Despite this, the result is similar: the transient mass flow into the catalyst bed causes rapid decomposition and a pressure rise, slowing or stopping the propellant flow until the pressure decreases and the flow rate can resume. At the higher flow rates the driving pressure forces some propellant into the bed, but the flow rate is highly unstable, shown in the 10 bar example in the Figure.

The oscillations in the mass flow rate data have an approximate frequency range of  $0.5 \text{ Hz} \leq Fq \leq 2 \text{ Hz}$ , which is lower than the expected range from literature. However, this is clearly an effect of the lack of injector, and it is therefore suggested to be the same phenomenon and will be referred to as 'chugging' going forward. All of the tests the pressures are surprisingly stable, despite the high degree of flow coupling, although the performance of the thruster is degraded so this mode of operation should be avoided.

Capturing the flow coupling during tests with an injector was more difficult given the limited selection of available functional injector geometries. Of the designs listed in Table 7.8, only the 10-20 Poiseuille injector and the 1-120-50 orifice injector showed obvious signs of coupling and only at low flow rates. These have particularly low predicted pressure drops based on their flow characterisation, as indicated in Table 7.8. Examples of the time domain data of the tests exhibiting flow coupling are shown in Figure 7.15. The coupling is shown by the oscillating mass flow rate, where a well-conditioned nominally operating thruster will have a very steady flow rate. Even in these tests, the thruster is still functioning well, with no apparent impact on the other steady state parameters besides increased variability and some minor instabilities in the chamber pressure and temperature channels. These observations suggest that the injectors are functioning in a degraded manner although the performance is significantly better than the case with no injector.

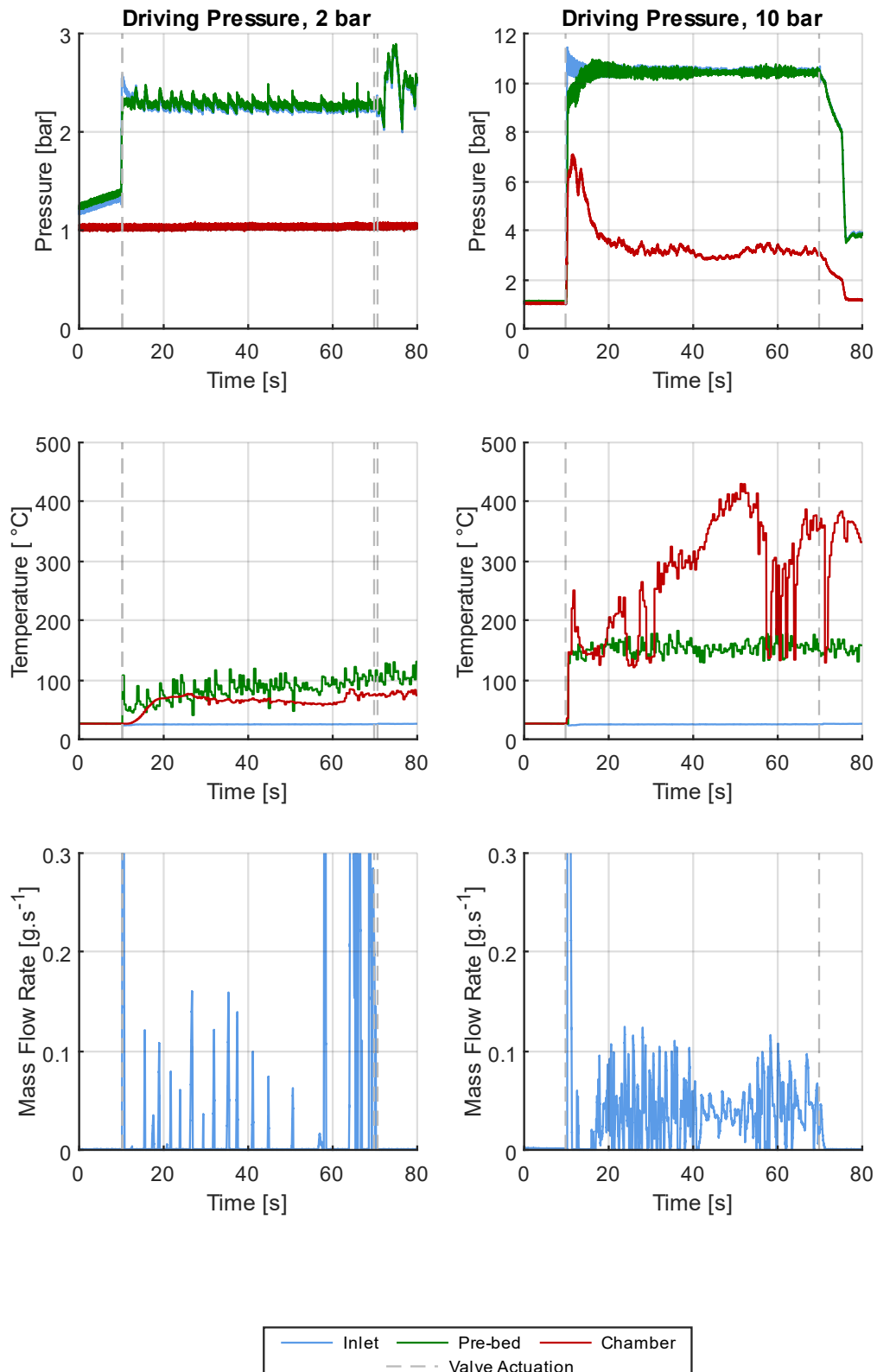


Figure 7.14 – Example time domain data of the thruster operating without any injector, with a set driving pressure of 2 bar and 10 bar.

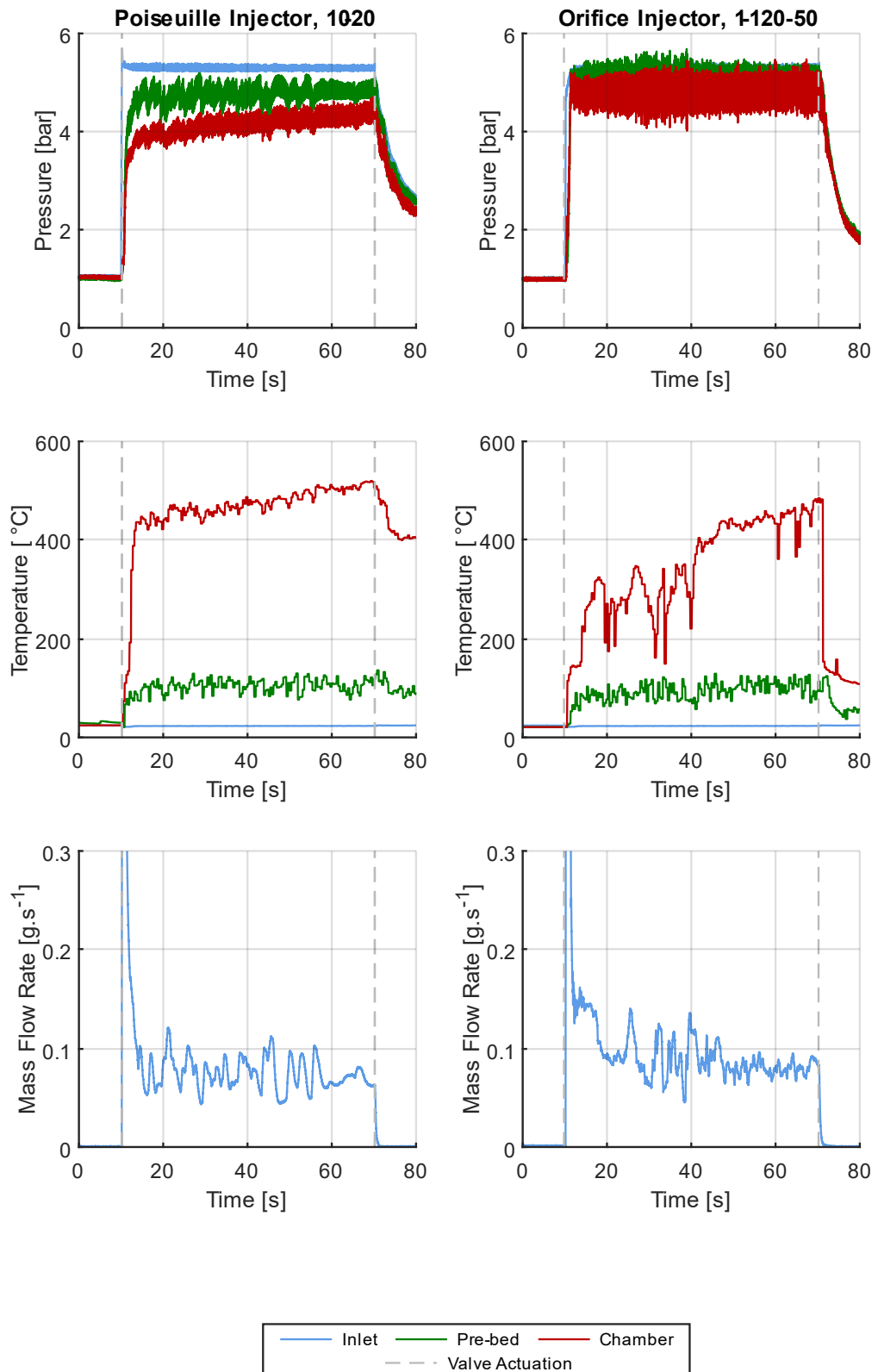


Figure 7.15 – Example time domain data of the thruster operating with pressure coupled across the injector. The two cases are for the 10-20 Poiseuille injector and the 1-120-50 orifice injector, both at a 5 bar target inlet pressure.

### 7.4.3. Quasi-Steady Performance

The flow coupling phenomenon, 'chugging', can be investigated quantitatively by considering the quasi-steady signal roughness. The absolute  $1\sigma$  steady state mass flow rate roughness is plotted against the mass flow rate in Figure 7.16. For both injector architectures, the bulk of the roughness results are below  $0.0075 \text{ g.s}^{-1}$ , with the unstable coupled flow tests above this group of data. This also identifies several other tests with these injectors that did not obviously show the variable mass flow from inspection of the data. This confirms that the mass flow rate roughness is a good predictor of 'chugging' and may also identify injectors operating near the onset. For both injector architectures the onset appears to be a gradual degradation of performance. There is clearly some run-to-run variability that affects the onset given that both injectors also operate with a steady mass flow rate.

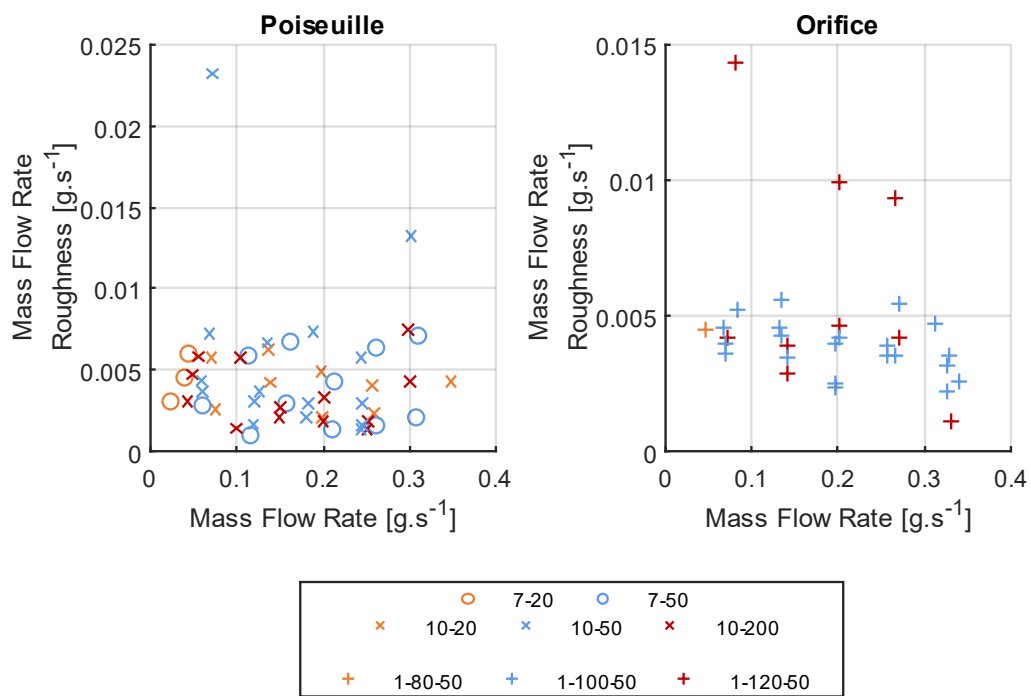


Figure 7.16 – Mass flow rate roughness' ( $1\sigma$  of the steady state) for the two injector architectures.

For both architectures, the stably operating injector tests,  $1\sigma$  mass flow rate roughness does not vary with the mass flow rate. However, for the unstable tests, the magnitude of the roughness decreases with increasing mass flow rate. This was seen in the tests without the injector, where the high flow rates and driving pressure can force propellant through the injector. The implication is that both architectures are most sensitive to 'chugging' at low propellant flow rates. The constant fractional pressure drop of the Poiseuille injector was thought to indicate that this was not the case. Therefore, the Hagen-Poiseuille Equation (7.1) does not fully describe the onset of flow coupling.

The mass flow rate roughness provides a method for identifying the onset of 'chugging', although it must be acknowledged that there is a very limited set of data that show the unstable flow, and some of these were not obvious from qualitative inspection of the test data. This metric does not provide

any insight into the decoupling process of either injector architectures as the mass flow rate phenomenon is an effect rather than a cause.

The fractional pressure drop may provide some insight into the cause of the instabilities. It is proposed that forces causing the coupling are a result of the oscillatory local expansion of decomposition products in the catalyst bed. These expanding bubbles transiently decrease or stop the mass flow rate, which leads to 'chugging'. Therefore, the driving pressure differential across the injector must be high enough to maintain flow into the catalyst bed, decoupling the flow from the downstream roughness in the bed. The injector fractional pressure drop ( $dP_{inj}/P_c$ ) of both architectures is plotted with respect to the steady state propellant mass flow rate in Figure 7.17. Unfortunately, there is no clear difference between the coupled and non-coupled tests, unlike with the mass flow rate roughness in Figure 7.16. Therefore, while the fractional pressure drop may be an estimation of the 'chugging' condition, it is clear that this does not provide a complete picture.

These data do allow some interesting observations. Since  $dP \propto \dot{m}$ , the Poiseuille injector fractional pressure drops are constant drop over the range of mass flow rates. This is expected and again suggests that the fractional pressure drop is not a good design parameter for the Poiseuille architecture. The orifice injector data is expected to have an increasing trend ( $dP \propto \dot{m}^2$ ), with a minimum stationary point at the origin, i.e.  $dP/P_c = 0$  for  $\dot{m} = 0 \text{ kg.s}^{-1}$ . The fractional pressure drop may increase with the mass flow rate, but the trend is weakly correlated. The low quality of the data is due to the high run-to-run uncertainty relative to the magnitude. The magnitude of the run-to-run variability is the same for both architectures: the apparent increased spread for the orifice data is due to y-axis scales in the Figure.

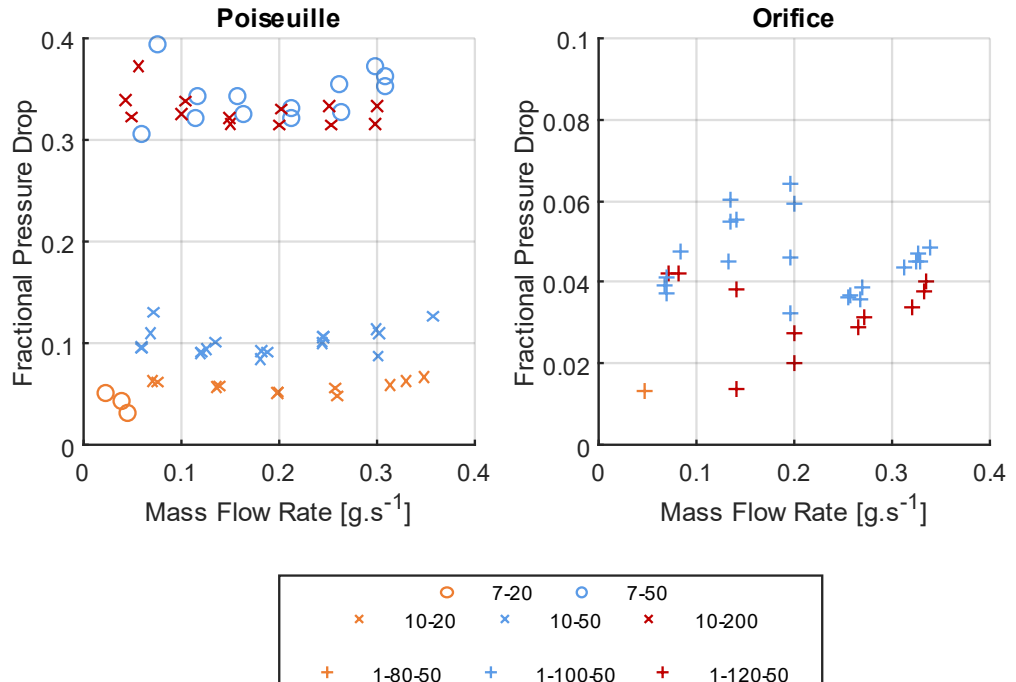


Figure 7.17 – Fractional injector pressure drop ( $dP/P_c$ ) for the two injector architectures.

A new metric, the fractional pressure drop roughness, is proposed. This is the ratio of the pressure roughness in the bed to the pressure drop over the injector,  $\sigma_{P_c}/dP_{inj}$ . This should capture the flow coupling since the pressure differential across the injector must be larger than the retarding forces from the catalyst bed roughness, i.e. if the roughness is similar to the injector pressure drop, the pressure drop may transiently drop to 0. This implies a limiting condition for stable operation of  $P_{in} \geq P_{prebed} + \sigma_{P_{prebed}}$ . However, given that neither of these injectors fully chokes, the propellant flow rate will still be reduced if the magnitude of the roughness is some significant fraction of the pressure drop. The fractional pressure drop roughness is plotted against mass flow rate in Figure 7.18. Here the injectors demonstrating flow coupling are more clearly differentiated with higher values. Despite this, there is still no clear differentiation between the tests that actually exhibit 'chugging' and the rest of the data, unlike with the mass flow rate roughness in Figure 7.18.

While this metric suggests that the turbulent roughness in the catalyst bed and pressure drop over the injector are related to 'chugging', there are clearly other factors that affect the onset. It is suggested that since the propellant flow has momentum, any retarding force must act on the propellant over a sufficiently long time period to initiate the coupling. The frequency of the roughness is therefore important, since higher frequencies will act over a shorter timescale, requiring a greater roughness magnitude to achieve the same effect. Since the frequency of the pressure roughness in the catalyst bed varies with propellant flow rate, investigating the impact of different injectors on the spectral response of the catalyst bed is important to test this.

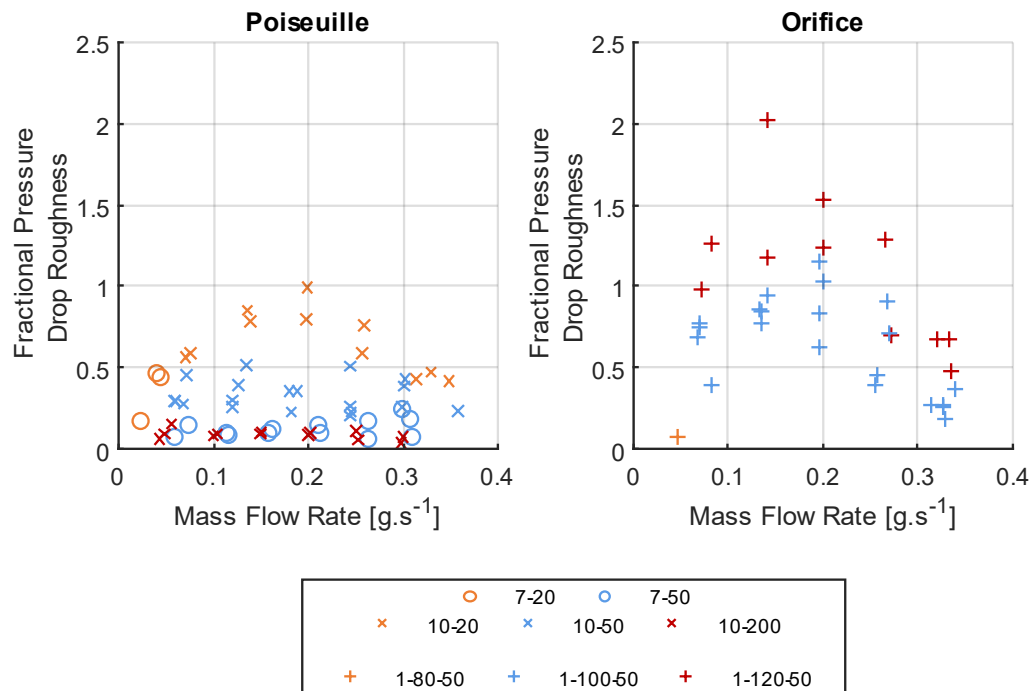


Figure 7.18 – Fractional pressure drop roughness,  $\sigma_{P_c}/dP_{inj}$ , for the two injector architectures.

#### 7.4.4. Spectral Analysis

The spectral response of the high frequency pressure data should contain information about 'chugging' since it is fundamentally an oscillatory coupled flow phenomenon. The data from the tests without an injector show that the fundamental frequency of this effect was approximately  $0.5 \text{ Hz} \leq F_q \leq 2 \text{ Hz}$ . This is lower than the expected range from literature,  $10 \text{ Hz} \leq F_q \leq 400 \text{ Hz}$ , but this is an extreme case of the inlet flow coupling with the catalyst bed. This analysis was expected to help identify the onset and cause of the phenomenon, confirming the suggested time dependency. In addition, as demonstrated with the baseline thruster in Chapter 5, the spectra can be correlated, providing a measure of the coupling between the pre- and post-injector pressure channels. The data were anticipated to provide further insight into how the different injector architectures decouple the flow. The techniques used in the spectral analysis are detailed in Appendix A.

The instrumentation and acquisition limit the scope of the analysis: From Chapter 3, the PDS samples at a frequency of 2 kHz, however the response of the pressure transducers is only 1 kHz. The maximum resolvable frequency is defined by the Nyquist frequency, half of the sampling frequency, i.e. 500 Hz for the pressure signals. This is above the maximum range of the spectral response of the 'chugging' condition from literature. The lower frequency limit is set by the spectral analysis algorithm and the quality of the data: The combination of discontinuities in the data and the windowing function used to condition the DFT mean that there is significant spectral leakage in the lower frequency bins  $< 10 \text{ Hz}$ . This is covered in more detail in Appendix A, but as a result the response below 10 Hz cannot be used. Direct observation of components of the instabilities below 10 Hz is not possible, and the low frequencies observed in the data without an injector are therefore not resolvable. Higher frequency components of the response will still be captured.

The principal oscillatory frequency, the most significant peak of the DFT spectrogram, describes the main mode of oscillation. Plots of the centre frequencies of this first significant peak are shown in Figure 7.19. The data upstream and downstream of the injector are plotted separately for the two injector architectures. For each dataset, the data follows a the linearly increasing trend with mass flow rate. There is also no appreciable difference between the different pressure channels of injector architectures. This implies that the injectors have very little impact on the roughness in the catalyst bed, and confirms that the roughness upstream of the injector is driven entirely by the turbulent downstream conditions.

The onset of the flow coupling is not captured by these data: There is no distinction between the nominally operating injectors and those exhibiting higher mass flow rate roughness, i.e. 'chugging'. However, the previous analysis showed that the magnitude of the oscillations, described by the  $1\sigma$  pressure roughness, was linked to the flow coupling. The unstable tests of both injector architectures occurred at the minimum propellant flow rates, corresponding to the lowest pressure roughness frequencies. This appears to confirm the proposed coupling mechanism: the momentum of the propellant flow rate must be significantly affected by the magnitude of the forces from roughness in the catalyst bed acting on the flow. However, the magnitude must be sufficiently high to affect the pressure differential across the injector, i.e. as is the case of no injector, or the timescale of the forces must be long enough for the flow rate to be sufficient slowed. Since the low-pressure roughness frequencies, i.e. longer timescales, are at the minimum mass flow rates, it follows that flow coupling

will occur under these conditions. This should be irrespective of the injector architecture since it is a property of the fluid.

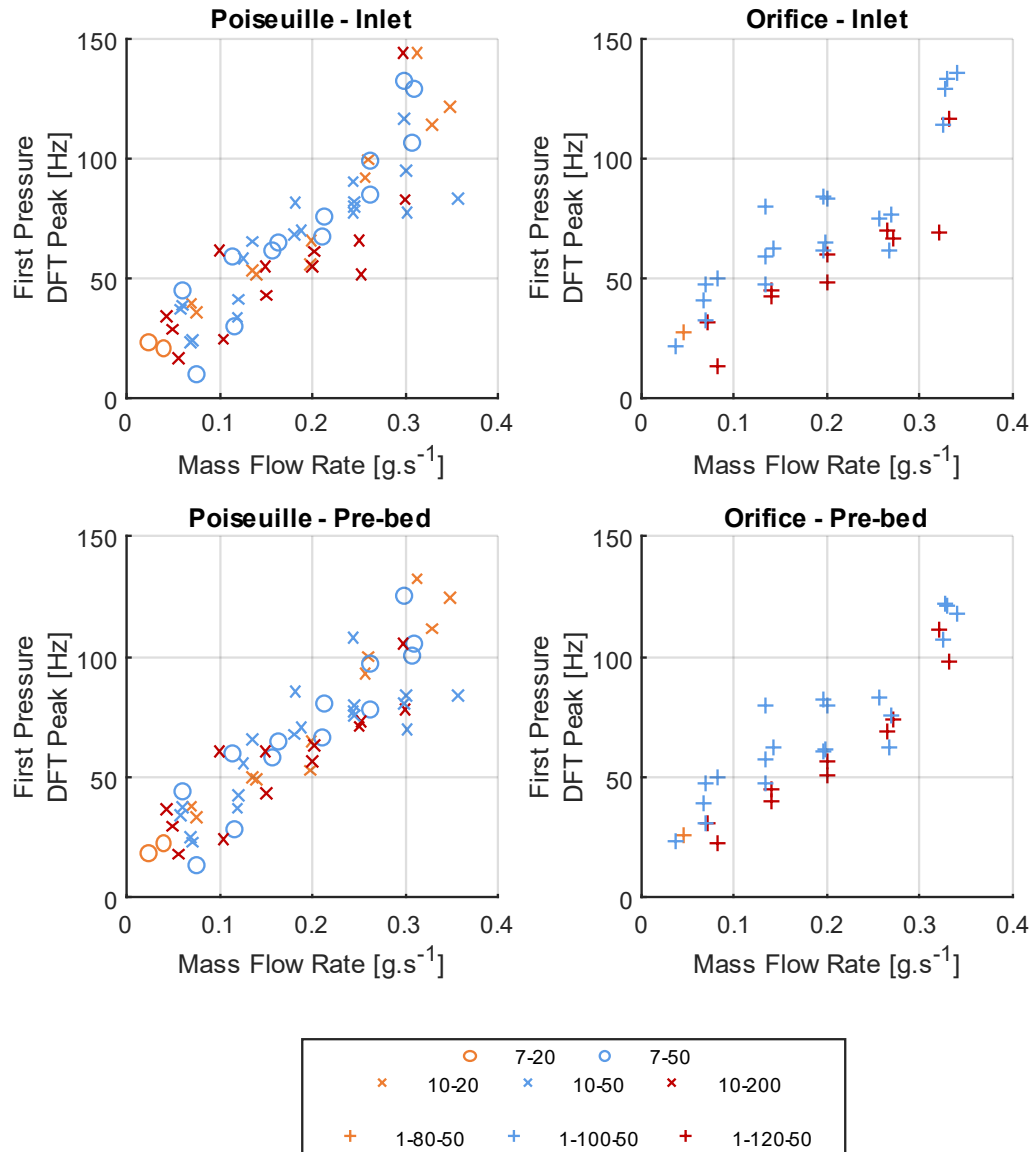


Figure 7.19 – First significant frequency peaks of the inlet and pre-bed pressure channels for both injector architectures.

Correlating the spectral responses of the upstream and downstream pressure channels provides insight into the decoupling process of the injectors. While the injector does not appear to affect the frequency or magnitude of the pressure roughness in the bed, it should affect the onset conditions of 'chugging'. The Poiseuille and Venturi architectures operate using completely different processes, viscous forces and Venturi cavitation respectively, so the degree of coupling was expected to be different. The steady state coupling is determined by correlating the DFTs of the two pressure channels. The result is a value between 0 and 1, representing the degree of linear correlation between the two spectra, where 0 represents random independent frequencies and 1 indicates perfectly

coupled data. The technique is discussed in more detail in Appendix A. Note that this does not consider the absolute magnitude of the response and the majority of the DFTs in the upstream region are heavily attenuated in comparison to the signals in the thruster.

Figure 7.20 includes plots of the steady state coupling of the pressure across the injectors with respect to mass flow rate for both injector architectures. The Poiseuille injector data shows a broad spread of values between 0 and 1, with values for each injector dataset approximately constant over the range of mass flow rates. These results indicate that different injector geometries decouple the flow to different degrees, and this is independent of the flow rate. Longer and narrower Poiseuille injectors couple less, although the length appears to have a more significant impact than the area. This agrees with the expected mode operation: the liquid flow through Poiseuille injectors is incompressible, so viscous effects will be the main process to attenuate the roughness.

Note that there are a number of datapoints at lower mass flow rates with unexpectedly low correlation values, for example some of the data for the 178  $\mu\text{m}$  diameter injectors (7-20 and 7-50). This is due to the limits of the pressure transducers: at the low flow rates the pressure roughness is heavily attenuated over the injector. Therefore, the magnitude of the inlet spectral response is very low, close to the noise floor of the pressure transducers, which makes it difficult to resolve the frequency peaks. This can be seen in the earlier DFTs for the baseline thruster testing in Figure 5.12 where it is difficult to visually identify any the data in the inlet spectrogram. As a result, the correlation at low flow rates is driven by the noise and will be low. Data below an approximate mass flow rate 0.1  $\text{g.s}^{-1}$  should not be considered as reliable as the data for the higher flow rates.

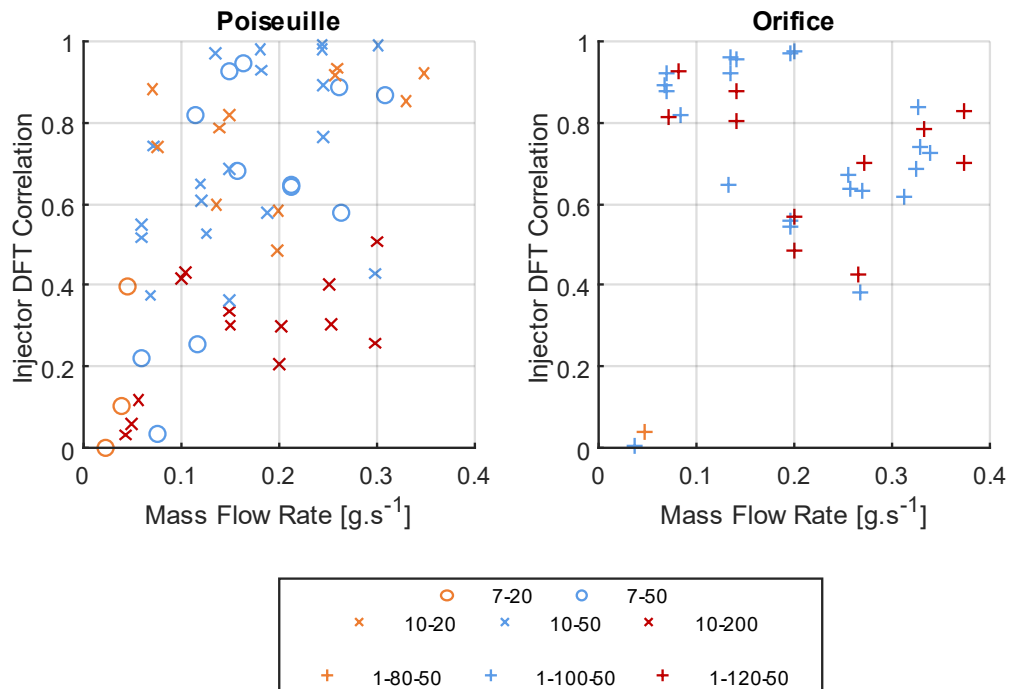


Figure 7.20 – Quasi-steady state correlation of the pressure channel DFTs across the Poiseuille and orifice injector architectures.

The steady state coupling data of the orifice injectors are generally above 0.5, indicating that the roughness is relatively well-coupled over the injectors, regardless of the throat geometry. There is an apparent trend of decreasing coupling with increasing propellant mass flow rate, i.e. the injectors decouple the instabilities more at higher flow rates, although the spread in the data is wide. This also agrees with the mode of operation for Venturi injectors: the decoupling is achieved by cavitation bubbles which are considerably larger at high flow rates, shown in the computational results in Figure 7.13. Since the gas phase is compressible, as cavitation increases, the bubbles are able to attenuate the roughness more. At the low flow rates, the majority of the fluid in the injector is liquid (incompressible) so any roughness is free to propagate upstream. As with the Poiseuille injector data, there are two outliers with very low correlation at the lower propellant flow rates. This is the same effect where the spectral response cannot be resolved from the noise floor.

Since the cavitation is a local effect, requiring a specific flow rate to reduce the static pressure below the vapour pressure, there will be some critical flow rate where the injector will no longer decouple the flow. This means that there must be some minimum pressure drop under which flow coupling will occur. Poiseuille injectors do not have a critical flow rate, and since there is no minimum flow rate for viscous forces, the injector should continue to function in a degraded fashion down to  $\dot{m} = 0$ . As a result, these data suggest that orifice injectors are more liable to 'chugging' than Poiseuille injectors, and specific attention must be paid to the coupling and the quasi-steady roughness to ensure that they are designed to operate above their critical flow rate.

#### 7.4.5. Thruster Start-Up Performance

A slow start-up transient reduces the overall performance of a propulsion system and affects their usage as AOCS thrusters: The faster the start-up transient of the thruster, the more precise the control over the spacecraft. This is particularly relevant for sub-newton thrusters as many of the designs tested in the catalyst bed study (Chapter 6) had protracted start-ups, even if they reached high performance steady state operation. The start-up transient is defined here as  $\tau_{90}$ , the time between the thruster firing valve (SV3) actuation and the thruster reaching 90 % of the steady state value. This accounts for the gradual increase of temperature over a short test caused by the heating up of the thruster and surrounding materials.

Figure 7.21 shows the chamber pressure and temperature start-up transient times for both injector architectures. These data should only capture the independent effect of the injectors as the catalyst bed and initial conditions were controlled: all tests use the baseline thruster and catalyst, with the preheating temperature  $< 50^\circ\text{C}$ . In all cases the start-up is directly tied to the mass flow rate: The system reaches steady state faster for higher propellant flow rates. This is due to the propellant filling the volume of the bed faster, and the increased enthalpy input rate. An important result is that there is little difference between the two architectures: with minimum pressure transients of 1.21 s and 0.97 s, and temperature transients of 0.90 s and 1.51 s, for the Poiseuille and orifice injectors

respectively. These minimum start-up transients are a product of the time taken to fill the thruster and the ullage volume downstream of the firing valve.

Despite this there are some minor differences between the two injectors. The different Poiseuille injector geometries change the length of the start-up transient. Tubes with a greater length have longer transients, which is indicative of the time for the flow to propagate through the injector, reaching steady state. For the orifice injectors, the time taken is relatively consistent given that they are thin plates. This should be true for all Venturi-type injectors as they do not require the long resistive flow path to operate. The orifice injector pressure start-up transient therefore represents the minimum time taken to fill the ullage volume and for the thruster to reach nominal operating conditions. A flight-representative system will minimise the volumes in the PDS and upstream of the catalyst bed to improve the start-up performance.

The thermal transient start-up time is also a function of the ullage filling time and the thermal performance of the catalyst bed, including the thermal mass of the thruster and supporting components. It is therefore less sensitive to the injector, and as a result the operation is more similar between different Poiseuille injectors than for the pressure start-up.

The very short temperature start-ups for the 7-20 Poiseuille injector at the low mass flow rates are an artefact of the generally poor thermal performance: the 'steady state' chamber temperatures reached by this thruster are all below 190.7 °C, and the  $\tau_{90}$  value is reached far quicker than for a bed operating nominally. Note that the thermal start-up transient of these atmospheric thrusters will be longer than that of a vacuum or on-orbit thruster. Under vacuum conditions the thermal losses from the thruster walls will not have the convective component. As a result, on-orbit thrusters are typically preheated to reduce the thermal shock to the catalyst material.

Reducing the upstream ullage volumes should reduce the minimum transient time, however 'long' start-up times ( $\tau_{90} \geq 1$  s) affect the minimum impulse bit that can be delivered to a spacecraft. This may affect the usability of these thrusters for AOCS applications, although the start-up performance is repeatable. the shutdown transients must also be taken into account for a flight- representative system, although they aren't considered here. For the testing here, the volume of propellant after the thruster firing valve is large and takes some time to blowdown, so analysis of the shut-down transients was not considered useful for the current work.

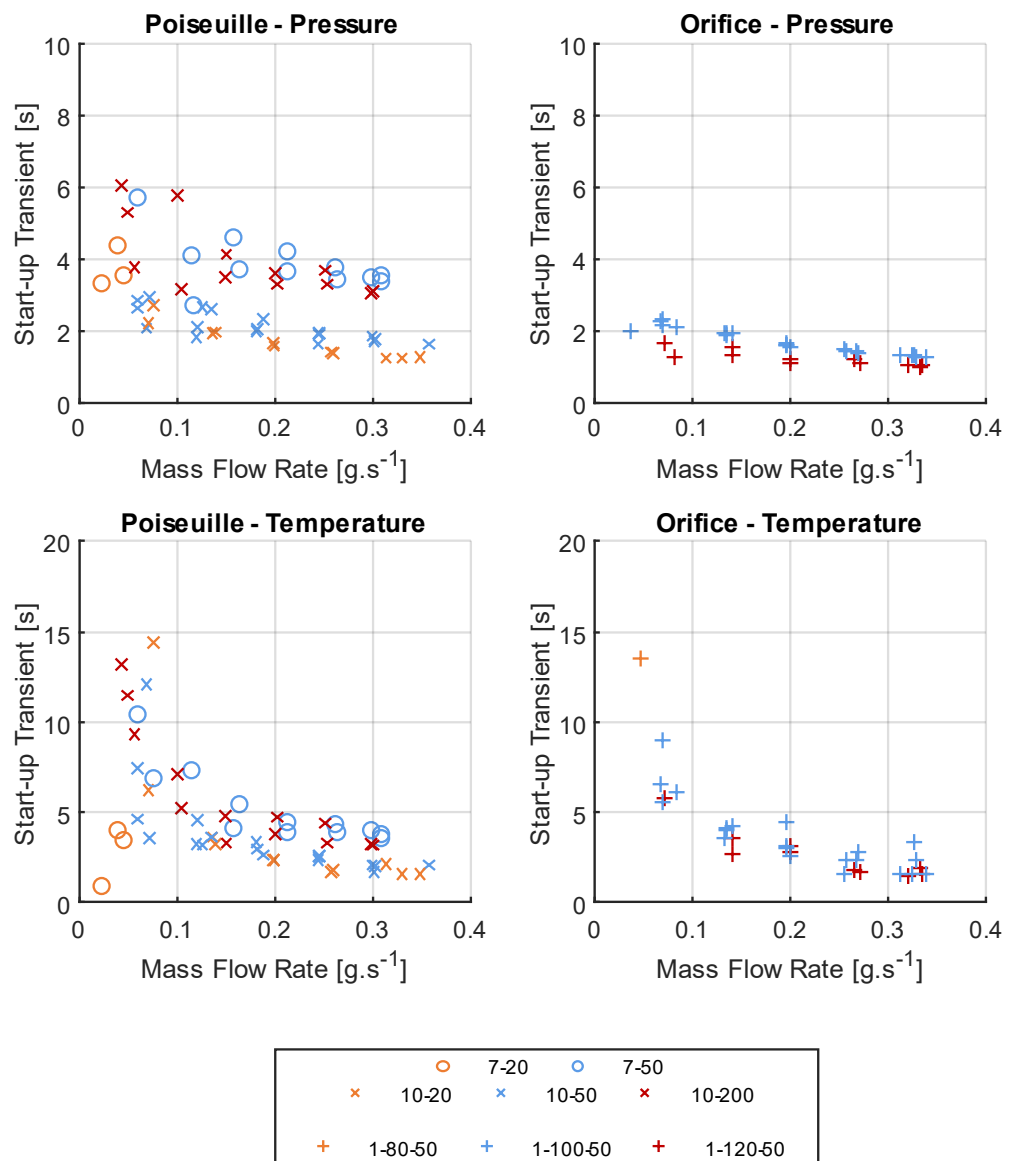


Figure 7.21 – Chamber pressure and temperature start-up transient times ( $\tau_{90}$ ) for both injector architectures.

## 7.5. Summary of the Microinjector Study

This Chapter presents an investigation of microinjector architectures, expanding on the previous analysis of the baseline 10-50 Poiseuille type injector. A discussion of the design and possible manufacturing techniques for Poiseuille and orifice Venturi injectors was provided, including an extensive study of their performance. The analysis includes cold flow characterisation, supported by computational simulations, and hot fire testing with the baseline catalyst bed. The main focus of the analysis was on identifying the onset of low frequency 'chugging' phenomena that degrades the performance of the thruster system, as well as investigating the governing processes.

The injector designs were based on the analytic models of the pressure differential across the respective architectures, resulting from the range of mass flow rates. The target pressure drops were selected from literature studies that demonstrated stable operation of monopropellant thrusters, typically  $0.05 \leq dP_{inj}/P_c \leq 0.20$ . The selected injector geometries included a number of over and undersized designs ( $0.016 \leq dP_{inj}/P_c \leq 1.999$ ) to test the performance outside of the stable range. The Poiseuille injectors were commercially procured SS 304 chromatography microbore tubes, while the orifice injectors were manufactured using both chemical etching and laser microdrilling. From inspection and characterisation, all injectors had a large degree of variability. More work is required to develop suitable processes for controlling the geometry at these scales. The small scales also highlighted the difficulty of preventing blockages: the majority of the orifice injectors blocked in both cold flow and hot firing tests. It is suggested that injectors with port diameters  $\leq 80 \mu\text{m}$  are particularly sensitive. Systems that require smaller injector throats will likely need to take specific measures to manage contamination.

There were difficulties measuring the geometry of both injector architectures. The experimental analysis instead relies on the effective geometric parameter  $C_d\zeta$ , which includes a coefficient of discharge to capture non-ideal flow effects. The manufacturing variabilities resulted in a wide range of discharge coefficients. For the Poiseuille injectors, it was suggested that this was an effect of the variability in the cross-sectional area. The orifice injectors were damaged by the pressure differential across the plate, enlarging the throat area. This may be mitigated by improving the manufacturing process. Despite these issues, the injector performance is repeatable and is described by the effective geometric parameter determined from flow characterisation. In all cases, the characterisation data follow the expected trend:  $dP \propto \dot{m}$  and  $dP \propto \dot{m}^2$  for the Poiseuille and orifice injectors respectively.

A subset of the manufactured injectors was tested with 87.5 %/wt. HTP and the baseline catalyst bed. Injectors with lower fractional pressure drops were selected to try and capture the onset of 'chugging' and the flow instabilities. No clear transition between the nominal and coupled flow operational modes was seen for either architecture. The  $1\sigma$  mass flow rate roughness is a good indicator of these instabilities, since it captures the coupling of the incoming propellant flow to the oscillatory decomposition processes in the catalyst bed. The lower frequency bound of this 'chugging' effect was in the  $0.5 \text{ Hz} \leq F_q \leq 2 \text{ Hz}$  range for thruster operation without an injector. This is less than the expected range of  $10 \text{ Hz} \leq F_q \leq 400 \text{ Hz}$ , although since it is caused by propellant injection this low frequency mode is considered 'chugging'.

The cause of the coupled flow condition is suggested to be the local expansion of gaseous decomposition products in the liquid/multi-phase regime, applying a force on the incoming propellant

flow. The pressure roughness ( $1\sigma_P$ ) in the bed and the fractional pressure drop roughness ( $1\sigma_P/dP_{inj}$ ) across the injector show evidence of this, although there is no clear differentiation between stable and unstable operation. However, since this roughness is oscillatory, there is an expected time-dependency on the onset of the flow coupling. The frequency of the first significant spectral response of the pressure signal (above 10 Hz) increases with the propellant flow rate. This may explain why both architectures were unstable at lower flow rates: the lower frequency roughness will affect the incoming propellant flow over a greater time period, i.e. imparting a greater impulse on the flow. These results are different from the analytical model prediction: that Poiseuille injectors will be equally sensitive to instabilities over the range of flow rates, while the orifice injector should couple at the lower flow rates. From an engineering perspective, a flight-representative injector must be designed for the EoL condition. However, since Poiseuille injectors have constant fractional pressure drops with respect to the mass flow rate, the thruster performance will be higher at BoL than for a comparable Venturi-type injector.

The coupling of the pressure spectral response also indicates that Poiseuille injectors are more robust: the coupling is constant over the mass flow rate range and can be reduced significantly by increasing the injector length. This appears to confirm that Poiseuille-type injectors rely on viscous effects to operate. For the orifice injector, the coupling is dependent on Venturi cavitation: at low flow rates the gas phase bubbles in the injector will be small so the coupling is high, while for high flow rates cavitation is much more significant and decouples the roughness. The cold flow characterisation simulations also illustrate this, although further work is suggested to fully capture physics, i.e. cavitation bubble formation. The cavitation phenomenon also implies a minimum critical flow rate, necessary for the local static pressure to drop below the vapour pressure. Conversely, Poiseuille injectors do not have a critical flow rate since viscous forces are present for any non-zero flow rate. This provides another indication of the benefits of the Poiseuille architecture over Venturi-type orifice injectors.

# Chapter 8

## Research Conclusions and Suggestions for Future Work

### 8.1. Conclusions

The research presented in this thesis sought to tackle two goals: Firstly, the demonstration of the design, manufacturing, inspection, and testing of a high performance 0.1 N HTP microthruster. This included detailing the methodology for optimising the design of the catalyst bed and injector elements, and to add to the limited performance data published at the time of writing, even for larger thrusters. The second goal was to analyse the underlying fundamental processes in the catalyst bed and injector elements of a microscale thruster. These processes are also tied to the optimisation of the thruster design and this work aimed to improve on the current design process which relies on best-practise principles and significant experimental testing. Given the small-scale geometries of the 0.1 N thruster architecture, the processes were captured by relating the direct measurements of the fluid in the thruster to the proposed theoretical pseudo-physical front model, derived from the simplified computational modelling studies from literature. The literature underpinning this model was from studies for larger thrusters, so understanding the microscale effects specific to the sub-newton architecture were key. Broadly, both of these goals have been fulfilled, and this section details some of the key conclusions from the work.

#### 8.1.1. Demonstrating the Sub-Newton Microthruster Architecture

The successful testing of the axisymmetric microthruster architecture developed in the current work is a major achievement. At the time of writing, there is a lack of high-quality performance data for sub-newton thrusters, so the results provide a good baseline for further work. SS 316/316L AM SLM was used to manufacture the thruster components, enabling the inclusion of complex integrated geometry including the atmospheric nozzle and catalyst retainer supports. Critically, this also enabled the inclusion of instrumentation standpipes, permitting the direct measurement of the internal fluid conditions throughout the bed. Previous efforts from other studies have relied on expensive and complex manufacturing techniques appropriate for MEMS. They do not typically include provision for instrumentation, which restricts the data collection and analysis. The flexible SLM process used here is suitable for thrusters at the 0.1 N scale even with minimal post processing. Some improvements could be made to account for thermal effects in manufacture, the rough as-printed surface, and variability in critical areas such as the nozzle. Despite these issues, the low-cost and

simple thruster architecture was ideal for the current work, and it permitted a large number of catalyst bed geometries to be produced and tested.

Ten different catalyst bed designs with similar atmospheric nozzles were tested using 87.5 %/wt. HTP as the propellant. Most of the tests showed good thermal performance, with chamber temperatures in excess of 400 °C, approaching 650 °C. These high temperatures correspond to mean catalytic thermal efficiencies of 0.746 and characteristic velocity efficiencies of 0.907. This thermal performance is slightly lower than the catalytic thermal efficiency of 0.8 used to initially size the thruster nozzle, however this value includes under and oversized catalyst beds with lower performance. The maximum thermal performance of these beds was for the baseline 3.5 mm diameter 7.0 mm long catalyst bed, with efficiencies approaching  $\eta_{cat} = 0.929$  and  $\eta_{c^*} = 0.963$ .

The initial concern that sub-newton monopropellant thrusters may suffer from significant thermal losses due to their small size was founded on results from studies in literature. This work definitively demonstrates that a high performance microthruster nominally targeting 0.1 N can operate with performances comparable to larger thrusters. This demonstrates the importance of the architecture: Axisymmetric thrusters minimising the surface area to volume ratio. The thin planar designs, common in literature, have much higher relative surface areas so may also suffer from significant losses. This has not been confirmed due to a lack of direct instrumentation in these literature studies, again highlighting that the importance of instrumentation and the successes of the implementation here should not be understated.

The baseline thruster was also tested with the higher enthalpy 98.0 %/wt. HTP propellant, the highest commercially available concentration of aqueous hydrogen peroxide. Unsurprisingly, the absolute thermal performance of the thruster was better than for the 87.5 %/wt. HTP results, with all measured steady state chamber temperatures above 630 °C, approaching a maximum of 790 °C. The relative performance with respect to ideal adiabatic operation, was lower than for the lower enthalpy propellant: the mean characteristic velocity efficiencies are 0.856 and 0.950 respectively for the 98.0 %/wt. and 87.5 %/wt. HTP. This is a due to the higher chamber temperatures resulting in steeper thermal gradients and therefore greater thermal flux, particularly under the atmospheric environment. Despite this, the testing and results are important as they not only demonstrate the maximum atmospheric performance of the current thruster architecture, but are also the first documented results of 98.0 %/wt. HTP in a sub-newton thruster. These results therefore serve as a baseline for further work looking to maximise the performance of a HTP monopropellant micropulsion system.

### 8.1.2. Optimising Microthruster Catalyst Beds

The ten different catalyst beds in this work were parametrically sized using the catalyst bed loading and aspect ratio. Values for these parameters were selected based on a literature survey of thrusters with thrusts below 1 N. Bed performance was characterised for a  $5 \text{ bar} \leq P_{in} \leq 30 \text{ bar}$  range of driving pressures, equivalent to catalyst bed loadings of  $1.48 \text{ kg.m}^{-2} \cdot \text{s}^{-1} \leq G \leq 64.8 \text{ kg.m}^{-2} \cdot \text{s}^{-1}$  and aspect ratios between 0.33 and 6. The performance was captured using the thermal characteristic velocity efficiency, corrected for the preheating of the propellant. This was shown to increase with the mass flow rate and was described by a convergent

exponential model. The model coefficients suggest that the optimal catalyst bed design will have a minimised volume, with a low bed loading and aspect ratio, i.e. a short and wide catalyst pack, where the thermal performance should be more consistent over the operational range. At the time of writing, this analysis represents the first significant attempt at finding an optimum bed sizing for a micro monopropellant bed, and is also one of the largest studies of its kind for small monopropellant thrusters.

The flooding onset was found to limit the minimum catalyst bed size. This condition sets the maximum supported mass flow rate, limiting the minimum volume and therefore affecting the optimal design. From analysis of the superficial bed residence time, the onset was directly tied to the volume of the catalyst bed, where the onset time corresponds to a superficial bed residence time of 0.341 s  $\pm$  0.047 s (1 $\sigma$ ). This confirms two things: firstly, the bed packing with the baseline 300  $\mu$ m spherical pellet material is relatively uniform between the different bed geometries, i.e. they are all well-packed. Secondly, flooding is directly tied to the amount of catalyst in the bed, implying that the flooding onset is a function of the reactivity. The data were recast as a Damköhler number using the estimated specific reactivity of the liquid-phase decomposition and propellant mass flow rate. Flooding was estimated to occur for a mean  $Da = 56$ , although the propagated uncertainties mean that the value may fall within the range of  $2.6 \leq Da \leq 159.9$ . Despite the uncertainty, all beds showed good comparative agreement. The demonstration of the superficial residence time and the Damköhler number analysis techniques is significant, since it implies that the design of a bed can be tied to catalytic decomposition processes. This could be used to supplement or replace the standard iterative experimental design approach. For the residence time, the flooding of a well-packed bed should describe the flooding onset for all beds with similar packing. More fundamentally, the Damköhler number suggests that experimental testing is not required given sufficient knowledge of the catalytic material and decomposition rates. Note that since this approach considers the fundamental chemistry, it should be extensible to any liquid catalytic monopropellant system.

#### 8.1.3. Micro Monopropellant Catalyst Bed Processes

The analysis of the flooding onset condition relied on the assumption that the onset was directly tied to the processes in the bed, captured by the pseudo-physical front model. This testing provided significant data in support of this model. Flooding is not a gradual change of phase and performance degradation, but is instead a catastrophic breaking of the nozzle choking condition. In addition, the thermal performance of the bed was shown to increase up to the point of flooding, implying that the timescale between the bulk phase change and complete decomposition is short. Therefore, it is valid to represent both processes as fronts with a specific axial position. This also confirms that the simplified models from literature are applicable to microthrusters.

The fronts were used to explain why the performance is optimised by decreasing the catalyst bed loading and aspect ratio: For a lower aspect ratio there will be less axial movement of the fronts for any change in the mass flow rate. Designing a catalyst bed with the full decomposition front aligned at the end of the bed will maximise the chamber temperature over the operational range. The model also suggests that the sensitivity of the bed to flooding will increase for lower aspect ratios. Here, roughness may transiently push liquid past the end of the bed, breaking the choking condition.

Although not definite, this appeared to agree with the trend in the Damköhler number for flooding, where higher catalyst bed loadings, i.e. lower aspect ratios, supported marginally higher flow rates. These results are important to justify the use of simple modelling of the catalyst bed processes.

The pressure signal roughness in the bed was characterised statistically using the robust steady state determination algorithm, with the spectral response captured using the DFT frequency analysis. The data provided a clearer picture of the proposed roughness mechanism: the cyclical local diffusion of propellant and products to and from the catalytically active area. This is forced diffusion, driven by the propellant flow and the expanding decomposition products. As expected, the magnitude and frequency of the pressure roughness increased with the propellant flow rate, although the frequency was not affected by the greater enthalpy of the 98.0 %/wt. HTP propellant. More work is needed to explore this process; however, the analysis techniques represent an initial attempt to quantitatively describe the phenomenon in these small thrusters. Previous similar work has either considered roughness as an effect to be measured, or not at all.

The suggested process causing roughness has some basis in literature, where bubble formation in the multiphase flow region has been visually captured. This has been tied to a minimum channel size as the bubbles transiently choke the flow, which was not investigated here. However, testing of the larger pellet variant catalyst material directly indicated that there is also a maximum channel size between the catalyst pellets. This results in propellant channelling, where the core of the propellant flow passes undecomposed through the bed and is entrained in the hot gases generated by the flow passing close to the catalyst surface. Channelling is caused by insufficient forced diffusion to the catalytically active surface to support complete decomposition within the catalyst bed. This was directly seen in the data for the larger catalyst beds. These beds were expected to support higher mass flow rates, matching the projected onsets derived using the Damköhler number for the baseline catalyst. However, for the larger pellets the flooding onset was constant for the different bed geometries: a mass flow rate of  $0.166 \text{ g.s}^{-1} \pm 0.041 \text{ g.s}^{-1} (1\sigma)$ . This is an important result given the open questions on both the reaction and mass transport rate for the Damköhler analysis, and it also confirms the importance of appropriately sizing pellets for a given catalyst bed size.

#### **8.1.4. Microinjector Architectures, and Flow Coupling Instabilities**

A number of different designs of Poiseuille-type and Venturi-type orifice injectors were tested in the microinjector study. The cold flow characterisation testing demonstrated significant variability in the parts as-manufactured, and also highlighted some significant issues with the small scale geometries. For the orifice injectors, the thin plates were liable to damage due to the pressure differential, and throats below 80  $\mu\text{m}$  diameter suffered from blockages. Despite this, both injector types showed repeatable performance and good agreement with their respective analytic flow models. Improvements to the manufacturing processes are required to control the effective geometry, however this study has demonstrated that both injector types can be manufactured and successfully integrated into an axisymmetric microthruster using relatively low-cost methods. The orifice injector blockage issues are of concern, this may be resolvable using filters upstream although Poiseuille injector are clearly more robust to contamination.

Understanding the operating principles and identifying the key design criteria for good performance was an important goal of this study. The main purpose of an injector is to isolate the turbulent environment in the catalyst bed from the incoming propellant flow stream. When the flow is coupled, instabilities known as 'chugging' degrade performance. The magnitude of the mass flow rate roughness was a good indicator of the condition; however, it was not possible to find a clear experimental metric to describe the effect. The pressure roughness exerting a force on the incoming propellant flow is the proposed coupling method. This was expected to be visible in the fractional pressure drop roughness  $1\sigma_{P_{prebed}}/dP$ . There was some difference between the nominal operation and injectors exhibiting 'chugging', although the results were not clearly differentiated. Despite this, the quality of the data in the current work has provided a better insight into the phenomenon, and the fractional pressure drop roughness also indicated that the Poiseuille-type injectors may be less sensitive to roughness than orifice injectors.

Spectral analysis of the pressure data permitted characterising the time-dependency of the roughness and the coupling across the injector. 'Chugging' is a low frequency phenomenon, expected in the  $10 \text{ Hz} \leq Fq \leq 400 \text{ Hz}$  range, however the coupled instabilities were observed at  $0.5 \text{ Hz} \leq Fq \leq 2 \text{ Hz}$  during testing of the baseline catalyst bed without an injector. Significant correlation between the pre- and post-injector pressure spectra was observed for both injector architectures. The orifice injector had consistently higher coupling and was affected by the mass flow rate, while the Poiseuille injector operation was insensitive to the flow rate but was strongly affected by the length of the injector. This agreed with the proposed mechanisms, liquid choking (cavitation) and viscous effects respectively, and again suggested that the Poiseuille injectors are the more robust design. The stability was linked to the operational mode: viscous forces are present for any non-zero flow velocity, while the cavitation phenomenon will not occur below a minimum critical flow rate. Therefore, the orifice injectors require a critical pressure drop to operate, while the performance of the Poiseuille injectors should continuously degrade with decreasing mass flow. The frequency of the roughness is also tied to the instabilities: a lower frequency response corresponds to a longer time period for the pressure roughness to act on the incoming propellant. This was not directly verified in the current work, however these results clearly demonstrated that there are many potential analysis techniques for characterising roughness and injector operation, especially using the spectral response. 'Chugging' is generally not well documented even for larger monopropellant thrusters. Understanding the proposed improved stability of the Poiseuille-type injectors is also important since this architecture is under-researched in the field.

## 8.2. Suggestions for Future Work

The demonstration of high thermal performance and steady operation of the sub-newton architecture shows that monopropellant microthrusters can have comparable performance to larger systems. Extensive work aiming to identify the optimum catalyst bed geometry was presented, and although a likely approach was identified, the optimum size for this thruster was not found. In addition, the nozzle was purposely not investigated, and the manufacturing processes needed for a high-performance vacuum nozzle were not developed. Considering these open questions, an important next step is to iterate the current architecture with a view towards representative vacuum testing. Some preliminary efforts were made towards demonstrating this, as shown by the photo and accompanying CT scan of a preliminary vacuum thruster in Figures 8.1 and 8.2 respectively. These were intended to be used to test the vacuum performance and characterise the convective thermal losses, however vacuum testing was not possible within the scope of the current research.

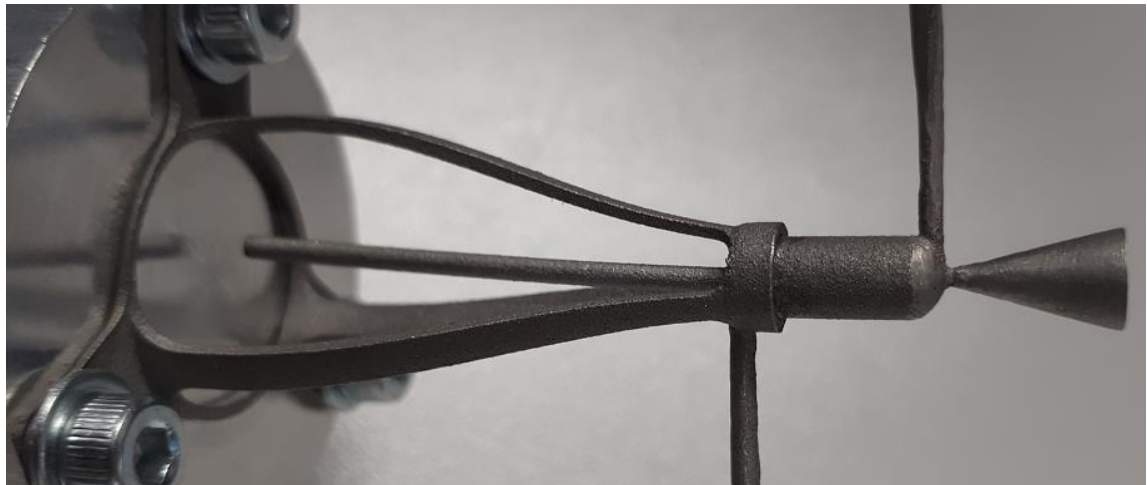


Figure 8.1 – A photo of a preliminary iteration of the vacuum thruster.

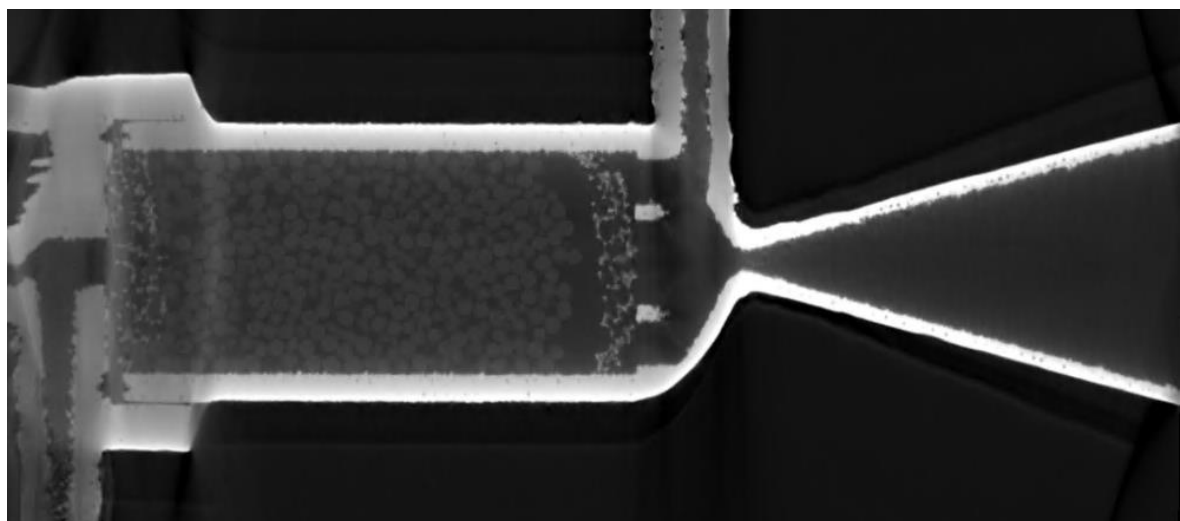


Figure 8.2 – An x-ray CT micrograph of a preliminary iteration of the vacuum thruster.

The injector manufacturing processes would also benefit from further refinement. The poor mechanical strength of the orifice injectors and significant variability of both architectures prevented conclusive flow characterisation results. These were identified as possible causes for the discrepant effective geometric parameters, although direct inspection was not possible to confirm this. They are also a significant concern for developing a system for use on-orbit. Further work refining these processes is therefore an important requirement for continuing the development of the thruster architecture. In addition, improving the components will also permit collection of higher-fidelity data to further validate the flow characterisation and derived results.

A significant contribution of the current work was in outlining the link between the fundamental processes in the catalyst bed and the experimentally-derived performance. This was used to validate the proposed simplified pseudo-physical front model, inferred from computational studies in literature. One of the promising techniques was relating the performance to the reaction kinetics through the Damköhler number. The main issue with the analysis in the current work was the uncertainty in the microstructure surface area and reactivity for both catalyst variants. The conclusions here mostly focused on relative comparisons between different datasets which are not impacted, however further work is recommended to confirm the absolute results and to investigate the application of the technique. This would include accurate measurement of the catalyst unit surface area, reactivity rates, and packing. In addition, investigating the catalytic and thermolytic decomposition rates in the different phases would also support the results from the 98.0 %/wt. testing, since the thermolytic decomposition rate appeared to be a non-negligible component of the liquid phase decomposition. A particularly important goal for further work is to confirm whether the mean Damköhler for the flooding onset is applicable to other propellant-catalyst systems. If so, this would provide a method for predicting flooding with limited experimental testing, which should be extensible to other monopropellant systems not using HTP. This could greatly simplify the process of designing a monopropellant thruster, which is currently reliant on a large amount of experimental iteration to optimise a specific design.

Another important process that was investigated in this work was the flow coupling effect over the injector. There is very little published discussion on 'chugging' for small monopropellant thrusters, and this aspect of sub-newton microthruster operation has received almost no attention at the time of writing. Considerable focus was placed on identifying the cause of the flow coupling, as well as the injector design implications. The results were limited by the issues with the injector manufacturing processes. Improving these processes, as well as increasing the measurable frequency range of the spectral response would support further analysis of the 'chugging' condition. In addition to providing further support for the suggested decoupling mechanism, this will support the design of higher performance injectors which will yield improvements for the whole propulsion system.



## 9. References

- [1] SpaceX, "Starlink Company Webpage," 2021. <https://www.starlink.com/> (accessed Oct. 24, 2021).
- [2] Planet Labs Inc., "Planet Company Webpage," 2021. <https://www.planet.com/> (accessed Oct. 24, 2021).
- [3] OneWeb, "OneWeb Company Webpage," 2021. <https://oneweb.net/> (accessed Oct. 24, 2021).
- [4] Surrey Satellite Technology Limited, "SSTL Company Webpage," 2021. <https://www.sstl.co.uk/> (accessed Oct. 24, 2021).
- [5] AAC Clyde Space, "AAC Clyde Space Company Webpage," 2021. <https://www.aac-clyde.space/> (accessed Oct. 24, 2021).
- [6] York Space Systems, "York Space Systems Company Webpage," 2018. <https://www.yorkspacesystems.com/> (accessed Oct. 24, 2021).
- [7] Blue Canyon Technologies, "Blue Canyon Technologies Company Webpage," 2021. <https://www.bluecanyontech.com/> (accessed Oct. 24, 2021).
- [8] Inter-Agency Space Debris Coordination Committee, "IADC-02-01 - Space Debris Mitigation Guidelines," 2020. [Online]. Available: <https://orbitaldebris.jsc.nasa.gov/library/iadc-space-debris-guidelines-revision-2.pdf>.
- [9] SpaceWorks Enterprises Incorporated, "Nano/Microsatellite Market Forecast, 8th Ed.," 2018. [Online]. Available: <https://spaceworks.aero/wp-content/uploads/Nano-Microsatellite-Market-Forecast-8th-Edition-2018.pdf>.
- [10] B. Lal *et al.*, "Global Trends in Small Satellites," 2017. [Online]. Available: <https://www.ida.org/-/media/feature/publications/g/gl/global-trends-in-small-satellites/p-8638.ashx>.
- [11] G. P. Sutton and O. Biblarz, *Rocket Propulsion Elements*, 9th Editio. John Wiley & Sons, 2016.
- [12] C. N. Ryan *et al.*, "Experimental Validation of a 1-Newton Hydrogen Peroxide Thruster," *J. Propuls. Power*, vol. 36, no. 2, pp. 158–166, Mar. 2020, doi: 10.2514/1.B37418.
- [13] Y. Batonneau *et al.*, "Green Propulsion: Catalysts for the European FP7 Project GRASP," *Top. Catal.*, vol. 57, no. 6–9, pp. 656–667, Apr. 2014, doi: 10.1007/s11244-013-0223-y.
- [14] C. H. McLean, "Green Propellant Infusion Mission Program Development and Technology Maturation," Jul. 2014, doi: 10.2514/6.2014-3481.
- [15] A. E. S. Nosseir, A. Cervone, and A. Pasini, "Review of State-of-the-Art Green Monopropellants: For Propulsion Systems Analysts and Designers," *Aerospace*, vol. 8, no. 1, p. 20, Jan. 2021, doi: 10.3390/aerospace8010020.
- [16] M. J. Palmer, "Experimental evaluation of hydrogen peroxide catalysts for monopropellant attitude control thrusters," Univeristy of Southampton, 2014.
- [17] S. Gordon and B. J. McBride, "Computer Program for Calculation of Complex Chemical Equilibrium Compositions and Applications. Part 1: Analysis," Cleveland, OH (USA), 1994.
- [18] B. J. McBride and S. Gordon, "Computer Program for Calculation of Complex Chemical Equilibrium Compositions and Applications. Part 2: Users Manual and Program Description," Cleveland, OH (USA), 1996.

- [19] R. Serra-Maia *et al.*, "Mechanism and Kinetics of Hydrogen Peroxide Decomposition on Platinum Nanocatalysts," *ACS Appl. Mater. Interfaces*, vol. 10, no. 25, pp. 21224–21234, Jun. 2018, doi: 10.1021/acsami.8b02345.
- [20] W. F. Louisos and D. L. Hitt, "Viscous Effects on Performance of Three-Dimensional Supersonic Micronozzles," *J. Spacecr. Rockets*, vol. 49, no. 1, pp. 51–58, Jan. 2012, doi: 10.2514/1.53026.
- [21] W. F. Louisos and D. L. Hitt, "Viscous Effects on Performance of Two-Dimensional Supersonic Linear Micronozzles," *J. Spacecr. Rockets*, vol. 45, no. 4, pp. 706–715, Jul. 2008, doi: 10.2514/1.33434.
- [22] L. T. Williams and M. F. Osborn, "Performance Impacts of Geometry and Operating Conditions on a Low Reynolds Number Micro-Nozzle Flow," 2017, doi: 201032210.
- [23] W. F. Louisos and D. L. Hitt, "Numerical Studies of Supersonic Flow in Bell-Shaped Micronozzles," *J. Spacecr. Rockets*, vol. 51, no. 2, pp. 491–500, Mar. 2014, doi: 10.2514/1.A32508.
- [24] W. F. Louisos and D. L. Hitt, "Influence of Wall Heat Transfer on Supersonic MicroNozzle Performance," *J. Spacecr. Rockets*, vol. 49, no. 3, pp. 450–460, May 2012, doi: 10.2514/1.A32206.
- [25] W. F. Louisos and D. L. Hitt, "Optimal Expansion Angle for Viscous Supersonic Flow in 2-D Micro-Nozzles," Jun. 2005, doi: 10.2514/6.2005-5032.
- [26] D. L. Hitt, C. M. Zakrzewski, and M. A. Thomas, "MEMS-based satellite micropulsion via catalyzed hydrogen peroxide decomposition," *Smart Mater. Struct.*, vol. 10, no. 6, pp. 1163–1175, Dec. 2001, doi: 10.1088/0964-1726/10/6/305.
- [27] K. Takahashi, I. Tatsuya, Y. Dan, K. Nagayama, and M. Kishida, "Catalytic Porous Microchannel for Hydrogen Peroxide MEMS Thruster," in *PROCEEDINGS OF THE 23RD SENSOR SYMPOSIUM*, 2006, pp. 513–516.
- [28] J. W. Cen and J. L. Xu, "Performance evaluation and flow visualization of a MEMS based vaporizing liquid micro-thruster," *Acta Astronaut.*, vol. 67, no. 3–4, pp. 468–482, Aug. 2010, doi: 10.1016/j.actaastro.2010.04.009.
- [29] T. Yuan, A. Li, B. Huang, Y.-T. Chen, and C. Chen, "Design, Fabrication, and Test of a Microelectromechanical-System-Based Millinewton-Level Hydrazine Thruster," *J. Propuls. Power*, vol. 27, no. 2, pp. 509–512, Mar. 2011, doi: 10.2514/1.50055.
- [30] P. Kundu, A. K. Sinha, T. K. Bhattacharyya, and S. Das, "MnO<sub>2</sub> Nanowire Embedded Hydrogen Peroxide Monopropellant MEMS Thruster," *J. Microelectromechanical Syst.*, vol. 22, no. 2, pp. 406–417, Apr. 2013, doi: 10.1109/JMEMS.2012.2226929.
- [31] A. Chaalane *et al.*, "A MEMS-based solid propellant microthruster array for space and military applications," *J. Phys. Conf. Ser.*, vol. 660, no. 1, 2015, doi: 10.1088/1742-6596/660/1/012137.
- [32] J. Lee, K. Su-Kyun, S. Kwon, and Y. Myoung-Jong, "Fabrication of Catalyst-Insertion-Type Microelectromechanical Systems Monopropellant Thruster," *J. Propuls. Power*, vol. 28, no. 2, pp. 396–404, Mar. 2012, doi: 10.2514/1.B34287.
- [33] J. Huh and S. Kwon, "Design, fabrication and thrust measurement of a micro liquid monopropellant thruster," *J. Micromechanics Microengineering*, vol. 24, no. 10, p. 104001, Oct. 2014, doi: 10.1088/0960-1317/24/10/104001.
- [34] J. Huh and S. Kwon, "Effect of micro cooling channels on a hydrogen peroxide monopropellant microthruster performance," *J. Phys. Conf. Ser.*, vol. 660, p. 012020, Dec. 2015, doi: 10.1088/1742-6596/660/1/012020.
- [35] J. Huh, D. Seo, and S. Kwon, "Fabrication of a liquid monopropellant microthruster with built-in regenerative micro-cooling channels," *Sensors Actuators A Phys.*, vol. 263, pp. 332–340, Aug. 2017, doi: 10.1016/j.sna.2017.06.028.

- [36] J. Huh and S. Kwon, "Microcooling Channel Effect on a Monopropellant Microelectromechanical System Thruster Performance," *J. Propuls. Power*, vol. 33, no. 6, pp. 1591–1595, Nov. 2017, doi: 10.2514/1.B36393.
- [37] K. H. Cheah, P. S. Khiew, and J. K. Chin, "Fabrication of a zirconia MEMS-based microthruster by gel casting on PDMS soft molds," *J. Micromechanics Microengineering*, vol. 22, no. 9, p. 095013, Sep. 2012, doi: 10.1088/0960-1317/22/9/095013.
- [38] K. H. Cheah and K.-S. Low, "Fabrication and performance evaluation of a high temperature co-fired ceramic vaporizing liquid microthruster," *J. Micromechanics Microengineering*, vol. 25, no. 1, p. 015013, Jan. 2015, doi: 10.1088/0960-1317/25/1/015013.
- [39] M.-H. Wu and R. A. Yetter, "A novel electrolytic ignition monopropellant microthruster based on low temperature co-fired ceramic tape technology," *Lab Chip*, vol. 9, no. 7, pp. 910–916, 2009, doi: 10.1039/B812737A.
- [40] K. Karthikeyan, S. K. Chou, L. E. Khoong, Y. M. Tan, C. W. Lu, and W. M. Yang, "Low temperature co-fired ceramic vaporizing liquid microthruster for microspacecraft applications," *Appl. Energy*, vol. 97, pp. 577–583, Sep. 2012, doi: 10.1016/j.apenergy.2011.11.078.
- [41] Z. Khaji, L. Klintberg, D. Barbade, K. Palmer, and G. Thornell, "Alumina-based monopropellant microthruster with integrated heater, catalytic bed and temperature sensors," *J. Phys. Conf. Ser.*, vol. 27, no. 5, p. 012025, May 2016, doi: 10.1088/1742-6596/757/1/012025.
- [42] Z. Khaji, L. Klintberg, D. Barbade, K. Palmer, and G. Thornell, "Endurance and failure of an alumina-based monopropellant microthruster with integrated heater, catalytic bed and temperature sensors," *J. Micromechanics Microengineering*, vol. 27, no. 5, p. 055011, May 2017, doi: 10.1088/1361-6439/aa6550.
- [43] R. Hebden *et al.*, "The development and test of a hydrogen peroxide monopropellant microrocket engine using MEMS technology," 2005.
- [44] S. Igarashi, Y. Matsuura, H. Ikeda, and K. Hatai, "Safe 0.5N Green Monopropellant Thruster for Small Satellite Propulsion Systems," Aug. 2019, doi: 10.2514/6.2019-4427.
- [45] M. Tsay, D. Lafko, J. Zwahlen, and W. Costa, "Development of Busek 0.5N Green Monopropellant Thruster," 2013, doi: SSC13-VII-7.
- [46] K. Gagne, M. McDevitt, and D. L. Hitt, "A Dual Mode Propulsion System for Small Satellite Applications," *Aerospace*, vol. 5, no. 2, p. 52, May 2018, doi: 10.3390/aerospace5020052.
- [47] C.-K. Kuan, G.-B. Chen, and Y.-C. Chao, "Development and Ground Tests of a 100-Millinewton Hydrogen Peroxide Monopropellant Microthruster," *J. Propuls. Power*, vol. 23, no. 6, pp. 1313–1320, Nov. 2007, doi: 10.2514/1.30440.
- [48] K. Xie, X. Chen, J. Li, and Y. Liu, "Steady Characteristics of a Gas–Gas Aerodynamic Throat," in *Fluidic Nozzle Throats in Solid Rocket Motors*, Singapore: Springer Singapore, 2019, pp. 21–51.
- [49] N. M. Kuluva and G. A. Hosack, "Supersonic nozzle discharge coefficients at low Reynolds numbers," *AIAA J.*, vol. 9, no. 9, pp. 1876–1879, Sep. 1971, doi: 10.2514/3.6443.
- [50] L. H. Back and R. F. Cuffel, "Flow coefficients for supersonic nozzles with comparatively small radius of curvature throats," *J. Spacecr. Rockets*, vol. 8, no. 2, pp. 196–198, Feb. 1971, doi: 10.2514/3.30247.
- [51] Z.-Q. Yin, D.-S. Li, J.-L. Meng, and M. Lou, "Discharge coefficient of small sonic nozzles," *Therm. Sci.*, vol. 18, no. 5, pp. 1505–1510, 2014, doi: 10.2298/TSCI1405505Y.
- [52] J. H. Kim, H. D. Kim, and T. Setoguchi, "The effect of diffuser angle on the discharge coefficient of a miniature critical nozzle," *J. Therm. Sci.*, vol. 19, no. 3, pp. 222–227, Jun. 2010, doi: 10.1007/s11630-010-0222-2.
- [53] J. H. Kim, S. H. Woo, and H. D. Kim, "A CFD prediction of a micro critical nozzle flow," in *Proceedings of the KSME 2001 fall annual meeting B*, 2001, p. 964.
- [54] R.-J. Koopmans, "Modelling of multiphase multicomponent chemically reacting flows through

packed beds," University of Southampton, 2013.

- [55] D. H. Kerr, A. R. Karagozian, D. Bilyeu, and D. Eckhardt, "Nondeterministic Analysis of Monopropellant Catalyst Bed Model," *J. Propuls. Power*, vol. 37, no. 1, pp. 126–138, Jan. 2021, doi: 10.2514/1.B37853.
- [56] S. Jung, S. Choi, and S. Kwon, "Design Optimization of Green Monopropellant Thruster Catalyst Beds Using Catalytic Decomposition Modeling," Jul. 2017, doi: 10.2514/6.2017-4924.
- [57] R.-J. Koopmans, J. S. Shrimpton, G. T. Roberts, and A. J. Musker, "A one-dimensional multicomponent two-fluid model of a reacting packed bed including mass, momentum and energy interphase transfer," *Int. J. Multiph. Flow*, vol. 57, pp. 10–28, Dec. 2013, doi: 10.1016/j.ijmultiphaseflow.2013.06.005.
- [58] A. Pasini, L. Torre, L. Romeo, A. Cervone, and L. D'Agostino, "Reduced-Order Model for H<sub>2</sub>O<sub>2</sub> Catalytic Reactor Performance Analysis," *J. Propuls. Power*, vol. 26, no. 3, pp. 446–453, May 2010, doi: 10.2514/1.44355.
- [59] X. Zhou and D. L. Hitt, "One-Dimensional Modeling of Catalyzed H<sub>2</sub>O<sub>2</sub> Decomposition in Microchannel Flows," Jun. 2003, doi: 10.2514/6.2003-3584.
- [60] G. Schulz-Ekloff and H.-G. Deppner, "Modelling and simulation of monopropellant hydrazine thrusters for spacecraft position control," *Chem. Eng. Technol. - CET*, vol. 12, no. 1, pp. 426–432, 1989, doi: 10.1002/ceat.270120161.
- [61] P. A. Giguère and O. Maass, "Vapour Pressures and Boiling Points of Binary Mixtures of Hydrogen Peroxide And Water," *Can. J. Res.*, vol. 18b, no. 7, pp. 181–193, Jul. 1940, doi: 10.1139/cjr40b-023.
- [62] EVONIK Industries, "PROPULSE 875 HTP Safety Data Sheet," 2016.
- [63] EVONIK Industries, "PROPULSE 980 HTP Safety Data Sheet," 2018.
- [64] D. MCKEE, "Catalytic decomposition of hydrogen peroxide by metals and alloys of the platinum group," *J. Catal.*, vol. 14, no. 4, pp. 355–364, Aug. 1969, doi: 10.1016/0021-9517(69)90326-1.
- [65] L. Pirault-Roy, C. Kappenstein, M. Guerin, R. Eloirdi, and N. Pillet, "Hydrogen Peroxide Decomposition on Various Supported Catalysts Effect of Stabilizers," *J. Propuls. Power*, vol. 18, no. 6, pp. 1235–1241, Nov. 2002, doi: 10.2514/2.6058.
- [66] I. Katsounaros *et al.*, "Hydrogen peroxide electrochemistry on platinum: towards understanding the oxygen reduction reaction mechanism," *Phys. Chem. Chem. Phys.*, vol. 14, no. 20, p. 7384, 2012, doi: 10.1039/c2cp40616k.
- [67] M. A. Hasan, M. I. Zaki, L. Pasupulety, and K. Kumari, "Promotion of the hydrogen peroxide decomposition activity of manganese oxide catalysts," *Appl. Catal. A Gen.*, vol. 181, no. 1, pp. 171–179, May 1999, doi: 10.1016/S0926-860X(98)00430-X.
- [68] A. Plauck, E. E. Stangland, J. A. Dumesic, and M. Mavrikakis, "Active sites and mechanisms for H<sub>2</sub>O<sub>2</sub> decomposition over Pd catalysts," *Proc. Natl. Acad. Sci.*, vol. 113, no. 14, pp. E1973–E1982, Apr. 2016, doi: 10.1073/pnas.1602172113.
- [69] D. Krejci *et al.*, "Assessment of Catalysts for Hydrogen-Peroxide-Based Thrusters in a Flow Reactor," *J. Propuls. Power*, vol. 29, no. 2, pp. 321–330, Mar. 2013, doi: 10.2514/1.B34615.
- [70] S. L. Guseinov, S. G. Fedorov, V. A. Kosykh, and P. A. Storozhenko, "Hydrogen Peroxide Decomposition Catalysts Used in Rocket Engines," *Russ. J. Appl. Chem.*, vol. 93, no. 4, pp. 467–487, Apr. 2020, doi: 10.1134/S1070427220040011.
- [71] S.-S. Lin and M. D. Gurol, "Catalytic Decomposition of Hydrogen Peroxide on Iron Oxide: Kinetics, Mechanism, and Implications," *Environ. Sci. Technol.*, vol. 32, no. 10, pp. 1417–1423, May 1998, doi: 10.1021/es970648k.
- [72] C. M. Lousada, A. J. Johansson, T. Brinck, and M. Jonsson, "Mechanism of H<sub>2</sub>O<sub>2</sub>

- Decomposition on Transition Metal Oxide Surfaces," *J. Phys. Chem. C*, vol. 116, no. 17, pp. 9533–9543, May 2012, doi: 10.1021/jp300255h.
- [73] Y. Liu, H. Wu, M. Li, J.-J. Yin, and Z. Nie, "pH dependent catalytic activities of platinum nanoparticles with respect to the decomposition of hydrogen peroxide and scavenging of superoxide and singlet oxygen," *Nanoscale*, vol. 6, no. 20, pp. 11904–11910, Aug. 2014, doi: 10.1039/C4NR03848G.
- [74] Y.-A. Chan, H. J. Liu, K.-C. Tseng, and T. C. Kuo, "Preliminary Development of a Hydrogen Peroxide Thruster," *World Acad. Sci. Eng. Technol.*, vol. 7, pp. 1226–1233, 2013.
- [75] R. Brahmi *et al.*, "Ceramic catalysts for the decomposition of H<sub>2</sub>O<sub>2</sub> - Influence of wash-coat procedure and active phase," 2006, pp. 649–656.
- [76] Z. Khaji, L. Klintberg, K. Palmer, and G. Thornell, "Catalytic effect of platinum and silver in a hydrogen peroxide monopropellant ceramic microthruster," *Propuls. Power Res.*, vol. 9, no. 3, pp. 216–224, Sep. 2020, doi: 10.1016/j.jppr.2020.08.003.
- [77] N. Miyakawa, W. Legner, T. Ziemann, D. Telitschkin, H.-J. Fecht, and A. Friedberger, "MEMS-based microthruster with integrated platinum thin film resistance temperature detector (RTD), heater meander and thermal insulation for operation up to 1,000°C," *Microsyst. Technol.*, vol. 18, no. 7–8, pp. 1077–1087, Aug. 2012, doi: 10.1007/s00542-012-1441-0.
- [78] D. Platt, "A Monopropellant Milli-Newton Thruster System for Attitude Control of Nanosatellites," 2002, [Online]. Available: <https://digitalcommons.usu.edu/smallsat/2002/all2002/42/>.
- [79] R.-J. Koopmans *et al.*, "Performance Comparison between Extruded and Printed Ceramic Monoliths for Catalysts," 2017, doi: 10.13009/EUCASS2017-349.
- [80] R.-J. Koopmans *et al.*, "Comparison of HTP catalyst performance for different internal monolith structures," *Acta Astronaut.*, vol. 164, pp. 106–111, Nov. 2019, doi: 10.1016/j.actaastro.2019.07.010.
- [81] K. Essa *et al.*, "Development and testing of an additively manufactured monolithic catalyst bed for HTP thruster applications," *Appl. Catal. A Gen.*, vol. 542, pp. 125–135, Jul. 2017, doi: 10.1016/j.apcata.2017.05.019.
- [82] C. Maleix *et al.*, "Development of catalytic materials for decomposition of ADN-based monopropellants," 2017, doi: 10.13009/EUCASS2017-479.
- [83] R.-J. Koopmans, J. S. Shrimpton, and G. T. Roberts, "Validation and Design Optimization for a Hydrogen Peroxide Thruster," Jul. 2011, doi: 10.2514/6.2011-5696.
- [84] S. Afandizadeh and E. A. Foumeny, "Design of packed bed reactors: guides to catalyst shape, size, and loading selection," *Appl. Therm. Eng.*, vol. 21, no. 6, pp. 669–682, Apr. 2001, doi: 10.1016/S1359-4311(00)00072-7.
- [85] J. Seckendorff and O. Hinrichsen, "Review on the structure of random packed-beds," *Can. J. Chem. Eng.*, vol. 99, no. S1, Oct. 2021, doi: 10.1002/cjce.23959.
- [86] F. Benyahia and K. E. O'Neill, "Enhanced Voidage Correlations for Packed Beds of Various Particle Shapes and Sizes," *Part. Sci. Technol.*, vol. 23, no. 2, pp. 169–177, Apr. 2005, doi: 10.1080/02726350590922242.
- [87] Y. Osaki and K. Takahashi, "Microfluidics of Liquid Propellant Microthruster for Pico-Satellites," *IEEJ Trans. Sensors Micromachines*, vol. 123, no. 10, pp. 436–441, 2003, doi: 10.1541/ieejsmas.123.436.
- [88] C. K. Murch and D. Asato, "Monopropellant Hydrazine Resistojet Engineering Model Fabrication and Test Task Summary Report," Greenbelt, MD (USA), 1973. [Online]. Available: <https://core.ac.uk/download/pdf/80639747.pdf>.
- [89] S. Jo, D. Jang, S. An, and S. Kwon, "Chugging Instability of H<sub>2</sub>O<sub>2</sub> Monopropellant Thrusters with Catalyst Reactivity and Support Sizes," *J. Propuls. Power*, vol. 27, no. 4, pp. 920–924, Jul. 2011, doi: 10.2514/1.B34222.

- [90] S. An, J. Jin, J. Lee, S. Jo, D. Park, and S. Kwon, "Chugging Instability of H<sub>2</sub>O<sub>2</sub> Monopropellant Thrusters with Reactor Aspect Ratio and Pressures," *J. Propuls. Power*, vol. 27, no. 2, pp. 422–427, Mar. 2011, doi: 10.2514/1.48939.
- [91] D. Jang, S. Kang, and S. Kwon, "Preheating characteristics of H<sub>2</sub>O<sub>2</sub> monopropellant thruster using manganese oxide catalyst," *Aerosp. Sci. Technol.*, vol. 41, pp. 24–27, Feb. 2015, doi: 10.1016/j.ast.2014.12.010.
- [92] W. L. OWENS, "A Combustion Stability Analysis for Catalytic Monopropellant Thrusters," *J. Spacecr. Rockets*, vol. 9, no. 3, pp. 148–152, Mar. 1972, doi: 10.2514/3.61644.
- [93] M. Popp, J. Hulka, V. Yang, and M. Habiballah, Eds., *Liquid Rocket Thrust Chambers*. Reston, VA: American Institute of Aeronautics and Astronautics, 2004.
- [94] G. Dressler, "Summary of Deep Throttling Rocket Engines with Emphasis on Apollo LMDE," Jul. 2006, doi: 10.2514/6.2006-5220.
- [95] Y. Kim, H. Kim, J. Jeong, and S. Kwon, "Dual-Plate Injector for Throttling of Hydrogen Peroxide Monopropellant Thruster," *J. Propuls. Power*, pp. 1–8, May 2021, doi: 10.2514/1.B38283.
- [96] A. Pasini, L. Torre, L. Romeo, A. Cervone, and L. D'Agostino, "Performance Characterization of Pellet Catalytic Beds for Hydrogen Peroxide Monopropellant Rockets," *J. Propuls. Power*, vol. 27, no. 2, pp. 428–436, Mar. 2011, doi: 10.2514/1.B34000.
- [97] J. Hinckel, "Development of a 115 newton thrust hydrazine catalytic thruster," Jun. 1993, doi: 10.2514/6.1993-1964.
- [98] J. Hinckel, J. Jorge, T. Soares, M. Zacharias, and J. Palandi, "Low Cost Catalysts for Hydrazine Monopropellant Thrusters," Aug. 2009, doi: 10.2514/6.2009-5232.
- [99] H. Ghassemi and H. F. Fasih, "Application of small size cavitating venturi as flow controller and flow meter," *Flow Meas. Instrum.*, vol. 22, no. 5, pp. 406–412, Oct. 2011, doi: 10.1016/j.flowmeasinst.2011.05.001.
- [100] C.-C. Chen *et al.*, "Simulation and experiment research on vaporizing liquid micro-thruster," *Sensors Actuators A Phys.*, vol. 157, no. 1, pp. 140–149, Jan. 2010, doi: 10.1016/j.sna.2009.10.025.
- [101] F. M. White, *Fluid Mechanics*, 7th ed. McGraw-Hill, 2010.
- [102] P.-F. Hao, X.-W. Zhang, Z.-H. Yao, and F. He, "Transitional and turbulent flow in a circular microtube," *Exp. Therm. Fluid Sci.*, vol. 32, no. 2, pp. 423–431, Nov. 2007, doi: 10.1016/j.expthermflusci.2007.05.004.
- [103] K. V. Sharp and R. J. Adrian, "Transition from laminar to turbulent flow in liquid filled microtubes," *Exp. Fluids*, vol. 38, no. 1, pp. 132–132, Jan. 2005, doi: 10.1007/s00348-004-0893-0.
- [104] E. V. Mukerjee, A. P. Wallace, K. Y. Yan, D. W. Howard, R. L. Smith, and S. D. Collins, "Vaporizing liquid microthruster," *Sensors Actuators A Phys.*, vol. 83, no. 1–3, pp. 231–236, May 2000, doi: 10.1016/S0924-4247(99)00389-1.
- [105] P. Kundu, T. K. Bhattacharyya, and S. Das, "Design, fabrication and performance evaluation of a vaporizing liquid microthruster," *J. Micromechanics Microengineering*, vol. 22, no. 2, p. 025016, Feb. 2012, doi: 10.1088/0960-1317/22/2/025016.
- [106] M. A. C. Silva, D. C. Guerrieri, H. van Zeijl, A. Cervone, and E. Gill, "Vaporizing Liquid Microthrusters with integrated heaters and temperature measurement," *Sensors Actuators A Phys.*, vol. 265, pp. 261–274, Oct. 2017, doi: 10.1016/j.sna.2017.07.032.
- [107] P.-W. Kwan, X. Huang, and X. Zhang, "Design and testing of a microelectromechanical-system-based high heat flux vaporizing liquid microthruster," *Acta Astronaut.*, vol. 170, pp. 719–734, May 2020, doi: 10.1016/j.actaastro.2020.01.017.
- [108] S. An and S. Kwon, "Catalyst Bed Sizing of 50 Newton Hydrogen Peroxide Monopropellant Thruster," Jul. 2008, doi: 10.2514/6.2008-5109.

- [109] F. F. Maia, L. H. Gouvea, L. G. F. Pereira, R. Vieira, and F. D. S. Costa, "Development and Optimization of a Catalytic Thruster for Hydrogen Peroxide Decomposition," *J. Aerosp. Technol. Manag.*, vol. 6, no. 1, pp. 61–67, Feb. 2014, doi: 10.5028/jatm.v6i1.286.
- [110] G. Pace, A. Pasini, and L. Torre, "PulCheR-Pulsed Chemical Rocket with Green High Performance Propellants: Second Year Project Overview," Jul. 2015, doi: 10.2514/6.2015-4058.
- [111] M. Wilson, "Demonstration Testing of a Long-Life 5-Lbf (22-N) MR-106L Monopropellant Hydrazine Rocket Engine Assembly," Jul. 2005, doi: 10.2514/6.2005-3954.
- [112] C. Nichith, P. K. P, S. Sharan, S. Mani, and V. Sanal Kumar, "Design Optimization and Performance Evaluation of A Monopropellant Satellite Thruster," Jul. 2016, doi: 10.2514/6.2016-4904.
- [113] R.-J. Koopmans *et al.*, "Additive Manufacturing of Ceramic Materials: a Performance Comparison of Catalysts for Monopropellant Thrusters," Jul. 2017, doi: 10.2514/6.2017-4603.
- [114] S. Schuh, T. Bartok, R.-J. Koopmans, and C. A. Scharlemann, "Results of material compatibility investigation of hydrogen peroxide," Jul. 2015, doi: 10.2514/6.2015-4252.
- [115] Chemical and Material Sciences Department, "Hydrogen Peroxide Handbook," 1967. [Online]. Available: [http://mae-nas.eng.usu.edu/Peroxide\\_Web\\_Page/documents/AFRL\\_TR\\_67\\_144.pdf](http://mae-nas.eng.usu.edu/Peroxide_Web_Page/documents/AFRL_TR_67_144.pdf).
- [116] H. H. Ku, "Notes on the use of propagation of error formulas," *J. Res. Natl. Bur. Stand. Sect. C Eng. Instrum.*, vol. 70C, no. 4, p. 263, Oct. 1966, doi: 10.6028/jres.070C.025.
- [117] NIST and SEMATECH, *Handbook of Statistical Methods*. 2013.
- [118] M. Santi, I. Dorgnach, F. Barato, and D. Pavarin, "Design and Testing of a 3D Printed 10 N Hydrogen Peroxide Monopropellant Thruster," Aug. 2019, doi: 10.2514/6.2019-4277.
- [119] Relativity Space, "Relativity Space Company Webpage," 2021. <https://www.relativityspace.com/> (accessed Sep. 14, 2021).
- [120] J. C. Kayser and R. L. Shambaugh, "Discharge coefficients for compressible flow through small-diameter orifices and convergent nozzles," *Chem. Eng. Sci.*, vol. 46, no. 7, pp. 1697–1711, 1991, doi: 10.1016/0009-2509(91)87017-7.
- [121] C. Song, P. Wang, and H. A. Makse, "A phase diagram for jammed matter," *Nature*, vol. 453, no. 7195, pp. 629–632, May 2008, doi: 10.1038/nature06981.
- [122] North American Stainless, "316/316L Stainless Steel Grade Sheet," 2010. <https://www.integritystainless.com/wp-content/uploads/2016/07/NAS-HR-Grade-316-316L.pdf> (accessed Apr. 15, 2020).
- [123] Granta Design Ltd., "CES EduPack." 2015.
- [124] J. R. Rumble, Ed., *CRC Handbook of Chemistry and Physics*, 102nd ed. CRC Press, 2021.



# Appendix A

## Experimental Data Analysis Techniques

This appendix covers the methodology and techniques for the analysis of experimental testing. This is different from the performance metrics discussed in Chapter 2 and focuses more on the extraction and processing of the raw data to determine the steady state, quasi-steady and transient phenomena, and other derived results. This Appendix covers:

- A.1 – Preliminary Data Processing: Initial preparation of the raw data.
- A.2 – Steady State Determination.
- A.3 – Regression Fitting and Convergent Analytical Model.
- A.4 – Spectral Analysis.
- A.5 – Signal Correlation.

Each section contains an overview of the algorithm or analysis technique, but the specific information of their application and interpretation of the results is given where they are used in the main body of the thesis.

It is important to introduce the typical experimental data to highlight the different features of a test. A standard thruster test is run for 60 s, aiming to capture start-up and steady state performance. Figure A.1 shows an example of a test, demonstrating the expected shape of the data for each of the instrumentation channels. Each test is split up into four main regimes, listed in Table A.1 along with their expected length and synchronised time stamps. The goal of standardising the raw data sets is to simplify the data analysis, increasing the rigour of the analysis and to remove the dependence on human objectivity or bias.

In general, the raw data is well-conditioned, with consistent and predictable data for each instrumentation channel. In this case the processing is superficially trivial, however there are a number of inconsistent physical phenomena that complicate the analyses. These are discussed in Section A.1.

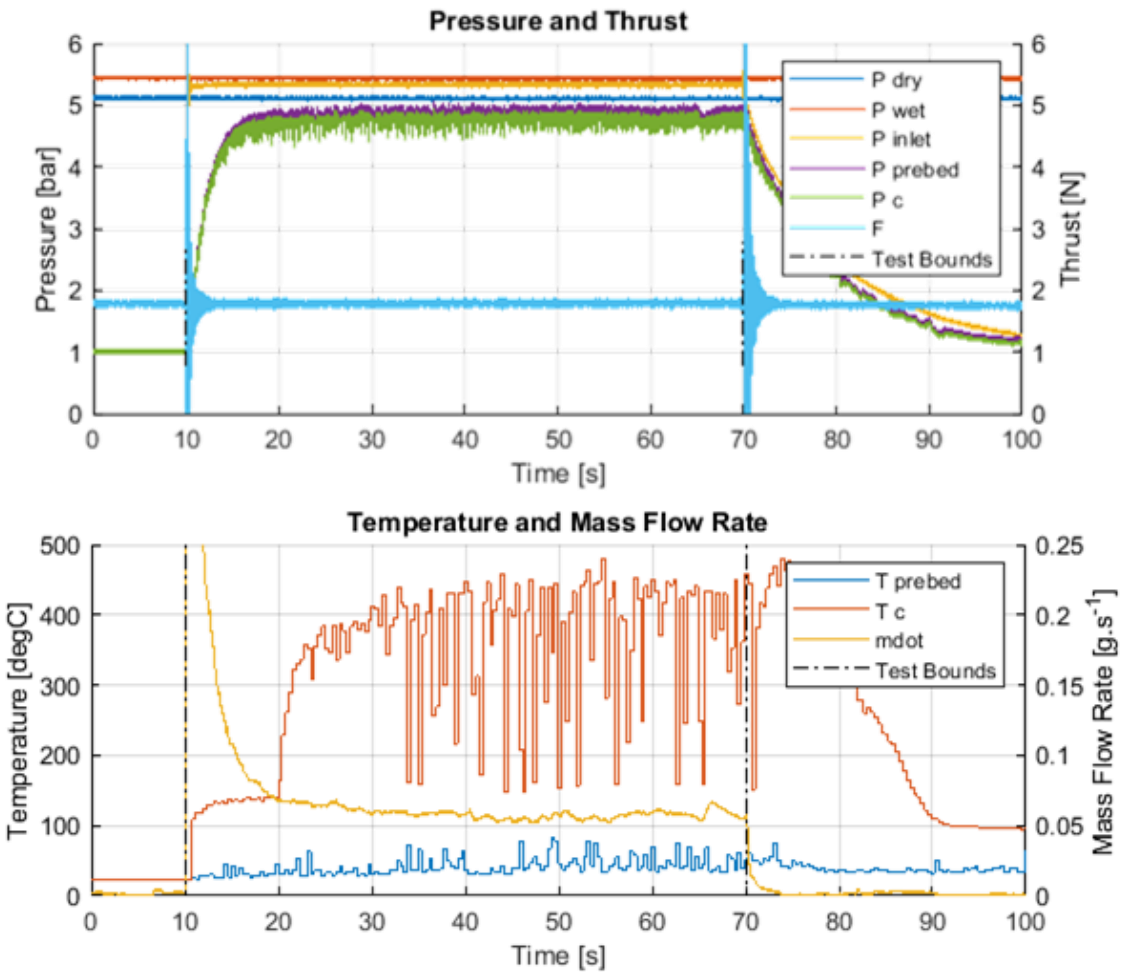


Figure A.1 – Example plots of the data from a typical thruster run.

Table A.1 – A list of the main operational regimes of a standard thruster test.

Regime	Typical Length [s]	Synchronised Time [s]	Description
Pre-Fire	10	0 – 10	Thruster baseline period with no propellant flow.
Firing	60	10 – $\tau_{90}$ *	Transient period where the thruster reaches nominal operational conditions
		$\tau_{90}$ – 70	Nominal thruster operation.
Shutdown	30	70 – 100	Transient post-firing operation where thruster bleeds down.

\*  $\tau_{90}$  is the time between the test start (valve actuation) and the signal reaching 90 % of the steady state value.

## A.1. Preliminary Data Processing

### A.1.1. Data Preparation

The data preparation step is essential to take the raw data and convert it into a standardised format. This includes a step to verifying the calibration of the data in each channel. The time-domain is synchronised to the opening actuation of the firing valve (SV3), detected as a sharp peak in the first order time differential of the inlet pressure transducer signal,  $dP_{in}/dt$ . This is shown in Figure A.2, with the two peaks aligned at 10 s and  $\sim 70$  s, corresponding to the firing valve (SV3) opening and closing at either end of the test. The  $dP_{in}/dt$  dataset is calculated using a centred sliding window algorithm, linearly regression fitting to 3 data points in the time and inlet pressure data:  $[ t_i \ P_{in_i} ]$ . Here the index  $i$  is incremented to sweep the window through the data. The algorithm uses the MATLAB `mldivide()` function to solve for the linear equation:

$$\mathbf{Ax} = \mathbf{B} \quad (\text{A.1})$$

$$\begin{bmatrix} 1 & t_{i-1} \\ 1 & t_i \\ 1 & t_{i+1} \end{bmatrix} \begin{bmatrix} b \\ a \end{bmatrix} = \begin{bmatrix} P_{i-1} \\ P_i \\ P_{i+1} \end{bmatrix} \quad (\text{A.2})$$

The resulting vector  $x$  gives the linear parameters, such that  $P_i = at_i + b$ , therefore giving the differential  $P_i = a \equiv dP_{in}/dt$ . The peaks are identified by sweeping from the highest  $dP_{in}/dt$  value, until two peaks are found. To account for noise, the two peaks must be separated by a minimum test time of 10 s. This algorithm is robust even in the case of significant pressure roughness in the  $P_{in}$  signal, or in the case of flow coupling across the injector, and therefore allows the exact time specification to the nearest sample (1 kHz for the pressure transducers).

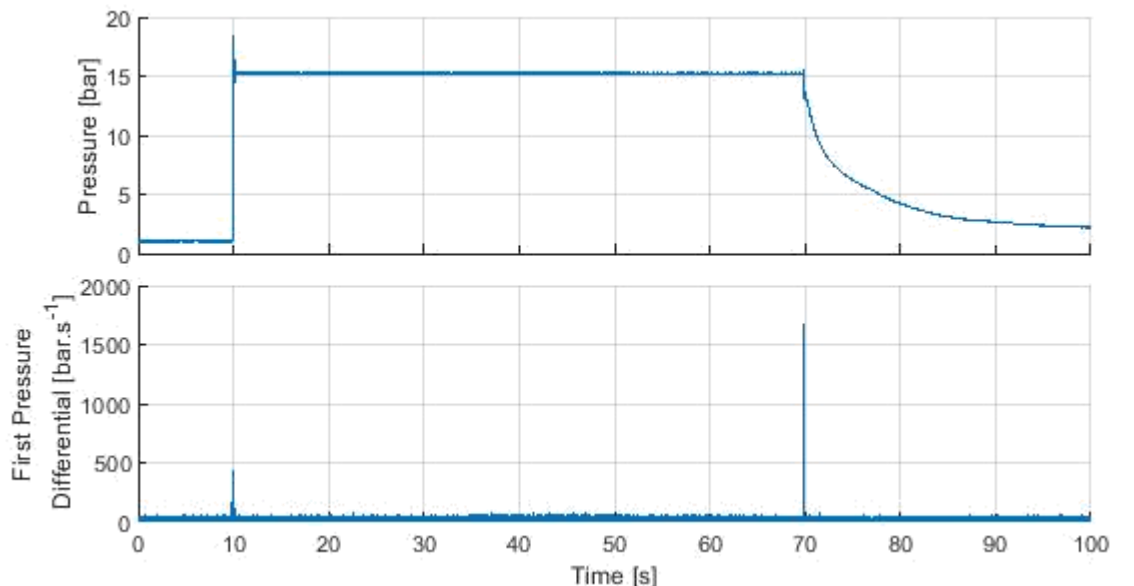


Figure A.2 – A typical plot of the inlet pressure signal and its time differential, demonstrating the actuation detection method.

### A.1.2. Experimental Phenomena

The experimental phenomena affecting the data and processing methods are grouped into quasi-steady and transient phenomena. The phenomena in the former quasi-steady category will generally affect the whole run, while those in the latter transient category are usually marked by notable changes in the operational mode of the thruster. Establishing the impact that these effects have on the data informs on how best to handle them in a robust process: they may be manually removed but this introduces potential bias, so an automated algorithmic method is preferable.

#### Quasi-Steady Phenomena

The main quasi-steady phenomenon of interest is signal roughness, which is implicitly handled when determining the steady state, discussed in Section A.2. However, there are quasi-steady changes in time domain steady state data that act over a long period of time. This effect is particularly apparent in both the hot fluid temperature and mass flow rate signals, with examples of both shown in Figure A.3. Over long tests, the pressure may drop noticeably, although in most cases the magnitude of the pressure roughness is higher than the decrease. The change in pressure and mass flow rate are attributed to the blowdown of the driving pressure. The PDS was operated in a blowdown mode to prevent any sharp changes in the signals due to the actuation of the bang-bang pressurant. The temperature change is due to the gradual increase in the temperature of the thermal mass of thruster materials and environment.

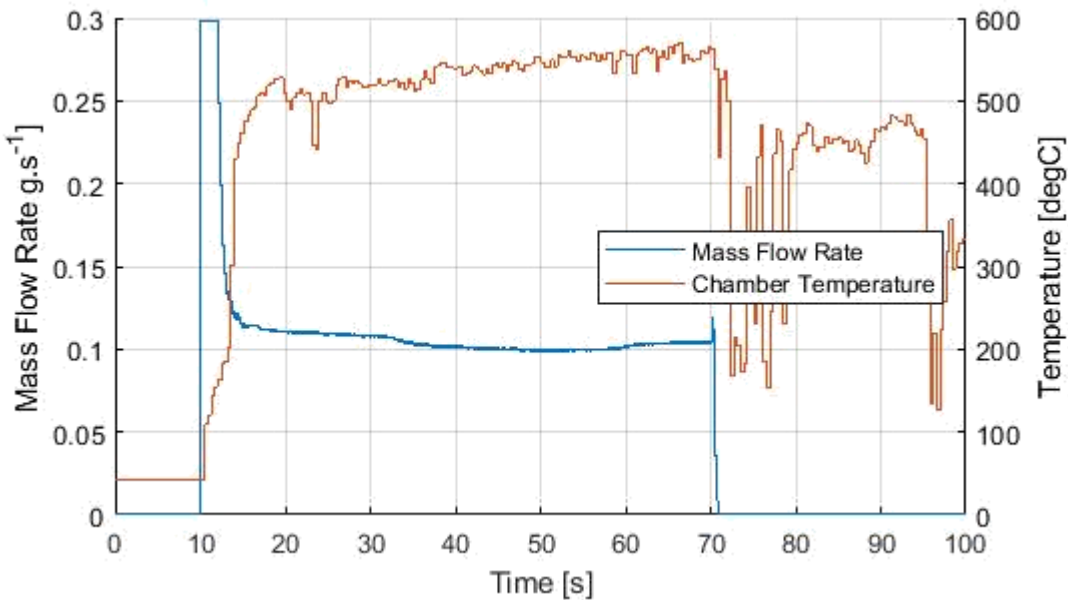


Figure A.3 – An example of the quasi-steady trends affecting signals throughout a test.

Unfortunately, it is difficult to account for the quasi-steady phenomena that act over the whole run. The data can be detrended, i.e. the gradient can be removed. However, this does not resolve the location of the true steady state: This value can be picked from any point within the range between the minimum and maximum of the ‘steady state’ period, most often the start and the end of the period respectively. It can be reasoned that the start of the run represents the pure response

from the catalytic decomposition, although this makes determining the steady state difficult since the start-up is defined by the steady state value:  $\tau_{90}$  is the transient between the start of the test and 90% of the steady state value. Alternatively, in some literature the steady state values use a time period at the end of the run [12], representing the highest performance of the system, although this also includes significant heating of the thermal mass of the thruster. This could represent the nominal performance of a preheated catalyst bed but it is difficult to account for the preheating temperature. Even in this case the data from literature show that there is some transient required to reach an equilibrium state.

The approach chosen in this work is to consider the effect of the quasi-static drift along with the instrumentation uncertainties and the signal roughness, i.e. to include any drift in the  $1\sigma$  uncertainty bounds. This accounts for the expected systematic change in the 'steady state' over the run but will overestimate the spread of the data. This should be a fairly minor increase in the spread of the steady state roughness.

### **Transient Phenomena**

The other category of atypical experimental phenomena are transient changes in the operational mode during the firing. In most cases they are inconsistent between runs even for identical operational conditions. They have been categorised by their apparent cause and effect on the specific data channels, listed in Table A.2, with examples shown in Figure A.4. Note that some of these are effects of the experimental set-up while others result from the specific operational conditions. Unlike with the quasi-static phenomena, these must be removed from the data before the statistical analysis.

Protracted start-up and flooding represent sudden changes in the operational mode of the thruster. These affect the start and end of the test, and they cause significant impact to the quality of the data. The protracted start-up is an initial period of lower temperature operation where the thermal mass of the thruster is insufficient to raise the bulk fluid enthalpy above the latent heat of vaporisation, so the fluid is kept in a pseudo steady state at  $\sim 140$  °C. Once the thruster has enough latent heat the temperature rises rapidly up to the true steady state. Given that the steady states are extracted using a GMM (see Section A.2), this initial period will appear as a second lower peak and can be ignored. However, many of these tests were lengthened to allow the system to reach the steady state: the temperature clearly does not stabilise in the nominal-length example test in Figure A.4.

Flooding of the catalyst bed is a sudden breaking of the nozzle choking condition by entrained liquid. This implicitly defines the end of a test. Since the nozzle choking condition sets the mass flow through the system, flooding causes the mass flow rate to increase rapidly as the chamber pressure drops. The influx of cool propellant also cools the bed. These can be seen in the example data in Figure A.4. The transition is clearly identified by the first order time differentials of the mass flow rate and chamber pressure channels, using the same algorithm as tagging the firing valve (SV3) actuation presented in Section A.1. Note that this is a semi-automatic process since this is only applied to tests tagged as flooded, which was noted during the experiment: flooding can be identified

by a steamy multiphase plume. These tags were checked manually to confirm the phenomenon in the data.

The pulsed steamy plume phenomenon does not have a significant impact on the data processing since the resulting transients can be readily distinguished and are easily filtered out. The effect results in a pulsed drop in the chamber temperature signal, with no noticeable impact to the other instrumentation. This is seen in the example data in Figure A.4 and is most likely caused by condensation of the water in the exhaust gases in the chamber instrumentation standpipe. This builds up over the run and dribbles back into the thruster heavily cooling the chamber thermocouple and passing through the nozzle. This is not possible to prevent if the standpipe is included, although in the majority of cases with otherwise stable, high temperature operation this does not affect the performance. This is automatically filtered out by the steady state GMM algorithm (see Section A.2), and in some extreme cases appears as a second 'steady state' peak in the chamber temperature signal.

Table A.2 – A list of non-typical non-steady state operational modes affecting some thruster runs, including the significance of the apparent cause to the operation of the catalyst bed (i.e. a flight-optimised thruster design rather than the experimental lab thruster).

Mode	Apparent Cause	Performance Impact	Affected Period	Affected Channels	Effect
Protracted Start-up Transient	Excessive bed loading, larger thermal mass	Yes Minimum Bed Loading	Start of firing	Chamber Temperature	Delayed and Stepped Increase
Catalyst Bed Flooding	Flooding	Yes Maximum Bed Loading	Any time, End of firing *1	Pressure	Rapid Increase
				Temperature	Rapid Decrease
				Mass Flow Rate	Rapid Increase
Pulsed Steamy Plume	Liquid in chamber standpipe	No Instrumentation Issues	Generally > 30 s into firing	Chamber Temperature	Transient Decrease

\* Flooding may occur at any point, but as it catastrophically degrades the performance, this also coincides with the end of firing. This may be before the full run has elapsed.

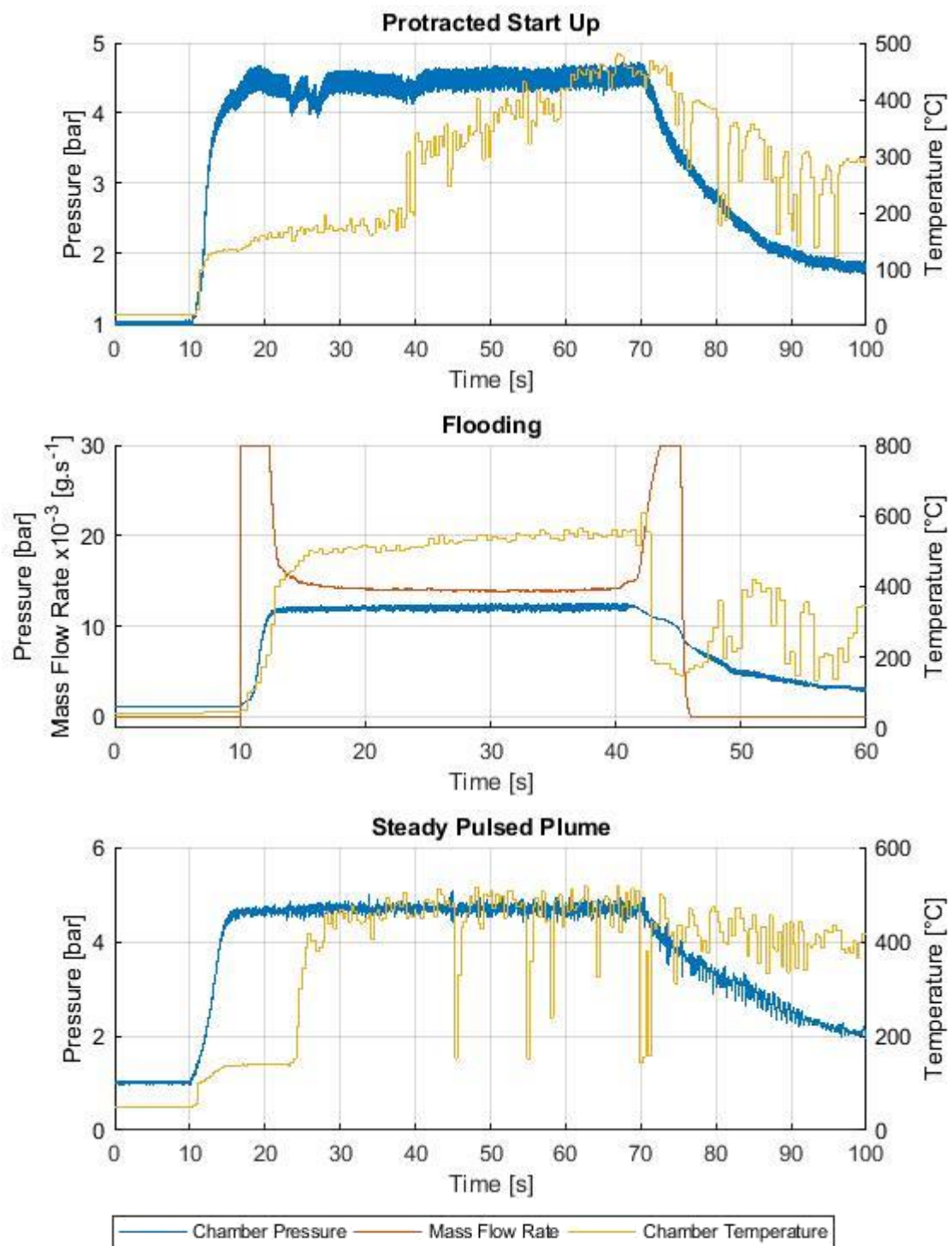


Figure A.4 – Examples of the non-typical transient modes showing the protracted start up (top), catalyst bed flooding (middle), and the pulsed steamy plume (bottom).

## A.2. Steady State Determination

Most of the propulsion performance metrics are steady state, i.e. representing the stable thruster performance. As discussed, a robust automatic algorithm to determine the steady state conditions in the thruster is necessary to prevent any human selection bias. Simple statistical methods are not suitable given the transient effects discussed. Instead, a more robust technique uses a GMM applied to a histogram of the entire set of time domain data, clipped to the actuations of the thruster firing valve (SV3), applied to each channel. This identifies multiple subpopulations in the data along with their gaussian (normal) statistical parameters automatically. Where necessary, the decomposition of each subpopulation of data in a channel, and the extraction of the steady state parameters from the specific corresponding peak can be used to filter out pseudo steady state regimes or poorly conditioned data, for example protracted start-ups and the pulsed steam plume phenomena respectively. These 'false' steady states can be easily identified since they are below the real steady state peak. Note that this may not necessarily be true for the mass flow rate data, however there were no examples of falsely identified steady state data in any of the tests.

An example of the chamber temperature channel with multiple transient modes, along with the histogram with decomposed peak normal fits is shown in Figure A.5. This example shows a data including the protracted start-up and pulse plume phenomena. Both peaks in the normal distribution are visible in the GMM model overlaid on the histogram, with the mean and  $1\sigma$  spread plotted as error bars on the time domain data. Note that as discussed in Section A.1.2, there is a quasi-steady increase in the temperature over the run due to the increasing temperature of the thermal mass of the thruster. This is included in the statistical spread. In this example, the GMM technique yields a steady state temperature (the upper peak) of  $542 \pm 83$  °C, which is particularly broad since the pulsed phenomenon in this example also corresponds to significant roughness throughout the test.

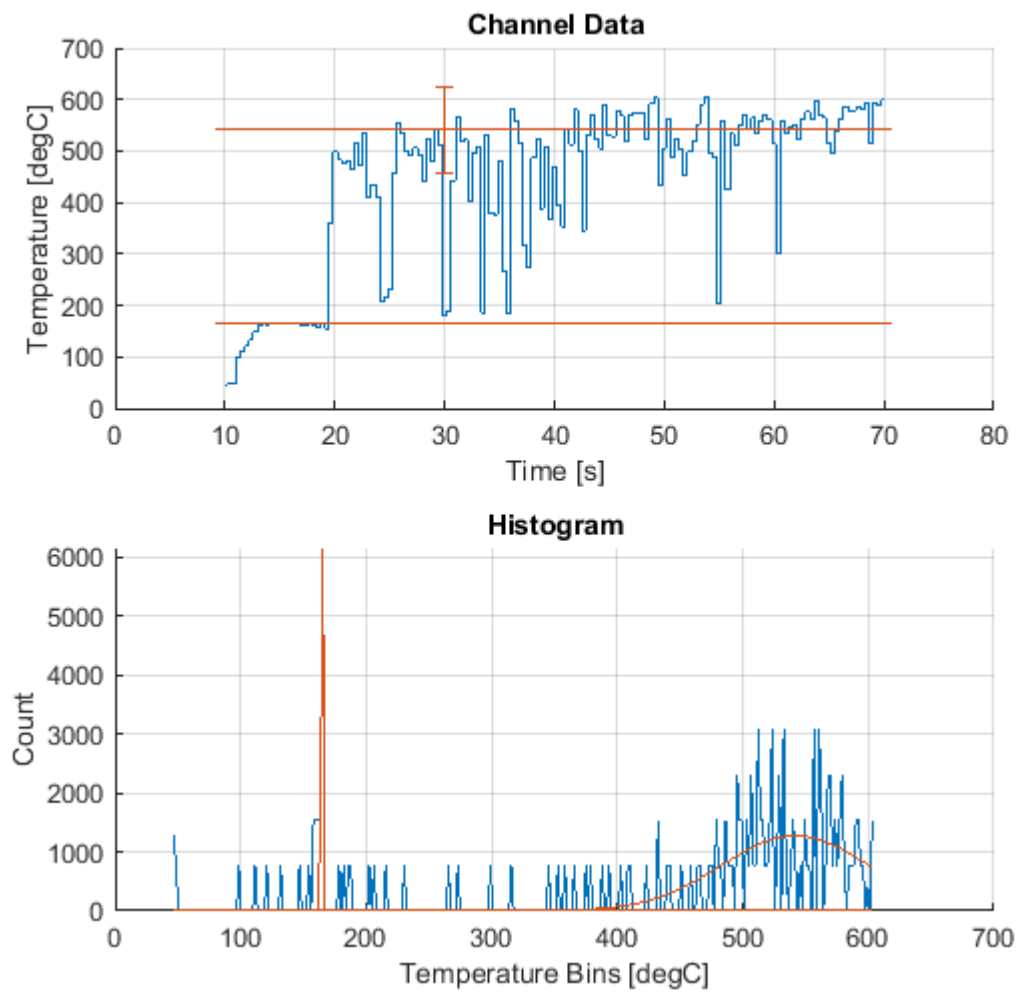


Figure A.5 – An example of the steady state analysis method results for a chamber temperature plot. This shows the time domain (top) and histogram data (bottom) along with the two resulting steady state regimes.

### A.3. Regression Fitting and Convergent Analytical Model

Regression fitting is a common technique to model data with simple analytical expressions. While many of the trends in the data are linear, there are a number of sets of data, notably the catalytic thermal efficiency and characteristic velocity efficiency results, that use non-linear models. To generalise the regression fitting algorithm, a non-linear technique using the ordinary least squares method, is employed here [117]. This iteratively minimises the sum of the squared residuals, and is calculated using the MATLAB `fit()` method.

An example of a non-linear analytical model is a convergence fit, used throughout this thesis. In this example the general unconstrained form of a suitable model equation is:

$$f(x) = a - b \exp(-cx) \quad (\text{A.3})$$

Where  $x$  is the dependant variable and  $a$ ,  $b$  and  $c$  are fitting coefficients. Here  $a$  represent the convergent value (limit) as  $x \rightarrow \infty$ ,  $b$  affects the position of the inflection point in the  $x$  axis, and  $c$  represents the rate of convergence or the curvature of the function. While this model can be useful in this form, it is often useful to constrain the model. One constraint is to fix the  $y$ -intercept such that the model has a known value,  $f_0$  at  $x = 0$ . Allowing for coefficients  $a$  and  $c$  to vary, the model equation becomes:

$$f(x) = a - (a - f_0) \exp(-cx) \quad (\text{A.4})$$

In this form the shape of the function is free to change about a known  $y$ -intercept, for example a known condition for when there is no mass flow rate. As with any other non-linear function, this can be fitted to experimental data. One additional feature of the regression fitting method is that confidence margins can be calculated for the coefficients. This provides a statistical measure of the fitness of the model beyond a standard  $R^2$  value.

## A.4. Spectral Analysis

Some of the quasi-static and transient performance metrics, for example the injector coupling and pressure roughness, benefit from spectral analysis in addition to the statistical results from the steady state data. In this work, an FFT algorithm is applied to the raw data to extract the spectral data in the frequency domain, which can be decomposed to analyse the frequency peaks. This is an involved process, so the theory is broken down in the following section.

### *Fast Fourier Transforms*

An FFT algorithm calculates the DFT of a signal, in this case transforming the data from the time to the frequency domain. This allows for analysis and comparison of the different frequencies and relative magnitudes of the components present. The frequency resolution of the resulting spectrum is fundamentally tied to the sampling rate, defined as:

$$dF = \frac{F_s}{N} \quad (\text{A.5})$$

Where  $dF$  is the width of the frequency bin,  $F_s$  is the sampling frequency and  $N$  is the number of data samples input into the FFT algorithm. The frequency resolution should be maximised, so a higher sampling frequency and longer signal is ideal. The data rate of the DAQC system is fixed to its maximum at 2 kHz, although most of the instruments have much lower resolvable data rates. The only way to increase the resolution is to increase the number of samples in an input signal, i.e. the signal length.

The DFT frequency domains are similarly bounded by the dataset parameters: the lowest resolvable frequency, and the upper bound (the Nyquist frequency), respectively given by:

$$F_{min} = \frac{1}{t_w} \quad (\text{A.6})$$

$$F_{max} = \frac{F_s}{2} \quad (\text{A.7})$$

Where  $t_w$  is the width of the input sample (time domain units), i.e.  $t_w = N/F_s = 1/dF$ . These limits result from the frequencies of the waveform that can be resolved given the parameters of a specific data sample. It is important to note that when frequencies are present in the raw data above the Nyquist frequency, digital aliasing will be apparent in the DFT. This is where false frequency peaks appear in the data due to synchronisation of the sampling rate and the higher true frequencies. The best way to mitigate this is to increase the sampling rate far above the expected frequency range of interest. This means that the 1000 Hz pressure signals are unlikely to have aliasing in the typical  $10 \text{ Hz} \leq F_q \leq 400 \text{ Hz}$  range for 'chugging' [11].

### *Time Domain Windowing*

A DFT will implicitly treat the input signal as periodic, i.e. that the data is a finite segment of an infinitely repeating signal. This means that any non-periodic signal may appear to have a false frequency in the output spectrum. These frequencies will be of the order of the length of the window so discontinuities of a similar size will be amplified. A method for handling this is to use a sliding

window algorithm resulting in a series of DFTs over the time domain. In this case the window can be sized such that the non-periodic effects can be minimised. Here a width of the window, i.e. the number of samples  $N$ , is selected so that it only captures quasi-periodic data. This has the added bonus of showing potential variations in the frequency domain at different times through the original dataset.

It is important to consider the effect of reducing the signal length in the frequency domain: as the window truncates the input signal into the FFT algorithm in terms of the time and number of data points, the spectral resolution will decrease while the minimum resolvable frequency will increase, as per Equations (A.5), (A.6) and (A.7). There is therefore a trade-off between the frequency and temporal resolution: a wider window will improve frequency resolution but will degrade the time resolution and discontinuous data is ‘smeared’ across the window. Conversely narrow windows reduce this ‘smearing’, improving the time resolution but reducing the resolution in the frequency domain. An example of the effect of the window width is given in Figure A.6, which highlights the trade between the resolution and the ‘smearing’, especially around the highly discontinuous regions during start-up and shutdown. In this Figure, the time domain of a raw chamber pressure dataset is plotted, with the sliding window applied over the data to extract the DFT spectrograms. In these spectrograms, the colour represents the amplitude of the frequency response. The three spectrograms use different sliding window widths, 0.025 s, 0.25 s and 1 s, and the relative resolution in the time and frequency domains (the  $x$  and  $y$  axes respectively) is apparent. Selecting the appropriate width of the windows is therefore important based on which domain requires the higher resolution, and the frequency of periodic effects and discontinuities.

The raw data from the instrumentation still have significant non-periodic and discontinuous trends in the raw signal dataset which cause false frequency peaks in the DFT. Linear trends are relatively easy to remove by using a detrending function (MATLAB’s `detrend()`), which uses linear regression to normalise the points in a dataset around the mean value. This has a negative impact on the accuracy of the resulting DFT amplitude, especially when correcting for large trends, however it improves the accuracy of the peaks in the frequency domain. It should be noted that this does not remove non-linearities in the data, for example during the start-up regime. In this case the rapid non-linear change of the signal causes a curve that cannot be easily removed from the data: linear detrending will just transform it around the mean value. The result is a wide band of low frequency peaks in the resulting spectrograms, which decrease moving away from the 0 Hz bin. The easiest method to remove them is to clip the data in either the time or frequency domain. In the example in Figure A.6, the minimum 10 Hz bound removes most of these issues, but also prevents analysis of the data below this boundary.

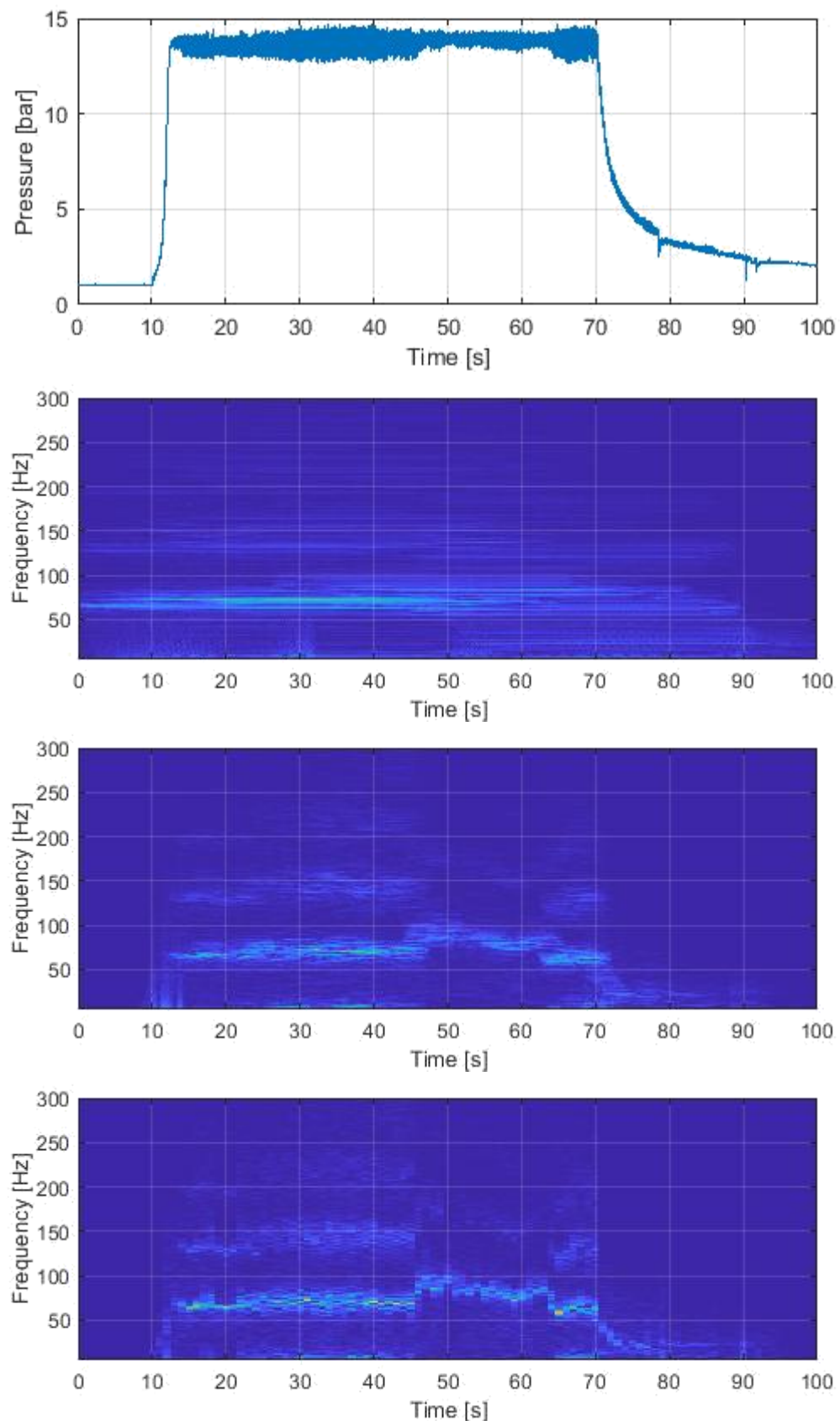


Figure A.6 – An of the effect of width of the window on the amplitude-normalised spectrograms of a chamber pressure dataset. The window sizes are 0.025 s, 0.25 s and 1.0 s respectively, with the frequency domain clipped between 10 Hz and 300 Hz.

The apparent frequency response of the non-linear trends may be discounted by using a small window width relative to the rate of change of the mean signal. In this case, if there is a non-linear trend that has fewer than two inflections, the discontinuity will appear in the spectrum as a peak at  $F_{min}$ . The data below this frequency can be discarded to remove these effects. In practise, the frequency peak will have some ‘spectral leakage’, where energy appears to leak into adjacent frequency bins. This is a result of discontinuities in the endpoints of the sample which are discussed in the Section on Windowing Functions below. Given the leakage, for the spectral analyses in this work, an arbitrary high-pass filter is used to truncate the lower frequency bound to  $Fq \geq 10$  Hz as this is found to reliably remove these peaks and no physical phenomenon is expected in this frequency range. This removes any data below this boundary, although given the low frequency noise from the discontinuities, any frequency peak in this range would be difficult to distinguish as real data.

### **Windowing Functions**

The spectral leakage is a direct result of the windowing process and discontinuities between the endpoints of the window: Even in the case of a periodic function, if the window is not aligned to the waveform, i.e. there is a non-integer number of cycles in the window, the resulting DFT will appear to have some frequency components in adjacent frequency bins. This is illustrated by the simple sinusoidal example given in Figure A.7 but for real data, the effect may be significant enough to preclude accurate peak determination as the noise in the resulting DFT function may obscure the shape. In the figure, the DFTs of three single frequency sine signals with integer and non-integer cycle numbers show the effect of this discontinuity.

From Figure A.7, when there is an integer number of waves in the window (the left subplot), the resulting peak is sharp and there is no leakage to adjacent frequency bins. If there is a non-integer number of waves in the window (the centre subplot), the FFT algorithm will not be able to resolve the waveform over the ends of the window: An FFT algorithm implicitly assumes that the waveform in the window will repeat to infinity. In this case, stacking multiple discontinuous waveforms will result in apparent frequency components in other bins. These are seen as ‘lobes’ on either side of the central peak of the true frequency component. In the example case in Figure A.7, the peak central frequency is still clearly in the 1 Hz bin, but for more complex waveforms this can be much harder to distinguish. This spectral leakage can be somewhat mitigated by the use of a windowing function.

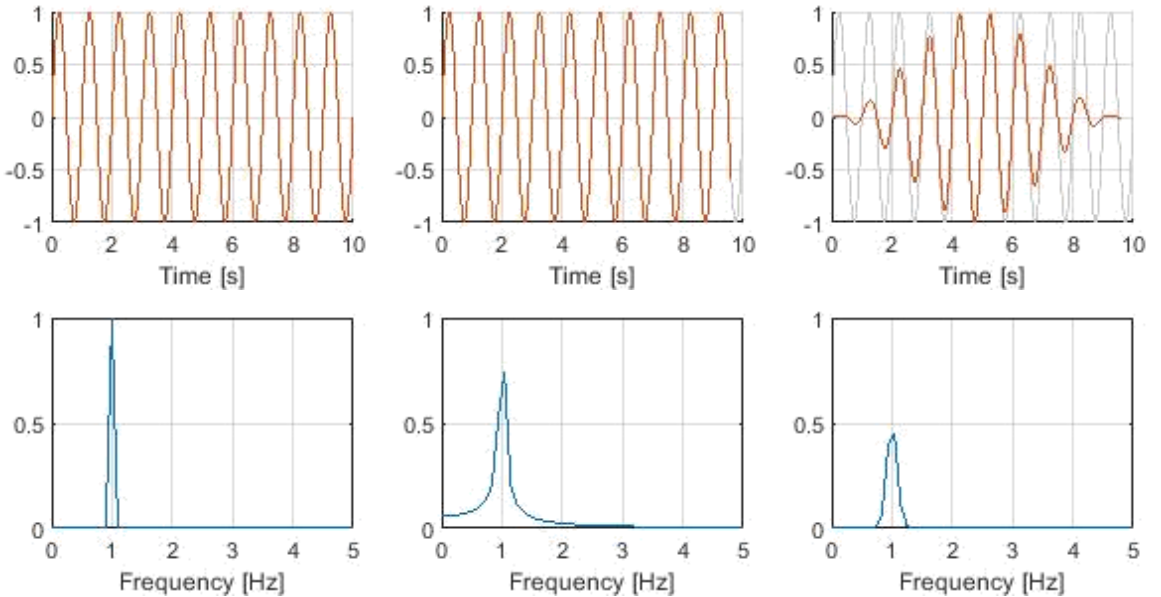


Figure A.7 – An illustration on the effect of discontinuities in windowed sinusoidal signal (top), and the resulting DFT (bottom). The windowing function example uses a hanning function.

It is common to use a windowing function to increase the peak sharpness to permit more accurate peak detection. Using a strict definition, the windowing procedure discussed so far uses a rectangular windowing function: i.e. where the dataset is multiplied by a ‘rectangular’ function which returns 1 inside the window, and 0 outside of the bounds. This considers all of the data in the window equally, but by decreasing the weighting of the data closer to the edges of the window, the FFT algorithm will ‘smooth’ the discontinuities and reduced spectral leakage. An example of the effect of this on the simple non-periodic sine is included in Figure A.7. The window function applied here is known as a ‘hanning’ or ‘Hann’ function, which is evaluated as  $w(n)$  in the window  $0 \leq n \leq N$  using the function:

$$w(n) = \frac{1}{2} \left( 1 - \cos \left( \frac{2\pi n}{N} \right) \right) = \sin^2 \left( \frac{\pi n}{N} \right) \quad (\text{A.8})$$

Here the window width is  $N + 1$  samples and the resulting function will evaluate between 0 and 1, with a single peak at the middle of the window ( $N/2$ ), and smoothly touching 0 at  $n = 0, N$ . In the example data in Figure A.7 the windowed signal and resulting DFT show a reduction in the spectral leakage. This is a trivial result for a system with a single frequency, but for more complex signals with multiple peaks and bands of frequencies, this can be essential to accurately resolve the centre frequencies of the peaks.

The hanning windowing function is one of the most common functions for signal processing, and there is a large selection of others which may be chosen depending on the specific application. The selection is made by trading off the relative shapes and fall offs of the main and side lobes especially focusing on the importance of the frequency and amplitude resolutions, which is an expansive topic of its own. The spectral analysis in this work focuses on comparison of the peak frequencies where the peaks are generally distinct. Therefore, a standard hanning window is suitable and is used throughout the spectral analysis in this work. However, it is important to note that, as illustrated in

Figure A.7, windowing functions destroy the specific amplitude of the DFT and is only used as it can help resolve peaks. Note that the amplitude contains information about the energy in certain frequency components, so may be useful in analysis of the signal roughness outside of the current scope. In the current work, the  $1\sigma$  roughness of the steady state is used to assess the energy in the high frequency data.

### ***Spectral Decomposition***

Even after selecting the window parameters to improve the peak sharpness and frequency resolution, in general the DFTs are not 'clean' enough to allow for easy peak detection and there may be some significant variation throughout the time domain, even between time-consecutive windows. To allow for robust and repeatable analyses, the spectral decomposition algorithm uses a GMM to determine the significant peaks in each time window. This gives the mean frequency and standard deviation of a specified number of peaks for each time window, but additionally includes the magnitude of each. The statistical data on the frequency peaks from each time window are aggregated, and the full dataset over the entire test is analysed using the steady state algorithm discussed in Section A.2. The result is a list of the significant steady state peaks over the run which can be ranked or filtered based upon either the occurrence or the mean amplitude of the peaks.

## A.5. Signal Correlation

The correlation between two signals is used to quantify the coupling between different signals in the system. This compares the spectral response of different pressure channels to determine the pressure coupling through the injector and catalyst beds. This method uses the Pearson Correlation Coefficient, calculated from two data vectors using the MATLAB `corrcoef()` function, which gives a measure of the correlation between two random variables [117]. The correlation is calculated from the covariance:

$$\text{cor}(X, Y) \equiv \frac{\text{cov}(X, Y)}{\sigma_X \sigma_Y} \quad (\text{A.9})$$

Here the independent variables are  $X$  and  $Y$ , with their respective standard deviations  $\sigma_X$  and  $\sigma_Y$ . The correlation coefficient is a single number between -1 and 1, where the magnitude represents the strength of the relationship, and the sign indicates whether they are correlated or anti-correlated, i.e. a matching or opposite trend respectively. In the case of the current work, correlation should fall between 0 and 1, where a correlation of 0 implies that the signals are completely un-coupled and a value of 1 represents fully coupled data. Note that this does not capture whether the spectral data are attenuated, i.e. two channels could be strongly correlated but the amplitudes, i.e. the strength of the oscillations could be dissimilar.

In the case of the pressure coupling, where the correlation coefficients are calculated from each DFT across the time domain, the result is not a single number, but rather a function of the correlation of the signals with respect to time. An example of two different time-dependant correlations of the injector pressure drop is given in Figure A.8, where one has a strongly correlating signal over the duration of the test, and the other is weakly correlated. This gives a quantitative description of how coupled the frequencies are across the injector. Note that the steady state signal correlations are included in the figure, determined the steady state algorithm discussed in Section A.2.

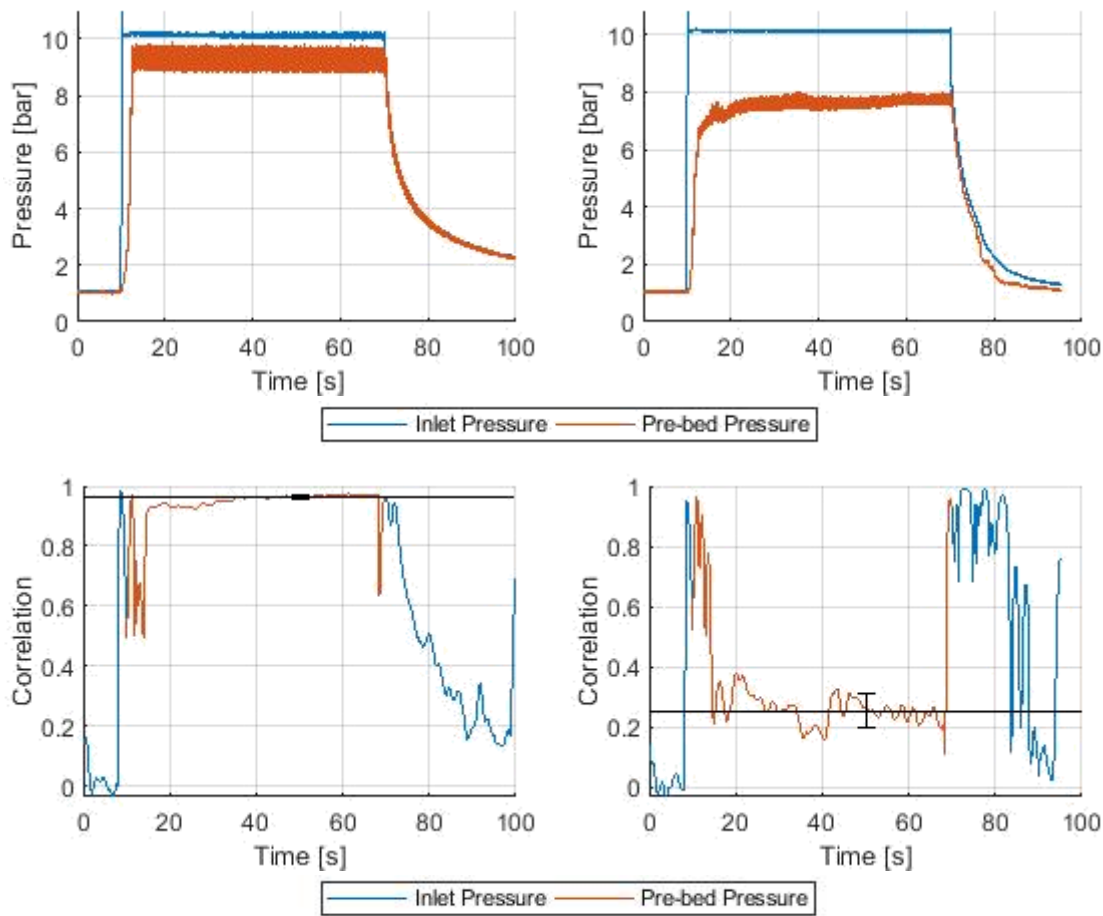


Figure A.8 – Examples of signal correlation outputs comparing the injector frequency coupling for strongly and weakly coupled systems.

# Appendix B

## Injector Computational Modelling

### B.1. Injector Computational Modelling

The experimental testing of the microinjectors in Chapter 7 is limited by the instrumentation which can only report the bulk fluid conditions upstream and downstream of the injector. This precludes any investigation into the local microscale flows, especially at the entrance and exit of the injector. A computational model can be used to validate some of the assumptions and conclusions drawn from the experimental results, while also providing insight into the local flows and processes in the injectors. This includes replicating the experimental flow characterisation as well as the local static pressure in the orifice injector.

This appendix discusses the computational model and methodology for this investigation. The model is heavily simplified and uses time-dependant multiphase laminar flow equations on a simple axisymmetric coordinate system. The model relies on the assumption that:

- The flow should be laminar.
- The flow can be described by an axisymmetric model, i.e. there are no rotational flow components.
- The fluids are idealised, i.e. incompressible liquids, ideal gases, no phase transitions.
- Multiphase fluids are separated by distinct boundaries.

The axisymmetric geometry cannot model a showerhead orifice injector, so the simulation results are limited to single port injectors. The operation of multi-port injectors should not affect the cold-flow results. The multiphase flow modelling was included since surface tension effects were originally expected to impact the results at the low flow rates, although the results do not show any evidence of this. It is important to note that phase changes, i.e. cavitation, are not modelled.

The model is built using the COMSOL Multiphysics commercial modelling software, since it was initially envisaged to include multiphysics simulation components, although the scope was reduced. The time-dependant/unsteady flow model was also a product of descoping: the computational investigation was intended to investigate the unsteady 'chugging' phenomenon, including downstream transient pressure fluctuations.

## B.2. Simulation Specification

The different injectors are modelled with a simplified parametric geometry matching the Poiseuille injector architecture, i.e. a flow constriction defined by a length and diameter. An ideal orifice injector plate will be analytically ‘thin’, i.e. with no thickness, but this model more closely matches the real components with a 50  $\mu\text{m}$  length. An example of the model geometry is shown in Figure B.1, in this case 50  $\mu\text{m}$  diameter  $\times$  50  $\mu\text{m}$  length, equivalent to a 1-50-50 orifice injector. The figure shows overlayed partitions of important flow regions and an example representative mesh (coarse for visualisation):

- The upstream bulk region, under high pressure with laminar slow-flowing fluid. The mesh here is relatively coarse as the flow is not expected to have any small flow features.
- The upstream injector entrance, under high pressure but with rapid acceleration of the flow into the injector hole. The mesh is much finer here, especially around the corner of the entrance to resolve the rapid change in flow direction and possible recirculation or cavitation region. The corner has a 1  $\mu\text{m}$  radius to help simulation convergence and reduce the effect of singularities.
- The injector throat, with a pressure gradient along the length. The mesh density here is between the coarse and fine settings: for longer injectors (i.e. Poiseuille), the flow is expected to be laminar and along the axial direction, however in the figure the mesh appears coarser given the influence of the entrance and exit regions.
- The downstream injector exit/fluid jet, under low/ambient conditions with an initial fluid phase boundary between the ambient gas and the propellant bubble or jet. The mesh in this region is finer than in the throat to capture any exit effects. The corner also has a 1  $\mu\text{m}$  radius as with the inlet.
- The downstream bulk region, under ambient low-pressure conditions, dominated by the ambient fluid with the expected phase boundary of the working fluid bubble/jet. The mesh here is coarse as this region should have negligible impact on the upstream flow.

The upstream and downstream bulk fluid regions are large compared to regions of interest near the injector, to reduce in impact of the boundaries on the flow. The radial wall dimension is  $15 \times R_{inj}$ , e.g. for a 50  $\mu\text{m}$  diameter injector, the radii of the region boundaries are 0.75 mm. The upstream and downstream regions have nominal axial lengths of 0.5 mm and 0.8 mm respectively. A preliminary sensitivity test was performed to demonstrate that the dimensions of these regions didn’t affect the flow, here a test of  $20 \times R_{inj}$  and 1.0 mm with a 1-50-50 injector showed no significant difference in the measured mass flow rate or flow field. This process is discussed in more detail in the mesh sensitivity analysis in section B.4, along with the definitions of the mesh refinement.

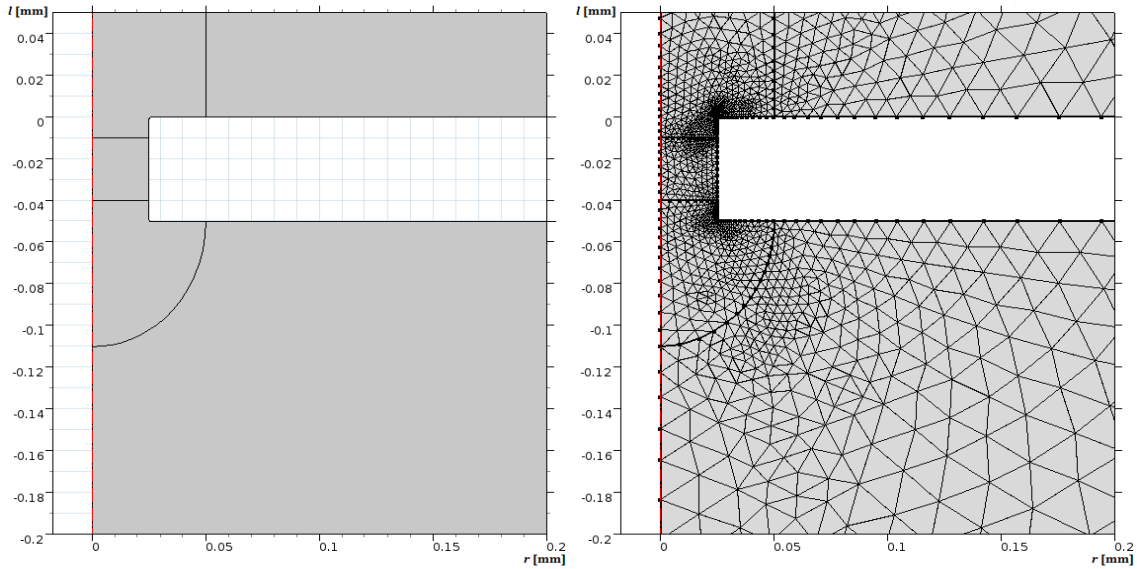


Figure B.1 – An example of the simplified injector geometry for computational modelling, showing the different partitioned regions (left), and mesh (right).

The specific fluid distribution in the regions is only enforced by the initial and in/outlet conditions. The two fluids are liquid water (incompressible) and ideal nitrogen gas. Their properties are listed in Table B.3. No fluid phase change is modelled so any cavitation effects are determined based on the comparison of the local static pressure to the liquid vapour pressure. The simulation boundaries have the following conditions:

- Axisymmetric boundary,  $r = 0$ : This is an axially symmetric boundary condition.
- Fluid Inlet,  $l = -(L_{inj} + 0.5 \text{ mm})$ : The inlet is a pressure inlet (liquid water), with a suppressed backflow constraint from the upstream fluid bulk region. The pressure condition is set to the inlet pressure.
- Walls: The simulation walls are no-slip walls.
- Fluid Outlet,  $l = 0.8 \text{ mm}$ : This is a pressure outlet (gaseous nitrogen), with a suppressed backflow constraint back into the regime. The pressure condition is set to the ambient pressure.
- Initial pseudo-boundary specifying the initial fluid separation condition,  $l = -0.01 \text{ mm}$ : This is an initial boundary condition towards the downstream end of the injector. This specifies the propellant-ambient fluid boundary and is set at ambient pressure conditions.

Table B.3 – Working fluid parameters for injector computational modelling.

Fluid	Phase	Temperature [°C]	Density [kg.m <sup>-3</sup> ]	Dynamic Viscosity [Pa.s]	Vapour pressure [Pa]
Water (pure)	Liquid	25	997	$8.9 \times 10^{-4}$	$31.69 \times 10^2$
Nitrogen (pure)	Gas	25	1.165 *	$17.8 \times 10^{-6}$	-

\* Modelled as an ideal gas, so variable parameter.

The simulation regions and boundaries were initialised with the following conditions:

- Upstream bulk and injector entrance regions:
  - Fluid: Water, liquid
  - $P = P_{in}$
  - $v_{radial} = v_{axial} = 0$
- Injector throat region:
  - Fluid: Water, liquid
  - $P = f(l) = (P_{in} - P_{amb})l + P_{amb}$  Linear pressure gradient (expected from Hagen-Poiseuille equation),
  - $v_{radial} = v_{axial} = 0$
- Downstream bulk and injector exit regions:
  - Fluid: Nitrogen, gas,
  - $P = P_{amb}$
  - $v_{radial} = v_{axial} = 0$
- Fluid boundary: As before, at the injector throat/exit region boundary. Fluid conditions specified by the adjacent regions.

### B.3. Measurements

Besides the qualitative observations, several measurement probes were specified at simulation and region boundaries. These measure the total mass flow rate, and are defined as:

- Inlet: The mass flow rate calculated using the mean fluid velocity vector along the probe using:  $|\mathbf{U} \cdot \rho_{liquid}(\pi D_{U/S}^2/4)|$
- Injector Inlet: The mass flow rate calculated using the mean fluid velocity vector along the probe using:  $|\mathbf{U} \cdot \rho_{liquid}(\pi D_{inj}^2/4)|$
- Injector Outlet: The mass flow rate calculated using the mean fluid velocity vector along the probe using:  $|\mathbf{U} \cdot \rho_{liquid}(\pi D_{inj}^2/4)|$
- Outlet: The liquid phase mass flow rate measured at the outlet.

Where  $\mathbf{U}$  is the velocity field with components in the  $l$  and  $r$  directions,  $\rho_{liquid}$  is the propellant density (DI water), and  $D_i$  are the diameters of each boundary  $i$ , located in the upstream pre-injector region ( $i = U/S$ ) and in the injector throat ( $i = inj$ ). The probes upstream of the injector outlet only use the propellant fluid density. This is not an issue since the ambient fluid will never enter the injector region. The injector outlet mass flow rate is an internally specified probe, defined as part of the fluid outlet boundary condition and implicitly considers the multiphase flow.

While mass should be conserved, there is some expected variability in the different probe measurements. Figure B.2 shows an example of the simulation mass flow rate results in the time domain for a 4 bar pressure drop over a 1-50-50 injector. Within 52 timesteps ( $8.5 \times 10^{-6}$  s) the inlet and both injector probes have converged to the steady state values  $0.044 \text{ g.s}^{-1}$  as the liquid phase flow stabilises. The outlet mass flow rate is slower to converge as the fluid propagates through the downstream regions, and it remains unsteady as the multiphase fluid flow breaks into liquid bubbles. The mass flow rate values from the four probes converge to a steady state value of  $0.0438 \text{ g.s}^{-1} \pm 0.0005 \text{ g.s}^{-1}$ , compared to the analytical orifice injector pressure drop of  $0.044 \text{ g.s}^{-1}$  (using a  $C_d = 0.8$ ). This suggests that the model captures the bulk flow, but further validation and results are discussed in the microinjector study in Chapter 7.

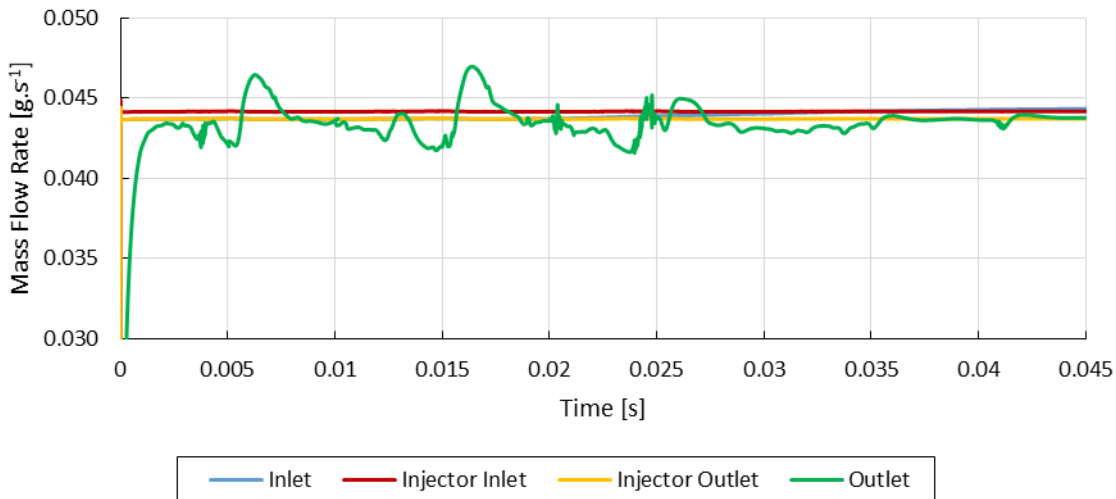


Figure B.2 – Example mass flow rate simulation data for a 4 bar pressure drop across a 1-100-50 injector.

The mass flow rate measurements and the pressure differential  $dP = |P_{in} - P_{amb}|$  from a number of simulations with different driving pressures can be used to fit a flow characterisation curve similar to experimental flow characterisation. This allows for the comparison between experimental and simulated results. In addition to mass flow rate probes, additional measurements are taken from the inspection of the finite difference nodes including:

- Minimum and Maximum pressures.
- Local flow velocities and Reynolds number.
- Local static pressure, comparing this to the liquid vapour pressure.

Plots of the static pressure and velocity magnitude results for the example simulation are shown in Figure B.3.

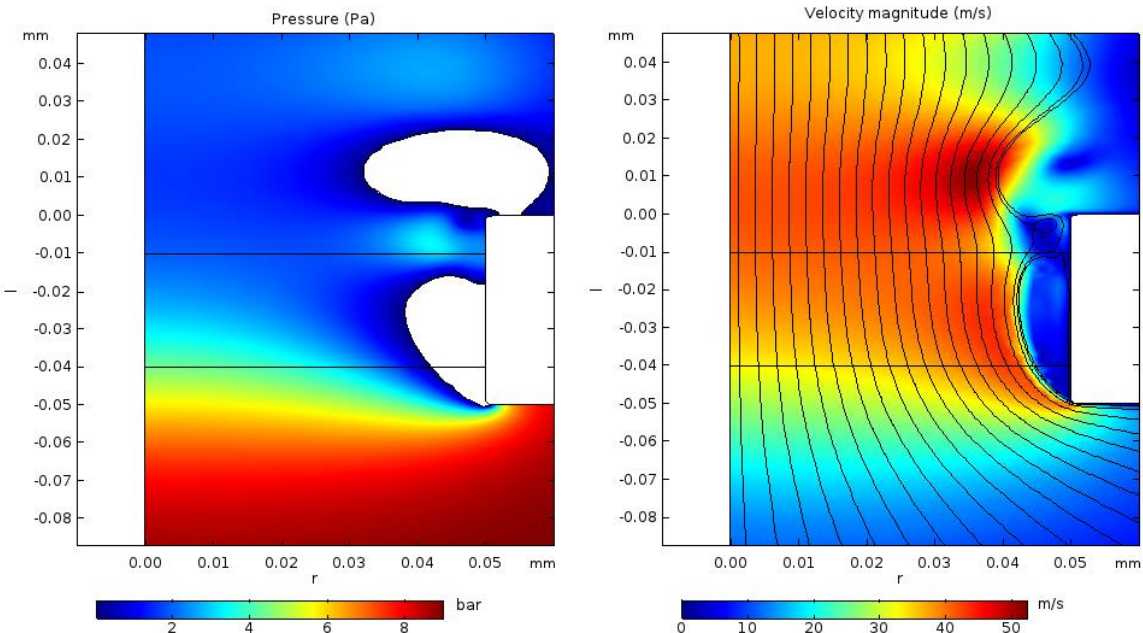


Figure B.3 – Computational results for the static pressure (left) and flow velocity magnitude (right) fields from a 4 bar pressure drop pressure drop across a 1-100-50 injector.

## B.4. Finite Difference Mesh Study

The finite difference mesh was briefly discussed above, however given the impact of the mesh topology on the results and the required computational resources; it is important to establish the sensitivity of the results to the mesh density. The built in COMSOL mesh generation package permits fine control over the element size, growth rate and curvature, with further refinement steps doubling the resolution in the regions around the injector and adding boundary layers. To simplify this process, the base mesh size (minimum and maximum element size) was set, and the meshing algorithm was allowed to select the other parameters. The parameters used to generate the base mesh are shown in Table B.4, and different levels of refinement in the regions shown in Figure B.1 were trialled to test the sensitivity of the mass flow rate with respect to the resulting mesh.

Table B.4 – A list of the base meshing parameters used for the mesh sensitivity study.

Mesh Descriptor	Maximum Element Size [ $\mu\text{m}$ ]	Minimum Element Size [ $\mu\text{m}$ ]	Maximum Growth Rate	Curvature Factor	Narrow Resolution
Extremely Coarse	165.0	5.250	1.4	1	0.9
Extra Coarse	97.50	3.750	1.3	0.8	1
Coarser	65.30	3.000	1.25	0.6	1
Coarse	50.30	2.250	1.2	0.4	1
Normal	33.80	1.500	1.15	0.3	1
Fine	26.30	0.7500	1.13	0.3	1
Finer	21.00	0.3000	1.1	0.25	1
Extra Fine	9.750	0.1130	1.08	0.25	1
Extremely Fine	9.750	0.1130	1.08	0.25	1

The steady state mass flow rate results of this study using the 1-50-50 injector are shown in the plot in Figure B.4, along with the analytical mass flow rate for a  $C_d = 0.8$ . For smaller mesh sizes (higher size descriptors on the plot), the mass flow rate converges. From these data, the ‘Fine’ base mesh with a single refinement of with injector and boundary layer were selected for all further simulations. The mass flow rate of this case is  $0.0438 \text{ g.s}^{-1}$ , within  $0.002 \text{ g.s}^{-1}$  of the maximum value, but with a computation time of 13400 s compared to 67900 s of the next finer base mesh (without any refinement). This was repeated with a reduced set of configurations for the 1-50-100 injector and found similar results.

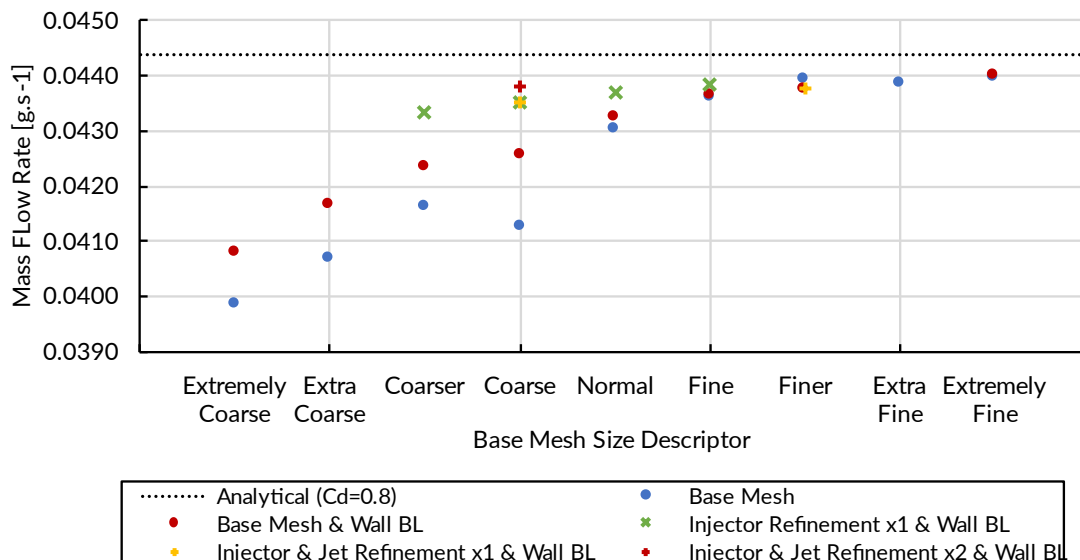


Figure B.4 – Mass flow rates results for the computational mesh refinement study.

## B.5. Simulated Injector Designs

A list of the simulated Poiseuille and orifice injector designs is given in Table B.5. The nominal simulation campaign for each injector consists of four test points defined by pressure drops of 0.25 bar, 0.5 bar, 1 bar, and 3 bar. Earlier simulations also included runs at 2 bar, 4 bar, and 5 bar but were found to not affect the results in a meaningful way since the characterisation curve fits were highly linear (see Chapter 7). In the case of a well-performing injector, i.e. one that doesn't result in a higher-than-necessary pressure drop, 3 bar is considered an upper limit as it represents an approximate 12 % /  $P_c$  pressure drop at BoL, considering the analytical model for the thruster presented in Chapter 4.

Table B.5 – A list of the simulated Poiseuille and orifice injectors designs.

Injector ID	Injector Type	Axisymmetric Diameter [ $\mu\text{m}$ ]	Axisymmetric Cross-sectional Area [ $\text{m}^2$ ]	Length [mm]	Geometric Parameter [ $\text{m}^3$ ] / [ $\text{m}^2$ ] (Poiseuille / Orifice)
5-50	Poiseuille	127	$1.267 \times 10^{-8}$	50	$3.209 \times 10^{-15}$
7-50	Poiseuille	178	$2.483 \times 10^{-8}$	50	$1.233 \times 10^{-14}$
7-100	Poiseuille	178	$2.483 \times 10^{-8}$	100	$6.165 \times 10^{-15}$
10-50	Poiseuille	254	$5.067 \times 10^{-8}$	50	$5.135 \times 10^{-14}$
10-100	Poiseuille	254	$5.067 \times 10^{-8}$	100	$2.568 \times 10^{-14}$
10-200	Poiseuille	254	$5.067 \times 10^{-8}$	200	$1.284 \times 10^{-14}$
1-20-50	Orifice	20	$3.142 \times 10^{-10}$	0.05	$9.870 \times 10^{-20}$
1-50-50	Orifice	50	$1.963 \times 10^{-9}$	0.05	$3.855 \times 10^{-18}$
1-80-50	Orifice	80	$5.027 \times 10^{-9}$	0.05	$2.527 \times 10^{-17}$
1-100-50	Orifice	100	$7.854 \times 10^{-9}$	0.05	$6.169 \times 10^{-17}$